Multi-scale modeling of damage in masonry structures

This research was partially supported by the Région Wallonne de Belgique in the frame of the Objective III programme, under grant number 215089 (HOMERE).

CIP-DATA LIBRARY TECHNISCHE UNIVERSITEIT EINDHOVEN

Massart, Thierry J.

Multi-scale modeling of damage in masonry structures / by Thierry J.
Massart. - Eindhoven : Technische Universiteit Eindhoven, 2003.
Proefschrift. - ISBN 90-386-2745-9
NUR 929
Subject headings: masonry / multi-scale modeling / damage /
homogenization methods / constitutive modeling

Printed by Universiteitsdrukkerij TU Eindhoven, Eindhoven, The Netherlands

Cover design by Paul Verspaget, based on a picture by A. & S. Massart.

Multi-scale modeling of damage in masonry structures

PROEFSCHRIFT

ter verkrijging van de graad van doctor aan de
Technische Universiteit Eindhoven, op gezag van
de Rector Magnificus prof.dr. R.A. van Santen,
voor een commissie aangewezen door het College
voor Promoties, in het openbaar te verdedigen
op dinsdag 2 december 2003 om 16.00 uur

door

Thierry Jacques Massart

geboren te Brussel, België

Dit proefschrift is goedgekeurd door de promotoren:

prof.dr.ir. M.G.D. Geers
en
prof.dr.ir. Ph. Bouillard

Copromotor:
dr.ir. R.H.J. Peerlings

Thesis carried out within a collaborative research project between
the Technische Universiteit Eindhoven (Mechanical Engineering Department) and
the Université Libre de Bruxelles (Faculty of Applied Sciences).

Multi-scale modeling of damage in masonry structures

THESE

présentée en vue de l'obtention du grade de
Docteur en Sciences Appliquées de l'Université
Libre de Bruxelles

Thierry Jacques Massart

To Christine, Alexandre and Mathieu

Contents

Notations

The following notations are used throughout the text, with the related definition in index notation between parentheses:

Vectors and tensors

Quantities

Scalar	a	
Vector	$\vec{a}$	(a_i)
Second-order tensor	$\mathbf{A}$	(A_{ij})
Fourth-order tensor	${}^4\mathbf{A}$	(A_{ijkl})

Operators

Inner product	$\mathbf{A}.\mathbf{B}$	$(A_{ij}B_{jk})$
Double inner product	$\mathbf{A} : \mathbf{B}$	$(A_{ij}B_{ij})$
	${}^4\mathbf{A} : \mathbf{B}$	$(A_{ijkl}B_{kl})$
Dyadic product	$\vec{a}\vec{b}$	$(a_i b_j)$
	$\mathbf{AB}$	$(A_{ij}B_{kl})$
Gradient operator	$\vec{\nabla}\vec{a}$	$(\partial_i a_j)$
Laplacian operator	∇^2a	$(\partial_{ii} a)$
Divergence operator	$\vec{\nabla}.\vec{a}$	$(\partial_i a_i)$

Matrix and columns

Quantities

Scalar	a
Column	$\{a\}$
Line	$\langle a \rangle$
Matrix	$[A]$

Operators

Matrix product	$[A]\,[B]$
Transposition	$[A]^T$
Inversion	$[A]^{-1}$

Any notation which has not been explicitly defined in this paragraph will be explained at its first point of use.

Chapter 1

Introduction

1.1 Structural analysis of masonry structures

Masonry is a building material that has been used extensively throughout the history. This originates from the fact that it is built with easily manufactured constituents made from widely available materials. However, the extensive use of this building technique was not always accompanied by a full understanding of the resulting structural behaviour. Most of the historical masonry structures still existing nowadays were built based on craftmanship and a trial and error approach due to a limited understanding of structural and material mechanics. The preservation of masonry structures is an increasing concern for public authorities in charge of the conservation of our cultural heritage. The technical planning of repair operations for these structures is therefore of great importance. Increasingly advanced techniques are used in structural rehabilitation in order to guarantee for instance safety under seismic activity, Mazzolani and Mandara (2002). Masonry is still widely used nowadays for aesthetic reasons and because of its good sound and heat insulation properties, Dialer (2002). However, even today, the detailed understanding of the structural behaviour of such structures is impeded by the complexity of the mechanical behaviour of the masonry material. This complexity manifests itself particularly when cracks appear as a result of foundation movements caused by differential soil settlements, or as a result of supporting structure deflections, thermal movements, moisture migration, or seismic loading.

The objective of developing a methodology for the structural analysis of masonry is to enable the prediction of its behaviour, including cracking and up to complete failure, with a proper identification of the potential failure mechanisms. This is indeed needed to allow the estimation of the residual strength and to assess the safety of structures and it consequently serves as a guide in evaluating the consequences of different repairing techniques and in optimizing them. A sound understanding of the behaviour of the - possibly damaged - material is therefore needed. Such an approach should include tractable material parameters so that their quantitative identification remains possible.

1.2 Motivation of the research

Although rules of thumb are still widely used, numerical methods have great potential in this context. They started to emerge during the last decade, and have been used as valuable tools for the analysis of masonry, e.g. Lourenço (1996); van Zijl (2000); Giordano et al. (2002); Berto et al. (2002); Pietruszczak and Ushaksarei (2003). A review of these approaches may be found in Lourenço (1998, 2002). Numerical models may be based on two methodologies. First, mesoscopic detailed descriptions consider masonry as a heterogeneous structure with separate descriptions of each constituent. At the other end of the spectrum, models intended for large-scale structural calculations are generally of a phenomenological nature, and represent the collective behaviour of constituents by closed-form macroscopic constitutive equations. Such numerical methods may be used for structural limit analyses if they are able to account realistically and efficiently for the possible failure modes of the masonry material, which evidently depend on the properties of its constituents. In order to have sufficient predictive power, they need to provide an accurate representation of the influence of mesoscopic characteristics such as the geometrical arrangement and the mechanical parameters on the strength and failure of the overall material. On the other hand such methods should be sufficiently efficient to allow large-scale structural computations. As a consequence, research dedicated to masonry modeling has been extended considerably in this sense in the last years.

Many of the existing computational approaches rely on strong simplifications, as for instance isotropy of the masonry material, Hanganu et al. (2002), or purely brittle behaviour of the constituents, Luciano and Sacco (1998). In addition, the phenomenological nature of many of these representations limits their predicting power and implies that the complexity of the behaviour is shifted to a troublesome identification of parameters. The formulation of closed-form constitutive relations which account for all the observed mechanical effects is also extremely complicated, if not impossible. The consequence is that debatable assumptions are needed in order to simplify the formulation of constitutive laws. Furthermore, a large scatter is observed in experiments used to identify material properties of the composite masonry material, making experimental identification procedures particularly troublesome. Such procedures also have to be reproduced for any new mesostructure. This renders the added value of closed-form macroscopic models questionable.

In spite of the considerable research efforts already invested in numerical approaches for masonry, a gap still remains between its mesoscopic and macroscopic representations, which complicates the exploitation of the information obtained through micro-mechanical approaches in structural computations. The development of a coupled multi-scale computational framework, allowing for interactions between both scales, would therefore constitute a major step forward in bridging these two classes of models.

1.3 Scope and outline

This dissertation focuses on the quasi-static mechanical behaviour and failure of masonry. Thermal and hygral effects are neglected and the focus is on the mechanical behaviour of planar ma-

sonry structures loaded in their plane. As a remedy to the deficiencies of existing approaches, the aim here is to use a strategy in which both relevant structural scales are integrated and interacting. With the increase of computational power in the last decade, classical (analytical or semi-analytical) homogenization methods for the representation of heterogeneous materials have been complemented by multi-scale computational approaches, Smit (1998); Feyel and Chaboche (2000); Kouznetsova (2002). The objective is to apply such a multi-scale approach for structural analyses. It is postulated that the structural failure process is dominated by the material behaviour at the scale of the constituents and by their arrangement. Consequently, and given the availability of accurate phenomenological constitutive formulations for isotropic materials, it is proposed to adopt these laws at the level of the constituents. The complexity of the overall behaviour of masonry is then naturally accounted for by a scale transition from the mesostructural to the structural scale.

The dissertation is organized as follows. As the mechanical behaviour of masonry is mainly determined by phenomena taking place at the scale of the individual bricks and mortar joints, a characterization of these is given in Chapter 2. Their main features are briefly commented upon, and relevant effects on the macroscopic behaviour of masonry such as damage-induced anisotropy and macroscopic damage localization are presented. The approach proposed in this dissertation is motivated by a brief literature survey showing that currently available macroscopic descriptions do not account sufficiently properly for these effects.

As multi-scale approaches extract the macroscopic 'constitutive' response from the mesostructure, Chapter 3 of the dissertation is devoted to the identification of a mesoscopic constitutive setting which allows to model the overall behaviour of masonry. The mesoscopic model is based on an implicit gradient damage mechanics framework, and uses a plane stress assumption. Using the periodicity of the structure, it is shown that realistic failure modes may be obtained for various loading directions based on homogenization of unit cell computations. It is also shown that macroscopic failure envelopes may be retrieved from these analyses, which compare well with typical experimental results. Accompanying induced anisotropy effects are quantified. This approach is extended in Chapter 4 in order to take three-dimensional effects into account using a generalised plane state assumption. This assumption allows to simplify a three-dimensional representation of the mesostructure to a two-dimensional representation of walls. Failure modes and failure envelopes obtained for plane stress and generalised plane state assumptions are again compared with experimental data.

The second part of the dissertation deals with the scale transition procedure allowing to couple the macroscopic, structural response to mesoscopic unit cell computations which provide the material response. Chapters 5 and 6 present a nested multi-scale computational scheme for structural analyses. Macroscopic damage localization is treated by embedding localization bands in the macroscopic description through the use of an approximate composite model. The finite size of the damage zone is properly taken into account, leading to a physically realistic prediction of the energy dissipation. The treatment of mesostructural snap-back, stemming from the mesoscopic response and emerging from the quasi-brittle nature of the constituents, is presented. Finally, the full multi-scale approach is applied in a structural computation in Chapter 7.

Chapter 2

Masonry failure and related computational methods

This chapter reviews the main features of masonry material and the requirements a material model should fulfill. The different scales of interest in the study of masonry behaviour are first pointed out. Next, the main issues which need to be addressed for the definition of a mesoscopically motivated mechanical description are identified. A brief description of the material is given, characterizing it both at the mesoscopic and at the structural level. Existing numerical methodologies for masonry computations are presented, and their respective advantages and drawbacks are discussed. The need for proper descriptions of damage-induced anisotropy and macroscopic localization of damage is emphasized. A literature survey of existing approaches which allow to represent these two features shows the potential benefits of a multi-scale description as proposed in this dissertation.

2.1 Scales of interest for masonry behaviour

As in any heterogeneous material, several length scales of interest may be identified in masonry. First, the structural or macroscopic scale, see Figure 2.1(a), on the order of meters, is identified as the typical size of masonry structures. The variables defined at this scale are related to average stress and strain fields and external loads. Most macroscopic models are formulated in terms of variables defined at this scale, all the underlying complexity being concentrated in closed-form constitutive laws. The complexity in formulating these laws is linked to the difficulty to quantify damage and its evolution at this scale.

Next, the mesoscopic scale, on the order of centimeters, is the characteristic size of the basic constituents of the masonry texture, namely bricks and mortar joints, see Figure 2.1(b). The local or mesoscopic stress, strain and damage fields in these constituents are the variables defined at this scale. Spatial variations of these fields over the bricks and joints are well visible at this scale. Effects such as damage-induced anisotropy which is observed at the macroscale is mainly governed by damage growth taking place at the mesoscopic scale.

Finally, a lower scale may be identified for each constituent, see Figure 2.1(c). This lower, microstructural scale, below one millimeter, is the scale at which the individual mechanical response of each constituent and their local interface is determined. It also has to be considered if one needs to introduce in a motivated way the interplay between the mechanical behaviour and

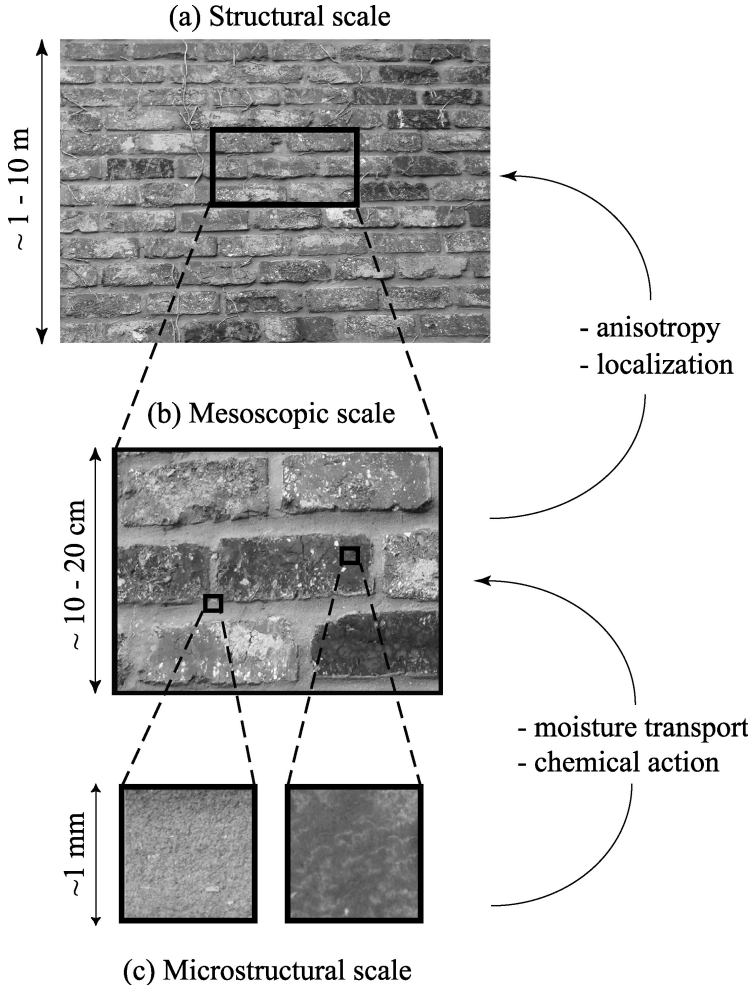

Figure 2.1: Representation of the three scales identified for masonry behaviour: (a) structural scale, (b) mesoscopic scale, (c) microstructural scale. The arrows indicate the typical upper scale effects that are caused by lower scale phenomena.

other physical processes such as water adsorption, shrinkage or environmental and chemical actions. The precise scales that have to be taken into account in modeling the behaviour of masonry depend on the type of phenomena to represent and the level of detail required. For instance, a physically motivated macroscopic representation of transport phenomena for the simulation of long term effects would require the inclusion of information from the lowest microstructural scale through scale transitions, while for a macroscopic mechanical model, the inclusion of information from the mesoscopic scale generally suffices to yield an accurate description.

At the macroscopic scale, the assumption that the heterogeneous masonry material can be represented by a homogeneous material, including in the description of the cracking process, is tacitly made in most of the available models. Applying this assumption implies the existence of a considerable scale jump between the macroscopic scale and the scale of constituents. It is evidently questionable whether a difference between the structural and the mesoscopic scales in the range of 10-100, as is the case for masonry structures, is sufficient to justify this assumption.

For such small separations of scales, the material structure which is present at the fine scale may still have a dominant influence on the behaviour observed at the coarse scale, especially if the material has a regular structure at the lower scale, as is clearly the case for masonry. A typical example thereof is the strong damage-induced anisotropy effect observed in cracked masonry.

It is emphasized that the phenomena characteristic of these different scales of representation are actually interacting, especially in the non-linear range. As the mesoscopic scale is not negligible with respect to the structural scale, the macroscopic stress and strain fields spatially vary over a length comparable to the mesoscopic size. Inelastic phenomena leading to structural failure initiate at the lowest scale and alter the stress and load distribution at the coarse scale. Such interactions call for a mesoscopically motivated macroscopic description.

2.2 Characteristics of the masonry material

The purpose of this section is to briefly describe the characteristics of the mechanical behaviour of masonry, including the desired properties of a material model. A complete and detailed review may be found in Lourenço (1996) for mechanical aspects at both scales or in van Zijl (2000) for creep and shrinkage.

2.2.1 Mesoscopic failure characteristics

In most masonry structures cracking is concentrated in the mortar joints. These joints act as weak links between the stronger bricks in the composite material. A detailed investigation of the behaviour of small scale masonry specimens containing a single joint was conducted by van der Pluijm (1999) in order to characterize the behaviour of mortar joints taking into account their interactions with bricks. In addition to the rather large experimental scatter, the values of material parameters were found to depend strongly on the type of bricks (clay or calcium silicate) and on the composition of the mortar. Some common features can nevertheless be identified. Young's modulus can be quantified for mortar from tensile tests on single joint specimens. However, this parameter is very sensitive for small joint thicknesses. A series of deformation controlled tests was done by van der Pluijm (1999) to characterize the mode I and mode II failure of mortar joints.

In mode I failure, the load-deformation curve exhibits a decrease of the stress with increasing deformation as illustrated in Figure 2.2. This decrease of strength is linked to the coalescence of microcracks towards a macroscopic crack, which is well approximated by an exponential decay. The tensile strength obtained in this type of test is governed by the failure of the interfaces between brick and mortar or by the bulk failure of mortar. The failure mode depends on the quality of the mortar, which mainly results from its composition, and on the quality of the bonding between both materials, which is influenced by the curing conditions, the porous nature of the brick material and the actual bonding area between brick and mortar. The area under the stress-displacement curve is related to the mode I fracture energy. As illustrated by the shaded area in Figure 2.2, experimental results present a large scatter in both the peak strength and the fracture energy. A rather weak correlation between the tensile bond strength and the

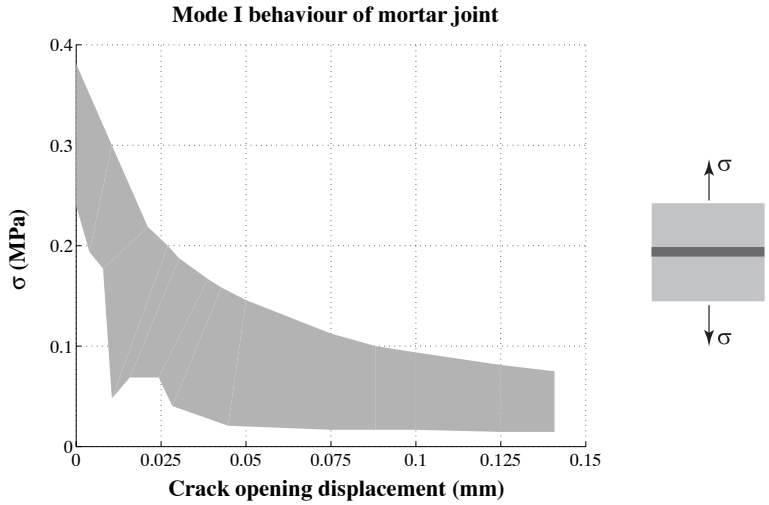

Figure 2.2: Typical tensile behaviour of mortar joint - averaged stress vs. crack displacement for clay brick masonry; after van der Pluijm and Vermeltfoort (1991). The scatter of experimental results is represented by the shaded area.

fracture energy was established experimentally in van der Pluijm (1997), depending on the type of constituent. For clay brick masonry, fracture energies were reported ranging from 0.005 to 0.015 N/mm. This order of magnitude clearly indicates that the fracture process is quasi-brittle rather than perfectly brittle as sometimes assumed, see Luciano and Sacco (1997).

The mode II behaviour of mortar joints also exhibits a gradual decrease of strength with increasing deformation, see Figure 2.3. Furthermore, the peak shear strength increases with the confining pressure, thus matching a Coulomb type of friction. Contrary to the mode I case, the shear strength exhibits a residual plateau associated to dry friction, and shows irreversible strains at a constant stress level. Mode II failure of joints is also accompanied by a dilatancy

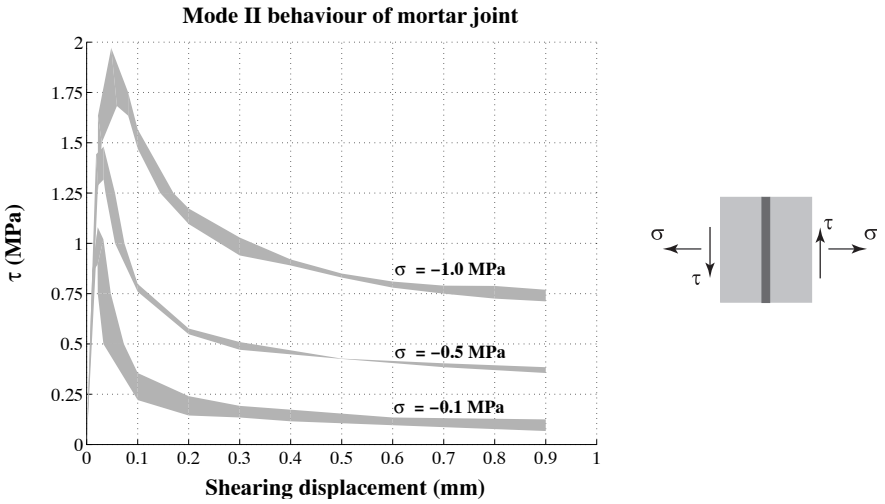

Figure 2.3: Shear behaviour of mortar joint - averaged stress vs. shear displacement for clay brick masonry and for different confining normal stresses after van der Pluijm (1992). The scatter of experimental results is represented by the shaded area.

phenomenon which is linked to the granular microstructure of the mortar. A normal uplift is observed upon shearing, the magnitude of which is dependent on the confining pressure. It may lead to a build-up of normal stresses when the normal uplift is restricted.

Note that the properties of joints summarized in van der Pluijm (1999) are strongly affected by the presence of the bricks because of water adsorption. As a consequence the reported values are characteristic of the mortar joints behaviour inside the masonry composite and differ strongly from the characteristics derived from bulk mortar tests on prisms or cylinders. It is believed that the data derived from the composite tests is more representative for the behaviour in real masonry structures because the microscopic interactions with bricks are then implicitly accounted for.

The characterization of the uniaxial compressive behaviour of mortar joints is more complicated. Compression tests are usually performed on cylinders or prisms which consist solely of mortar. They are thus not representative of the strength of joints, because interaction effects with bricks are absent. It is emphasized that the compressive strength of mortar is bounded as a result of its composition, featuring a large proportion of sand.

Experimental data related to the properties of the brick material used in masonry structures is scarce. The mechanical behaviour of brick materials is also quasi-brittle. The internal composition and the manufacturing process result in a higher cohesion and higher tensile and compressive strengths compared to mortar joints, leading to a higher mode I fracture energy. The overall properties of the bricks also depend on their geometry, e.g. on the possible presence of perforations.

2.2.2 Macroscopic characterization

As masonry material may be seen as a composite, the periodic texture defined by the stacking of the bricks results in an initial macroscopic anisotropy of the material. For instance, the effective properties of running bond masonry are orthotropic as it has two perpendicular axes of symmetry, see Figure 2.4(a). The arrows in this figure represent the periodicity of the material structure. A key macroscopic feature of masonry in the non-linear range is the stiffness degradation caused by cracking of its quasi-brittle constituents, mainly the mortar. Due to the periodic arrangement of the two phases, preferential cracking orientations are present in the

Figure 2.4: Running bond masonry: (a) initial orthotropy and periodicity, (b) damage-induced orthotropic state and (c) damage-induced non-orthotropic state

mesostructure. This may result in a second type of anisotropy, which is induced by the cracking and which is also closely connected to the mesostructure of the material. This is illustrated in Figures 2.4(b) and 2.4(c) which show two different cracking patterns. In the first case (Figure 2.4(b)), damage degrades the stiffness in the horizontal direction. However, the symmetry planes of the initial material are clearly preserved in the damaged configuration. This means that the overall behaviour is still orthotropic, although the degree of anisotropy has changed. In the other case, the initial orthotropic symmetry of the material is completely broken by the staircase crack pattern (Figure 2.4(c)). As a consequence, the overall behaviour is no longer orthotropic, but shows a more general form of anisotropy. This type of crack pattern is common in practice and easily reproduced in experimental tests performed on small scale panels, see Page (1981, 1983); Dhanasekar et al. (1985). The damage-induced anisotropy shows the need for a model to represent in a rigorous way the occurring stiffness degradation, as the type of stiffness evolution may have a strong impact on stress redistributions in structural computations.

The anisotropic mechanical behaviour of masonry manifests itself in the strong dependence of its strength on the direction of loading. Page (1981, 1983) and Dhanasekar et al. (1985) established a macroscopic failure envelope for biaxial loading of clay brick running bond masonry. This failure envelope is based on the peak strength values obtained from running bond masonry panel tests in which a uniform loading was applied proportionally. As the initial overall properties of the material are orthotropic, different biaxial envelopes were obtained depending on the orientation of the applied principal stresses with respect to the orthotropy axes (i.e. the bed and head joint orientations). The characteristic shape of this experimental envelope has in-

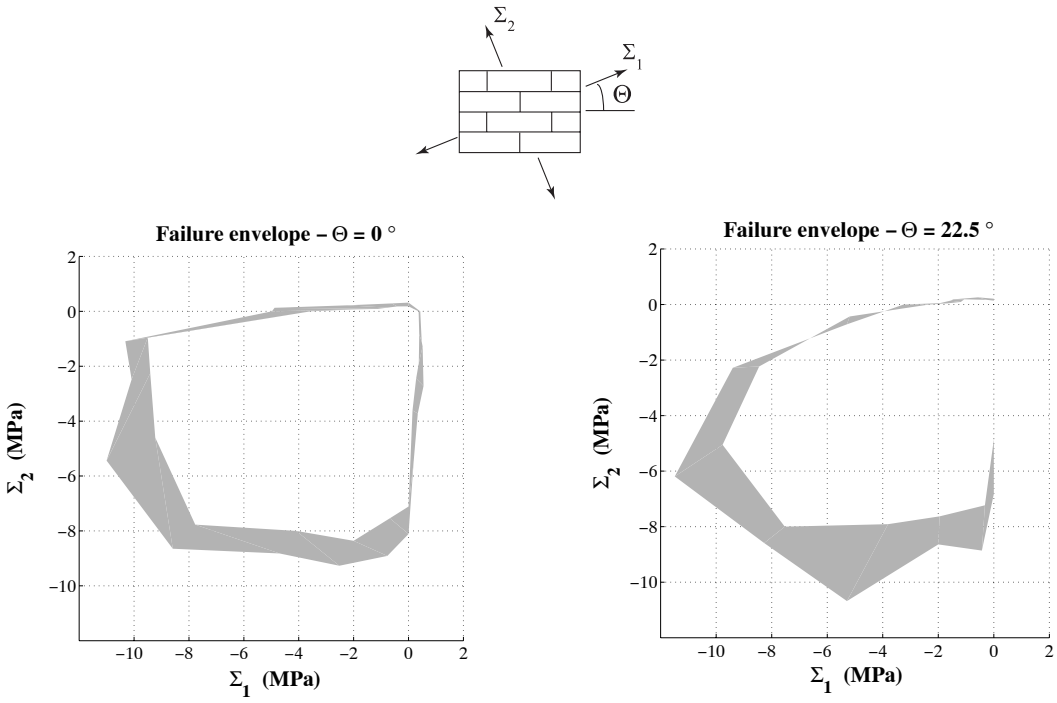

Figure 2.5: Typical failure envelopes obtained by Dhanasekar and co-workers for clay brick masonry; after Dhanasekar et al. (1985)

spired most of the so far developed phenomenological constitutive descriptions, see for instance Lourenço et al. (1997); van Zijl (2000); Berto et al. (2002). Typical experimental envelopes are depicted in Figure 2.5 with the reported experimental scatter. The non-symmetric shape of the envelopes with respect to the equibiaxial stress axis ($\Sigma_1 = \Sigma_2$) reflects the anisotropy of the overall strength. The shape of the envelope changes when the principal stress directions are inclined with respect to the bed and head joints directions, which reflects the influence of overall shear. It should however be emphasized that since such a failure envelope was obtained for proportional loading, its use for structural computations is still questionable, because cracking and related stiffness evolutions may cause considerable stress redistributions in structural computations. In other words, this may lead to strong rotations of the principal stress and strain directions and to the appearance of path dependency effects for which no information may be extracted from this envelope. Furthermore, nothing indicates that this type of envelope can be scaled to cover the softening regime, even under proportional stress loading.

Another important macroscopic effect of damage growth resides in the fact that damage localizes in narrow zones on the order of the thickness of mortar joints. Again, the consequence is that the macroscopic failure behaviour is directly related to the mesoscopic structure. This localization phenomenon should be taken into account properly in terms of its size and orientation to yield an accurate description of both the failure modes and the associated energy dissipation.

2.3 Review of masonry related computational models

The existing numerical models intended for masonry may be classified in three categories based on their objectives and on their level of mesostructural detail.

A first category uses the mesoscopic material information associated to the scale of the constituents and can therefore be referred to as ‘mesoscopic models’. This results in detailed models in which mesoscopic features such as the stacking mode are explicitly taken into account. Potential cracks are usually lumped into a discrete interface (cohesive zone), assuming that their position is known on beforehand. This type of approach was adopted by several authors, e.g. Lourenço (1996); Giambanco and Di Gati (1997); Giambanco et al. (2001). Interface laws are generally formulated using plasticity concepts, without taking into account stiffness degradation. Non-associated flow rules are used in combination with Coulomb friction laws, as in Lourenço (1996),van Zijl (2000); van Zijl et al. (2001), in order to account for dilatancy under compressive-shearing stresses. Despite the use of physically motivated mesoscopic material parameters, the compressive behaviour has to be represented by a phenomenological cap on the yield surface to take crushing into account. This is due to the fact that out-of-plane effects cannot be modeled simply using interfaces. The concentration of all inelastic phenomena in the interface elements however allows to preserve a well-posed equilibrium problem upon damage development. This approach allows in most cases the identification of the true failure mechanisms in structural applications, at least when in-plane failure occurs. It remains however dedicated to small scale computations for efficiency reasons.

At the other end of the scale spectrum, the experimental work of Page (1981, 1983) and

Dhanasekar et al. (1985) inspired several authors in the elaboration of macroscopic phenomenological models. These models include plasticity effects as in Lourenço et al. (1997), damage with stiffness degradation, see Berto et al. (2002), or both effects, Papa and Nappi (1997). They tacitly assume that the failure envelope obtained under proportional loading remains valid throughout the failure process for proportional as well as non proportional loading. In the refined model of Lourenço et al. (1997), the tensile and compressive behaviour are split and the frictional nature of the material under compressive stress states is accounted for by the use of non-associated plasticity laws. Other phenomenological approaches were proposed based on a no-tension material assumption (Cuomo and Ventura (2000), Alfano et al. (2000)) or on approaches combining the identification of critical planes with traction-separation constitutive laws, Pietruszczak and Ushaksarei (2003). In relation with stiffness degradation, it is emphasized that, despite the intensive research dedicated to this field, the representation of full damage-induced anisotropy by means of closed-form constitutive laws remains far from complete, even for initially isotropic materials. A common example of the anisotropy development is due to crack formation in concrete. Isotropic damage is an approximation which is probably not accurate enough for the representation of failure under fully general loading conditions. However, an isotropic damage representation using a scalar damage quantity has been used with some degree of success in applications related to initially isotropic materials, see for instance Geers et al. (2000). On the contrary, the assumption of isotropic damage is not acceptable for masonry as a consequence of the coupling between the initial and induced anisotropy. Even for initially isotropic materials, the representation of damage-induced anisotropy in macroscopic constitutive formulations is complex. All existing frameworks essentially make use of tensorial damage variables of order two for orthotropic damage or of higher order for more complex anisotropy evolutions. This results in elegant, but complex frameworks, see Cormery (1994); Halm (1997); Dragon (2000), featuring large numbers of parameters and/or model relations, see for instance Carol et al. (2000a,b); Godvindjee et al. (1995). This type of approach was only recently improved to include the coupling between initial and induced orthotropy by Halm et al. (2002). The identification of material specific relations and parameters in such models poses a substantial difficulty, which must be faced again for each new composition of the masonry.

The microplane concept offers an alternative approach to tensorial damage models. The constitutive behaviour in a material point is decomposed along various orientations, followed by a directional 'homogenization' step. This concept was applied to initially isotropic materials, Bažant and Prat (1989), and shown to be equivalent to a tensorial damage description by Carol et al. (1992). A first anisotropic version of this technique was proposed for creep of anisotropic clays by Bažant and Prat (1987) based on the concept of an orientation distribution function, followed by an extension by Prat and Gens (1994) to couple initial and damage-induced anisotropy. The decomposition of the initial elastic behaviour along the different directions is however not straightforward, and the related material parameter identification is also difficult.

As a second common feature, most of the macroscopic models are formulated in terms of first order continua and do not include intrinsic length scale parameters nor embedded discontinuities. This inevitably leads to ill-posedness of the description at the onset of damage localization due the loss of ellipticity of the governing equations. In numerical analyses this

causes spurious mesh sensitivity and convergence towards perfectly brittle failure. To avoid this, it is by now well accepted that some degree of non-locality can be used in such descriptions, thereby introducing a material intrinsic length scale, Bažant (1990); Bažant and Planas (1998); de Borst (2003); Peerlings et al. (2001). Other approaches are found in the literature, mainly for isotropic materials, and are based on the introduction of displacement or strain discontinuities into which the material non-linearity is lumped, while the bulk of the material remains elastic, Sluys and Berends (1998); Wells (2001); de Borst et al. (2001). For masonry, the introduction of an intrinsic length scale is however made more complex by the anisotropy, as the length parameter should reflect the anisotropic structure of the material. With the exception of the recent approach by Trovalusci and Masiani (2003), the only anisotropic damage framework introducing some kind of spatial non-locality is based on the microplane model, see Kuhl and Ramm (1999); Kuhl et al. (2000), and is restricted to initially isotropic materials. As a result, most macroscopic masonry models use the so-called crack band approach in order to avoid the pathological influence of the mesh size. This approach however completely neglects the directional character of the localizing behaviour.

In conclusion, anisotropy evolution effects combined with a mesoscopically motivated regularisation technique for damage localization seem to be extremely difficult to represent in a phenomenological constitutive setting, which explains the ongoing research in these fields.

To overcome these problems, some research effort has been invested in the last decade in the definition of links between the mesoscopic and macroscopic representations of masonry, as a part of a wider field of research on homogenization strategies for heterogeneous materials. Two main objectives are pursued with this type of method.

The first aim resides in the identification of macroscopic strength or elastic stiffness parameters based on mesoscopic information, usually on unit cell computations. The overall material properties are then obtained by fitting phenomenological macroscopic constitutive laws to the results of unit cell computations. This methodology allows to avoid costly experimental identification procedures at the macroscopic scale. Most of the work on homogenization of masonry has been concentrated on this objective. The linear elastic case was studied extensively in the literature. Approximate homogenization techniques were applied in Pande et al. (1989) to identify apparent elastic moduli of masonry. Methods based on periodic homogenization or asymptotic homogenization (Bakhvalov and Panasenko (1989), Sanchez-Hubert and Sanchez-Palencia (1992)), requiring the solution of a boundary value problem, were applied to the elastic behaviour of masonry by Anthoine (1995) and Cecchi et al. (Cecchi and Di Marco (2000); Cecchi and Rizzi (2001); Cecchi and Di Marco (2002); Cecchi and Sab (2001)). A physically appealing approximate approach was recently proposed by Zucchini and Lourenço (2002) for the identification of the elastic moduli. All these approaches are however not easily extended to the non-linear range as they strongly depend on a linearity assumption. Homogenization schemes have also been used to identify non-linear material parameters or ultimate strength for some specific sets of loading conditions. Approximate two-step homogenization procedures based on homogenization of layered media were used by Lourenço (1996) for the identification of the plastic behaviour of masonry. Anthoine applied periodic homogenization concepts for the identification of strength and failure mechanisms of running bond masonry under uniaxial

horizontal and vertical compression, Anthoine (1997); Pegon and Anthoine (1997). Finally, a more analytical approach to the ultimate strength of masonry was proposed by De Buhan and De Felice (1997).

A second possible objective of homogenization is to include the scale bridging explicitly in structural computations. This is straightforward if the constitutive response of the material is available in a closed format. But it can also be done by nesting a computational mesoscopic scale model in the macroscopic, structural computation. To the knowledge of the author, only few approaches reported in the literature present these features. Luciano and Sacco (1997, 1998) presented a nested solution scheme based on periodic homogenization. An elastic-brittle behaviour of mortar and a linear elastic behaviour of bricks were however assumed. As mentioned earlier, these assumptions are rather questionable from a physical standpoint. Another approach is due to Trovalusci and Masiani (1999, 2003). It consists in the definition of a Cosserat medium equivalent to a discrete system of rigid bricks connected by translational and rotational springs, the non-linear behaviour of mortar joints being approximately taken into account. An appealing feature of this model is the natural derivation of an internal length scale associated to the periodic stacking of the material, allowing the problem to remain well-posed when damage localization takes place. Brick cracking is however not included in the description, and the identification of the material properties characterizing the springs is not straightforward.

2.4 Adopted strategy

The most difficult issue in setting up an accurate modeling strategy is related to the definition of a constitutive law. The scale bridging models mentioned in Section 2.3 are at present the most developed, yet each of them is restricted to particular assumptions. The essential difficulty in those models resides in capturing the complex behaviour of masonry in closed form relations. A multi-scale computational approach could offer an attractive and flexible solution to this problem. This type of strategy, Smit (1998); Feyel and Chaboche (2000); Kouznetsova (2002), is based on a scale transition to extract macroscopic quantities from mesoscopic computational analyses which are nested in the structural computations. This avoids the formulation of closed-form macroscopic constitutive laws and therefore allows one to consider complex mesostructure, which may furthermore evolve during the loading process. This higher flexibility in the description of the material response is obtained with a higher computational cost linked to the solution of the mesoscopic analyses. Therefore, the mesoscopic representation will be restricted to isotropic damage modeling of the constituents, as the macroscopic anisotropy evolution is mainly invoked through the stacking mode in the material. The mesoscopic behaviour of the constituents will be represented by phenomenological laws, without a detailed representation of the microstructural scale of the material. The complexity of the overall anisotropy evolution is then captured in a natural way. The inherent versatility of this methodology seems to be well suited to the complexity of the masonry behaviour. This dissertation proposes a multi-scale approach adapted for this type of computation, by developing a dedicated meso-scale constitutive setting and by adapting the scale transitions.

Chapter 3

Mesoscopic modeling of failure and damage-induced anisotropy in brick masonry

Masonry may be considered macroscopically as a periodic two-phase material. The possible occurrence of cracking in each of the phases leads to a complex mechanical behaviour. Most existing macroscopic models defined for such materials are phenomenological and either isotropic or orthotropic. In this paper, a scalar damage model is used in a mesoscopic study to assess the need for incorporating non-orthotropic induced anisotropy in macrocopic models. Based on unit cell computations under a plane stress assumption, it is shown that scalar damage meso-models allow to obtain realistic in-plane damage patterns encountered in experiments. Results suggest that at the meso-scale, it is possible to use a scalar damage model for the individual phases which naturally leads to an overall anisotropy evolution. This evolving macroscopic anisotropy is illustrated using a numerical homogenization procedure to identify the degraded stiffness associated to the obtained damage patterns. It is shown that the characteristic shape of experimentally observed failure envelopes for masonry may be reproduced by unit cell computations, as far as in-plane failure mechanisms are concerned.

3.1 Introduction

The technical planning of repair operations is of prime importance for the maintenance of historical masonry structures. These operations usually require an estimation of the residual strength of structures to analyse and optimize the consequences of the different repairing techniques. Numerical simulations are a potentially useful tool in this respect if they are able to account realistically for the possible failure modes of such a complex material.

A thorough experimental characterization was performed by Dhanasekar et al. (1985) in order to identify a macroscopic failure surface for a given masonry mesostructure together with the triggered failure modes. Figure 3.1 shows that the failure patterns obtained in this study substantially differ depending on the loading case. The influence of the head and bed mortar

This chapter is reproduced from: T.J. Massart, R.H.J. Peerlings and M.G.D. Geers, Mesoscopic modeling of failure and damage-induced anisotropy in brick masonry, Submitted for publication in European Journal of Mechanics A/Solids.

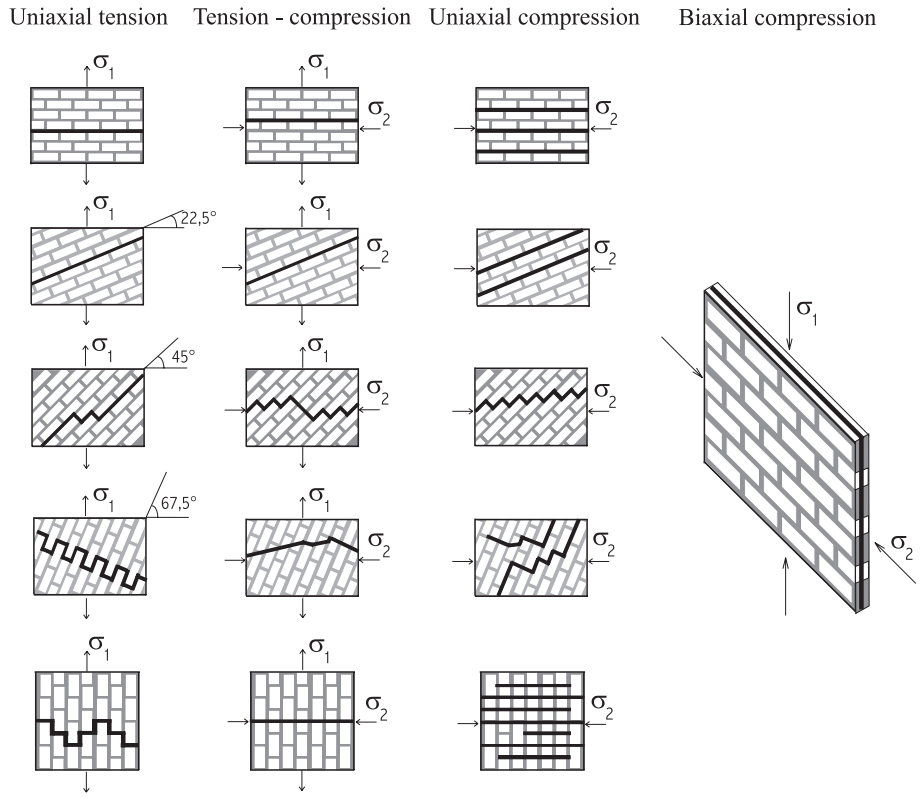

Figure 3.1: Typical failure patterns in terms of principal stresses, resketched after Dhanasekar et al. (1985)

joints is determinant for biaxial tension and tension-compression stress states, in which fracture occurs almost exclusively in the joints. In the case of biaxial compression, a transition is found between in-plane failure mechanisms for high principal stress ratios and out-of-plane failure for nearly equal principal compressive stresses. Failure envelopes were also obtained from these experiments by recording the stress state at the peak load for all loading paths. These failure envelopes inspired various authors in the definition of macroscopic loading surfaces used in damage or plasticity models. It should however be emphasized that the failure points defining these envelopes were obtained for different failure patterns including patterns corresponding to non-orthotropic induced anisotropy. Therefore, the post-peak behaviour of masonry corresponding to these points might substantially differ. This fact is usually neglected in macroscopic models although it may affect stress redistribution in structural analyses in a significant way.

Structural calculations usually apply material laws based on homogeneous equivalent descriptions, Lourenço et al. (1997); Berto et al. (2002); Papa (1996). Scale transitions from mesoscopic to macroscopic representations of masonry material have been built by several authors for the linear elastic case, see e.g. Cecchi and Di Marco (2000, 2002); Anthoine (1995). Unfortunately these scale jumps are still missing for the fully non-linear range. As a consequence, macroscopic non-linear models are usually based on weakly motivated phenomenological assumptions. In particular, the influence of the initial mesostructure and its orthotropy on the damage induced anisotropy is poorly accounted for in macro-models. Most aspects of the

macroscopic behaviour (among which the evolving anisotropy) actually find their origin in the mesostructure of the material. As can be noticed from Figure 3.1, preferential damage orientations imposed by the orientation of mortar joints are linked to the mesostructural stacking mode and cause a strong coupling between initial and damage-induced anisotropy at the macroscale, a fact that is almost systematically neglected in the elaboration of macro-models. In most models, the principal directions of damage are indeed fixed and aligned with the initial orthotropy axes as in Lourenço et al. (1997); Berto et al. (2002); Papa (1996). This assumption neglects the effect of the periodic offset of head joints, and may therefore not always be justified.

As initial and induced anisotropy are so closely related to the mesostructure, the idea pursued in this paper is that the essential character of the anisotropy evolution can be studied using a separate isotropic model for each of the constituents at the mesoscopic scale. Our first objective is to show that realistic failure patterns may be obtained on the basis of nowadays well-established mesoscopic damage models. Once this has been established, the mesoscopic model will be used to study the macroscopic anisotropy evolution and its interaction with the initial orthotropy. The analysis will be limited to in-plane effects and to a plane stress state. This implies that some failure patterns and failure loads in the biaxial compression regime may be unrealistic, where out-of-plane failure is to be expected (Figure 3.1). The implication of this limitation and possible enhancements will be studied in forthcoming work.

Section 3.2 of this paper details the simplifying assumptions made, recalls basic principles of (non-local) scalar damage mechanics and details the damage criteria used to represent each constituent. The way unit cell computations and numerical homogenization principles are used to assess the macroscopic degradation behaviour are next presented in Section 3.3. Typical failure patterns obtained for various loading schemes are compared qualitatively with experimentally obtained failure modes in Section 3.4. The corresponding homogenized degraded stiffness is also computed in order to illustrate the material symmetry evolution associated to the mesoscopic damage growth and propagation. In Section 3.5, the macroscopic failure envelope obtained from the unit cell computations is presented. The influence of the assumed description of induced anisotropy used in phenomenological models on the post-peak response is illustrated in Section 3.6 in order to emphasize the importance of taking into account full anisotropy evolution.

3.2 Mesoscopic non-local scalar damage model

3.2.1 Modeling assumptions

The mechanical behaviour of masonry material is determined by a large number of factors. At the mesoscopic scale, the failure of masonry is governed by different phenomena, i.e. failure of each of the constituents and of the interface between them. Each of these phenomena may call for detailed and complex computational representations. A complete and accurate representation of the bulk failure of each constituent would for instance require the inclusion of anisotropic damage effects. The failure of the interface between both constituents is even more complex as it results from several effects, such as shrinkage cracks, penetration of cement

into the brick or poor workmanship. The resulting complex mechanical behaviour of these interfaces can therefore be modeled by the use of cohesive zones. The focus in this contribution is set on the extraction of macroscopic behaviour features from the mesoscopic scale. A considerable simplifying assumptions will thus be introduced in order to identify a number of mesoscopic phenomenological description. It should allow to capture the average strength and stiffness degradation correctly for all stress states, as well as to represent the underlying damage patterns.

In this spirit, the average response of the mortar joints is frequently represented with cohesive surface elements as in Lourenço (1996). This type of formulation leads to effective computations, with the possibility to incorporate in a natural way plasticity effects and independent mode I and mode II responses. On the other hand, such formulations are impeded by several difficulties. Their use may lead to stress oscillations or to mesoscopic bifurcations when mode I brick cracking is incorporated. The general representation of brick cracking is not straightforward since multiple or diagonal cracking is difficult to obtain. Geometrical corrections also have to be introduced to account for the real geometry of the constituents. Most importantly, the use of cohesive zones does not allow an easy representation of out-of-plane effects responsible for biaxial compressive failure, as will be dealt with in Chapter 4.

As a result, the mortar joints are here represented with a continuum approach. In contrast with the cohesive surface approach, this allows to include the Poisson effect in the mortar joints, to account for the real dimensions of bricks and joints, and to get a better description of cracking evolution from head to bed joints. The interface between both constituents is assumed to be perfect and interface failure is thus not explicitly taken into account. Its effect on the average behaviour is however incorporated by a modification of the tensile characteristics of mortar (strength and mode I fracture energy) such that they represent the tensile bond strength. The compressive strength and bulk material properties of mortar are preserved in the model. A scalar damage model is used for mortar and bricks, which are both considered as isotropic materials. This assumption is motivated by the fact that the geometrical arrangement of the constituents is mainly responsible for the macroscopic induced anisotropy, whereas local anisotropy in the constituents may be neglected in the overall response of the material.

The study is performed under a plane stress assumption. This choice is often made given the small thickness with respect to the in-plane dimensions of walls. However, the consequence of this assumption is that the out-of-plane components of the stress tensor are assumed to vanish throughout the thickness of the wall, which means that the out-of-plane failure mode under biaxial compression cannot be described.

3.2.2 Continuum damage mechanics on the basis of a non-local implicit gradient framework

Damage mechanics is a well-established tool to incorporate effects of the material degradation into the constitutive behaviour of the single phases at the mesoscopic scale. Application of local damage mechanics theories to cracking in quasi-brittle materials may result in loss of ellipticity of the equilibrium problem causing loss of well-posedness. Spurious mesh sensitivity and con-

vergence towards physically non-admissible solutions are the numerical outcomes. Therefore, a non-local character of the constitutive relation is incorporated using a strain based implicit gradient damage framework, see Peerlings et al. (1996). In this framework, a damage criterion allows to determine whether a strain state change is accompanied by further damage

$$f(\overline{\varepsilon}_{eq}, \kappa) = \overline{\varepsilon}_{eq} - \kappa \leq 0 \tag{3.1}$$

with the use of the Kuhn-Tucker relations

$$f \leq 0 \qquad \dot{\kappa} \geq 0 \qquad f\ \dot{\kappa} = 0 \qquad \kappa\,(t=0) = \kappa_i \tag{3.2}$$

where κ represents the ultimate non-local equivalent strain state experienced so far by the material point (or the initial value κ_i if this threshold has not been exceeded yet); $\overline{\varepsilon}_{eq}$ is a non-local averaged equivalent strain introduced as the solution of the following partial differential equation incorporating a material intrinsic length scale in the constitutive setting, Peerlings et al. (2001)

$$\overline{\varepsilon}_{eq} - l_c^2 \nabla^2 \overline{\varepsilon}_{eq} = \varepsilon_{eq} \tag{3.3}$$

together with a natural boundary condition for the non-local strain field at the boundary

$$\vec{\nabla}\overline{\varepsilon}_{eq}.\vec{n} = 0 \tag{3.4}$$

and ε_{eq} is a local equivalent (damage-sensitive) scalar measure of the tensorial strain state. A damage evolution law relates the value of damage to the most severe non-local strain experienced, κ,

$$D = D(\kappa) \tag{3.5}$$

Finally, the stress-strain relationship is formulated in a standard continuum damage setting

$$\boldsymbol{\sigma} = (1 - D)\ {}^4\mathbf{L} : \boldsymbol{\varepsilon} \tag{3.6}$$

Details on the solution of equation (3.3) coupled to the static equilibrium equation may be found in Peerlings et al. (1996).

Care should be taken when using the non-local averaging procedure with two-phase materials in which the constituents' moduli differ strongly. If the composite were treated as a single domain, continuity of the $\overline{\varepsilon}_{eq}$ field would be prescribed across interfaces between the materials, and the strain field in the soft phase would strongly influence the non-local field in the stiff phase, thereby causing premature damage initiation in the stiffest material. Because of the penetration of cement in the brick during curing, it is recognized that some non-local interaction between the constituents may actually be present. A detailed mesoscopic modeling could therefore be incorporate such an effect. However, since the objective is here to describe the macroscopic effect of mesoscopic damage growth, the non-local strain field is allowed to be discontinuous at interfaces between bricks and mortar joints to avoid unrealistic results. Note that this implies that interfaces are considered as internal boundaries and that consequently the natural boundary condition (3.4) is applied to the non-local strain field at interfaces. Physically, this means that the non-local interaction acts within each of the materials, but is not allowed to cross the interface between them. The standard interaction between both materials however is still present through the displacement field and tractions.

3.2.3 Failure criteria and damage evolution laws for the constituents

Two ingredients of the damage model described in the previous Section are material dependent: the damage loading function, or actually the equivalent strain $\varepsilon_{eq}(\boldsymbol{\varepsilon})$, and the damage evolution law $D(\kappa)$. These relations are now defined for each of the constituents. The loading functions should reflect the different sensitivities to shear and the different tensile and compressive strengths of the materials. A criterion similar to the one developed for concrete is chosen for bricks because of their comparable values of cohesion and their similar resistance to shear stresses. For the plane stress case, a modified von Mises criterion has been successfully applied to concrete damage, Geers et al. (2000). In this criterion, a dependency on the first stress invariant is added to the classical von Mises criterion to accommodate different tensile and compressive responses. The criterion is expressed using the ratio k between the uniaxial compressive and tensile strengths. Its transformation into strain space is used in the considered strain-based scalar damage model:

$$\varepsilon_{eq} = \frac{(k-1)\, I_1}{2k\,(1-2\nu)} + \frac{1}{2k}\sqrt{\frac{(k-1)^2\,(I_1)^2}{(1-2\nu)^2} + \frac{2kJ_2}{(1+\nu)^2}} \tag{3.7}$$

with the strain tensor invariants defined for the plane stress case as

$$I_1 = \frac{1-\nu}{1-2\nu}\,(\varepsilon_x + \varepsilon_y) \tag{3.8}$$

$$J_2 = 2\left(\varepsilon_x^2 + \varepsilon_y^2 - \varepsilon_x\varepsilon_y\right) + \frac{2}{3}\gamma_{xy}^2 + \frac{2\nu}{(1-\nu)^2}\,(\varepsilon_x + \varepsilon_y)^2 \tag{3.9}$$

The mortar damage criterion has to feature a higher shear strain sensitivity than the criterion used for bricks. Several authors postulated a Coulomb friction law for interface plasticity models in masonry modeling, Luciano and Sacco (1997); Lourenço (1996). In order to avoid the normal discontinuities present in the Mohr-Coulomb criterion for 2D continuum elements, a Drucker-Prager criterion type is used here, together with a compressive cap to limit the admissible biaxial compressive states. Its analytical form is also expressed using the invariants of the strain tensor. Quantitatively different linear expressions are used for the classical Drucker-Prager criterion and the limiting compressive part as illustrated in Figure 3.2. The classical

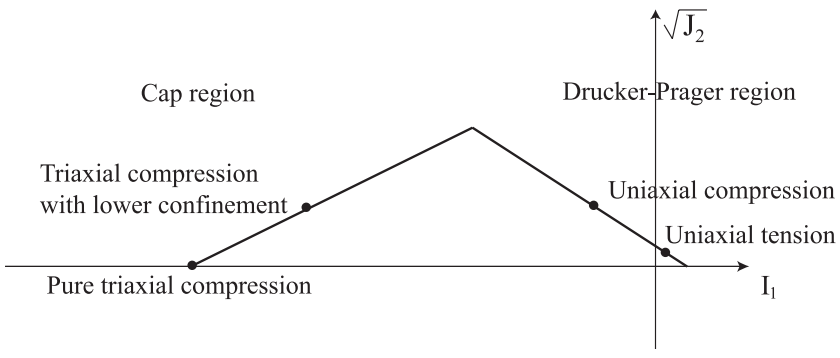

Figure 3.2: Drucker-Prager type criterion with compressive cap used for mortar

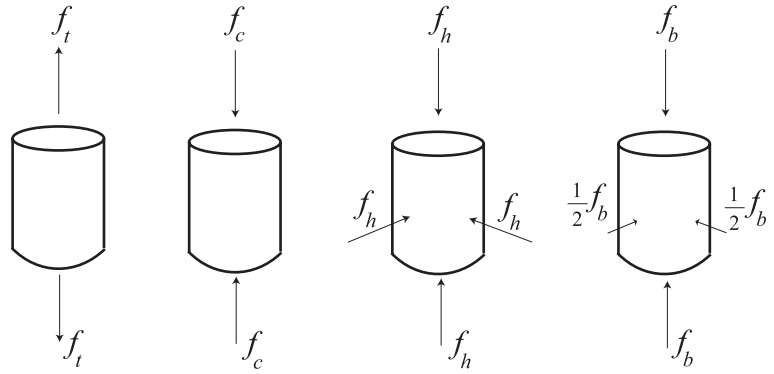

Figure 3.3: Tests for identification of mortar damage criterion

Drucker-Prager part is controlled by the uniaxial tensile and compressive strengths. The compressive part may be identified from a pure triaxial compressive strength test and a triaxial compressive test where the confining pressure is not equal to the major principal stress, as illustrated in Figure 3.3. The following expression then follows for the mortar criterion in terms of the proposed identification tests

$$\begin{aligned} \varepsilon_{eq} &= \frac{A}{(1-2\nu)} I_1 + \frac{B}{(1+\nu)}\sqrt{J_2} \qquad \text{if} \qquad \frac{\sqrt{J_2}}{(1+\nu)} \geq \frac{A-C}{D-B}\frac{I_1}{(1-2\nu)} \\ \varepsilon_{eq} &= \frac{C}{(1-2\nu)} I_1 + \frac{D}{(1+\nu)}\sqrt{J_2} \qquad \text{if} \qquad \frac{\sqrt{J_2}}{(1+\nu)} \leq \frac{A-C}{D-B}\frac{I_1}{(1-2\nu)} \end{aligned} \tag{3.10}$$

where

$$\begin{aligned} A &= \frac{f_c - f_t}{2f_c} \\ B &= \sqrt{3}\frac{f_c + f_t}{2f_c} \\ C &= -\frac{f_t}{3f_h} \\ D &= 2\sqrt{3}\frac{f_t}{f_b} - \frac{4}{\sqrt{3}}\frac{f_t}{f_h} \end{aligned} \tag{3.11}$$

The criteria for bricks and mortar are represented in principal stress space for the material parameters used in the sequel and for different levels of equivalent strain measure in Figure 3.4 where iso-ε_{eq} curves are shown. The same format of damage evolution law as proposed in Geers et al. (2000) was used for both constituents

$$D = 1 - \frac{\kappa_i}{\kappa}\left[(1-\alpha) + \alpha e^{-\beta(\kappa-\kappa_i)}\right] \tag{3.12}$$

where α and β control the softening behaviour and κ_i is the threshold for damage initiation. This law gives exponential softening for uniaxial loading of an homogeneous body. It is emphasized that the chosen equivalent strain definitions are homogeneous of degree one in terms of the strain tensor components and do not allow for an independent representation of mode I and mode II energy dissipation in the constituents.

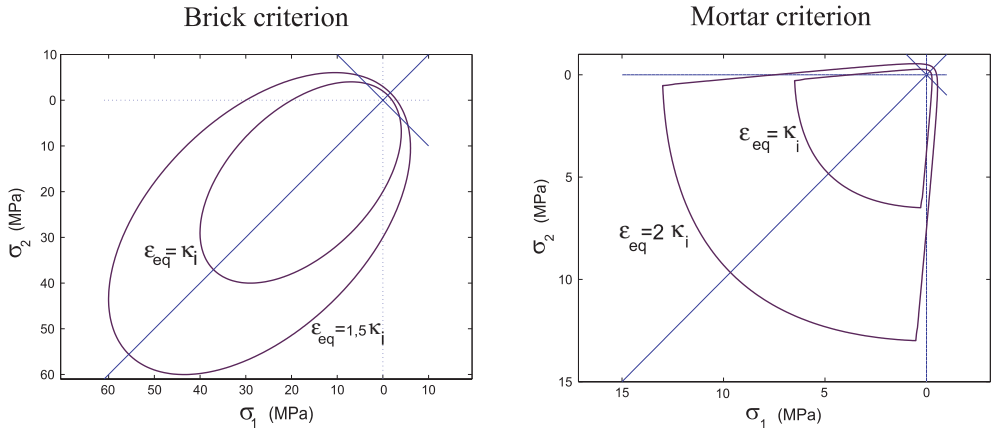

Figure 3.4: Modified von Mises and capped Drucker-Prager mesoscopic damage criteria in principal stress space (plane stress)

Finally, it should be emphasized that the internal length parameter l_c entering the non-local formulation sets the width of the localization zone. It should ideally be identified experimentally from full field measurements and may even be made non constant, see Geers et al. (1998). Bažant and Planas (1998) advocated that this parameter could be related to the size of the largest heterogeneity in the material. Values on the order of 1 mm are classically used for concrete and according to this last argument the value used for mortar should be lower because of the charateristic size of its microstructure. However, quantitatively, this type of information for masonry mortar is not available in the literature. Because of the lack of precise experimental information, and given the fact that the mortar damage in our calculations represents the collective effect of mortar damage and interface failure, the internal length parameter value will be set equal to that of the brick, even though damage will spread over the whole joint thickness in that case. With the use of such an internal length value, it could be argued that the constitutive setting used for mortar tends towards a cohesive zone description. The use of classical continuum laws however allows to take other features into account as already mentioned (Poisson effect, real geometry, interaction between damaging head and bed joints). This internal length is still much lower than the length of the joints, such that damage propagation along the length of the joints will nevertheless be realistic. The latter is judged to be most dominant in the development of mesoscopic failure patterns.

3.3 Unit cell computations

3.3.1 Periodicity conditions

One of our objectives is to verify whether a scalar damage model is able to represent the main in-plane failure mechanisms encountered experimentally. Failure patterns will be determined here assuming perfect periodicity of the masonry texture and uniform loading (assuming distributed cracking locally). Together, these assumptions imply periodicity of the mesoscopic mechanical fields, Smit (1998); Anthoine (1995); Kouznetsova (2002). Computations can therefore be

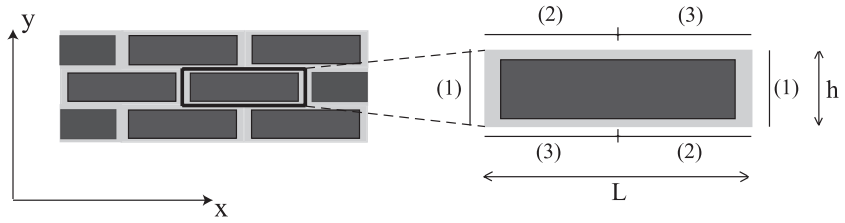

Figure 3.5: Unit cell definition (running bond masonry); numbers indicate periodicity relations

performed on a single unit cell in which the entire local mesostructural information is present. The equilibrium boundary value problem on the cell will be solved using the finite element method, in which the displacements and non-local strain fields are interpolated independently, see Peerlings et al. (1996). The periodic cell may be defined as one brick surrounded by half a mortar joint as illustrated in Figure 3.5. The running bond stacking of bricks is reflected in the periodicity tyings at the cell boundary, which is split into six parts, tied two by two as indicated in Figure 3.5. For each pair, it must be ensured that neighbouring deformed cells still 'fit together', or equivalently that the tractions $\boldsymbol{\sigma}.\vec{n}$ are anti-periodic. In a small strain context, the displacement field structure ensuring periodicity of mesoscopic mechanical fields (called strain-periodic displacement field) has the form (Smit (1998); Anthoine (1995))

$$\vec{u}\,(\vec{x}) = \mathbf{E}.\vec{x} + \ \vec{w}\,(\vec{x}) \tag{3.13}$$

where $\mathbf{E}$ is the constant overall strain tensor, $\vec{x}$ is the position vector of a point in the cell and $\vec{w}$ is a fluctuation displacement field which is unknown inside the unit cell and forced to be periodic at its boundary. It may be shown using Stokes' theorem that the macroscopic strain tensor is the volume average of the mesoscopic strain tensor:

$$\begin{aligned} \frac{1}{V}\int_V \boldsymbol{\varepsilon}\,(\vec{u})\,dV &= \frac{1}{V}\int_V \nabla^{sym}\,(\mathbf{E}.\vec{x})\,dV + \frac{1}{V}\int_V \nabla^{sym}\vec{w}\ dV \\ &= \mathbf{E} + \frac{1}{V}\int_{\partial V} (\vec{w}\ \vec{n})^{sym}\,dS = \mathbf{E} \end{aligned} \tag{3.14}$$

where V indicates the cell volume and the last integral vanishes due to the periodicity of $\vec{w}$ and the anti-periodicity of $\vec{n}$ at the coupled boundaries. The Hill-Mandel work equivalence is classically used in order to link the mesoscopic and overall virtual works, Anthoine (1995)

$$\boldsymbol{\Sigma} : \delta\mathbf{E} = \frac{1}{V}\int_V \boldsymbol{\sigma} : \delta\boldsymbol{\varepsilon} dV \tag{3.15}$$

which results in the expression of the overall stress as the average of the mesoscopic stress tensor

$$\boldsymbol{\Sigma} = \frac{1}{V}\int_V \boldsymbol{\sigma} dV \tag{3.16}$$

The use of non-local damage in the mesoscopic unit cell computations involves the solution of a coupled set of partial differential equations, Peerlings et al. (1996). In order to implement periodicity of all mechanical fields, periodicity tyings are applied for the non-local strain field

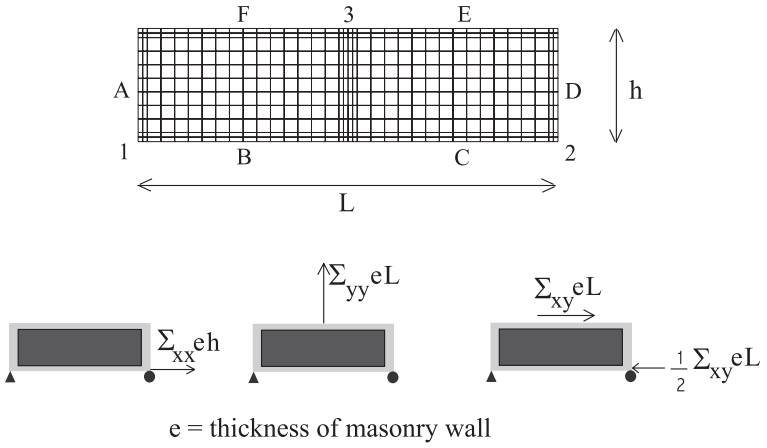

Figure 3.6: Periodicity conditions, controlling nodes and loading modes for running bond masonry cell: (a) macroscopic horizontal tension (b) macroscopic vertical tension (c) macroscopic shear for the running bond cell

as well as the displacements at the coupled boundaries of the cell. The overall loading is applied through three controlling nodes (numbers 1-3 in Figure 3.6) by applying the three macroscopic stress components via the forces indicated in Figure 3.6 (see Anthoine (1995); Smit (1998) for formal justifications). The periodicity conditions for edges A-F can then be formulated in terms of the controlling nodes as

$$\begin{aligned} \vec{u}_D &= \vec{u}_A + \vec{u}_2 - \vec{u}_1 \\ \vec{u}_E &= \vec{u}_B + \vec{u}_3 - \vec{u}_1 \\ \vec{u}_F &= \vec{u}_C + \vec{u}_3 - \vec{u}_2 \\ \overline{\varepsilon}_{eq,D} &= \overline{\varepsilon}_{eq,A} \\ \overline{\varepsilon}_{eq,C} &= \overline{\varepsilon}_{eq,F} \\ \overline{\varepsilon}_{eq,B} &= \overline{\varepsilon}_{eq,E} \end{aligned} \tag{3.17}$$

It is emphasized that the periodicity assumption also implies that the damage development will be periodic. The periodicity of the displacement fluctuation field $\vec{w}$ coupled to the periodicity of the mesostructure contained in the unit cell (geometry and material properties) leads to periodic mesoscopic stresses and strains. This means that the localised failure patterns obtained in experiments (Figure 3.1) are represented in a distributed manner, obtained by translating the periodic cell. The correspondence between experimental failure modes and their appearance on the unit cell is shown in Figure 3.7 for a selection of cases from Figure 3.1. The assumption of a periodic distribution of damage that we have used here clearly is not satisfied all the way until

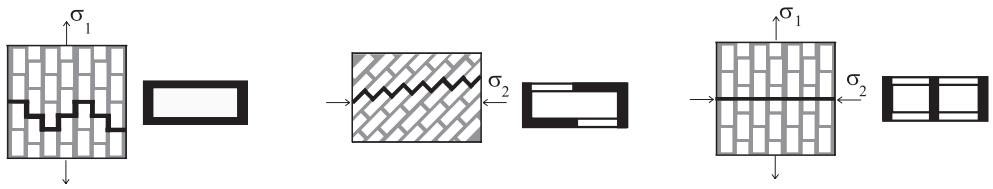

Figure 3.7: Experimentally observed failure modes and equivalent damage patterns on the unit cell

final failure in reality. At some stage of the degradation process, damage growth may localise in a limited part of the entire structure, ultimately leading to a single crack path. During this localization phase, the periodicity conditions which we are imposing upon the cell may be too constraining. However, it is believed that a reasonable representation of the overall behaviour within this localization zone can nevertheless be obtained using these conditions. This also suggests that this limitation does not influence significantly the peak load values deduced here.

3.3.2 Homogenization for fixed damage states

In order to illustrate the macroscopic anisotropy evolution, the stiffness of the cell has been determined in terms of the overall strain tensor $\mathbf{E}$ and the overall stress tensor $\mathbf{\Sigma}$ for fixed damage states. The fourth order tensor which relates $\mathbf{E}$ and $\mathbf{\Sigma}$ can be regarded as the elasticity tensor of an homogeneous elastic material with effective material properties equal to those of the damaged mesostructure. The relevant components with respect to the considered cartersian vector basis (see Figure 3.5) are given by

$$\begin{bmatrix} \Sigma_{xx} \\ \Sigma_{yy} \\ \Sigma_{xy} \end{bmatrix} = \begin{bmatrix} \mathrm{L}^{hom}_{1111} & \mathrm{L}^{hom}_{1122} & \mathrm{L}^{hom}_{1112} \\ \mathrm{L}^{hom}_{2211} & \mathrm{L}^{hom}_{2222} & \mathrm{L}^{hom}_{2212} \\ \mathrm{L}^{hom}_{1211} & \mathrm{L}^{hom}_{1222} & \mathrm{L}^{hom}_{1212} \end{bmatrix} \begin{bmatrix} E_{xx} \\ E_{yy} \\ E_{xy} \end{bmatrix} \tag{3.18}$$

and can be determined by applying unit overall strain modes to the damaged unit cell, considering its state of damage as frozen.

3.4 Predicted failure patterns

Failure patterns presented in this Section were obtained for proportional stress paths. Adaptive path following techniques, defined in Geers (1999a), were used in order to pass possible snap-back points. The mesostructure of the masonry material in simulations is made out of bricks of dimensions $L \times h = 220 \times 52$ mm^2 and of 10 mm thick head and bed joints; the out-of-plane thickness e is 100 mm (see Figure 3.5). The geometrical arrangement is similar to the one used in shear wall tests performed in the frame of the CUR project, Rots (1997). Experimental failure patterns in relation with the loading cases were not reported for this material. Due to this lack of information, qualitative comparisons are made with the only experimental results available from Dhanasekar et al. (1985) as sketched in Figure 3.1. As the mesostructure used in these experiments differs from the one used in our computations, the comparisons are restricted to be qualitative. The mesh used for the computations is the one represented in Figure 3.6 and consists of 396 elements with biquadratic interpolation of the displacement field and bilinear interpolation of the non-local strain field. Smaller elements are used in the mortar joints and in the central part of the brick where damage is likely to occur for in-plane load cases. Unless otherwise specified, the material properties used for the constituents are those listed in Table 3.1. Most of these parameters were derived from the tests reported in Rots (1997); van der Pluijm (1999). The mortar characteristics refer to a volumetric ratio of 1:2:9 (cement:lime:sand), which may be considered as a rather poor testing mortar due to the high proportion of sand. Note that

Table 3.1: Material parameters

Material	E (MPa)	ν	l_c^2 (mm^2)	f_t (MPa)	α	β	f_c (MPa)	f_b (MPa)	f_h (MPa)
Brick	16700	0.15	3	2	1.	800	20	-	-
Mortar	2900	0.20	3	0.25	1.	140	3.75	6.37	6.25

these material parameters are average values. A high scatter was reported, particularly for the mortar joint characteristics, for which a strong dependency on the nature of the bricks used was also found. The parameter β of the damage evolution law (3.12) has been fitted such that the correct tensile fracture energy is obtained, accepting that the damage is allowed to spread on the full joint thickness.
For the elastic parameters in Table 3.1, the initial stiffness operator of the equivalent homogeneous continuum is given by

$$\mathbf{L}^{hom} = \begin{bmatrix} 12.7 & 1.4 & 0 \\ 1.4 & 9.5 & 0 \\ 0 & 0 & 3.7 \end{bmatrix} \quad \text{(GPa)} \tag{3.19}$$

In the remainder of this Section, a qualitative comparison of the unit cell failure patterns with the experimental failure modes of Figure 3.1 is made. A discussion of the results and their relation with the assumed mechanical characteristics of the constituents follows.

3.4.1 Qualitative comparison with experimentally observed failure modes

In order to enable a comparison with experimental failure patterns, each of the loading cases of Figure 3.1 has been applied to the computational cell. Since the ratio of compressive and tensile stresses in the tension-compression load cases is not reported in Dhanasekar et al. (1985), this ratio has been set to 1 in the computations. The failure modes obtained from unit cell computations are depicted in Figure 3.8 together with the experimentally observed ones. The loading cases for which the correct failure modes were captured are outlined. From Figure 3.8, one notices that the agreement between the experimental and unit cell failure patterns is fairly good. In particular, the occurrence of staircase cracking is captured by the unit cell computations when the principal stress directions are inclined with respect to the bed joints. The disagreement in some of the cases (particularly cases 4, 8 and 9) may be due to the lack of information about the aspect ratio of the bricks used in the experiments. This aspect ratio directly determines the staircase failure pattern orientation with respect to the bed joints. It may therefore have a strong influence on the appearance of this failure mode instead of failure of the bed joints or vice-versa. For case 8 the unknown ratio between the principal stresses in experiments may also play a role. For the case of uniaxial compression parallel to the bed joints (case 3), the failure pattern looks different because the unit cell computation has been continued far beyond the moment the maximum load-bearing capacity was reached. This is clearly not the

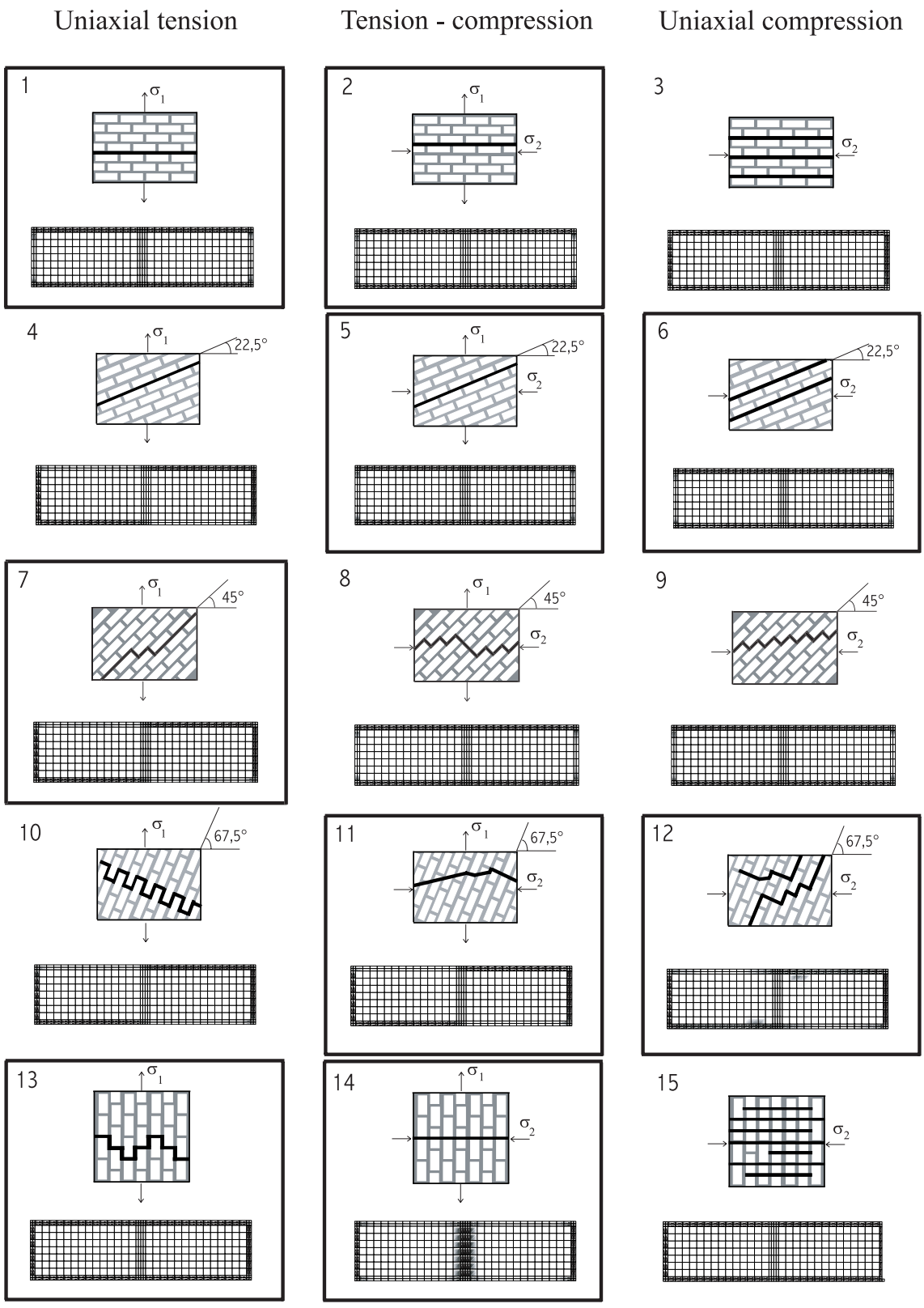

Figure 3.8: Qualitative comparison of unit cell damage patterns with experimentally observed failure modes

case in the experimental pattern. Like in the experiment, however, the computation first shows failure of the bed joints, followed by crushing of the head joints. Finally, the failure mode under uniaxial compression parallel to the head joints (case 15) is not captured. This may be caused by the use of a weak mortar in the unit cell computations causing early compressive failure of bed joints and preventing the occurrence of brick cracking.

3.4.2 Influence of the mesoscopic characteristics

As mentioned above, the disagreement between simulations and experiments for some loading cases may be due to the lack of material or geometrical data from the experiments. In order to further explore this hypothesis, the influence of material properties for some of these load cases will be examined in the sequel of this Section.

Variation of the geometrical characteristics and of the biaxial loading conditions

A correct failure pattern may be obtained if the aspect ratio of the brick is modified for case 4 and if the principal stress ratio is modified for case 8. For case 4, a change in the geometrical characteristics causes a modification of the orientation of the potential staircase crack pattern with respect to the bed joint. This may affect the failure mode which is obtained. The dimensions of the cell were modified to L $\times$ h = 175 $\times$ 62 mm^2 (see Figure 3.6), keeping the thickness of joints unchanged. This means that the angle between the bed joint and the staircase crack pattern is increased. For this geometry, the failure mode observed for case 4 indeed changes as represented in Figure 3.9. The change in the orientation clearly makes the staircase crack pattern less critical thereby causing the failure to occur in the bed joints only. As suggested

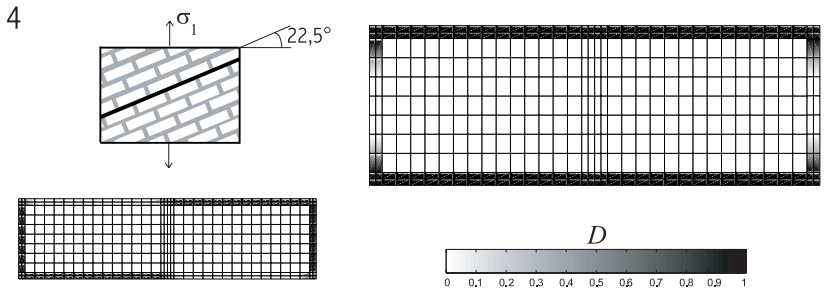

Figure 3.9: Final damage distribution for case 4 with initial geometry (left) and with modified geometry (right)

before, the lack of information about the loading case may also explain disagreements for the tension-compression cases. As an example, case 8 is re-examined with a tensile principal stress twice as high as the compressive stress. The associated damage distribution, depicted in Figure 3.10, now clearly shows the staircase pattern observed in the experiment.

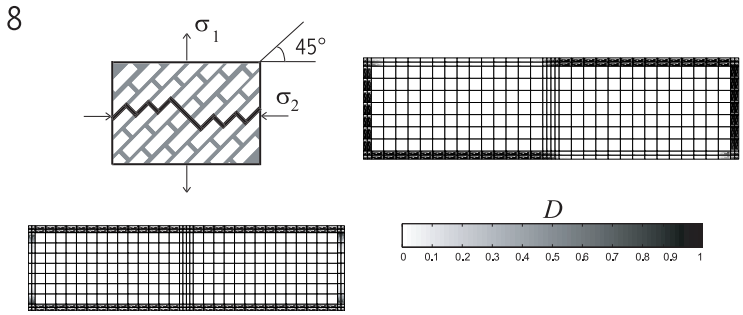

Figure 3.10: Final damage distribution for case 8 with initial loading case (left) and with modified loading case (right)

Compression parallel and perpendicular to the bed joints

When the cell is subjected to uniaxial vertical compression (case 15 in Figure 3.8), the damage development presented in Figure 3.11 is obtained. The head joints are first completely damaged due to tensile horizontal stresses. Damage then propagates into the bed joints. This failure mode is thus entirely controlled by the strength of mortar and is actually obtained only when the mortar strength is such that it is exhausted before the brick cracks. Furthermore, this definition of failure may not coincide with the one used in experiments because compressive failure of bed joints could occur before the peak load. In experiments, the bricks might touch after degradation of the bed joints and allow further increase of the applied load, leading to higher peak stress than recorded in our computation. Failure by compressive crushing of bed joints was obtained for the shear wall tests reported in Lourenço (1996), because of the high proportion of sand in the mortar used in these experiments.

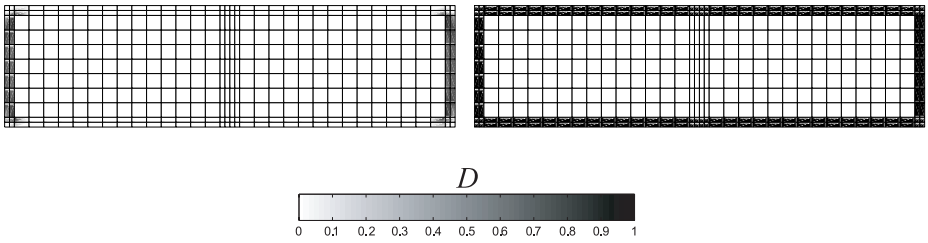

Figure 3.11: Damage evolution under vertical compression

Because of the high scatter obtained for mortar material parameters in experiments, it is interesting to verify whether a modification of these parameters may lead to a correct compressive failure pattern. Indeed, if the mortar is given sufficient strength in the compressive regime, a damage pattern similar to the experimental failure mechanism reported in Figure 3.8 (case 15) may be recovered. In order to demonstrate this, two additional computations have been performed with increased f_c, f_h and f_b parameters for mortar 1 as well as a slight increase of Young's modulus and tensile bond strength for mortar 2, see Table 3.2. Note that the modified material parameters are also extracted from experimental values reported in Rots (1997);

Table 3.2: Material parameters for additional compressive computations

Improved mortar	E (MPa)	f_t (MPa)	f_c (MPa)	f_b (MPa)	$f_h(MPa)$
Strong mortar 1	2900	0.25	6.25	13.9	10.43
Strong mortar 2	3900	0.34	6.72	16.4	11.2

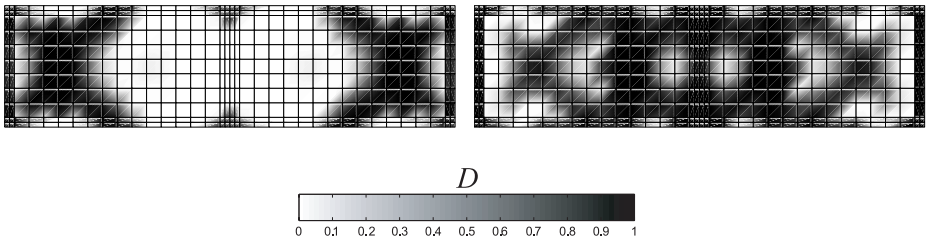

Figure 3.12: Failure (damage distribution) under vertical compression for (a) strong mortar 1 (b) strong mortar 2

van der Pluijm (1999). The final failure patterns for both simulations are shown in Figure 3.12. Because of the higher strength of the mortar, damage propagates into the brick rather than into the bed joint, leading to diagonal cracking in the first case, and to mixed diagonal/vertical cracking for the second set of material parameters. It thus appears to be possible to obtain such a failure mode with a plane stress assumption with realistic values of the mesoscopic material parameters. The diagonal cracking mode was also obtained in the analyses of Anthoine (1997), but with material parameters leading to a much higher overall compression strength (about 50 MPa) and with a model including the effect of out-of-plane stresses. In these computations, also a vertical in-plane crack in the middle of the brick was obtained, which is only captured here for the second case (mortar 2).

3.5 Identification of a macroscopic failure envelope

In this Section, a failure envelope for masonry is reconstructed, starting from the unit cell computations presented above. A quantitative comparison with experimental results is difficult to perform as no experimental stress envelopes seem to be available in literature, except that by Dhanasekar et al. (1985) for which incomplete material and geometrical data was reported. This envelope will nevertheless be used for a qualitative comparison. For this purpose, a stress based failure envelope is built from unit cell computations for different directions in the stress space $(\Sigma_x, \Sigma_y, \Sigma_{xy})$. As in the experiments, failure is defined as the locus of maximum load bearing capacity of the unit cell. These points have been marked in $\Sigma_x - \Sigma_y$ space in figure 3.13. The size of the marker indicates the shear stress Σ_{xy} for which it has been obtained. Different kind of markers have been used to indicate the pattern by which final failure occurs. These patterns have been determined by continuing the computation beyond the peak load until the load bearing capacity has been reduced by 50 %.

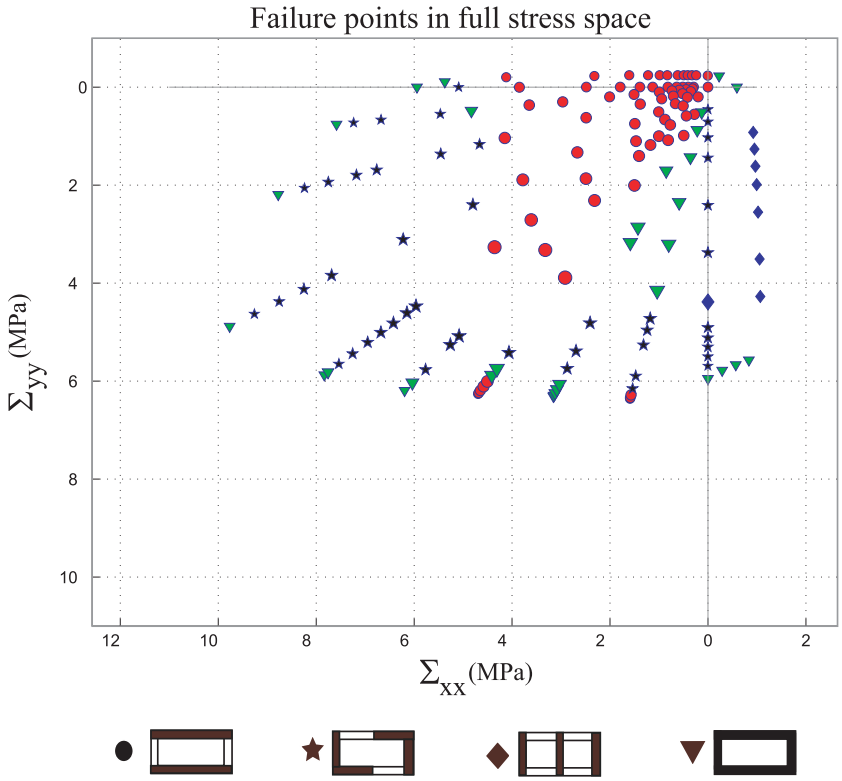

Figure 3.13: Failure points in stress space for running bond masonry

The diagram clearly shows that the failure mechanism highly depends on the stress path which is followed by the specimen, even for proportional loading and for a fixed mesostructure. The failure points corresponding to zero shear stress, i.e. the outer ring of points, exhibit the expected behaviour. Failure is caused by bed joints when tension parallel to the head joints is dominant, by vertical cracking when tension parallel to the bed joints is dominant and with failure in both types of joints under biaxial stresses. The staircase failure type becomes important when overall shear is applied to the cell. This type of failure is present for most loading cases combining compression parallel to the head joints and shear. It is also present in the biaxial compressive regime for moderate shear loading. The consequence of the diversity of failure modes observed is that the macroscopic stiffness evolution associated to failure patterns drastically differs even for neighbouring stress orientations. The occurrence of these different failure modes may be accompanied with an energy dissipation that strongly differs depending on the type of failure mode.

In order to show the influence of the shear stress on the load carrying capacity more clearly, the data of Figure 3.13 has been represented as a set of isocurves in Figure 3.14. Each of these curves represents an intersection of the failure surface with planes of constant shear Σ_{xy}. In order to support the qualitative comparison, the envelope for zero shear stress paths is compared to that obtained experimentally by Dhanasekar et al. (1985) in Figure 3.15. Given the assumptions that had to be made due to the lack of data, and the simplifications introduced in this paper, the agreement with the experimental failure envelope is reasonable. Some characteristics of the

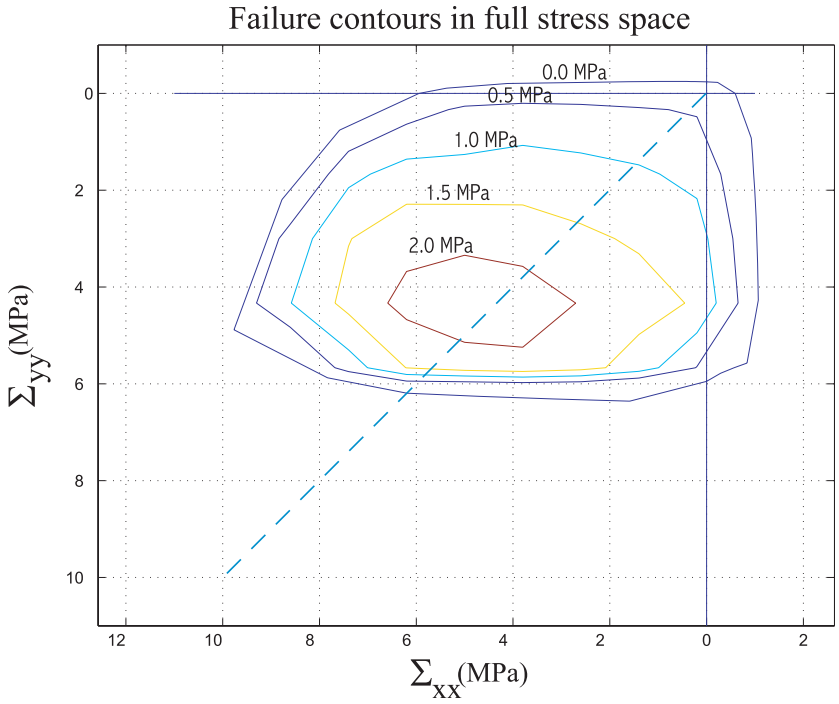

Figure 3.14: Failure envelope contours in stress space for running bond masonry (contour spacing 0.5 MPa)

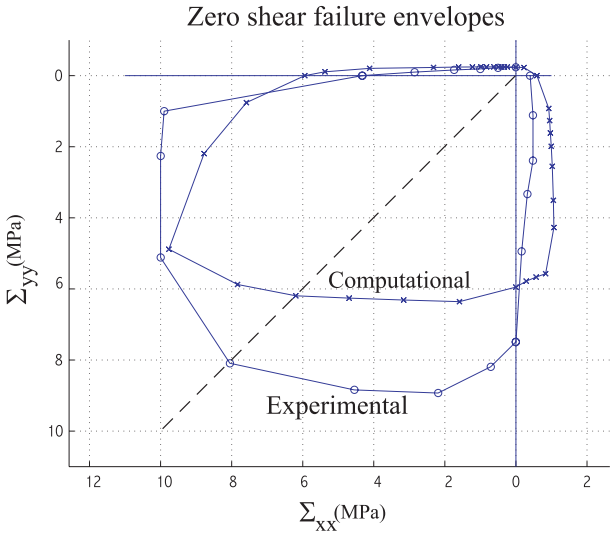

Figure 3.15: Best fit experimental failure envelope for zero shear stress states obtained by Dhanasekar et al. (1985)

failure envelope shape are recovered. The anisotropy in the compressive regime (asymmetry with respect to the $\Sigma_{xx} = \Sigma_{yy}$ axis) is also found in the experimental results with a higher strength for loading cases dominated by compression along the bed joints. It is much more pronounced in the results obtained computationally because of the higher aspect ratio of the brick used in the computations. The anisotropy in the tensile regime is also captured. The shape of the numerical envelope could however be improved for stress states where the compression

parallel to the head joints is dominant. This would yield a better description in the related biaxial compression region of the stress space and in the horizontal tension – vertical compression regime, even though experimental scatter was pronounced for these stress paths. The use of the modified von Mises damage criterion for the brick probably leads to an overestimation of the masonry strength under vertical compression combined with low horizontal traction, because the shape of this criterion overestimates the brick strength for the same stress paths. It is emphasized also that the failure patterns in the biaxial compression regime are mostly determined by the mortar degradation because of the plane stress assumption. As a result, the shape of the brick damage criterion in the biaxial compressive regime does not influence the failure envelope in plane stress. An improvement of the computed envelope could be obtained by including out-of-plane effects or by using other expressions of the damage loading functions. The high strength level for compression parallel to the bed joints with respect to the experimental case is linked to the failure definition used in Dhanasekar et al. (1985) as already explained in Section 3.4. This explains (at least partially) the identical values of the uniaxial compressive strength parallel to head and bed joints.

The shape of the failure surface is also similar to the macroscopic plasticity loading surface defined by Lourenço et al. (1997) to approximate the results reported in Dhanasekar et al. (1985). This suggests that the present mesoscopic approach could also constitute a useful tool in order to identify phenomenological macroscopic models based on the knowledge of the properties of the constituents.

3.6 Anisotropy evolution induced by damage

3.6.1 Induced full anisotropy effects

The staircase crack pattern encountered in experiments and captured in unit cell computations for cases 7, 10 and 11 of Figure 3.8 naturally leads to a full anisotropy at the macro-level. This is for instance the case when the cell is loaded through vertical compression and horizontal shear according to $\Sigma_{xy} = -\frac{1}{2}\Sigma_{yy}$. The failure mode obtained for this loading is represented in Figure 3.16. The head joint is first partially damaged, leaving the orthotropy of the equivalent homogeneous material unchanged as illustrated by the homogenized stiffness in Figure 3.16a. Only part of the bed joint subsequently fails while the head joints are completely degraded. While orthotropy is preserved in the first stage, it is clearly lost when the asymmetric damage growth sets in. The homogenized stiffness operator now incorporates coupling terms between normal stresses and shear strains which are of the same order as the other terms. It is clearly not acceptable to assume invariance of the material directions at the macroscopic scale for such a loading path. As this example relates to a macroscopic stress state often encountered in masonry structures, it illustrates the need for a macroscopic damage model to be capable of representing a more general form of induced anisotropy than orthotropy. However, such models are difficult to formulate because complex tensorial laws have to be postulated which must be fitted to experiments. Furthermore, the sequence in which the different joints are damaged

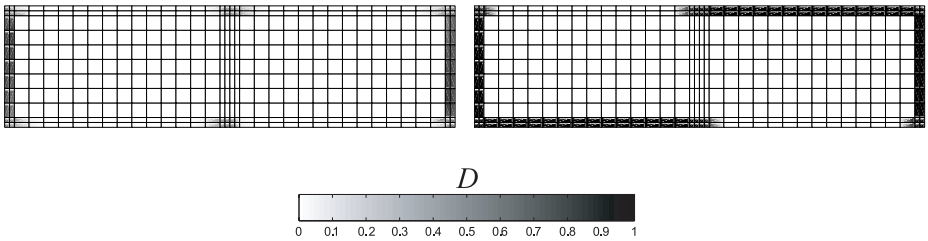

$$\mathbf{L}^{hom} = \begin{bmatrix} 10.6 & 1.2 & 0.0 \\ 1.2 & 9.2 & 0.0 \\ 0.0 & 0.0 & 3.3 \end{bmatrix} \qquad \mathbf{L}^{hom} = \begin{bmatrix} 3.5 & 0.9 & -1.8 \\ 0.9 & 0.5 & -0.5 \\ -1.8 & -0.5 & 1.0 \end{bmatrix}$$

Figure 3.16: Damage evolution under simultaneous vertical compression plus shear and resulting macroscopic homogenized stiffness (in GPa): (left) intermediate stage, (right) final pattern

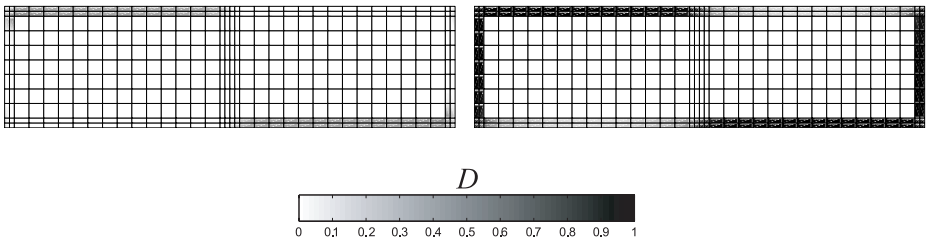

$$\mathbf{L}^{hom} = \begin{bmatrix} 12.5 & 1.3 & 0.1 \\ 1.3 & 8.4 & 0.1 \\ 0.1 & 0.1 & 3.4 \end{bmatrix} \qquad \mathbf{L}^{hom} = \begin{bmatrix} 3.5 & 1.0 & 1.8 \\ 1.0 & 0.4 & 0.5 \\ 1.8 & 0.5 & 1.0 \end{bmatrix}$$

Figure 3.17: Damage evolution under biaxial compression with shear and resulting homogenized stiffness(in GPa): (left) intermediate stage (right) final pattern

highly depends on the stress path which is followed and would therefore be difficult to represent phenomenologically. As an illustration of this fact, the evolution of the damage state of the cell is next represented in Figure 3.17 for the loading along the stress path $(\Sigma_x, \Sigma_y, \Sigma_{xy}) = (-1, -1, 0.25)$ (MPa). The early damage development appears in an asymmetric mode in the bed joint, leading to loss of orthotropy in the early stage of the degradation process. It thus seems that the only way to account for them in large scale computations would consist in using multiscale techniques, using damage laws postulated at the level of constituents. This should allow to approximate complex mechanical effects while preserving simplified models with a minimal set of material parameters. It should however be emphasized that such an approach leads to higher computational costs.

3.6.2 Importance of full anisotropy for the post-peak regime

Neglecting full anisotropy effects, as is generally done in macroscopic models, has a strong impact on the post-peak behaviour of masonry. Even if the peak load may be predicted correctly, residual strengths and energy dissipation may be inaccurate, thereby affecting stress redistri-

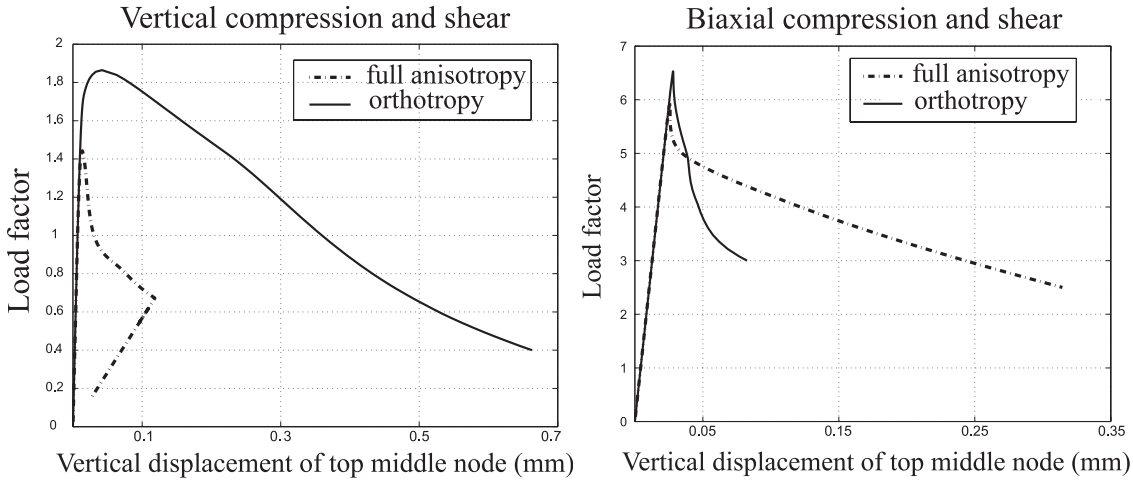

Figure 3.18: Load factor against vertical displacement of top middle node: (a) stress path along $(\Sigma_x, \Sigma_y, \Sigma_{xy}) = (0, -1, 0.5)$, (b) stress path along $(\Sigma_x, \Sigma_y, \Sigma_{xy}) = (-1, -0.75, 0.4)$

bution due to damage in structural calculations. To illustrate this, load-displacement curves were determined for two loading paths leading to full induced anisotropy. These curves are compared in Figure 3.18 with the response obtained when orthotropy is enforced during the complete degradation process in the cell. Orthotropic degradation was imposed by prescribing symmetry of the non-local strain field with respect to the vertical and horizontal symmetry axes of the unit cell. No symmetry constraint was applied to the displacement field. The load factor is given with respect to the vertical displacement of the top middle node of the cell in Figure 3.18. It clearly appears that the post-peak response and the associated energy dissipation are highly dependent on the assumption used for damage development. Assuming orthotropic degradation with fixed orthotropy directions leads to an overestimation of the load bearing capacity under vertical compression with shear, but not for the biaxial compression and shear case. In both cases, the orthotropy assumption leads to a wrong representation of the fracture energy of the masonry material.

This leads to the conclusion that macroscopic computations based on multiscale techniques should be based on a cell description allowing full anisotropy development. This also shows that the exact representation of the material behaviour cannot be captured with a macroscopic orthotropic description where the orthotropy axes are fixed to the initial symmetry axes of the material. Note however that no quantitative conclusion may be deduced on the error introduced by a fitted phenomenological orthotropic assumption. This is due to the fact that the orthotropic symmetry of damage was imposed here at the mesoscopic level, and that a phenomenological orthotropic fit could still yield a better agreement for this particular stress path.

3.7 Conclusions

A study based on unit cell computations was performed in order to verify that scalar mesoscopic damage constitutive laws are able to account for in-plane failure of running bond masonry walls.

Classical numerical homogenization techniques were used to identify a macroscopic failure surface in the plane stress space.
It was also shown that such a single failure surface actually relates to various failure patterns leading to very different macroscopic material symmetries and exhibiting different post-peak responses. As a consequence, only the load bearing capacity may be matched with a macroscopic phenomenological model without properly representing the mesostructural damage evolution. In particular, the assumption of fixed damage principal directions and orthotropic damage used in most macroscopic damage models is not acceptable because full anisotropy plays an important role for many relevant loading directions.
The results thus suggest that the only viable way to overcome these deficiencies of phenomenological approaches would consist in postulating the damage evolution at the mesoscale in a multiscale framework. In such an approach, the description at the mesoscopic scale should allow fully anisotropic stiffness degradation.

Chapter 4

Mesoscopic modeling of failure in brick masonry accounting for three-dimensional effects

The generalised plane state assumption is examined in order to assess its ability to represent in a simplified fashion three-dimensional effects in the behaviour of planar masonry structures subjected to in-plane loads. Realistic failure mode prediction for various loading directions is verified. It is shown that the generalised plane state allows to account in a simplified way for the presence of out-of-plane mesoscopic normal stresses by neglecting out-of-plane shear in the constituents. When introduced in a homogenization scheme, the resulting macroscopic continuum presents a two-dimensional format, suggesting that generalised plane state could be used fruitfully in multi-scale approaches where three-dimensional effects have to be taken into account.

4.1 Introduction

The conservation of historical masonry structures is an increasing concern nowadays for public authorities. The technical planning of repair operations for these structures is of prime importance. These operations usually require an estimation of the residual strength of structures to analyse and optimize the consequences of the different repairing techniques. Although rules of thumb are still widely used for most cases, numerical simulations are starting to emerge as valuable alternatives. However, such methods may be useful only if they are able to account realistically for the possible failure modes of such a complex material. To achieve this, an accurate representation of the influence of mesoscopic characteristics such as geometrical arrangement and mechanical parameters on the strength and failure of the overall material is needed.

An extended experimental characterization was performed by Page (1981, 1983); Dhanasekar et al. (1985) in order to identify a macroscopic failure surface for a given mesostructure in connection with the triggered failure modes. The failure mechanisms were found to substantially differ according to the loading case. The influence of the mortar joints is determinant for biaxial

This chapter is reproduced from: T.J. Massart, R.H.J. Peerlings and M.G.D. Geers, Mesoscopic modeling of failure in brick masonry accounting for three-dimensional effects, Submitted for publication in Engineering Fracture Mechanics.

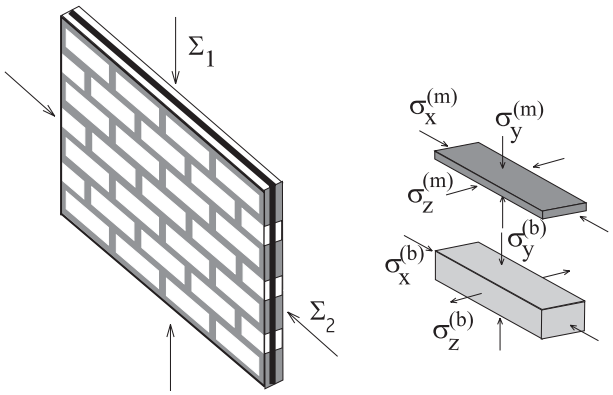

Figure 4.1: Mesoscopic stress states under vertical compression of masonry

tension, compression-tension and most of the tension-compression stress states. In these cases, fracture occurs mainly in mortar joints or through vertical brick cracking in a plane perpendicular to the wall. As shown in Massart et al. (2004a), these failure mechanisms can be captured well by a mesoscopic model which assumes a plane stress state throughout the wall. In the case of biaxial compression however, the experiments show a transition between in-plane failure mechanisms for high principal stress ratios and out-of-plane failure for nearly equal principal compressive stresses. This last failure mode may only be captured if three-dimensional effects are included in the description and therefore cannot be simulated with plane stress models, Massart et al. (2004a). Due to the difference in the elastic characteristics of the constituents, a biaxial overall compressive loading causes a triaxial stress state in the constituents in the mid-thickness plane. The mortar joints are subjected to a triaxial compressive stress state and the bricks to an in-plane compression/out-of-plane tension state, see Figure 4.1. Since both materials have a much lower strength in tension than in compression, the tensile stress in the brick may cause mid-thickness plane splitting. The presence of this out-of-plane failure mechanism is thus highly dependent on the relative stiffness and strength of bricks and mortar.

As a transition exists between the out-of-plane splitting and in-plane failure mechanisms, the out-of-plane stress components may also have an impact on compressive in-plane failure of masonry, for instance for compression parallel to the head joints. Three-dimensional failure criteria for the constituents are needed to account for such effects. Their presence results from the assumptions made for the mesoscopic or local out-of-plane stresses and for their coupling with the in-plane stress fields. Even though a fully three-dimensional analysis is needed to account for certain situations (out-of-plane bending, non constant properties across thickness), this type of approach is often computationally too expensive for practical problems. As a consequence, two-dimensional approximations are generally used. The plane stress assumption, which was used in Massart et al. (2004a) and in most masonry models based on the geometrical aspect ratio of the wall, neglects the out-of-plane stresses everywhere. However, this assumption is questionable here because of the highly heterogeneous nature of the masonry material and the fact that the thickness is of the same order as the characteristic size of the in-plane mesostructure. This plane stress approach is however often claimed to represent well the behaviour at the external faces of a masonry wall, Anthoine (1997). As a compromise between a plane stress

and a fully three-dimensional description, a generalised plane state assumption leading to a two-dimensional description at the macroscopic scale can be used. It is usually used to approximate the behaviour of the material at the mid-thickness position, far from the external faces, Anthoine (1997). Of course, any of the two-dimensional approaches is an approximation of the real three-dimensional solution, in particular because the damage growth at the mid-thickness and at the external faces are intimately related in the three-dimensional situation. Also the stiffness coupling terms between out-of-plane and in-plane quantities are different in the plane stress, generalised plane state and three-dimensional representations.

The idea of using the generalised plane state for masonry structures was originally suggested by Anthoine (1997); Pegon and Anthoine (1997). It was applied for a limited set of loading conditions and material parameters using a specific type of damage evolution law and applied on a fully three-dimensional description. In these situations, the plane stress assumption lead to a considerably lower overall masonry compressive strength than the generalised plane state assumption, Anthoine (1997). This difference was linked to the appearance of different failure mechanisms under both assumptions. However, it is not known whether this conclusion may be extended to other loading paths or to other constitutive models.

The objective of this study is to examine failure envelopes in terms of overall stresses obtained with the generalised plane state assumption and to compare them with those obtained using a plane stress assumption as in Massart et al. (2004a). This comparison is made on the basis of the predicted failure modes as well as the obtained load-carrying capacity. This contribution is organized as follows. First, homogenization principles are briefly recalled in Section 4.2 with an outline of some salient features needed for the case of plane masonry structures. A classification of plane state descriptions is then sketched in Section 4.3. The main simplifications with respect to a general three-dimensional representation are outlined. The generalised plane state is introduced and applied to a laminate material, showing the merits of the generalised plane state description and the two-dimensional structure of the resulting overall description. A slightly modified two-dimensional finite element implementation including the simplified three-dimensional effect of generalised plane state is briefly presented in Section 4.4. Section 4.5 presents its numerical assessment. The plane stress and generalised plane state assumptions are used in masonry unit cell computations in order to identify failure envelopes. These results are compared with each other and with experimental evidence on the basis of the obtained failure modes and of the load-carrying capacity.

4.2 Homogenization principles

4.2.1 Displacement field in a periodic two-dimensional medium

In the following the mesostructure of masonry and the loading applied to it are assumed to be perfectly periodic in the plane of the wall. In a two-dimensional description, a homogeneous equivalent material may then be identified if the displacement field is also assumed to exhibit some form periodicity. These assumptions allow to identify a unit cell which contains all the mesostructural information and on which the equilibrium problem can be formulated and

solved, Anthoine (1995). The displacement field has the form

$$\vec{u} = \mathbf{E}.\vec{x} + \vec{w} \tag{4.1}$$

where $\mathbf{E}$ is a constant overall strain tensor, $\vec{x}$ is the position vector within the cell and $\vec{w}$ is a mesoscopic fluctuation field which is unknown inside the unit cell but is forced to be periodic at its boundary. In the remainder of this contribution, lowercase greek letters will denote mesoscopic quantities while capital greek letters will represent their macroscopic counterparts.

Using the periodicity conditions, the overall stress tensor is obtained as the volume average of the mesoscopic stress tensor

$$\mathbf{\Sigma} = \frac{1}{V}\int_V \boldsymbol{\sigma} dV \tag{4.2}$$

Using mesoscopic equilibrium in the absence of body forces permits to write

$$\vec{\nabla}.(\boldsymbol{\sigma}\vec{x}) = \left(\vec{\nabla}.\boldsymbol{\sigma}\right)\vec{x} + \boldsymbol{\sigma}.\left(\vec{\nabla}\vec{x}\right) = \boldsymbol{\sigma} \tag{4.3}$$

and using this result together with the divergence theorem, the overall stress tensor may be expressed in terms of boundary contributions as

$$\mathbf{\Sigma} = \frac{1}{V}\int_V \boldsymbol{\sigma} dV = \frac{1}{V}\int_V \vec{\nabla}.(\boldsymbol{\sigma}\vec{x})\, dV = \frac{1}{V}\int_{\partial V} (\vec{p}\ \vec{x})\, d\partial V \tag{4.4}$$

where $\vec{p}$ is the traction vector and $\vec{x}$ is the position vector with respect to the center of the cell of a point of the boundary.

The simplest unit cell allowing to represent general two-dimensional loading conditions under the periodicity assumption is sketched in Figure 4.2. It consists of one brick surrounded

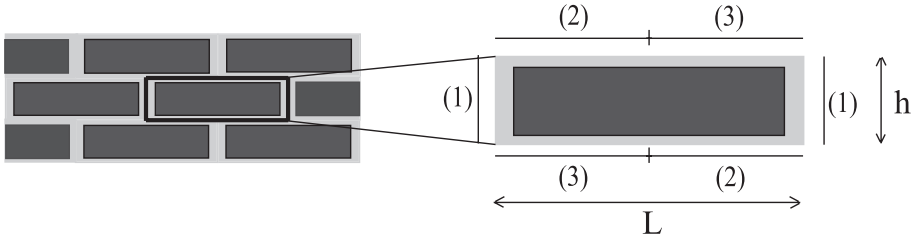

Figure 4.2: Periodicity tyings for running bond two-dimensional unit cell

by half a joint on all sides. The offset of the head joints in the running bond stacking mode is reflected in the periodicity tyings at the cell boundary, which is split in 6 parts, tied two by two as indicated in Figure 4.2, Anthoine (1995); Massart et al. (2004a).

4.2.2 Extension for three-dimensional effects

The aim is to extend the concept of homogenization techniques to include three-dimensional effects in the mesostructure. The concept of a unit cell may be extended noting that the periodicity conditions apply only to a part of the boundary of the cell, the external faces not being

subjected to this condition, Anthoine (1997). A complete two-dimensional approach is tacitly assumed when the plane stress format is applied to both the macroscopic and mesoscopic descriptions. The difference between this simplified approach and a representation accounting for mesoscopic three-dimensional effects is illustrated in Figure 4.3. As illustrated, the ability to capture three-dimensional effects depends on the assumptions introduced at both the mesoscopic and the macroscopic scales. As no external load is applied along the thickness direction at the macroscopic scale, three options are possible, ranging from fully two-dimensional to fully three-dimensional representations. The intermediate option keeps a macroscopically two-dimensional formulation, but includes simplified three-dimensional effects at the mesoscopic scale. When full three-dimensional effects are included in the homogenization approach at both the meso- and macroscales, the extension of relation (4.1) however leads to a more complex expression of the displacement field, Anthoine (1995). This is linked to the fact that no periodicity is required on the faces perpendicular to the thickness direction thus opening the possibility of non-symmetric modes of deformation with respect to the mid-thickness plane. Many planar structures exhibit a planar behaviour, for which an overall two-dimensional representation is sufficient. However, three-dimensional effects are needed at the mesoscale in order to capture the effect of out-of-plane stresses.

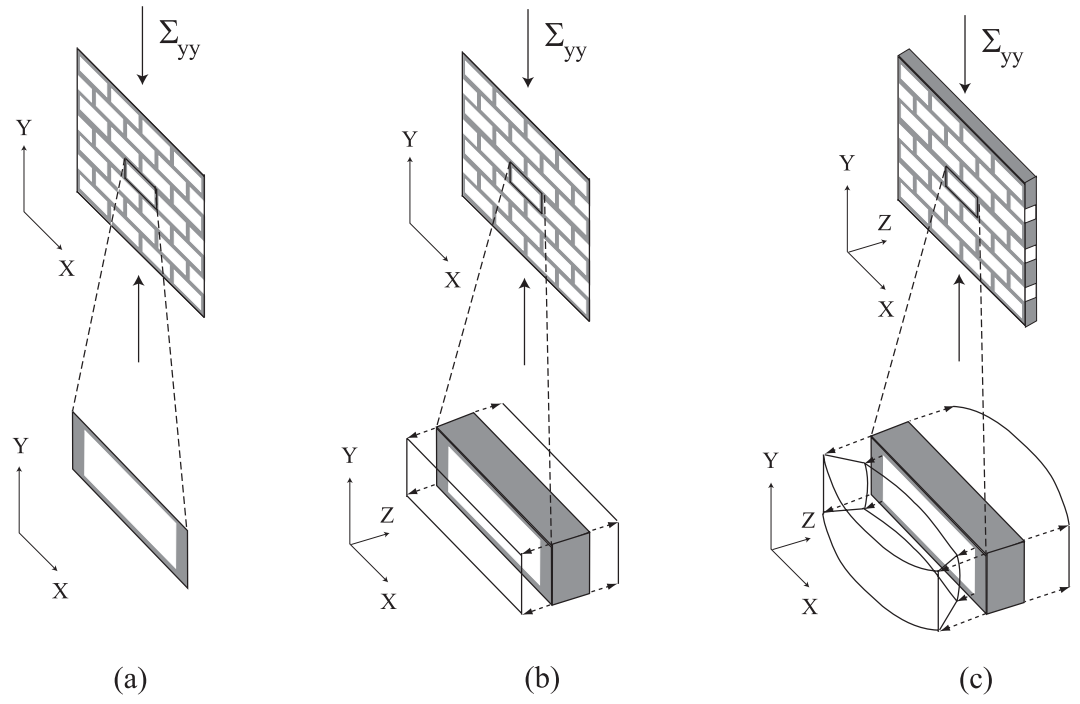

Figure 4.3: Illustration of assumptions for a masonry wall under uniform vertical compression: (a) fully two-dimensional representation, (b) macroscopically two-dimensional representation with approximate representation of mesocopic out-of-plane effects, (c) fully three-dimensional representation. For each assumption the macroscopic assumption is illustrated on the wall. The topology of the unit cell and its deformed shape (except for the plane stress case where it is not displayed) indicate the kinematical assumption applied at the mesoscale (dashed lines represent the out-of-plane displacement of the points).

Our objective here is to examine if the intermediate option is a viable, more efficient alternative, as it allows the introduction of simplified three-dimensional effects in the mesoscopic description, but avoids a fully three-dimensional modeling at any of the scales. Here, we will develop a two-dimensional finite element formulation of the unit cell problem and examine its behaviour for a wider range of loading directions than hitherto, Anthoine (1997).

4.3 Plane stress and generalised plane state assumptions

In this section, particular attention is given to the consequences of classically used plane state assumptions on the mesoscopic strain and stress fields when applied to a cell in which constituents of masonry (brick and mortar) are used. For clarity, each option is illustrated by the case of elastic compression of a laminate characterised by the unit cell presented in Figure 4.4. The material parameters in Table 4.1 were considered for the constituents in order to simulate typical mortar and brick materials.

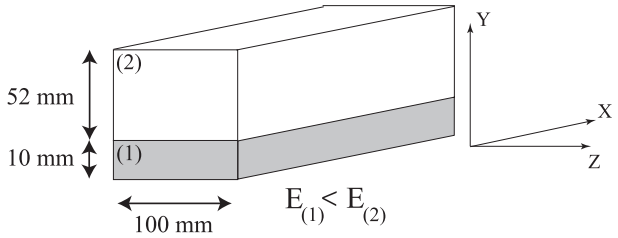

Figure 4.4: Laminate structure for illustration

Table 4.1: Material parameters for laminate illustration

Material	E (MPa)	ν
(1)	3900	0.20
(2)	16700	0.15

4.3.1 Three-dimensional modeling

The laminate is subjected to a compression of 10 MPa perpendicular to the laminate direction (direction y in Figure 4.4) and confined in the x direction. As a result, all deformations take place in the yz plane and a two-dimensional plane strain analysis suffices. This analysis is performed on a mesh containing 300 eight-noded elements. The mesoscopic out-of-plane stress components σ_{zz} and τ_{yz} are plotted in Figure 4.5. The deformed configuration (with an amplification factor of 1200 for the horizontal displacement) is given to visualise the deformed shape of external faces. Concentrations of stresses appear at the interfaces between the constituents.

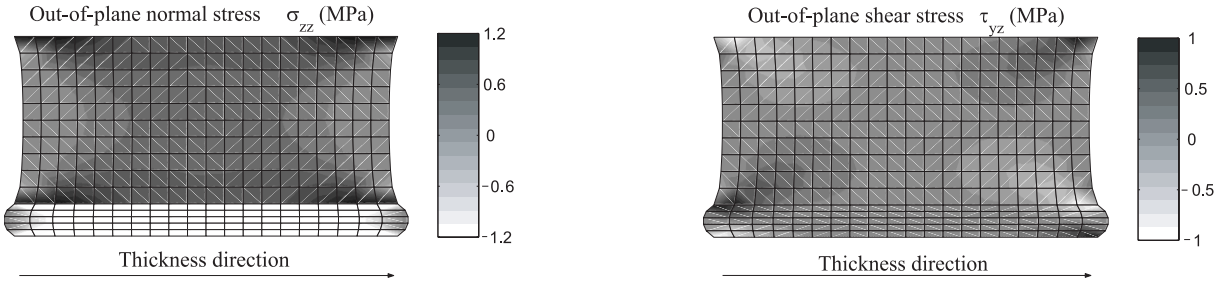

Figure 4.5: Normal (left) and shear (right) out-of-plane mesoscopic stresses in laminate under compression (in MPa)

Within each phase, a symmetrical variation with respect to the mid-thickness plane is observed for the normal stress. The stiff material is subjected to tension while the soft phase undergoes out-of-plane compression. The shear stress vanishes at the mid-height of each phase. Near the interfaces, the shear component is anti-symmetric with respect to the mid-thickness plane. The out-of-plane tension generated in the stiff material is on the order of 10 % of the applied compression. Neglecting this component by assuming a plane stress state may therefore be justified in many situations. However, the strength of brick in tension may well be less than 10 % of its compressive strength, so that the small tensile stress component may nevertheless become dominant for failure.

4.3.2 Plane stress assumption

Most models used for masonry structure calculations are based on the plane stress assumption, i.e. the assumption that $\sigma_{zz} = \sigma_{yz} = \sigma_{xz} = 0$ at the *mesoscopic scale*. As a consequence, the mid-plane splitting which may result from lateral expansion effects cannot be captured. This is sometimes compensated in phenomenological models by the introduction of an artificially low limitation of the compressive stress states in the definition of two-dimensional failure criteria. This approach has been applied in existing macroscopic phenomenological models (see Lourenço et al. (1997) for multi-surface plasticity or Berto et al. (2002) for damage models) but also for micromechanical descriptions (phenomenological compressive cap for mortar joints behaviour in Lourenço (1996)). It should be realised however that it does not reflect the real failure behaviour and therefore cannot incorporate rigorously the effect of mesostructural properties on the failure process.

4.3.3 Generalised plane state

A generalised plane state allows to describe the out-of-plane stress components in an approximate sense, keeping the macroscopic scale description two-dimensional. The following assumptions are introduced for this purpose:

- the external faces remain planar and vertical after deformation (see Figure 4.3b),

- at the *macroscopic scale*, no external load is applied to the wall in the thickness direction (neither surface traction nor body forces). At the *mesoscopic scale*, such surface tractions in the thickness direction may however exist in the generalised plane state approach at the external faces as a result of the first assumption and of the interaction between the different phases,
- the in-plane loads are applied uniformly along the thickness direction,
- all mesoscopic quantities are such that the wall remains symmetric with respect to the mid-thickness plane,
- the out-of-plane component of the displacement at a given in-plane position (x, y) varies linearly through the thickness,
- out-of-plane equilibrium is satisfied at the *macroscopic scale*.

Note that the second and third conditions are also assumed in plane stress descriptions. For the symmetric problem considered here, the above conditions respect the more general definition used by Anthoine (1997) or Grisard (1995), who defined the generalised plane state assumption as a plane strain state superposed with three constant overall strain components E_{iz} being such that their dual stresses Σ_{iz} vanish. This may be shown using periodic homogenization techniques on a masonry unit cell, see appendix. It results in constant mesoscopic strain and stress components along the thickness direction, which is clearly an approximation with respect to the three-dimensional description, but more accurate than a plane stress state. This is illustrated in Figure 4.6 for the case of the laminate in which mesoscopic piecewise homogeneous normal stresses are depicted for the generalised plane state assumption on the deformed configuration of the mesh. Note that the deformed shape of external faces now remains planar. The stress concentrations at the interfaces between the two materials as illustrated in Figure 4.5 for the three-dimensional representation no longer occur here. The crucial point is however that mesoscopic out-of-plane normal strains and stresses can now exist.

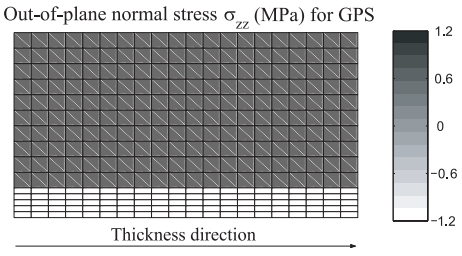

Figure 4.6: Mesoscopic normal stresses in a laminate under vertical compression in a generalised plane state of deformation

4.3.4 Consequences for the modeling of masonry structures

The generalised plane state is a simplification of the three-dimensional case in the sense that the mesoscopic stresses and strains are assumed constant through the thickness. In a complete three-

dimensional representation, the out-of-plane stress components evolve along the thickness. The out-of-plane displacement being an odd function of the z coordinate, the out-of-plane normal strain and stress components are even functions and the out-of-plane shear components are odd functions of the thickness coordinate. The additional conditions introduced for the external faces to remain vertical planes constrains these quantities to be uniform through the thickness. For the mesoscopic out-of-plane shear components, this means that they are forced to vanish. The generalised plane state is therefore an approximation of the behaviour of a thin slice of material centered on the mid-thickness plane.

To illustrate this fact, the variation of the mesoscopic stresses along the thickness direction under in-plane confined vertical compression of a laminate is shown in Figure 4.8. The stress profiles are obtained along three cuts in the laminate at heights indicated in Figure 4.7 (cut CC is in the mortar material). The out-of-plane normal stress components are reported for cuts AA and CC in each of the phases of the laminate material. The out-of-plane shear stress vanishes at mid-height of each constituent and is therefore only reported for the cut BB. It may be concluded from these stress profiles that the generalised plane state offers a quantitatively good approximation of the full three-dimensional solution for a thin slice of material centered on the mid-thickness plane. It should however be noted that the concentration of out-of-plane shear stress near the interface between phases cannot be captured by any two-dimensional approximation. Evidently, the interfacial concentrations reflect the three-dimensional nature of the problem at the mesoscale. Nevertheless, the mid-thickness plane is precisely the position where the out-of-plane failure mechanism is likely to occur under strong overall biaxial compression, justifying the need for an enhanced two-dimensional mesoscale representation of this type. Furthermore, it is also possible to compare the phase-averaged stress components obtained by both assumptions to the average values delivered by a three-dimensional approach. These values are listed in Table 4.2. In addition to the presence of the out-of-plane stress components, it is seen that the generalised plane state offers a better estimation of the in-plane averaged stress components in each phase than the plane stress assumption. This improvement is linked to the stiffness coupling terms between the out-of-plane and in-plane stress components which are taken into account in the generalised plane state and neglected in plane stress.

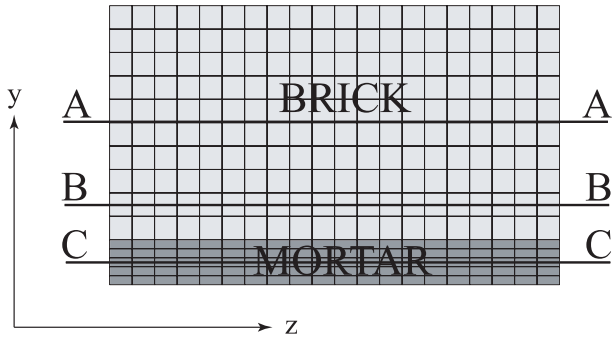

Figure 4.7: Slice of laminate: heights of cuts for stress profiles

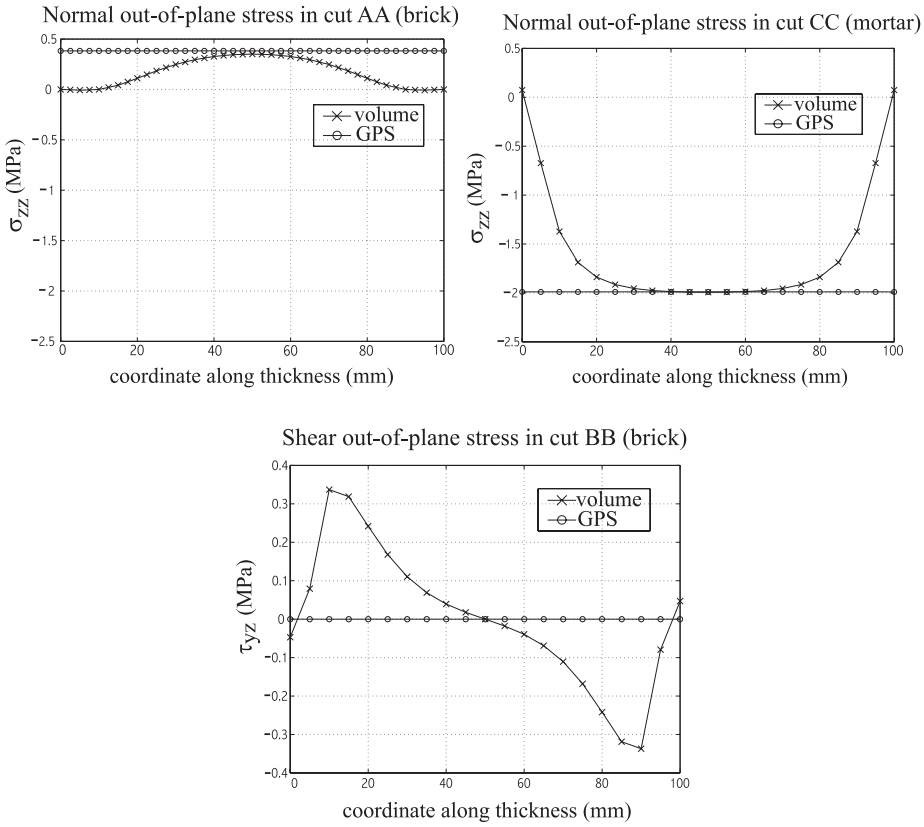

Figure 4.8: Out-of-plane stress distribution along thickness coordinate. 'volume' denotes the fully three-dimensional solution, 'GPS' means Generalised Plane State

Table 4.2: Phase averaged normal stress components for the laminate under confined vertical compression in (1) mortar and (2) brick phases for the three-dimensional, generalised plane state and plane stress assumptions

Assumption	$\Sigma_{xx}^{(1)}$	$\Sigma_{yy}^{(1)}$	$\Sigma_{zz}^{(1)}$	$\Sigma_{xx}^{(2)}$	$\Sigma_{yy}^{(2)}$	$\Sigma_{zz}^{(2)}$
3D	-2.340	-10	-1.700	-1.451	-10	0.327
GPS	-2.400	-10	-1.989	-1.443	-10	0.383
PS	-2.000	-10	0.	-1.500	-10	0.

4.4 Finite element implementation

In order to represent the kinematics associated to the generalised plane state assumption, the virtual work statement now has to include a term related to the out-of-plane normal components of the mesoscopic fields. The internal virtual work expression is then

$$\delta W_{int} = \int_V \boldsymbol{\sigma} : \delta\boldsymbol{\varepsilon}\, dV = \int_V \left(\sigma_{xx}\delta\varepsilon_{xx} + \sigma_{yy}\delta\varepsilon_{yy} + \sigma_{xy}\delta\gamma_{xy} + \sigma_{zz}\delta\varepsilon_{zz}\right)\, dV \qquad (4.5)$$

Given the fact that external surfaces remain planar and vertical, the variation of thickness should be constant on the whole problem. A single degree of freedom Δe may therefore be used to represent the relative displacement of the external faces in the out-of-plane direction. The out-of-plane normal strain is then given as

$$\mathrm{E}_{zz} = \varepsilon_{zz} = \frac{\Delta e}{e} \tag{4.6}$$

where e is the initial thickness of the cell. A classical biquadratic (serendipity) displacement interpolation is used in order to capture accurately the in-plane kinematics. The set of nodal displacements is thus augmented as

$$\{q\}^T = \left\{ \begin{array}{cccccccc} u_1 & v_1 & u_2 & v_2 & \dots & u_8 & v_8 & \Delta e \end{array} \right\}^T \tag{4.7}$$

and the interpolated displacement field is given by

$$\left\{u^h(x)\right\} = \left[\begin{array}{cc|cc|c|c} N_1 & 0 & N_2 & 0 & & 0 \\ 0 & N_1 & 0 & N_2 & \dots & 0 \\ 0 & 0 & 0 & 0 & & 1 \end{array}\right] \{q\} \tag{4.8}$$

where N_i is the shape function attached to node i. The strain tensor follows from the derivation of relation (4.8) as

$$\{\boldsymbol{\varepsilon}\} = \{\varepsilon_{xx}\, \varepsilon_{yy}\, \gamma_{xy}\, \varepsilon_{zz}\}^t = [B_{GPS}]\{q\} \tag{4.9}$$

where the strain-nodal displacement matrix $[B_{GPS}]$ is given by

$$[B_{GPS}] = \left[\begin{array}{cc|cc|c|c} \dfrac{\partial N_1}{\partial x} & 0 & \dfrac{\partial N_2}{\partial x} & 0 & & 0 \\ 0 & \dfrac{\partial N_1}{\partial y} & 0 & \dfrac{\partial N_2}{\partial y} & & 0 \\ \dfrac{\partial N_1}{\partial y} & \dfrac{\partial N_1}{\partial x} & \dfrac{\partial N_2}{\partial y} & \dfrac{\partial N_2}{\partial x} & \dots & 0 \\ 0 & 0 & 0 & 0 & & \dfrac{1}{e} \end{array}\right] \tag{4.10}$$

Practically, compared to a plane stress computation, the generalised plane state assumption leads to a single additional degree of freedom for the entire (meso-)structure. The finite element formulation can now be elaborated in the standard way but using the modified interpolation definitions (4.7),(4.8) and (4.10). This is not detailed here for brevity.

4.5 Failure patterns and envelopes

In this section, the effect of the generalised plane state assumption on the predicted failure behaviour of masonry is assessed. The generalised plane state is compared to the usual plane stress assumption for running bond masonry. This is done by comparing failure modes and failure envelopes obtained from both models in stress directions where it is expected that the

plane stress assumption delivers debatable results from a physical point of view. As an extension of the study performed by Anthoine (1997), partial failure envelopes are determined for a given masonry mesostructure as represented in Figure 4.2. The considered brick has dimensions $L \times h \times e$ of $165 \times 52 \times 100$ mm^3 and mortar joints are 10 mm thick. The mesh of this unit cell (which is represented in results) consists of 396 eight-noded elements and 1440 nodes.

The results for the plane stress and generalised plane state assumptions are compared on the basis of the identified failure modes as well as with respect to the load-carrying capacity. The envelopes are determined for proportional loading in the overall macroscopic stress space as already presented in Massart et al. (2004a). The constitutive laws and the related material parameters for the constituents are first presented. The failure envelopes are identified for overall stress paths which do not have a shear component and for mixed vertical compression/shear stress paths.

4.5.1 Constitutive laws and parameters for mortar and brick materials

A strain-based implicit gradient (non-local) damage model is used as first presented in Peerlings et al. (1996) for both the brick and the mortar material. This model uses a scalar damage variable entering the stress-strain relationship

$$\boldsymbol{\sigma} = (1 - D)\ {}^4\mathbf{L} : \boldsymbol{\varepsilon} \tag{4.11}$$

A damage criterion allows to determine whether a strain state change is accompanied by further damage

$$f(\overline{\varepsilon}_{eq}, \kappa) = \overline{\varepsilon}_{eq} - \kappa \leq 0 \tag{4.12}$$

along with the set of Kuhn-Tucker relations

$$f \leq 0 \qquad \dot{\kappa} \geq 0 \qquad f\ \dot{\kappa} = 0 \qquad \kappa\,(t = 0) = \kappa_i \tag{4.13}$$

where κ represents the ultimate non-local equivalent strain state experienced so far by the material point (or the initial value κ_i if this threshold has not been exceeded yet); $\overline{\varepsilon}_{eq}$ is a non-local (weighted averaged) equivalent strain introduced as the solution of the following partial differential equation incorporating a material intrinsic length scale in the constitutive setting, Peerlings et al. (2001)

$$\overline{\varepsilon}_{eq} - l_c^2 \nabla^2 \overline{\varepsilon}_{eq} = \varepsilon_{eq} \tag{4.14}$$

This partial differential equation is complemented by a boundary condition, which is here of the Neumann type, i.e. a natural boundary condition for the gradient of the non-local strain field at the boundary

$$\vec{\nabla}\overline{\varepsilon}_{eq}.\vec{n} = 0 \tag{4.15}$$

The right hand side in (4.14) is the source term for the non-local averaging, i.e. ε_{eq}, which is a local equivalent (damage-sensitive) scalar measure of the tensorial strain state. A damage evolution law relates the value of the damage D to the most severe non-local strain experienced by the material κ which is given further on. Details related to the implementation of the implicit

gradient damage model are available in Peerlings et al. (1996) and the consequences of its use for masonry mesostructures are discussed in Massart et al. (2004a).

The formulation of the damage model requires the definition of the scalar equivalent strain which is chosen differently here for each of the constituents. For the brick material, the equivalent strain is defined in terms of the principal effective stresses by

$$\varepsilon_{eq} = \max_i \left(\frac{\langle \tilde{\sigma}_i \rangle}{E}, \frac{\langle -\tilde{\sigma}_i \rangle}{kE} \right) \tag{4.16}$$

where $\tilde{\sigma}_i$ are the principal values of the effective stress tensor $\tilde{\boldsymbol{\sigma}} = {}^4\mathbf{L} : \boldsymbol{\varepsilon}$ and k represents the ratio of compressive strength to tensile strength for the material. The McAuley brackets $\langle . \rangle$ are defined as $\langle x \rangle = \frac{1}{2}(x + |x|)$ and ${}^4\mathbf{L}$ is the undamaged stiffness tensor of the material. Definition (4.16) is different from the one used in Massart et al. (2004a). The present form yields a better representation of the effect of tensile stresses in the brick material and thus of the in-plane failure modes for overall horizontal tension – vertical compression. Since out-of-plane effects are included in the description, this also allows a better description of failure for the biaxial compressive stress states when the mortar compressive strength is sufficiently high for out-of-plane tension to trigger cracking of the bricks.

For the mortar, a Drucker-Prager criterion, modified with a cap in the compressive regime has been used. It is defined in terms of the strain tensor invariants (summation on repeated indices)

$$I_1 = \varepsilon_{ii} \qquad J_2 = \frac{1}{6} I_1^2 - \frac{1}{2} \varepsilon_{ij} \varepsilon_{ij} \tag{4.17}$$

as

$$\varepsilon_{eq} = \begin{cases} \dfrac{A}{(1-2\nu)} I_1 + \dfrac{B}{(1+\nu)} \sqrt{J_2} & \text{if} \quad \dfrac{\sqrt{J_2}}{(1+\nu)} \geq \dfrac{A-C}{D-B} \dfrac{I_1}{(1-2\nu)} \\ \dfrac{C}{(1-2\nu)} I_1 + \dfrac{D}{(1+\nu)} \sqrt{J_2} & \text{if} \quad \dfrac{\sqrt{J_2}}{(1+\nu)} \leq \dfrac{A-C}{D-B} \dfrac{I_1}{(1-2\nu)}, \end{cases} \tag{4.18}$$

where

$$A = \frac{f_c - f_t}{2 f_c} \qquad B = \sqrt{3} \frac{f_c + f_t}{2 f_c}$$
$$C = -\frac{f_t}{3 f_h} \qquad D = 2\sqrt{3} \frac{f_t}{f_b} - \frac{4}{\sqrt{3}} \frac{f_t}{f_h},$$

and where f_t, f_c, f_h, f_b represent the fracture strengths respectively in uniaxial tension, uniaxial compression, hydrostatic triaxial compression and a special case of triaxial compression (with two of the principal stress values halved with respect to the major one), see Massart et al. (2004a) for details. The shape of these criteria in the principal stress space is illustrated in Figure 4.9 for the material parameters used in the computations and for the case of plane stress. A graphical representation of the mortar criterion when out-of-plane effects are present can be obtained in the three-dimensional space of principal stresses components. In this space, its shape presents a symmetry of revolution as a double conical surface (one cone for each of the tensile and compressive parts) centered on the hydrostatic axis. The shape of the brick damage

loading function in three-dimensional principal stress space is a square box and does not exhibit a symmetry of revolution.

In addition to the definition of an equivalent strain, the implicit gradient damage model requires the definition of a damage evolution law to quantify damage growth. An exponential damage law is used here for that purpose:

$$D = 1 - \frac{\kappa_i}{\kappa}\left(1 - \alpha + \alpha\, e^{-\beta(\kappa - \kappa_i)}\right) \tag{4.19}$$

In order to allow a quantitative comparison with experimental results, the constitutive parameters used in this study were partially extracted from Page (1981, 1983); Dhanasekar et al. (1985), where the required data corresponding to the constituents has been partially reported. The brick-mortar interface failure mechanism is only accounted for in an implicit way. The bulk tensile properties of the mortar are adjusted in order to represent correctly the tensile strength and fracture energy of joints in mode I, dominated by the interface failure mechanism. The compressive properties of mortar are taken without modification from literature. The uniaxial compressive strength of mortar and bricks as well as the tensile bond strength used for tensile

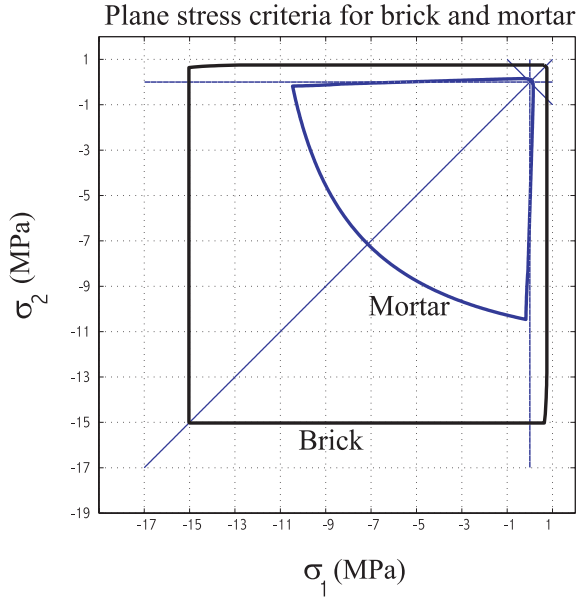

Figure 4.9: Shape of constituents damage loading function in plane stress space

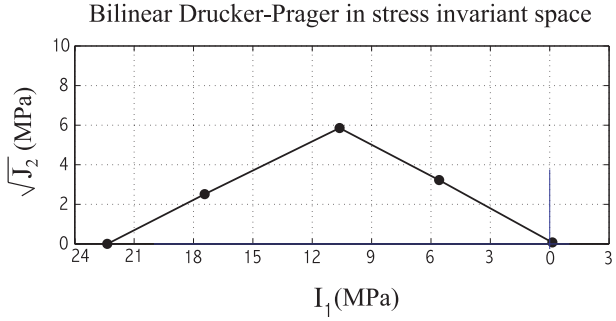

Figure 4.10: Shape of the mortar damage loading function in the space of principal stresses

mortar strength here were obtained in Page (1981, 1983); Dhanasekar et al. (1985). It should also be noted that the use of continuum elements to represent mortar joints (instead of interface elements as often used) is here strongly motivated by the use of a generalised plane state of deformation. The interactions between the materials due to their different elastic properties - the main cause of the presence of out-of-plane effects - are then included in a natural fashion.

Table 4.3: Material parameters (values with a * are typical values retrieved from various sources in the literature)

Material	E (MPa)	ν	l_c (mm)	f_t (MPa)	α	β	f_c (MPa)	f_b (MPa)	f_h (MPa)
Brick	16700*	0.15*	1.73	0.75	1.*	800*	15*	-	-
Mortar	3900*	0.20*	1.73	0.13*	1.*	140*	5.6*	8.72	7.45

The material parameters used in the simulations are summarized in Table 4.3. Only the average experimentally reported values were considered for our computations, ignoring the relatively important scatter on these mesoscopic parameters (for instance, the reported values of tensile bond strength range from 0.07 to 0.28 MPa). For the other parameters, typical values were extracted from Rots (1997); van der Pluijm (1999). In particular, the Young's modulus of mortar was obtained from Rots (1997) based on the mortar composition reported in Dhanasekar et al. (1985) (cement:lime:sand volumetric ratio of 1:1:6).

The damage evolution law parameter β may be obtained by fitting the adopted tensile fracture energy. Using the uniaxial tensile stress-strain relation obtained from the postulated damage evolution law, the fracture energy density, represented by the area under the softening part of the diagram, is expressed in terms of β. The parameter β was identified by integrating this fracture energy density over the full joint thickness (damage is allowed to spread over the whole thickness of joints) and equating it to the experimental estimation of the tensile fracture energy. These values for the tensile fracture energies are 9 Nm/m^2 and 16.2 Nm/m^2 for the mortar and brick materials respectively. For the considered mortar composition and tensile bond strengths similar to the ones reported in Page (1981), van der Pluijm (1999) reported tensile fracture energies of the same order of magnitude. The order of magnitude is also realistic for the brick material, even though the lack of brick related information in Page (1981, 1983); Dhanasekar et al. (1985) does not allow further validation of this point. It is however emphasized that the experimental values available for fracture energy parameters usually exhibit a high scatter. Finally, values for the remaining parameters were chosen to yield an acceptable shape of the failure criteria of materials. In particular, the value of the tensile strength used for bricks seems to yield an acceptable fit of experimental results in the overall tension-compression range where brick cracking is dominant (see paragraph 4.5.4).

4.5.2 Failure patterns for non shearing overall stress states

The type of failure mode (obtained computationally) is an important result that allows to assess the validity of a description, as it may impact the stress redistribution in structural computations. A relevant model should allow to identify the correct failure mechanisms for all stress states. Therefore, the damage distributions at the end of the unit cell computations obtained for both assumptions are depicted in Figure 4.11. Note that these patterns are obtained only well beyond the peak loads needed to construct the failure envelopes. As a consequence advanced path following techniques had to be used in order to trace the equilibrium path up to the identification of a complete failure mechanism, Geers (1999a). Similar failure modes have been found for most of the loading paths for both assumptions. In particular, a distributed vertical cracking of bricks for both assumptions is captured under vertical compression of masonry (case A) as reported in experiments, Page (1981, 1983); Dhanasekar et al. (1985). For tension dominated loading paths also (cases B and C), the failure modes are consistent with the reported experiments. Noteworthy is fact that the use of the maximum principal stress criterion for bricks indeed allows to capture accurately the complete envelope in the horizontal tension - vertical compression regime, which was not captured properly with the criterion used in Massart et al. (2004a). This conclusion applies to the plane stress case as well as to the generalised plane state case. As expected, the results delivered by the plane stress and generalised plane state assumptions differ in the biaxial compressive range (cases D, E and F) in terms of identified failure modes. A transition was found experimentally between in-plane and out-of-plane failure mechanisms, respectively for high and low ratios of applied macroscopic principal stresses, Page (1981, 1983); Dhanasekar et al. (1985). This transition is captured in the generalised plane state description as a result of its ability to capture mesoscopic out-of-plane stresses, while it is not found for the plane stress description in which these stresses are neglected. Case F still exhibits an in-plane failure mechanism for both assumptions. Case D represents a transition from an in-plane to an out-of-plane failure (some damage is present over the whole surface of the brick in the generalised plane state failure mode). In case E, the applied macroscopic principal stresses are nearly equal and the failure mode detected in the generalised plane state description indicates almost complete failure of both the brick (i.e. through mid-plane failure) and the mortar (damage reaches at least $D = 0.7$ value in the whole brick). For the corresponding plane stress computation, an in-plane failure mode is found with vertical brick cracking and partial bed joint failure. This difference of failure mode coupled to the observation that the generalised plane state description yields a (slightly) lower peak stress is consistent with the experimentally observed failure mode, i.e. out-of-plane splitting at mid-thickness plane.

It should be noted that strong local softening may appear before the peak load in such computations. It may therefore not be rigorously argued that the plane stress and generalised plane state descriptions may be applied for the outer and mid-thickness positions in an uncoupled fashion. The real phenomenon is three-dimensional at the mesoscale, and damage growth at both positions in the thickness may not be independent. Nevertheless, the generalised plane state description yields a qualitatively correct prediction for both the failure envelope and the failure mechanisms, for all non shearing overall stress states.

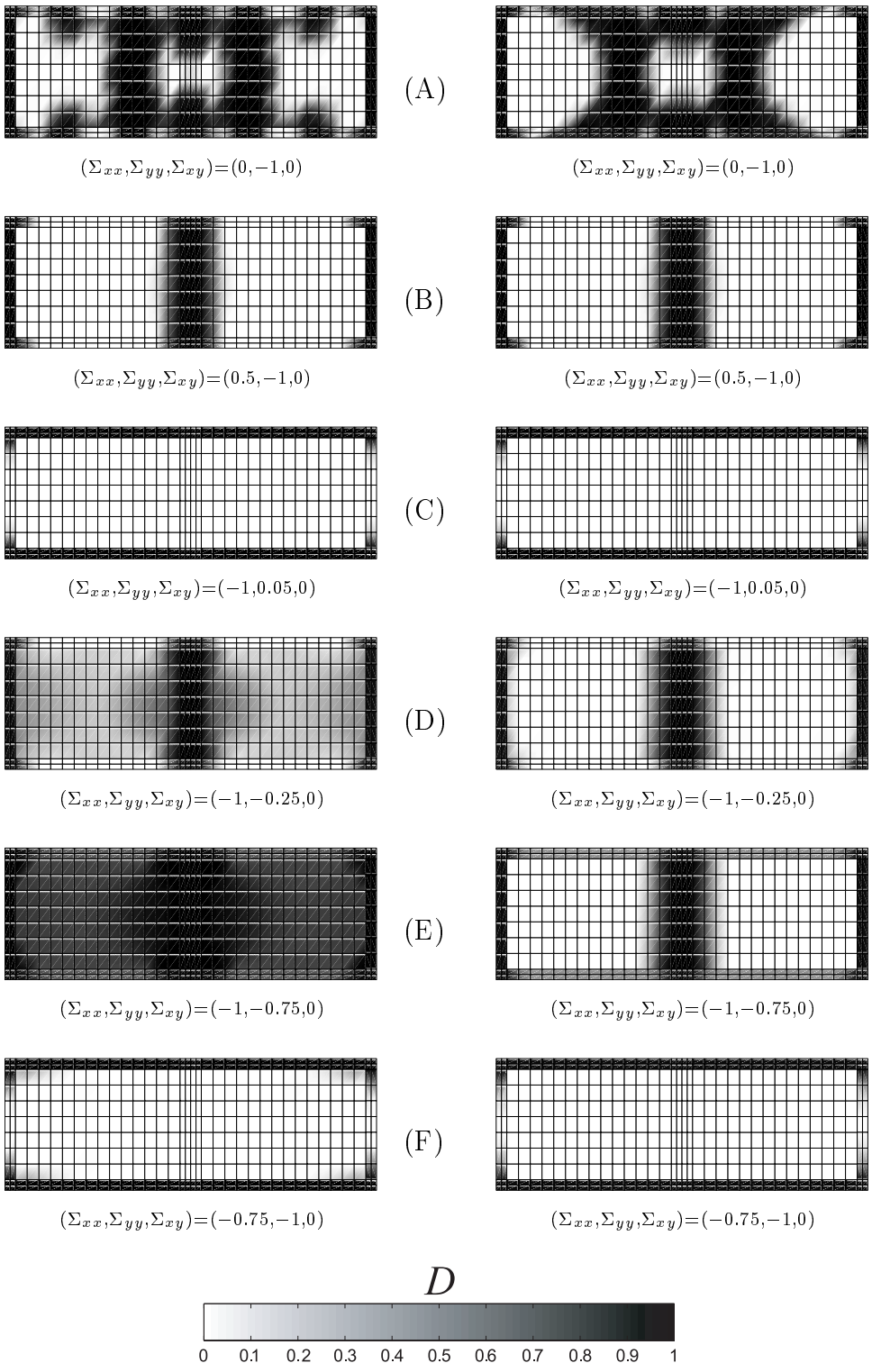

Figure 4.11: Failure (damage distribution) for loading directions defined in Figure 4.13 for generalised plane state (left) and plane stress (right) assumptions

4.5.3 Failure patterns for overall compression combined with shear

The failure patterns obtained for both assumptions along various compressive-shear loading paths are illustrated in Figure 4.12. They are similar, except under pure shear. For this case, the head joints fail for the generalised plane state description, while only bed joints fail in the plane stress description. When shear is of the same order of magnitude as the compressive stress, the anisotropy development is prescribed by the geometrical arrangement as damage only appears in part of the bed joints. For these two first stress paths illustrated in Figure 4.12, the overall induced anisotropy strongly alters the initial orthotropic symmetry of the material. For moderate shear, brick cracking appears. In such loading conditions, the loss of orthotropy is still present, but is less pronounced and is mainly driven by the damage growth in the brick.

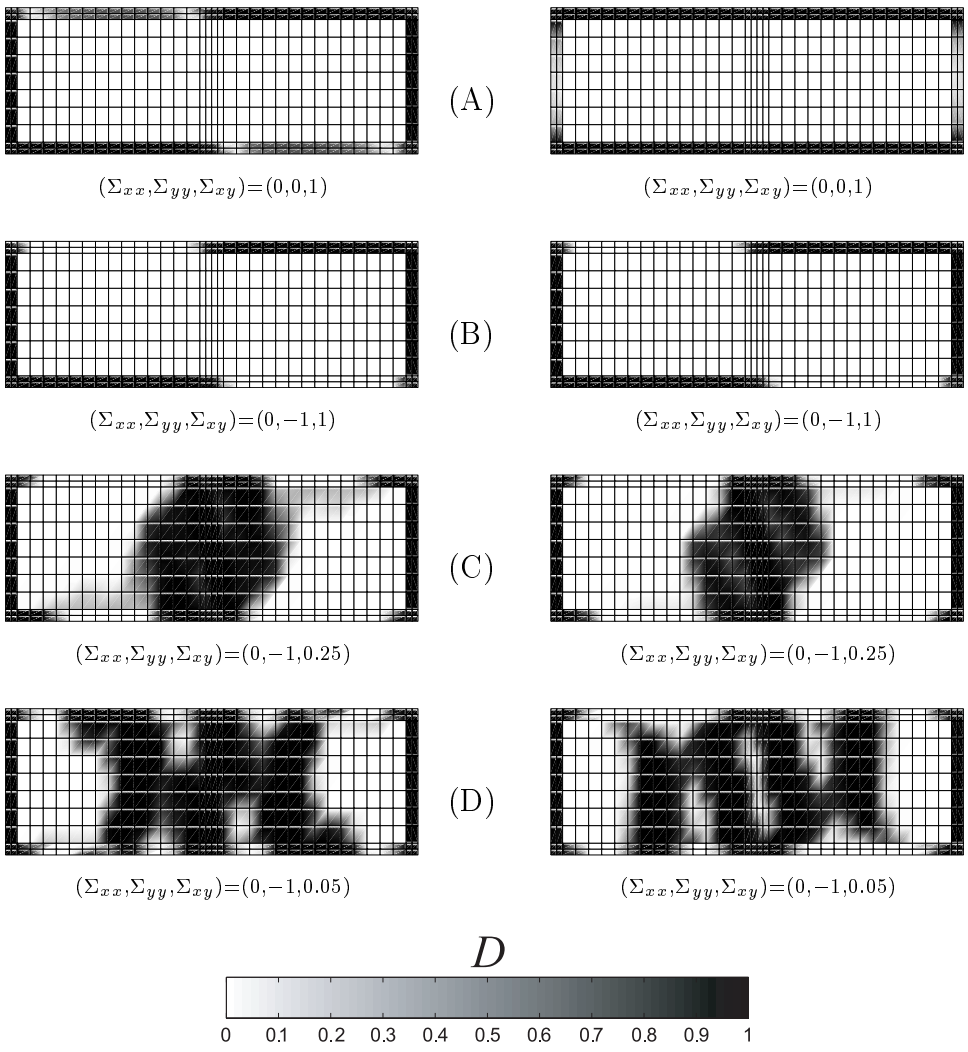

Figure 4.12: Failure (damage distribution) for compression combined with shear for generalised plane state (left) and plane stress (right) assumptions

4.5.4 Envelopes for non shearing overall stress states

The failure envelopes obtained for the plane stress and generalised plane state assumptions are next compared for non shearing overall stress states with experimental results reported in Page (1981, 1983); Dhanasekar et al. (1985). The computational envelopes are built based on the maximum load bearing capacity reached for each proportional stress direction. The envelopes which were thus obtained are shown in Figure 4.13 where each of the dots represents a finite element computation (the capital letters refer to the corresponding failure patterns reported in figure 4.11). The shaded area in this Figure represents the experimentally obtained envelopes with their observed scatter, Page (1981, 1983); Dhanasekar et al. (1985). For the considered damage laws and constitutive parameters, the failure envelopes determined for plane stress and generalised plane state nearly coincide. A maximum difference of 5 % is found, which is much lower than the experimental scatter. From the load-carrying capacity point of view (i.e. without considering failure pattern prediction), the benefit of using the generalised plane state description thus seems negligible for this case. The use of other damage laws or material parameters (for other mortar compositions for instance) might however change this conclusion. The shape of both computational failure envelopes is qualitatively similar to the experimental envelope, given the limited knowledge of material parameters from Page (1981, 1983); Dhanasekar et al. (1985) and the unknown geometrical data. The quantitative agreement is fairly good in the ten-

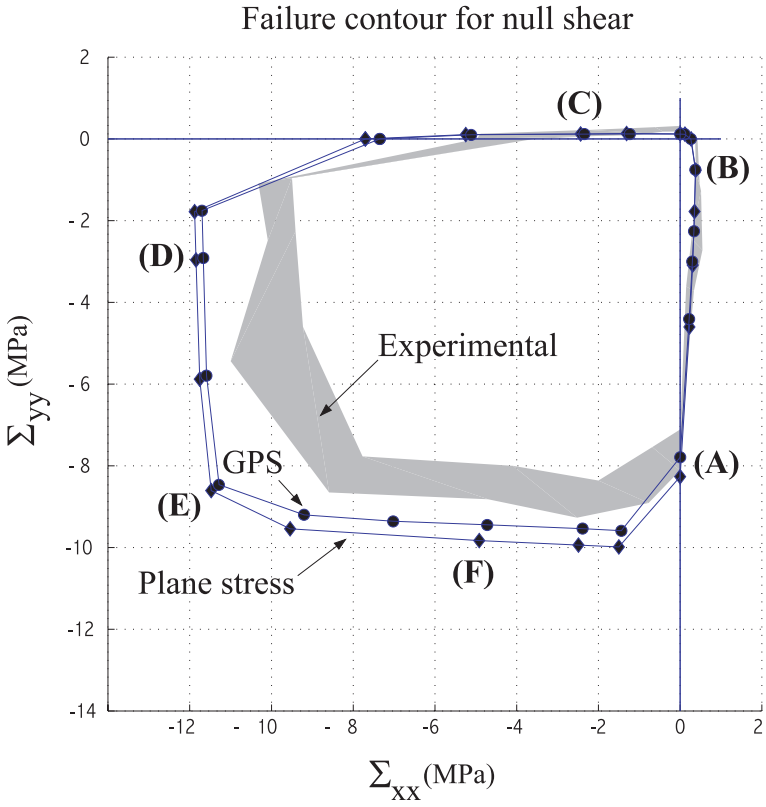

Figure 4.13: Experimental and computational failure envelopes for non shearing overall stress states

sion related quadrants. The difference in the horizontal compressive strength is linked to the definition of failure used in Page (1981, 1983); Dhanasekar et al. (1985), which does not match the maximum load-carrying capacity for this loading direction. Indeed, the experimental failure was defined as failure of bed joints for this loading case. The horizontal compressive stress may however further increase after this point if the head joints are not crushed, and this indeed happens in computations. In the biaxial compressive range, the non-symmetric shape of the envelope with respect to the equibiaxial compression axis is captured. This anisotropy is slightly stronger for the computational envelopes than for the experiments. This may be explained by the lack of experimental knowledge of compressive material parameters for multiaxial stress states (only uniaxial compressive strength was reported in Page (1981, 1983); Dhanasekar et al. (1985)). Differences in the aspect ratio of the bricks (unknown for the experimental case) and the rather simple brick failure criterion in the biaxial compressive range may also contribute to this deviation.

In the results reported in Figure 4.13, the plane stress assumption consistently yields a higher load bearing capacity than the generalised plane state. This difference in strength originates from two competing phenomena. The use of a generalised plane state description yields an increase of the overall stiffness of the unit cell as explained in Anthoine (1997). Under stress-control and for a given loading state, this leads to a decrease of strains in the elastic regime. On the other hand, the presence of out-of-plane normal stresses and strains has an impact on the obtained equivalent strain, potentially leading to an increase of this quantity (depending on the individual contributions of the different tensor components in the adopted definition). As a consequence, the net effect of the generalised plane state assumption with respect to the plane stress one may lead to an accelerated or delayed damage initiation in the cell, depending on the equivalent strain definition used for the materials. The reduced strength values (i.e. more critical) observed here for the generalised plane state are in contradiction with the observation reported in Anthoine (1997) for vertical compression, where the generalised plane state yielded a higher peak value. A modified Mazars damage evolution setting with distinct tensile and compressive damage parameters was used in Anthoine (1997), leading to different failure mechanisms under vertical compression for the plane stress and generalised plane state descriptions. Failure was obtained through damage of bed and head mortar joints for plane stress, while bed joints remained undamaged and brick cracking occurred under generalised plane state. This analysis was performed with higher strength values for the constituents. In the present computations, the vertical compressive failure mechanisms are nearly identical for both assumptions and lead to brick cracking, the only difference being that the damage in bed joints is more developed for the plane stress case. Nevertheless the failure patterns obtained for vertical compression with both assumptions agree well with the experimentally observed ones.

A physical interpretation of the patterns obtained in our analyses and of the different conclusions related to strength with respect to the results reported in Anthoine (1997) for this vertical compression case may be given as follows. For such a loading case, head joints are subjected to horizontal tensile stresses. These in-plane tensile stresses combined with an additional out-of-plane compressive stress under generalised plane state lead to a more critical stress state in the head joints than for plane stress. This leads to an earlier damage initiation in head joints under

Table 4.4: Stress states in mortar bed joint and brick for the vertical compression case. The two first components are in-plane principal stresses, the third one is the out-of-plane normal stress. 'T' denotes a tensile component, 'C' denotes a compressive component

	Plane Stress $(\sigma_1, \sigma_2, \sigma_{zz})$	Generalised Plane State $(\sigma_1, \sigma_2, \sigma_{zz})$
Bed joint	(C, C, 0)	(C, C, C)
Brick	(T, C, 0)	(T, C, T)

generalised plane state. The peak load and the final failure pattern are however also strongly governed by the stress redistribution that follows failure of the head joints. Upon almost complete failure of the head joints, the bed joints are submitted to a biaxial compressive stress state in the plane stress description, or triaxial compression for the generalised plane state case. As a result of head joint failure, in-plane tensile stresses appear in the brick, potentially leading to diagonal cracking. As a consequence, the bed joint and brick are subjected to the stress states reported in Table 4.4 for the plane stress and generalised plane state assumptions respectively. In the generalised plane state description, out-of-plane tensile stresses are causing the stress state in the brick to be even more critical than for the plane stress case. The out-of-plane compression generated in the bed joint by the generalised plane state leads to a less critical stress state than for the plane stress assumption. The ultimate failure in the generalised plane state case is thus governed by a competition between triaxial compressive failure of mortar and compressive - biaxial tension of bricks. The peak stress obtained depends on the triggered mechanism, and may be lower for the generalised plane state if brick cracking occurs. In the present computations, tensile failure in the brick seems to be predominant for both the generalised plane state and plane stress assumptions as illustrated in Figure 4.11(A). Note however that for the plane stress final failure pattern, the bed joints are also mostly degraded, while this is less the case for generalised plane state. This is linked to the fact that the biaxial compressive stress state in bed joints under the plane stress case is more critical than the triaxial compression in the generalised plane state case. The peak stress obtained for the generalised plane state assumption is lower than that in plane stress because the tensile failure of the brick is accelerated by the presence of the out-of-plane component. The difference obtained between the peak loads is however limited because both failure mechanisms (compressive crushing of joints and tensile failure of bricks) correspond to similar ultimate loads.

On the contrary, the Mazars criterion used in Anthoine (1997) exhibits an infinite strength for hydrostatic triaxial compression. This increases the strength for all multiaxial compressive stress states. As a consequence the out-of-plane compression generated in the bed mortar joints by the generalised plane state assumption has the effect of decreasing drastically the obtained equivalent strain in this joint. In Anthoine (1997), the biaxial compressive strength of mortar is rather low and is such that the bed joint failure is dominant in the plane stress case. This effect is however completely switched off in the generalised plane state description due to the shape of the damage criterion. This allows the development of brick cracking in the generalised plane

state case and leads to a change in the ultimate failure mechanism with respect to the plane stress case. Given the high brick tensile strength postulated in Anthoine (1997) (5 MPa), this resulted in a drastic peak load increase in the generalised plane state case compared with the plane stress case.

The obtained masonry failure pattern thus largely depends on the shape of the mortar damage criterion in the triaxial compressive range. This is confirmed by the observation that a similar transition may be obtained with the capped Drucker-Prager criterion used in this study. An increase of the values of the f_b and f_h parameters for the mortar to 14.5 MPa and 22.4 MPa respectively, and of the f_t and f_c parameters for brick to 1 MPa and 30 MPa respectively inverts the peak strengths obtained for plane stress and generalised plane state descriptions. In such a case, the peak load obtained with the generalised plane state assumption was found to be slightly higher than with plane stress. A worse fit between the experimental compressive strength and the computational result was however obtained with these parameters.
Given the composition of mortar (high sand proportion), it is believed that a bounded compressive hydrostatic strength should be used for this type of material. Even with the variation mentioned above, and for the set of experimental parameters used here, the difference in vertical compressive strength of masonry obtained with both assumptions did not exceed 5%. As a consequence, this effect seems to have a limited influence on the identified load-carrying capacity, at least for the vertical compression case, the chosen damage evolution laws, and bounded compressive triaxial strength values.

4.5.5 Envelopes for overall compression combined with shear

The envelope corresponding to vertical compression combined with shear is next identified. This type of overall stress state is usually encountered in masonry structures under normal loading conditions. Both plane stress and generalised plane state envelopes are represented in Figure 4.14. The obtained failure envelopes are nearly coincident when shear is dominant while the difference is more pronounced for low values of shear. For high shear stress values, the plane stress assumption leads to lower peak stresses than the generalised plane state assumption. The

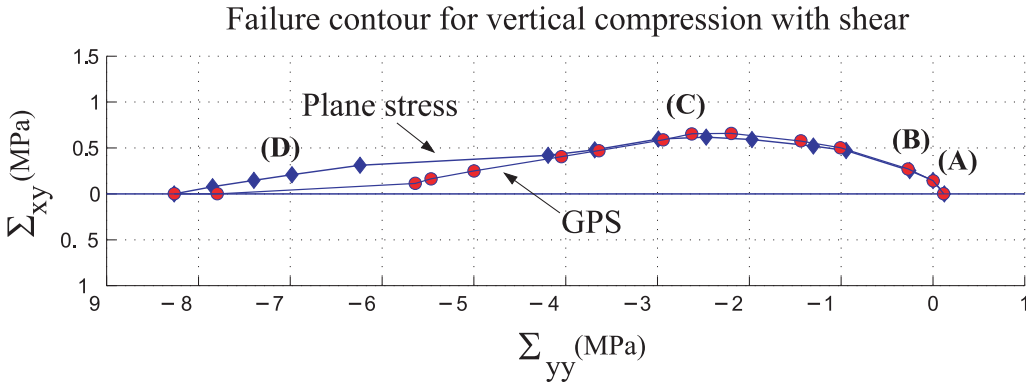

Figure 4.14: Computational failure envelopes for vertical compression combined with shear

generalised plane state becomes more critical for lower shear stresses. In addition, the envelope obtained with the generalised plane state description is (slightly) non-convex for low values of shear stresses combined with strong compression.

4.6 Conclusions

A generalised plane stress state formulation has been developed as an extension of mesoscopic analyses of masonry fracture performed in earlier work, Massart et al. (2004a). Using a classical homogenization technique, the two-dimensional format of the resulting overall behaviour has been illustrated. A two-dimensional implementation of this kinematic assumption has been used with an implicit gradient damage model. Based on typical material parameters found in the literature, a comparison with experimental evidence shows that the generalised plane state assumption allows to capture correctly the failure mechanisms for various stress paths, while the plane stress assumption is not able to detect the failure modes under biaxial compressive states. In addition, a good qualitative approximation may be obtained for the load-carrying capacity with the generalised plane state as well as with the plane stress descriptions, at least for the considered masonry mesostructure. Indeed, quantitative differences between the computed strengths are largely negligible compared to experimental scatter. Coupled to the overall two-dimensional format of the homogenized behaviour, these results strongly suggest that the generalised plane state assumption is the proper tool for mesostructural and structural computations as both failure patterns and envelopes are well predicted.

Chapter 5

A multi-scale approach for structural masonry walls computations - Part I. Concepts and treatment of localization

This first part of a two-paper contribution presents a multi-scale framework for the computational study of masonry structures, based on computational homogenization techniques. In order to overcome the troublesome formulation of closed-form constitutive equations, a first-order computational homogenization framework is applied to infer the non-linear material behaviour of brick masonry in the presence of quasi-brittle damage. A localization analysis is carried out based on the macroscopic homogenized tangent stiffness. It is shown that localization along preferential orientations is detected, which are consistent with the underlying mesostructural failure patterns and with the applied loading. An enhanced first-order computational multi-scale solution scheme is outlined, allowing to include microstructurally based damage localization in structural computations. Detailed computational aspects related to the presented framework and illustrative applications are treated in the second part of this contribution.

5.1 Introduction

Masonry has frequently been used in the past as a building material for structural applications. Due to the complexity and the heterogeneous nature of the material, the design of masonry structures is essentially based on codes and rules of thumb, often leading to a lack of control on safety factors and over-dimensioning. The complexity is even further increased for historical structures as a result of earthquake damage, structural changes, or foundation movements. The commonly made conservative approximations in design are too inaccurate in order to assess the residual strength and load bearing capacity of such structures. In this respect, modern computational methods start to emerge as valuable tools for the study of masonry structures, see for instance Lourenço (1998, 2002). The interest in such modeling tools originates in their rational approach towards the stability studies, allowing to complement codes, rules of thumb and the experience of the analysts. However, these computational approaches require reliable

This chapter is reproduced from: T.J. Massart, R.H.J. Peerlings and M.G.D. Geers, A multi-scale approach for structural masonry walls computations - Part I. Concepts and treatment of localization, To be submitted for publication in International Journal for Numerical Methods in Engineering.

constitutive models which are difficult to formulate for masonry.

At the structural scale, masonry may be considered as a two-phase composite material in which the phases, bricks and mortar, are assembled in a periodic manner. This periodic mesostructure and the different elastic characteristics of its constituents render the elastic behaviour of masonry anisotropic. In addition, the mortar phase is relatively weak, which due to the periodic arrangement of the phases leads to a stiffness degradation along preferential orientations. This results in a pronounced crack-induced anisotropy. The initial as well as the induced anisotropy of the overall material are strongly coupled to the underlying mesostructure, particularly to the geometry, the stacking mode, and the material properties of the brick and mortar. It is important to take both types of anisotropy into account in structural analyses because they may have a big impact on stress redistributions, Massart et al. (2004a). The mesostructure also has an important effect on the structural failure mechanisms that are observed. For instance, final crack patterns tend to follow the mortar joints and therefore depend on the geometry of the joint network. This suggests that the mesostructure should also be taken into account for accurate structural failure analyses.

The formulation of computational models which represent this type of behaviour is rather delicate. The last decade has shown to the development of dedicated numerical models which can be classified as follows according to their objectives and to the scales of representation they use.

The first class makes use of a mesoscopic approach. The constituents are modeled individually, see for instance Lourenço (1996); Giambanco and Di Gati (1997); Giambanco et al. (2001). Potential crack sites (mortar joints and sometimes cracks through the middle of bricks) are usually represented by interfaces, in which the material non-linearity is concentrated in terms of plasticity-like traction-displacement laws. This approach allows to capture accurately and in detail most of the in-plane failure mechanisms. It is the most versatile method to study structural details, but it is inefficient for large scale structural computations because the explicit modeling of the mesostructure requires an excessive computational effort.

A second class of models overcomes this drawback by formulating closed-form macroscopic constitutive laws for an equivalent homogeneous continuum. These approaches link average stresses to average strains in a phenomenological manner. They are based on plasticity concepts, Lourenço et al. (1997), damage with stiffness degradation, Berto et al. (2002) or couple both types of effects as in Papa and Nappi (1997). Considerable progress has been achieved, see e.g. Lourenço (1996). Yet, this type of approach still suffers from the inherent drawback that overall closed-form laws are troublesome to formulate, in particular when the interaction between initial and damaged-induced anisotropy has to be represented, see for instance Halm et al. (2002). As a consequence, phenomenological laws are often based on debatable assumptions, and their experimental identification and quantification is usually difficult and expensive.

The drawbacks of the approaches described above may be alleviated by coupling them in a multi-scale approach, where the mesoscopic and macroscopic scales of representation are intrinsically linked. A first class of multi-scale approaches bridges both scales by the identification of macroscopically used material parameters from mesoscopic models. A detailed model of the mesostructure is used to fit the parameters in a closed-form macroscopic constitutive

model. The actual structural computation is performed afterwards with the macroscopic model only. Closed-form constitutive relations still need to be postulated for both scales in such an approach. This can be done efficiently for the elastic behaviour of masonry, see Anthoine (1995); Cecchi and Di Marco (2000, 2002); Cecchi and Sab (2001). Extensions to the non-linear regime were proposed by Anthoine (1997) and Pegon and Anthoine (1997) for specific loading cases based on a periodic homogenization scheme and by Lourenço (1996) based on a two-step approximation method. These approaches may be used to solve at least partially the identification problem in macroscopic descriptions as mentioned above.

Nevertheless, retrieving and formulating an accurate closed-form macroscopic constitutive law constitutes a major problem. This may be overcome by adopting another type of multi-scale approach, in which both scales of representation are fully coupled in the entire structural computation. Using such a computationally coupled scheme avoids the use of an explicit formulation of constitutive equations at the macroscopic scale. At least two approaches for masonry have been developed in this spirit. The first is due to Luciano and Sacco (1997, 1998) who adopted an elastic-brittle representation for the constituents, an assumption which seems rather restrictive. More recently, Trovalusci and Masiani (2003) proposed a Cosserat model equivalent to a network of springs connecting rigid bricks. This particular implementation has the advantage that it naturally leads to a well-posed problem upon localization, even though it neglects the cracking of bricks which is required to yield realistic results, see Lourenço (1996). More realistic meso-scale models may be used if the overall material behaviour is determined online during the structural computation by numerical homogenization. This idea has been used by Smit (1998); Feyel and Chaboche (2000); Kouznetsova et al. (2002) to model the plastic behaviour of heterogeneous polymer and metal systems. The material representation is based on a representative volume of the mesostructure, which is used to formulate a classical boundary value problem (BVP) in each of the sampling points of a macro-structural computation. The solution of this mesostuctural BVP requires the detailed geometry of the mesostructure and the material behaviour of the individual phases. This approach will be used here since it fits particularly well for the representation of masonry structures. In addition to the fact that macroscopic closed-form relations are not needed, material data can be directly implemented at the scale of individual components. The identification problem is thus transferred to the mesoscopic level, where reliable experimental data is more readily available, van der Pluijm (1999). Most computational homogenization schemes rely on standard periodicity assumptions, which corresponds well with the initial periodicity of the masonry material. Effects which emerge from the mesostructure are captured naturally and the mesostructural representation may be refined if necessary. The main disadvantage of this type of approach resides in the increased computational cost.

The first-order multi-scale approach presented in Smit (1998) and Kouznetsova et al. (2001) homogenizes the mesoscopic description towards a classical stress-strain response, obtained in a numerical format only. Such a constitutive response naturally complies with the principle of local action in standard continuum mechanics. The use of softening damage laws at the mesoscale is accompanied by localization of damage in narrow zones, see de Borst et al. (1993), which may lead to structural failure. Mesostructural softening coupled to a macroscop-

ically local scheme generally leads to the loss of ellipticity of the governing set of equations. This occurs for closed-form phenomenological models as well as for computationally homogenized descriptions. Consequently, the macroscopic boundary value problem becomes ill-posed, and the width of macroscopic localization zones is mathematically undetermined and is set by the macroscopic discretization, leading to a non-objective energy dissipation, see for instance de Borst et al. (1993) or Kouznetsova et al. (2002). This difficulty is avoided here by imposing a finite bandwidth for a localization band. Given the periodicity of the mesostructure, this bandwidth follows in a natural way from the mesosopic geometry and damage development.

This paper is organized as follows. The principles of the adopted multi-scale framework are first recalled in Section 5.2, after which they are refined for the modeling of masonry. The choice of the mesoscopic representative volume element is briefly commented upon, and the derivation of the macroscopic consistent tangent material operator is recalled. The principles used to treat damage localization by means of embedded bands are highlighted in Section 5.3. Localization is considered as a bifurcation problem for this purpose. Classical criteria for the detection of material loss of stability and of ellipticity are presented. In Section 5.4, the use of these criteria is illustrated based on a localization analysis performed on the fundamental paths of a masonry unit cell for two typical loading cases. The results obtained from the applied criteria are compared with the mesostructural damage patterns and a procedure is proposed for the detection of macroscopic localization together with the associated localization orientation. The governing equations of a modified first order multi-scale scheme taking into account localization are highlighted in Section 5.5. This modified scheme is used to trace bifurcated solutions, as illustrated for a compression-shearing test in Section 5.6. Bifurcated solutions are compared, showing that the most critical solution is well captured by the proposed model. Finally, conclusions are drawn in Section 5.7.

5.2 Local multi-scale solution scheme

A first-order two-scale solution scheme has been presented by Smit et al. (1998). The main features of this framework are summarized here for the sake of clarity, with an emphasis on some specific issues related to its use for a periodically structured material like masonry.

5.2.1 Principles and assumptions

The multi-scale computational scheme is based on the extraction of the macroscopic material behaviour from a detailed representation at a lower scale given by a representative volume element (RVE) of the material. For the application to masonry structures considered here, the macroscopic or coarse scale is the structural scale. The lower or fine scale is that of individual bricks and joints, also denoted as the 'mesoscopic' scale in the sequel. With the exception of the displacement field, uppercase symbols relate to macroscopic quantities, while lowercase symbols denote mesoscopic variables. The differential operator $\vec{\nabla}$ is suffixed by a lowercase m when derivatives are taken with respect to mesoscopic coordinates, and by an uppercase M when derivatives are taken with respect to the macroscopic coordinates.

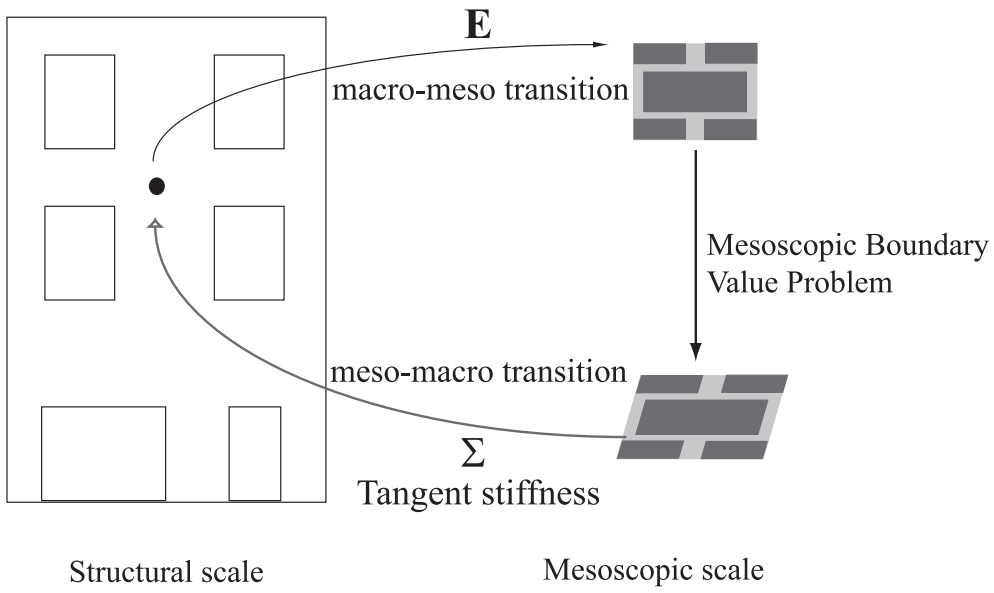

Figure 5.1: Principle of first-order multi-scale solution scheme

The key principle of the nested multi-scale approach is illustrated in Figure 5.1 and may be summarized as follows. A macroscopic strain $\mathbf{E}$ is obtained at each iteration of the nonlinear macroscopic solution procedure for all macroscopic sampling points (Gauss points). The solution procedure then requires the macroscopic stress tensor $\boldsymbol{\Sigma}$ which results from that iterative strain $\mathbf{E}$. Instead of feeding $\mathbf{E}$ into a closed-form constitutive relation at the macro-scale, it is transferred to the meso-scale by applying it to an RVE. This step constitutes the kinematical part of the multi-scale scheme, also denoted as the *macro-meso scale transition* and is detailed later in this section. A BVP needs to be constructed at the meso-scale, which may be implemented by means of several approximations. The response of the RVE is obtained as the solution of this BVP, which is a standard mesoscopic equilibrium problem. As a result, the mesoscopic strain field $\boldsymbol{\varepsilon}$, the mesoscopic stress field $\boldsymbol{\sigma}$, and potentially other field variables inside the RVE are available. Note that solving the mesoscopic equilibrium problem for history dependent constituents requires storing history data as well. The macroscopic stress $\boldsymbol{\Sigma}$ is then computed by averaging the mesoscopic stress field. This step is called the *meso-macro transition* and involves the statics of the problem. As a result of the procedure, the macroscopic stress-strain response of the material is fully determined, although it is only available numerically and not in terms of macroscopic constitutive relations. The meso-macro transition also permits to extract the constitutive tangent, which relates variations of $\boldsymbol{\Sigma}$ to variations of $\mathbf{E}$, which is required quantity for the next iteration of the macroscopic solution procedure, Kouznetsova et al. (2001).

It is emphasized that in the first-order multi-scale approach, the scale transition procedure attributes a stress-strain relationship extracted from a mesoscopic *structure* to a macroscopic *material point*. Therefore, the validity of the approach is theoretically restricted to situations in which the principle of separation of scales applies, i.e. where the mesoscopic characteristic length is much smaller than the length scale associated to spatial variations of the macroscopic strain fields, Kouznetsova et al. (2002).

5.2.2 Definition of the mesoscopic boundary value problem

Macro-meso scale transition

The macro-meso scale transition consists in applying the macroscopic strain tensor to an RVE. Boundary conditions are therefore required, which are defined such that the volume average of the mesoscopic strain on the RVE equals the imposed macroscopic strain. Three types of boundary conditions are classically used in homogenization:

- fully kinematically constrained boundaries determined from $\mathbf{E}$,
- fully statically loaded boundaries, determined by $\mathbf{\Sigma}$,
- periodic boundary conditions.

Generally, the periodicity requirement delivers the best results in terms of stiffness estimation even for random mesostructures, van der Sluis (2001). Furthermore, the periodicity of the initial mesostructure of the material suggests the use of periodicity conditions in the case of masonry. To this end, a mesoscopic displacement field of the form

$$\vec{u} = \mathbf{E}.\vec{x} + \ \vec{w} \tag{5.1}$$

is assumed in each point of the mesostructure, where $\mathbf{E}$ is the macroscopic strain tensor, $\vec{x}$ is the position vector within the RVE, and $\vec{w}$ is a mesoscopic displacement fluctuation field which distinguishes the real mesostructural displacement field from the linear $\mathbf{E}.\vec{x}$ field. The fluctuation field is assumed to be periodic. The volume average of the mesoscopic strain field $\boldsymbol{\varepsilon}$ ensuing from relation (5.1) is given by

$$\begin{aligned} \langle \boldsymbol{\varepsilon} \rangle &= \frac{1}{V_{\mathrm{RVE}}} \int_{V_{\mathrm{RVE}}} \left[\vec{\nabla}_m \left(\mathbf{E}.\vec{x} + \vec{w} \right) \right]^{sym} dV \\ &= \mathbf{E} + \frac{1}{V_{\mathrm{RVE}}} \int_{\partial V_{\mathrm{RVE}}} (\vec{w}\vec{n})^{sym} \, dS \end{aligned} \tag{5.2}$$

Since the boundary integral in (5.2) vanishes because of the periodicity of $\vec{w}$, $\langle \boldsymbol{\varepsilon} \rangle$ thus indeed equals $\mathbf{E}$.

Mesoscale equilibrium problem

As the macroscopic response is obtained from the RVE response, an equilibrium problem needs to be solved at the RVE level for the imposed macroscopic strain. Theoretically any modeling technique could be used at the mesoscopic scale. Here, the finite element method is used with a continuum description of the constituents.
The progressive degradation of the quasi-brittle constituents is represented using a damage mechanics framework. A gradient-enhanced constitutive description is used in order to prevent spurious mesh sensitivity of the results with respect to the spatial discretization, see Section

5.3, see Peerlings et al. (1996). In this model, a scalar isotropic damage quantity is introduced in the stress-strain relationship in the following way:

$$\boldsymbol{\sigma} = (1 - D)\ {}^{4}\mathbf{L} : \boldsymbol{\varepsilon} \tag{5.3}$$

The damage value D is deduced from a damage evolution law based on a strain history parameter κ, which represents the most severe strain state experienced so far by the material

$$D = D(\kappa) \tag{5.4}$$

In order to determine whether a strain state change is accompanied by further damage growth, a damage loading function is expressed in terms of a non-local or averaged scalar measure of the strain state $\overline{\varepsilon}_{eq}$ and of the parameter κ as

$$f(\overline{\varepsilon}_{eq}, \kappa) = \overline{\varepsilon}_{eq} - \kappa \tag{5.5}$$

The damage loading function f and the history parameter κ in addition satisfy the Kuhn-Tucker relations

$$f \leq 0 \qquad \dot{\kappa} \geq 0 \qquad f\,\dot{\kappa} = 0 \tag{5.6}$$

and an initial condition

$$\kappa(t = 0) = \kappa_i \tag{5.7}$$

The non-local $\overline{\varepsilon}_{eq}$ field is introduced as the solution of an additional partial differential equation (PDE) incorporating a material intrinsic length scale l_c in the description.

$$\overline{\varepsilon}_{eq} - l_c^2 \nabla_m^2 \overline{\varepsilon}_{eq} = \varepsilon_{eq} \tag{5.8}$$

This partial differential equation is complemented by a boundary condition of the Neumann type that is applied at the interface between materials.

$$\vec{\nabla}_m \overline{\varepsilon}_{eq} . \vec{n} = 0 \tag{5.9}$$

Details related to the damage criteria used for the constituents and the consequences of the use of this framework for masonry mesostructures are discussed in Massart et al. (2004a,c).

Choice of the RVE and periodicity implementation

As the macroscopic material response is extracted from mesostructural modeling, the selection of the RVE should be performed with care. It should be as small as possible in order to ensure that the computational effort remains limited at the mesoscopic level, yet sufficiently large in order to capture the average response for all possible failure mechanisms. In order to keep the multi-scale calculation feasible, and based on the periodicity of the initial mesostructure of masonry, the RVE is replaced here by smallest possible unit cell of the mesostructure. This cell is illustrated for the case of running bond masonry in Figure 5.2. The periodicity conditions have been indicated on the cell by arrows linking mutually tied boundary segments. It is noted

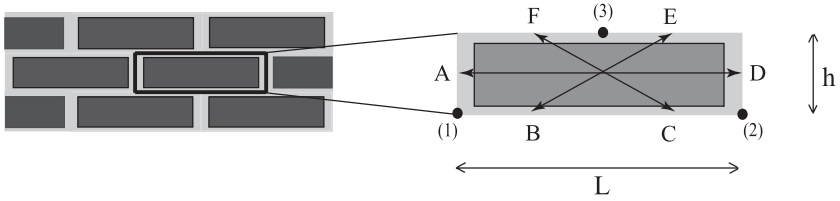

Figure 5.2: Unit cell and periodicity tyings for running bond masonry

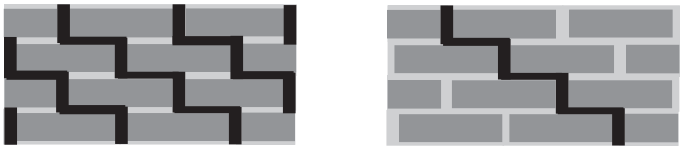

(a) Periodic failure pattern (b) Real failure pattern

Figure 5.3: Influence of the periodicity assumption on the representation of failure patterns in the vicinity of a macroscopic material point: (a) failure pattern satisfying the periodicity condition, (b) real failure pattern

that this periodic cell can only describe failure mechanisms which satisfy the same periodicity conditions. This is illustrated in Figure 5.3. The applied periodicity conditions imply the assumption that the damage pattern in a unit cell attributed to a macroscopic material point repeats itself in the vicinity of this point as sketched in Figure 5.3a. Actual damaged configurations usually exhibit strongly localized crack patterns as depicted in Figure 5.3b. A possible solution to obtain a more realistic representation consists in relaxing the periodicity conditions applied here, for instance using weaker (integral) conditions to ensure that the last integral term vanishes in relation (5.2), see Miehe (2002). However, the simplest unit cell will be used here in order to keep the computational effort reasonable.

Practically, the periodicity conditions are implemented using linear constraint relations between points of the corresponding edges of the unit cell as indicated in Figure 5.2. The three macroscopic strain components are imposed on the cell through imposed displacements of three controlling points, indicated in Figure 5.2 by (1), (2) and (3). The same points are also used to eliminate rigid body motion. The displacements imposed for these purposes may be expressed in terms of the components of the macroscopic displacement gradient $(u_{,x}, v_{,y}, u_{,y}, v_{,x})$ as

$$\begin{array}{rcl} (u_1, v_1) & = & (0,0) \\ (u_2, v_2) & = & (L\, u_{,x}\, ,\; L\, v_{,x}) \\ (u_3, v_3) & = & \left(h\, u_{,y} + \frac{L}{2}\, u_{,x}\, ,\; h\, v_{,y} + \frac{L}{2}\, v_{,x}\right) \end{array} \tag{5.10}$$

where L and h are the horizontal and vertical size of the unit cell respectively. The periodicity tyings are then expressed through the relations

$$\begin{array}{l} \vec{u}_D = \vec{u}_A + \vec{u}_2 - \vec{u}_1 \\ \vec{u}_E = \vec{u}_B + \vec{u}_3 - \vec{u}_1 \\ \vec{u}_F = \vec{u}_C + \vec{u}_3 - \vec{u}_2 \end{array} \tag{5.11}$$

Energy equivalence and meso-macro scale transition

In addition to the kinematic constraint defining the macro-meso scale transition, homogenization schemes usually rely on a work equivalence to identify the macroscopic stress tensor. This equivalence between the variations of macroscopic and mesoscopic work is known as the Hill-Mandel condition and reads

$$\boldsymbol{\Sigma} : \delta\mathbf{E} = \frac{1}{V_{cell}} \int_{V_{cell}} \boldsymbol{\sigma} : \delta\boldsymbol{\varepsilon} \; dV_{cell} \tag{5.12}$$

which is to be satisfied for any strain variation. With the use of mesoscopic equilibrium and of the Gauss theorem, the mesostructural displacement field (5.1) may be introduced in (5.12), yielding

$$\boldsymbol{\Sigma} : \delta\mathbf{E} = \frac{1}{V_{cell}} \left(\int_{\partial V_{cell}} (\vec{p}\vec{x})^{sym} \, dS_{cell} \right) : \delta\mathbf{E} + \frac{1}{V_{cell}} \left(\int_{\partial V_{cell}} (\vec{p}.\vec{w})^{sym} \, dS_{cell} \right) \tag{5.13}$$

where $\vec{p}$ is the traction vector acting on the boundary S_{cell} of the unit cell. Taking into account the periodicity of $\vec{w}$ and the resulting anti-periodicity of $\vec{p}$ at the unit cell boundary, the macroscopic stress tensor is obtained as

$$\boldsymbol{\Sigma} = \frac{1}{V_{cell}} \int_{\partial V_{cell}} (\vec{p}\vec{x})^{sym} \, dS_{cell} \tag{5.14}$$

Relation (5.14) identifies the macroscopic stress tensor as an integral over the cell boundary of mesoscopic boundary quantities obtained through the solution of the mesoscopic boundary value problem.

Due to the applied periodicity tyings, the contribution in (5.14) of homologous points of opposite edges cancel each other, Kouznetsova et al. (2001). The macroscopic stress can therefore be obtained directly from the forces acting on the controlling points only:

$$\boldsymbol{\Sigma} = \frac{1}{V_{cell}} \sum_{i=1}^{3} \vec{x}^{(i)} \vec{f}^{(i)} \tag{5.15}$$

where $\vec{f}^{(i)}$ is the external force applied at the controlling point (i) and $\vec{x}^{(i)}$ its position. It is noted that this macroscopic stress tensor is automatically symmetric, since mesostructural rotational equilibrium is satisfied.

In order to obtain an asymptotically quadratic convergence of Newton-Raphson iterations in non-linear computations, consistent tangent operators have to be obtained from a consistent linearization of the stress update, Simo and Taylor (1985). Furthermore, the material tangent operator is needed for the localization analysis as performed in Section 5.4. The consistent tangent linking the variations of macroscopic stresses and strains can be directly obtained by condensation of the discrete mesostructural tangent stiffness as proposed by Kouznetsova et al. (2001). This condensed tangent relation, after mesoscopic convergence to equilibrium, may be written as

$$\sum_{p=1}^{3} \mathbf{K}_{M}^{(np)} . \, \delta\vec{u}^{(p)} = \delta\vec{f}^{(n)}, \qquad n = 1,2,3 \tag{5.16}$$

where $\mathbf{K}_M^{(np)}$ is a second-order tensor relating the variation of the displacement vector of controlling point (p) to the variations of the mesoscopic force vector at controlling point (n). Substituting relation (5.16) in the variation of (5.15), and making use of (5.1) permits to define the fourth-order tangent ${}^4\mathbf{L}$ according to

$$\delta\boldsymbol{\Sigma} = \underbrace{\left(\sum_{n=1}^{3}\sum_{p=1}^{3}\vec{x}^{(n)}\mathbf{K}_M^{(np)}\vec{x}^{(p)}\right)^{(rs)}}_{{}^4\mathbf{L}} : \delta\mathbf{E} \tag{5.17}$$

where $(.)^{(rs)}$ denotes that condensation has been performed on the tensor by taking into account right symmetry to relate stresses to the infinitesimal strain tensor, and $\vec{x}^{(p)}$ denotes the position vector of controlling point (p). As the multi-scale solution scheme nests mesosopic computations in the macroscopic solution procedure to characterize and quantify the macroscopic material behaviour, this tangent is indicative for the real equilibrium path in macroscopically converged configurations only. As a consequence, localization analyses based on the macroscopic tangent operator as presented in Section 5.3 have to be performed in macroscopically converged states only (i.e. on the equilibrium path).

5.3 Macroscopic localization

5.3.1 Macroscopic and mesoscopic localization of damage

An important issue in modeling failure by continuum methods is the localization of deformation and degradation. Classical constitutive theories notoriously suffer from pathological localization when used to model damage and fracture, see de Borst et al. (1993). This means that at a certain stage of the degradation process any further deformation tends to localize in a surface, while the remaining volume unloads elastically. As a consequence, no energy dissipation is predicted anymore. This deficiency is intimately linked to a loss of well-posedness of the underlying boundary value problem. In numerical analyses it results in an excessive sensitivity of analysis results to the spatial discretization.
A number of approaches have been proposed in order to enhance continuum formulations by including an intrinsic length parameter to avoid the loss of ellipticity, Pijaudier-Cabot (1991); de Borst et al. (1993); Peerlings et al. (1996). At the mesoscopic level, pathological localization is prevented here by the use of a gradient damage model, see Peerlings et al. (1996). The internal length scale which is present in this model implicitly sets the width of damage bands and thus prohibits bands of zero width.

However, the macroscopic continuum used in the multi-scale approach remains *local*, and a pathologically localized response may therefore be expected at the macroscale. The characteristic spatial variation of the macroscopic solution would localize in an infinitesimal volume, whereas that of the underlying mesostructural analysis remains finite, thus violating the scale separation which was assumed between the meso- and macroscale. For disordered random heterogeneous materials, Kouznetsova et al. (2002) proposed an elegant solution to the above

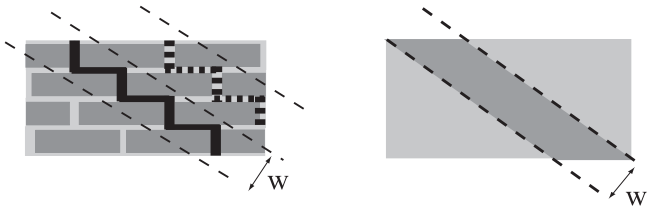

Figure 5.4: Extraction of a localization bandwidth based on the periodicity of the material. The dashed crack pattern indicates the periodicity for the considered pattern.

localization issue, by extending the macroscopic continuum with a higher order kinematic measure and a corresponding higher-order stress in the sense of Toupin (1962) and Mindlin (1964). In this so-called second-order framework, the physical size of the mesostructural RVE enters the macroscopic equilibrium problem in a natural way, and provides the length scale on which the macroscopic deformation field tends to localize. In the case of masonry however, higher-order continua can be avoided by further exploiting the periodicity of the mesostructure. For each possible failure mechanism, a localization bandwidth can be determined in a natural way by selecting the smallest possible period by which the damage pattern may be repeated. This is illustrated in Figure 5.4 for the case of a staircase crack pattern.

The inclusion of such localization bands requires the following ingredients:

- a criterion to decide when to introduce a localization band (detection),
- a criterion to determine the orientation of this band.

These elements can be taken from parallel concepts defined in continuum mechanics for closed-form constitutive relations. In homogeneous problems, the appearance of a band in which further growth of damage localizes may be considered as the bifurcation of a secondary solution from the homogeneous fundamental solution. This approach is used in classical continuum mechanics to derive the conditions for the onset of localization, see e.g. Rice (1976). The conditions on the material behaviour which are thus obtained are related to the mathematical concepts of loss of ellipticity and loss of stability.

These different concepts are therefore reviewed in the following sections in order to apply them in subsequent localization detection analyses. The discussion focuses on the distinction between loss of stability and loss of ellipticity and summarizes the work of Pijaudier-Cabot (1991) and de Borst et al. (1993) on this topic.

5.3.2 Loss of material stability and loss of ellipticity

A material response is said stable if, de Borst et al. (1993),

$$\delta^2 w \;=\; \delta\boldsymbol{\Sigma} \;:\; \delta\mathbf{E} \;=\; \delta\mathbf{E} \;:\; {}^4\mathbf{L} \;:\; \delta\mathbf{E} \;>\; 0 \tag{5.18}$$

where $\delta^2 w$ denotes the second variation of work density and ${}^4\mathbf{L}$ is the - macroscopic - material tangent. It is noted that the last part of condition (5.18) assumes that the tangent stiffness ${}^4\mathbf{L}$

corresponds to a linear comparison solid. Based on this criterion, the stability of the material response is lost if the symmetric part of the constitutive tangent ${}^4\mathbf{L}^{sym}$ becomes non-positive definite. Material instability may appear in the rising part of the load-deflection path if the tangent operator ${}^4\mathbf{L}$ is non-symmetric. A well-known illustration of this is the case of non-associated plasticity, often used to represent frictional effects in for instance granular materials. This also occurs for elastic-damage laws when the postulated damage criterion is not expressed in terms of the energy release rate. The loss of material stability does not necessarily imply the appearance of localized straining modes.

The local elliptic character of the static equilibrium equations is guaranteed whenever the condition

$$\det\left(\mathbf{A}\right) = \det\left(\vec{n}.\,{}^4\mathbf{L}.\vec{n}\right) > 0 \tag{5.19}$$

is satisfied, where the tensor $\mathbf{A}$ is called the acoustic tensor. Under the linear comparison solid assumption, violating this criterion is a sufficient condition for the boundary value problem to become ill-posed. It may be shown that the loss of ellipticity is equivalent to the condition for material bifurcation with appearance of strain discontinuities, see Peerlings (1999) and the following section. It may also be shown that loss of stability always precedes loss of ellipticity, de Borst et al. (1993).

The criterion for loss of ellipticity should not be confused with the condition allowing to detect limit points in the homogenized stress-strain response. Such a limit point condition may be expressed in terms of the eigenvalues of the tangent operator ${}^4\mathbf{L}$ obtained from the following eigenvalue problem

$${}^4\mathbf{L} : \mathbf{N}_i^R = \lambda_i^{\mathbf{L}}\,\mathbf{N}_i^R \tag{5.20}$$

The tangent operator may be expressed through the spectral decomposition

$${}^4\mathbf{L} = \sum_{i=1}^{3} \lambda_i^{\mathbf{L}}\,\mathbf{N}^L\,\mathbf{N}^R \tag{5.21}$$

where $\mathbf{N}^L$ and $\mathbf{N}^R$ are left and right second-rank eigentensors. A limit point is reached when the lowest of these eigenvalues vanishes, i.e.

$$\lambda^{\mathbf{L}} = 0 \tag{5.22}$$

In an infinitesimal strain setting, this limit point is also a bifurcation point. For symmetric operators ${}^4\mathbf{L}$ (i.e. $\mathbf{N}^L = \mathbf{N}^R$), conditions (5.19) and (5.22) coincide and loss of ellipticity occurs at the peak of the stress-strain response. For non-symmetric operators, loss of ellipticity (and thus material bifurcation) may appear before the limit point, e.g. Willam et al. (1998). As the loss of material stability as defined by (5.19) is related to the symmetric part of the material tangent, it also always occurs before the appearance of a limit point.

5.3.3 Macroscopic localization as a bifurcation problem

The localization of deformation and damage growth into a uniform band as considered in the present approach (see Figure 5.4) always requires passing a bifurcation. This can be understood

by realizing that a solution in which the behaviour of the band is followed outside the band is also a valid solution of the equilibrum problem. At some stage during the loading process, at least two equilibrium paths must thus have become available instead of the single path before localization. The onset of localization may therefore be detected by a bifurcation analysis as considered for instance in Rice (1976) or Lemaitre (1990). Such an analysis identifies the conditions under which the appearance of the strain discontinuity which exists between the band and the surrounding material is possible. More precisely, consider a piece of material under a uniform stress state $\mathbf{\Sigma}$, and separated in two sub-regions '+' and '–' by a surface S. The normal to S in the direction of the '+' sub-region is denoted by $\vec{n}$. It is assumed that the material in the '+' sub-region continues to load. In the present context, this means that damage further grows in this sub-region. As to the '–' sub-region, we consider two distinct cases: the case where this sub-region also keeps loading, but in a different straining direction from that in the '+' sub-region, and the case where it unloads elastically. The former is called a 'continuous bifurcation', in order to indicate that the same tangent ${}^4\mathbf{L}$ is valid on both sides of S precisely at the bifurcation point. The loading-unloading type of bifurcation has two different tangents and is therefore referred to as a 'discontinuous bifurcation'.

Continuous bifurcation

Equilibrium requires the traction vector at the interface between both sub-regions to be continuous, hence

$$\vec{n}.\left(\delta\mathbf{\Sigma}_+ - \delta\mathbf{\Sigma}_-\right) = \vec{0} \tag{5.23}$$

Continuity of the displacement field requires the strain jump across S to be of the form

$$\delta\mathbf{E}_+ - \delta\mathbf{E}_- = \frac{1}{2}\left(\delta\vec{m}\,\vec{n} + \vec{n}\,\delta\vec{m}\right) \tag{5.24}$$

where $\vec{m}$ is a strain mode vector, which vanishes in the initial, homogeneous situation, and must become nonzero for a bifurcated state to exist. The classical linear comparison solid assumption consists in postulating the same material tangent operator for both sub-regions. As a consequence, the traction continuity requirement (5.23) becomes

$$\vec{n}.\,{}^4\mathbf{L} : \left(\delta\mathbf{E}_+ - \delta\mathbf{E}_-\right) = \vec{0} \tag{5.25}$$

Introducing (5.24) into (5.25) and taking into account the right minor symmetry of ${}^4\mathbf{L}$, the traction continuity requirement finally yields

$$\left(\vec{n}.\,{}^4\mathbf{L}.\vec{n}\right).\delta\vec{m} \;=\; \vec{0} \tag{5.26}$$

For a strain discontinuity to appear, this system of equations should admit a non trivial solution $\delta\vec{m}$ for some direction $\vec{n}$, which is only possible if for this $\vec{n}$

$$\det\left(\vec{n}.\,{}^4\mathbf{L}.\vec{n}\right) = 0 \tag{5.27}$$

This condition is equivalent to the loss of ellipticity of the underlying rate equilibrium equations. It is often used in numerical procedures in order to identify the load level and the orientations

for which localization arises when closed-form constitutive relations are used. It has been used in numerous contributions both for plasticity and brittle damage models, see Cormery (1994), or Wells (2001) for instance.

Discontinuous bifurcation

The continuous bifurcation condition was extended to discontinuous bifurcation for the case of non-associative plasticity by Rice and Rudnicki (1980) and Borre and Maier (1989). This means that the tangent ${}^4\mathbf{L}$ is no longer identical on both sides of S. The set of orientations $\vec{n}$ for which localization may appear is then determined by the inequality

$$\det\left(\vec{n}.\,{}^4\mathbf{L}.\vec{n}\right) \leq 0 \tag{5.28}$$

Since initially ${}^4\mathbf{L}$ is positive-definite, this condition is first met when the equality holds for some $\vec{n}$. Some analytical results for non-associated plasticity in plane stress and plane strain configurations were obtained by Runesson et al. (1991). This criterion has been used for plasticity applications as well as for elastic-damage formulations as in Dragon et al. (1994). It is emphasized however that its use in damage models, where the unloading stiffness depends on the damage state, does not seem to have a rigorous motivation. Its validity may be established for damage evolution laws based on the energy release rate, but this proof is difficult to extend to general damage laws. This is even more true for a computational multi-scale framework, in which no closed-form constitutive equation is available.

5.3.4 Consequences for localization detection in the multi-scale procedure

Despite the lack of a rigorous motivation, relation (5.27) is used in the present framework to detect the possible occurrence of macroscopic localization. Note that this condition uses the acoustic tensor associated to the macroscopic, homogenized tangent stiffness. It is a necessary and sufficient condition for the appearance of a bifurcation under the linear comparison solid assumption. In addition, the eigenvalues of the tangent operator – relations (5.21) and (5.22) – allow to detect a limit point, the appearance of which is a sufficient (but not necessary) condition for bifurcation. This latter criterion offers a more efficient way of detecting localization since it is computationally cheaper than the inspection of the acoustic tensor eigenvalues for all possible orientations, even though it is unable to detect bifurcations arising before the limit point. The orientation associated to the localization can only be determined by an eigenspectrum analysis of the acoustic tensor.

5.4 Localization analysis illustration

In this section, the localization conditions discussed above are illustrated in the computational homogenization scheme for running bond masonry. An analysis is performed on the eigenspectrum of the acoustic tensor associated with the macroscopic material tangent ${}^4\mathbf{L}$ obtained

from equation (5.17). An eigenvalue analysis of the homogenized tangent stiffness is also performed. These eigenvalue analyses are done for the entire deformation path in a uniformly and proportionally stressed 'structure'. The macroscopic 'structure' consists of a single finite element which has dimensions that are identical to the unit cell dimensions in order to obtain the same load-displacement curves as in single unit cell computations. The considered brick has dimensions $L \times h \times e$ equal to $165 \times 52 \times 100$ mm^3 and mortar joints which are 10 mm thick. The mesostructure is represented by means of a finite element mesh containing 396 eight-noded elements and 1440 nodes. A plane stress behaviour is assumed as the failure patterns for the considered loading cases are not strongly affected by potential three-dimensional effects, see Massart et al. (2004c). The damage criteria used for the brick and mortar materials are the same as in Massart et al. (2004c), namely a maximum principal stress criterion for the brick material and a Drucker-Prager-like criterion with a compressive cap for mortar. In order to follow the solution path up to complete failure, advanced path following techniques are used. For more details about these methods, the reader is referred to Geers (1999a) and to Part 2 of this paper, dealing with the computational aspects.

Two loading cases are investigated here, which both lead to typical failure patterns. For both cases, the loading is applied proportionally in terms of stresses. As a first case, vertical compression is combined with a smaller amount of horizontal tension, leading to a failure mechanism which involves mode I failure of the head joints and vertical cracking of the bricks. The second test considers a combination of vertical compression and shear and leads to the formation of a staircase crack. Figure 5.5 shows the final damage patterns which are typically obtained for the two loading cases. If complete failure is assumed, an overall crack direction can be identified for each of the patterns, purely based on geometric arguments, as indicated by the normal vector $\vec{n}$ in Figure 5.5. For the geometry used here, orientations of $\Theta = 0^\circ$ and $\Theta = 54.7^\circ$ are found respectively for the considered loading cases. These are approximately the directions which one would like to extract from the overall mesostructural response, without a priori knowledge of the final failure pattern. We will demonstrate below that these orientations are indeed intimately related to the localization direction predicted by the lowest eigenvalue of the homogenized acoustic tensor and the homogenized tangent stiffness. As the localization cri-

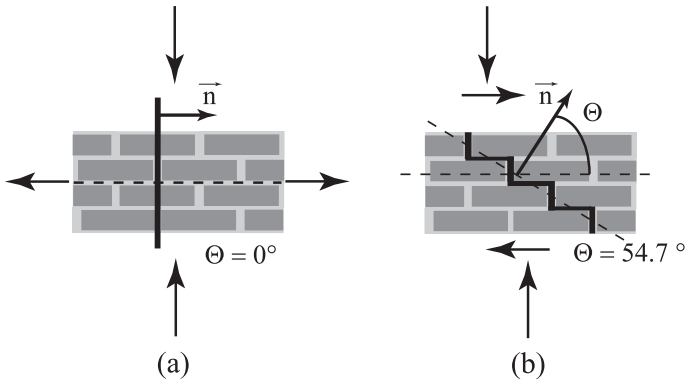

Figure 5.5: Average crack orientations defined by their normal $\vec{n}$ for the considered failure patterns

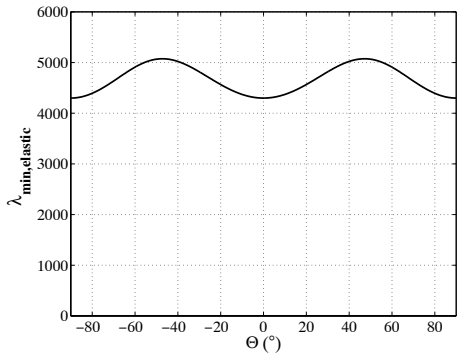

Figure 5.6: Acoustic tensor eigenspectrum for undamaged material

terion corresponds to the smallest eigenvalue of the acoustic tensor passing from the positive to the negative regime, only the lowest eigenvalue for each possible orientation $\vec{n}$ is represented in the related eigenspectrum. Loss of ellipticity occurs when λ_{min} vanishes for a certain direction $\vec{n}$. Note that as a consequence of the initial orthotropy of the material, the eigenspectrum of the acoustic tensor corresponding to the undamaged material is not constant as illustrated in Figure 5.6.

5.4.1 Vertical compression combined with horizontal traction

For the first loading case, mode I failure of the head joints is first observed, followed by vertical cracking in the brick due to a combined tension-compression stress state. As proportional loading is applied, all stress components remain proportional to the imposed load factor. The load-displacement curve depicted in Figure 5.7a represents the variation of the load factor as a function of the horizontal displacement of the right controlling node of the unit cell. The state corresponding to each point denoted by a capital letter in Figure 5.7 is analyzed below. The evolution of the lowest eigenvalue of the homogenized tangent operator ${}^4\mathbf{L}$ is given in Figure 5.7b as a function of the same displacement as in the load-displacement curve. The damage distribution in the cell for each state is shown in Figure 5.8 together with the corresponding acoustic tensor eigenspectrum. The eigenspectrum for damaged configurations is normalized by dividing it by the homogenized horizontal stiffness of the undamaged material, $L_{1111} = 12957$ MPa.

As illustrated in state B in Figure 5.8, the failure of head joints is accompanied by a decrease of the lowest eigenvalue, particularly for angles around $\Theta = 0°$. The depicted eigenvalue for $\Theta = 90°$ is affected much less by the initial stages of damage growth. At the same time, the lowest eigenvalue of the homogenized tangent stiffness also decreases (Figure 5.7b). A portion of the acoustic tensor eigenspectrum only goes to the negative range when damage initiates in the brick, Figure 5.8, state C, indicating the possibility for localization. The negative portion of the eigenspectrum is centered around $0°$. It exhibits at this stage a local maximum for $\Theta = 0°$ and two local minima at approximately $\Theta = \pm 20°$. These minima, which are identical in intensity, seem to stem from the original curve as in state B, and disappear almost immediately after they have become negative. Simultaneously, the lowest eigenvalue of the homogenized tangent stiffness becomes negative, see Figure 5.7b - point C. When the computation is contin-

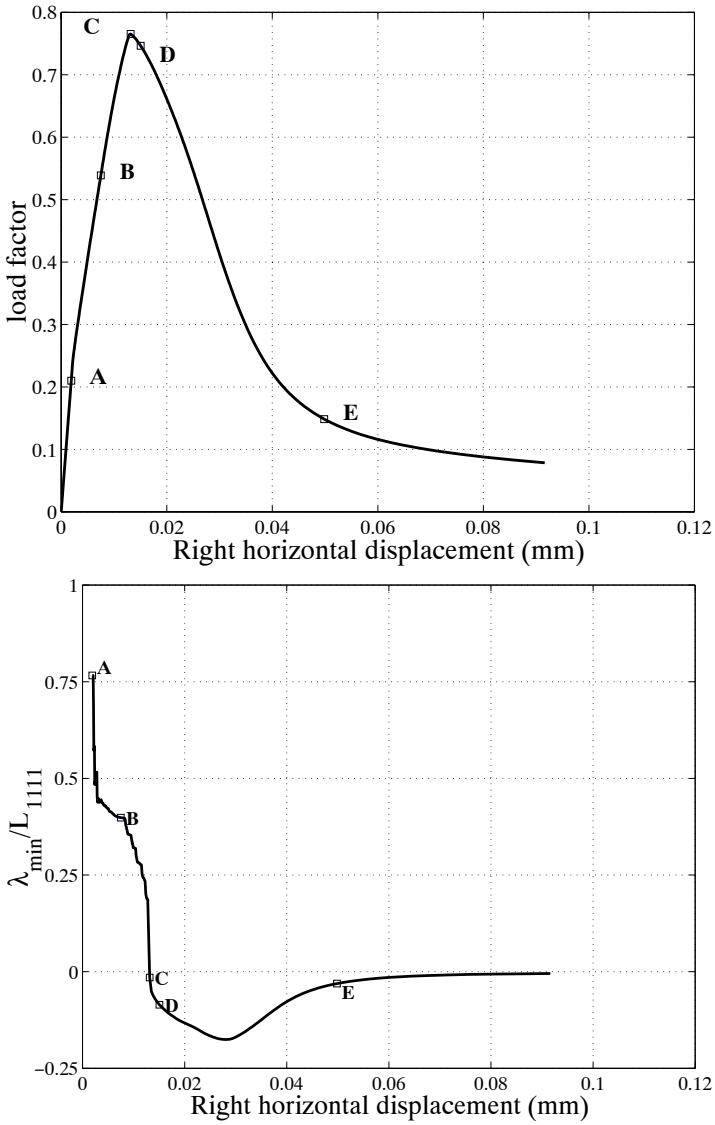

Figure 5.7: (a) Loading factor vs horizontal displacement of right controlling node of the cell for vertical compression combined with horizontal tension, (b) Corresponding evolution of the lowest eigenvalue of the homogenized tangent operator

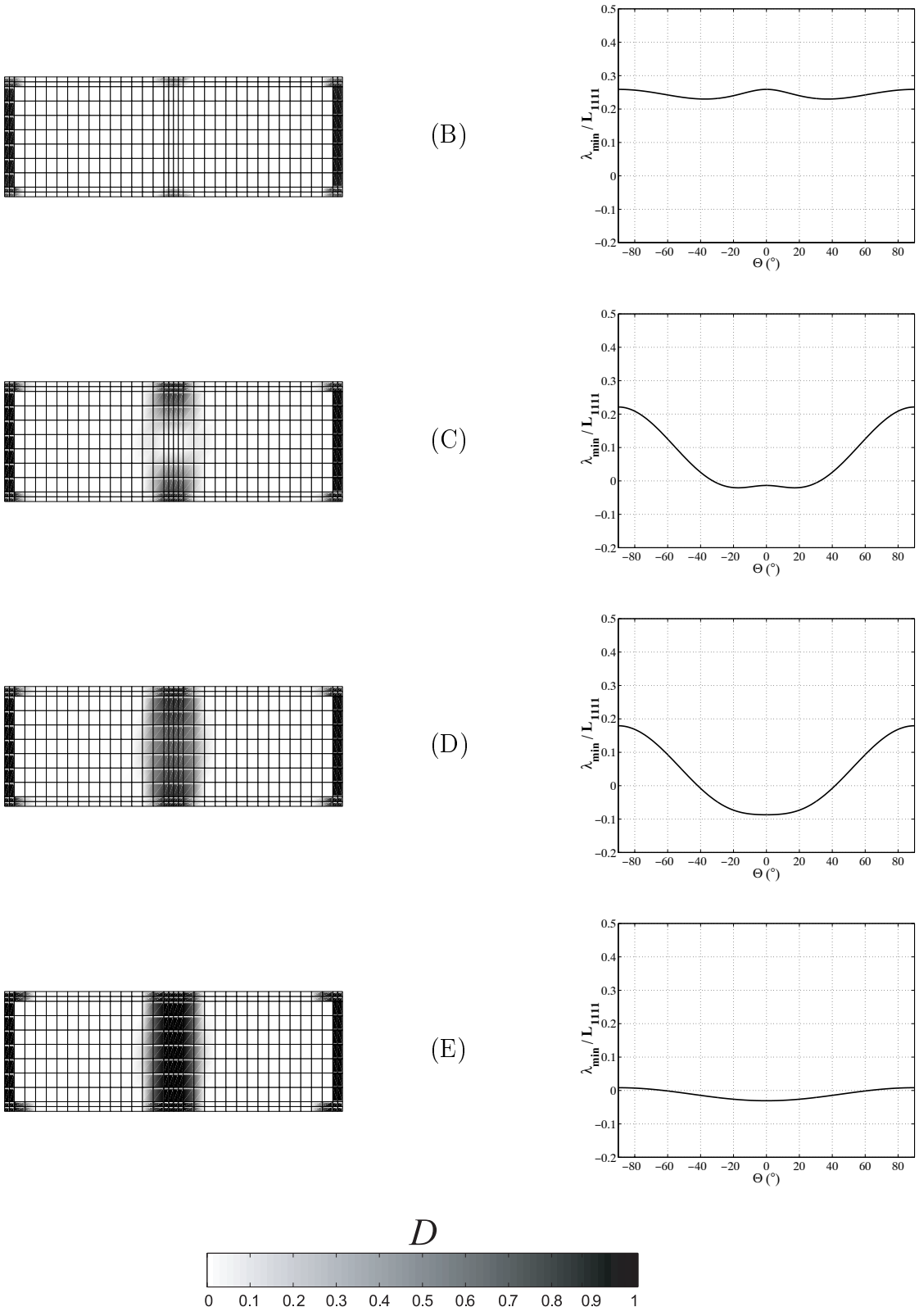

Figure 5.8: Damage distribution for compression combined with horizontal tension (left) and related acoustic tensor eigenspectrum (right). The orientation Θ is defined as the angle between the normal to the potential localization surface and the horizontal direction.

ued on this fundamental path, the eigenvalue analysis indicates a vertical band ($\Theta = 0°$) which clearly corresponds with the orientation predicted in Figure 5.5. When almost complete failure is reached, the localization orientation is still found as a minimum in the acoustic tensor eigenspectrum.
These results show that useful information related to the mesostructural damage pattern may be obtained from the localization analysis on the homogenized tangent material stiffness. In particular, it is possible to detect the macroscopic bifurcation in terms of the applied load level and to determine its orientation. Note in particular that both indicators, i.e. the lowest eigenvalue of ${}^4\mathbf{L}$ and of $\mathbf{A}$, indicate localization at the same moment.

5.4.2 Vertical compression combined with shear

The eigenvalue data for the case of vertical compression combined with shear is shown in Figures 5.9 and 5.10. Initially, the head joint is partially degraded and damage is initiated in parts of the bed joints, as a precursor to the expected staircase crack pattern, Figure 5.10. The damaged segment of the bed joint however still contains some undamaged material. This evolution is seen in the corresponding acoustic tensor eigenspectrum (on the right in Figure 5.10) in which the values are decreasing faster for orientations between $\Theta = 0°$ and $\Theta = 90°$ than between $\Theta = -90°$ and $\Theta = 0°$. The lowest eigenvalue of the homogenized tangent stiffness remains positive. This crack pattern continues to evolve as shown in Figure 5.10 - state C and a first minimum of the acoustic tensor eigenspectrum becomes negative at an orientation of $\Theta = 4.1°$. Note that the damaged bed joint segment still contains some undamaged mortar as shown in Figure 5.10 (state C). This means that the acoustic tensor criterion (5.27) detects a loss of ellipticity at this stage. However, the lowest eigenvalue of the tangent stiffness remains positive as can be seen in Figure 5.9 (point C), and the limit point of the homogenized stress-strain response has not yet been reached. Upon further loading, damage spreads over the complete bed joint segment as illustrated for state D, leading to the formation of a staircase crack pattern. This happens when the macroscopic limit point is reached. Simultaneously, a second minimum of the acoustic tensor eigenspectrum becomes negative for an orientation of approximately $\Theta = 58.3°$, see Figure 5.10 - state D. This orientation is similar to the averaged crack orientation specified above, the difference being linked to the non uniform damage distribution inside the damaged zone at this stage. As from this point, the lowest eigenvalue of the homogenized tangent stiffness becomes negative as well, see Figure 5.9b, and both the loss of ellipticity criterion (5.27) and the limit point condition (5.22) are now satisfied. Finally, upon further loading, the orientation corresponding to this new minimum slightly evolves towards $\Theta = 53.8°$ for the last computed point. This value differs by less than $1°$ from the angle of $\Theta = 54.7°$ which was predicted based on geometric arguments and thus corresponds well to the expected result. Again, these results strongly suggest that mainly the localization analysis based on the homogenized tangent stiffness delivers useful information related to the mesostructural evolution inside the unit cell. Localization seems best detected from the homogenized tangent via criterion (5.22), as the average damage pattern orientation seems to be linked to the second bifurcation point detected by the loss of ellipticity criterion (5.27), which is reached at the limit point in the

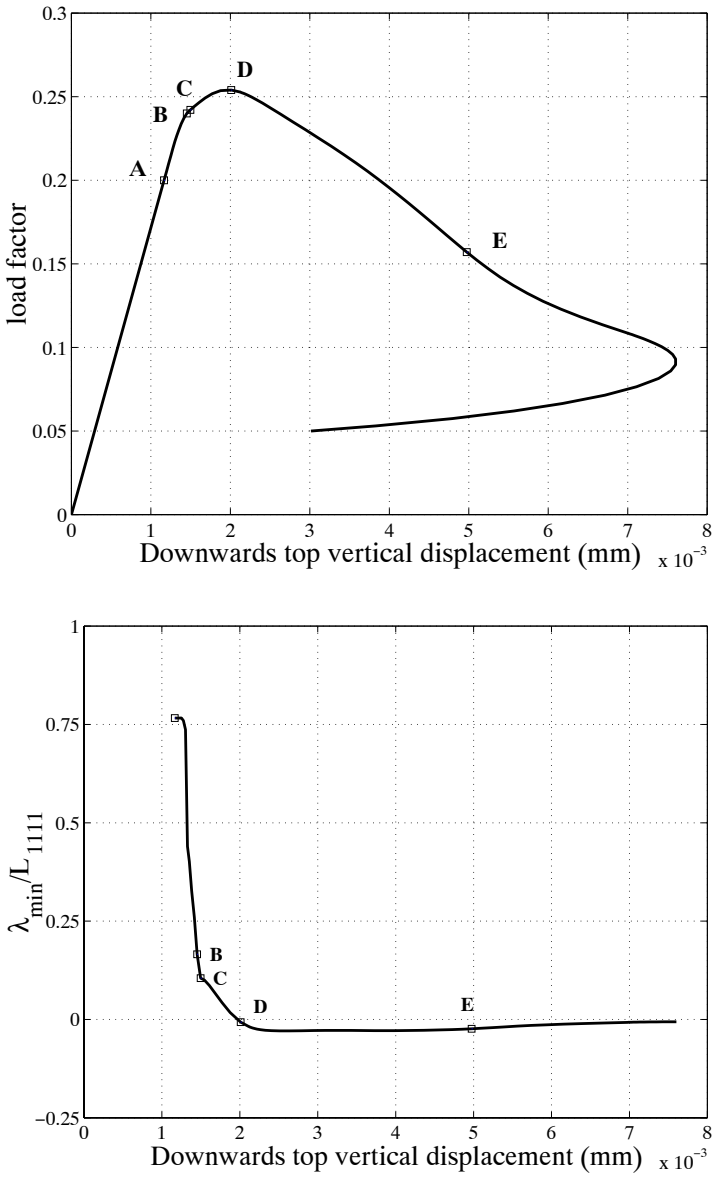

Figure 5.9: (a) Load factor vs vertical displacement of the top controlling node of the cell for vertical compression combined with shear, (b) Evolution of the lowest eigenvalue of the homogenized tangent stiffness

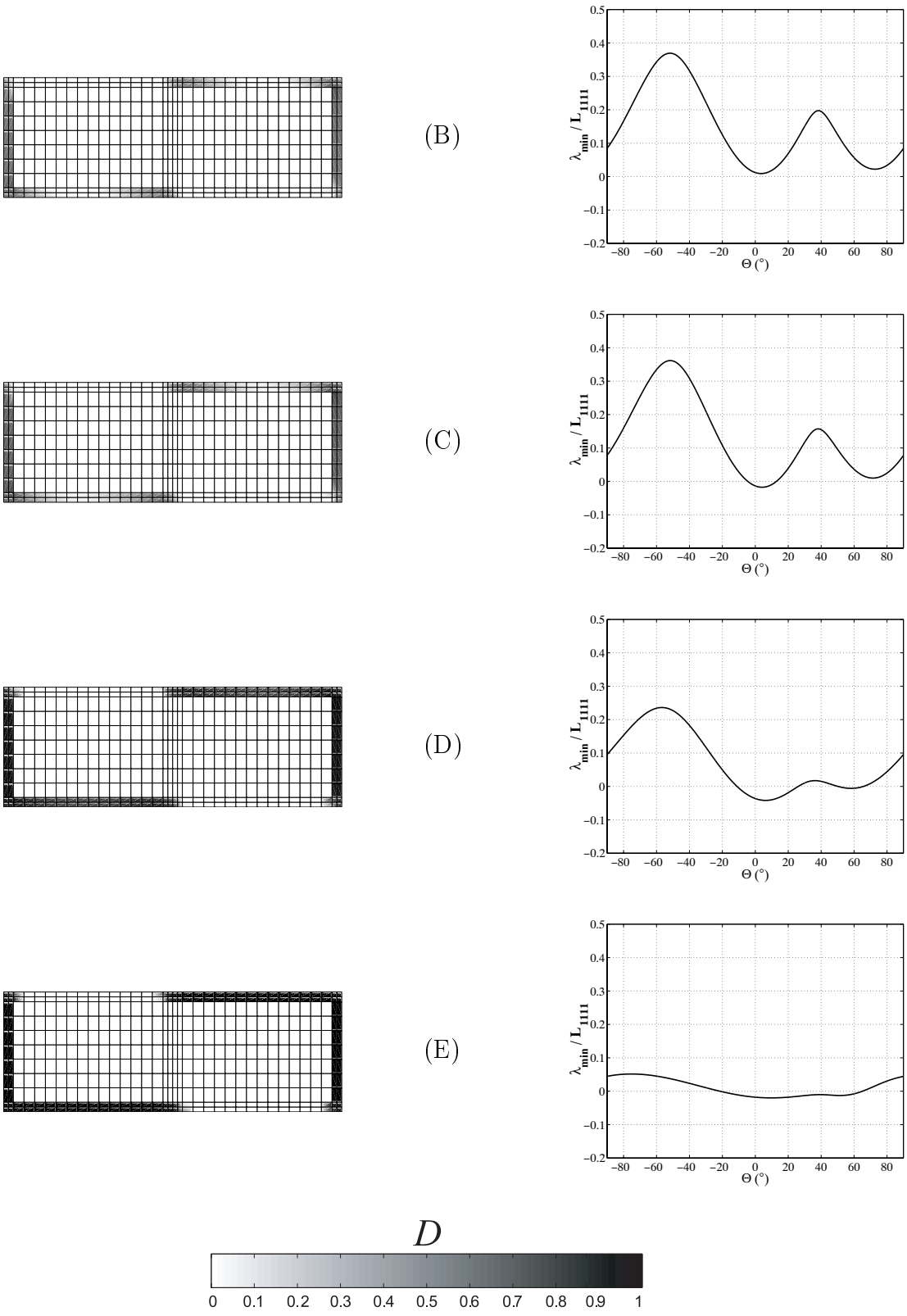

Figure 5.10: Damage distribution for compression combined with shear (left) and related acoustic tensor eigenspectrum (right).

stress-strain response. Note that the minima of the acoustic tensor eigenspectrum first pick up another orientation than the desired orientation. This first negative minimum in the rising part of the load-displacement curve is linked to the non-symmetry of the homogenized tangent material operator.

5.4.3 Identification and selection of the localization orientation

Based on the above observations, we will use the limit point criterion as an indicator of localization in the following. Although this choice is in principle pragmatic, it will be supported by energy considerations below. For the shearing-compression case presented above, this means that the first bifurcation indication obtained from the acoustic tensor is ignored. This choice is only justified if the fundamental homogeneous solution path is more critical than the localized solution at this first bifurcation. It will be demonstrated in Section 5.6 that this is indeed true. Once localization is detected, the orientation of the strain discontinuity can be determined as that corresponding to the last minimum of the acoustic tensor eigenspectrum that became negative.

5.5 Localization band enhanced multi-scale solution scheme

5.5.1 Motivation

The first-order multi-scale technique has to be amended in order to include localization bands as suggested in Section 5.3. Localization bands in the form of a pair of weak discontinuities embedded in an element were already used by Sluys and Berends (1998) to simulate strain localization in isotropic materials. Jirásek (2000) and de Borst et al. (2001) showed that the proper representation of a true discontinuity, i.e. with complete separation of the crack faces for mode I or mode II opening, would require the use of kinematically enhanced strain fields. This improvement is however only clearly motivated for constant strain elements and does not solve completely the mesh alignment sensitivity, see Wells (2001) for a detailed discussion.

In the approach proposed here, strain discontinuities defining a localization band are introduced to derive the material behaviour of a volume associated with a macroscopic sample point (Gauss point) when macroscopic localization is detected. The localization detection is based on the criterion presented in Section 5.3, whereas the localization width is extracted from the unit cell dimensions along the direction $\vec{n}$ given by the localization detection.

5.5.2 Introduction of the localization band

In order to include a discontinuous bifurcation in a simple and efficient way in a macroscopic Gauss point, an approximate embedded band model is used, based on a relaxed Taylor assumption, see Evers et al. (2002). The Gauss point volume is split into a localized band, indicated by (b), and its surrounding volume (s), see Figure 5.11. Each sub-region is characterized by

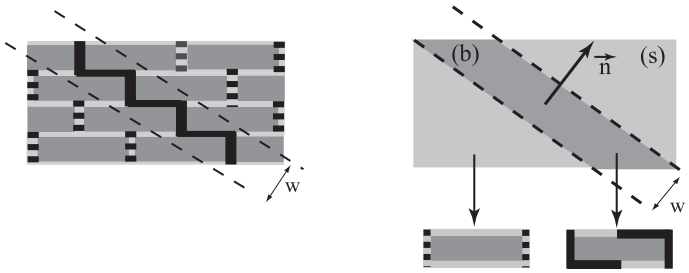

Figure 5.11: Idealization of the constitutive response for a macroscopic material point using a relaxed Taylor model

its volume fraction, which is the only geometrical feature taken into account besides the orientation $\vec{n}$. The strain and stress states are assumed to be uniform in each sub-region. Note that these approximations are equivalent to the assumption of a laminate structure for the material. Based on these assumptions, a relaxed Taylor model is formulated. The volume fractions of the band and surrounding material are denoted by f^b and f^s, and the strain jump between the band and surrounding phase is defined by the normal to the band $\vec{n}$ and the strain jump mode $\vec{m}$. For a given macroscopic strain $\mathbf{E}$, the classical Taylor assumption would consist in assuming that each sub-region undergoes the same macroscopic strain. The relaxed Taylor model weakens this kinematic constraint by assuming that the strain in each sub-region is determined according to

$$\begin{aligned} \mathbf{E}^b &= \mathbf{E} + f^s \left(\vec{m}\vec{n}\right)^{sym} \\ \mathbf{E}^s &= \mathbf{E} - f^b \left(\vec{m}\vec{n}\right)^{sym} \end{aligned} \tag{5.29}$$

It may be verified that with this strain concentration rule and the assumption of piecewise constant strain states, the volume-averaged strain is identical to the macroscopically applied strain as

$$\mathbf{E} = f^b \mathbf{E}^b + f^s \mathbf{E}^s \tag{5.30}$$

The stress variations in the two phases can be deduced using their respective material tangent operator

$$\begin{aligned} \delta\boldsymbol{\Sigma}^b &= {}^4\mathbf{L}^b : \delta\mathbf{E}^b \\ \delta\boldsymbol{\Sigma}^s &= {}^4\mathbf{L}^s : \delta\mathbf{E}^s \end{aligned} \tag{5.31}$$

and the macroscopic stress variation $\delta\boldsymbol{\Sigma}$ is obtained by volume averaging via

$$\delta\boldsymbol{\Sigma} = f^b \delta\boldsymbol{\Sigma}^b + f^s \delta\boldsymbol{\Sigma}^s \tag{5.32}$$

As suggested in Figure 5.11, the assumption is made that the material responses of the band and of its surrounding volume can be deduced from the mesostructure according to the same scale transition as in the initial first-order framework. This clearly introduces an approximation since this scale transition is based on a periodicity assumption. According to this assumption, a cell within the band behaves as if it were surrounded by identically behaving cells, whereas in the real mesostructure the adjacent cells may be unloading. Similarly, the behaviour of the surrounding material outside the band does not take into account the presence of weaker, localizing cells in the band. This assumption may have some influence on the predicted post-peak response, e.g. on the resulting energy dissipation. An improvement could be obtained

by using larger periodic cells which include several periods of the mesostructure together with weaker (integral) boundary conditions at their boundaries, but these options require further research.

5.5.3 Coupled multi-scale scheme for localization

Based on the relaxed Taylor assumption made in the previous paragraph, the first-order multi-scale solution scheme is enhanced in order to capture localization. Prior to localization, the multi-scale scheme sketched in Figure 5.1 is still applied. Upon the detection of localization in a certain point, a band is inserted and the updated scheme illustrated in Figure 5.12 is initiated. Based on the localization orientation $\vec{n}$ and the related volume fractions, the macroscopic strain is decomposed into strains within the band and within its surrounding volume according to the relaxed Taylor assumption (5.29). The band material material response is then evaluated through the first-order multi-scale scheme using a unit cell computation. The material surrounding the band is assumed to unload elastically. Its secant stiffness ${}^4\mathbf{L}^s$ is evaluated once at the bifurcation introduction, and fixed in all subsequent increments. Next, the macroscopic stress is obtained from the averaging relation (5.32). The determination of the complete macroscopic material response now consists in solving the following problem: given a macroscopic strain variation $\delta\mathbf{E}$ and the orientation of the localization band $\vec{n}$, determine

- the macroscopic stress variation $\delta\boldsymbol{\Sigma}$ (3 independent scalar unknowns),
- the variation of the strain jump $\delta\vec{m}$ (2 scalar unknowns).

These unknowns are determined from the traction continuity requirement at the interface between the band and surrounding material (2 scalar equations)

$$\vec{n}.\left(\delta\boldsymbol{\Sigma}^b - \delta\boldsymbol{\Sigma}^s\right) = \vec{0} \tag{5.33}$$

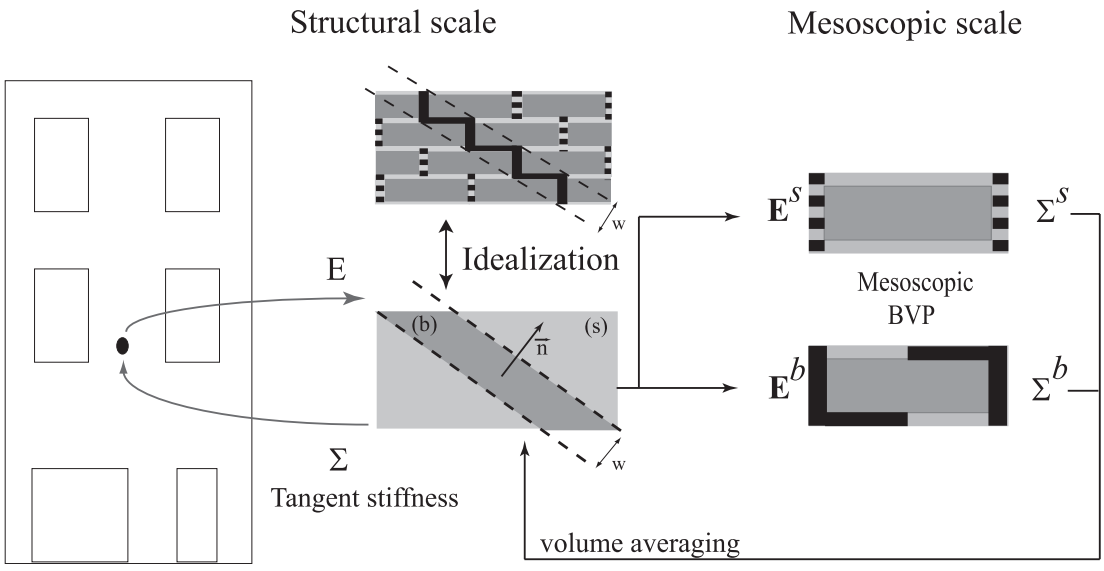

Figure 5.12: Enhanced first-order multi-scale scheme with embedded strain discontinuity for localized behaviour.

and the stress averaging relation (3 scalar equations)

$$\delta\boldsymbol{\Sigma} = f^b\,{}^4\mathbf{L}^b : \delta\mathbf{E}^b + f^s\,{}^4\mathbf{L}^s : \delta\mathbf{E}^s \tag{5.34}$$

It is emphasized that this problem (eqns. 5.33 and 5.34) is non-linear and thus requires an additional iterative solution procedure at the level of a macroscopic point. This becomes apparent by expressing the traction continuity in (5.33) in terms of the strain increments in the band and the surrounding material as defined in relation (5.29)

$$\vec{n}.\left({}^4\mathbf{L}^b - {}^4\,\mathbf{L}^s\right) : \delta\mathbf{E} + \vec{n}.\left(f^s\,{}^4\mathbf{L}^b + f^b\,{}^4\mathbf{L}^s\right) : (\delta\vec{m}\vec{n})^{sym} = \vec{0} \tag{5.35}$$

In relation (5.35), the tangent material stiffness in the band, ${}^4\mathbf{L}^b$, is a non-linear function of the strain variation in the band $\delta\mathbf{E}^b$ and thus also of the strain jump variation $\delta\vec{m}$. As a consequence, three nested solution procedures are used in this enhanced framework:

- a solution procedure for equilibrium at the macroscopic scale,
- a solution procedure to solve the non-linear set of equations of the localization band model,
- a solution procedure at the unit cell level for the solution of the mesostructural boundary value problem.

In the above equations, the orientation of the localization band was not considered as an unknown as it is determined by the localization analysis. As shown in Section 5.4 for fundamental equilibrium paths, a rotation of the localization orientation may occur as a result of mesoscopic damage evolution inside the unit cell. This effect has to be taken into account in order to avoid any stress locking effect at the macroscopic scale.
For this purpose, the acoustic tensor associated to the band material tangent is re-analyzed at each converged configuration and the band orientation is updated accordingly.

More details on the numerical algorithms used to solve the above non-linear set of equations are given in Part 2 of this paper.

5.6 Selection of localized solutions

As illustrated and discussed in Section 5.4, the macroscopic localization criterion detects loss of ellipticity in the rising part of the load-displacement curve, prior to the satisfaction of the limit point criterion. The question thus arises whether the proposed algorithm for the selection of the solution path detects the most critical path.

To verify this, the enhanced multi-scale technique presented in Section 5.5 is applied to a 'structure' made of a single finite element subjected to homogeneous vertical compression combined with shear. The same unit cell is used as in Section 5.4 and in Massart et al. (2004c) with the same material parameters. The macroscopic element dimensions are 800×800 mm^2. The computation is performed for the fundamental, homogeneous path, as well as for all bifurcated

paths detected by the loss of ellipticity criterion and by the limit point criterion. The corresponding load-displacement curves are depicted in Figure 5.13. It can be noticed that an equilibrium path can indeed be traced for both detected bifurcation points. When the localized solution is followed at the first bifurcation, a new path is found which shows rather large rotations of the localization band. Localization is first detected for an orientation of approximately $\Theta = 4°$, and the last equilibrium configuration for this bifurcated solution is obtained with an orientation of $\Theta = 35°$. The final damage pattern is a staircase crack pattern, as for the fundamental solution. If the homogeneous path is followed at this first bifurcation, another bifurcation point is detected when the limit point is reached. A secondary solution is also available in this case as illustrated in Figure 5.13. The band orientation associated to this bifurcation is consistent with the average orientation of the staircase crack pattern.

The most critical solution at each bifurcation point is that for which the smallest amount of incremental work must be supplied to the material. As no closed-form material law is available here, the supplied work is evaluated numerically, based on the computed overall stress $\boldsymbol{\Sigma}$ and strain increment $\Delta\mathbf{E}$ for the obtained solution paths. The equilibrium paths are traced with small loading steps around each bifurcation point. The supplied energy density variation is depicted for both solutions at each bifurcation point versus the load factor in Figure 5.14. Figure 5.14 (top) indicates that for the first bifurcation, the material needs incrementally less energy to proceed along the fundamental path compared to the localized solution. This suggests that the first bifurcation point should indeed be passed without introducing a localization band, as predicted by the limit criterion. At the bifurcation detected by the limit point criterion on the contrary, the localized solution is more critical than the fundamental path, as it minimizes the incremental energy supply to the material.

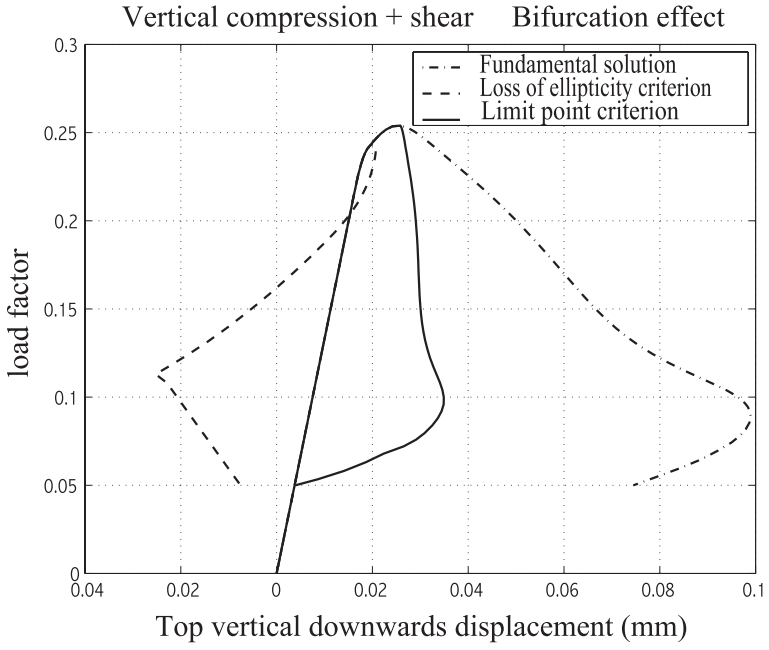

Figure 5.13: Load-displacement curve for vertical compression combined with shear for fundamental and bifurcated solutions based on loss of ellipticity and limit point criteria.

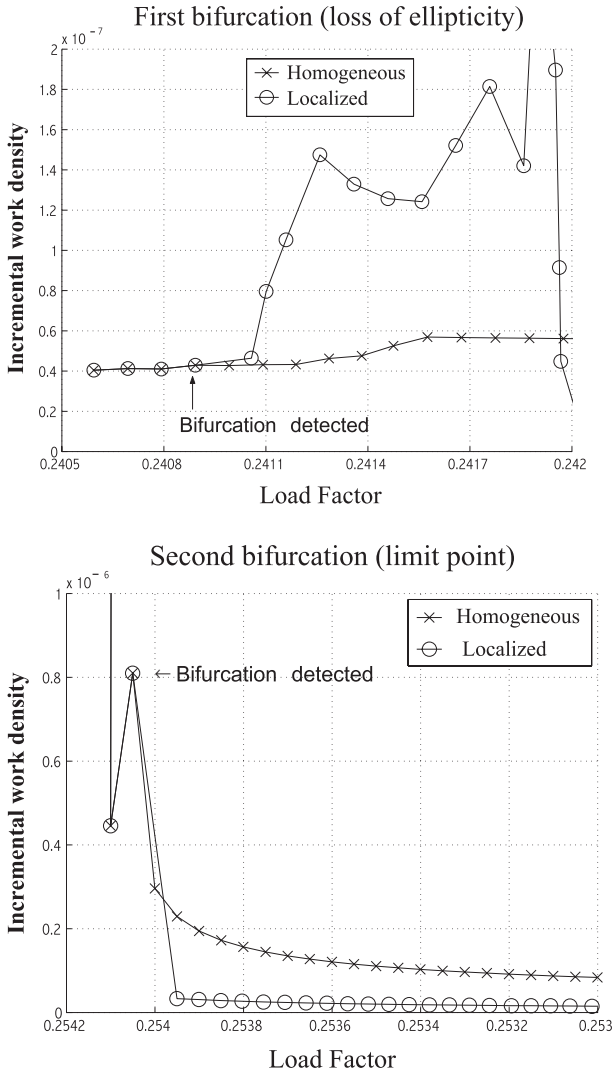

Figure 5.14: Supplied incremental work density for the alternative solution paths in the compression-shear test: (top) first bifurcation detected by loss of ellipticity criterion, (bottom) second bifurcation detected by limit point criterion. At the second bifurcation load factor is decreasing.

This illustration thus gives an heuristic justification for the procedure defined for localization detection in Section 5.4. It is however emphasized that this verification is difficult to implement in real structural computations since it requires the knowledge of all the bifurcated paths to decide on which path to follow.

5.7 Summary

A first-order multi-scale computational framework was proposed for the failure behaviour of masonry structures. The overall response of the material is deduced from unit cell computations on the scale of the mesostructure. The behaviour observed in these meso-analyses is transferred

to the structural scale by a scale transition. Based on the homogenized tangent operator, it was possible to identify physically relevant macroscopic localization. This was achieved using the classical concept of material bifurcation associated to loss of ellipticity as well as the eigenvalue analysis of the material tangent operator. In particular, it was shown that the detected localization orientation is aligned with the average orientation of the mesostructural damage patterns inside the unit cells for two typical loading schemes. As a result, a procedure for localization detection was defined and an enhanced first-order framework was sketched which allows the treatment of localization, by means of embedded bands introduced via a relaxed Taylor assumption. The proposed approach was applied for the determination of the solution paths for a compression-shear test, showing that the most critical solution is captured for this particular case. The detailed description of the computational aspects of this enhanced framework are the subject of the second part of this twofold contribution, which will furthermore show some results obtained with it.

Chapter 6

A multi-scale approach for masonry wall computations - Part II. Computational aspects

The second part of this twofold contribution deals with the computational aspects of a multi-scale framework for the computational analysis of planar masonry structures. The model uses a first-order computational homogenization technique enhanced with a finite width damage band model in order to allow the treatment of localization resulting from damage growth in the constituents. The implementation of the multi-scale solution scheme using a finite element method is outlined. As a result of the use of homogenization techniques on finite volumes and the presence of quasi-brittle constituents, mesostructural snap-back may occur. A methodology to introduce this type of response in the multi-scale technique is proposed. Its impact on the implementation of the framework as well as on the path following techniques needed to trace complete load-deflection paths are detailed. The results obtained by the framework are illustrated by means of simple examples which show the numerical robustness of the method.

6.1 Introduction

In the second part of this twofold contribution, the implementation of the enhanced multi-scale model for planar masonry structure computations presented in the first part is detailed. In this framework, instead of using closed-form constitutive equations, the macroscopic material response is obtained from the solution of a mesostructural boundary value problem formulated on a unit cell. In this mesostructural problem, the macroscopic strain tensor is imposed on the unit cell by means of boundary conditions, taking into account the periodicity of the material. The masonry constituents, bricks and mortar joints, are modeled at the mesostructural scale using an implicit gradient damage model. Based on the solution of this mesostructural boundary value problem, the macroscopic stress tensor is obtained by averaging the mesoscopic stress field, whereas the homogenized constitutive tangent is obtained through static condensation of the mesostructural stiffness matrix. The presence and the orientation of macroscopic localization

This chapter is reproduced from: T.J. Massart, R.H.J. Peerlings and M.G.D. Geers, A multi-scale approach for masonry wall computations - Part II. Computational aspects, To be submitted for publication in International Journal for Numerical Methods in Engineering.

of damage are detected by means of classical continuum mechanics material bifurcation criteria. The occurrence of localization is taken into account in the macroscopic material response by the introduction of a couple of weak discontinuities which together form an embedded localization band, the width of which is determined from the periodicity of the masonry mesostructure.

As a result of the overall softening of the masonry material, macroscopic localization eventually appears, i.e. part of the structure continues to be more damaged, whereas the remaining part of the structure unloads. Depending on the relative size of these parts, the structural response may show snap-back. Snap-back is a structural phenomenon that is due to the inability of the damaging part of the structure to completely dissipate the energy which is released in the unloading part. Tracing this behaviour in computational analyses requires special control techniques such as advanced path following techniques, see e.g. Geers (1999a). In contrast with structural computations which use closed-form constitutive relations, the presented multi-scale method may also exhibit snap-back in the response of macroscopic material points. This is due to the fact that this material response reflects the presence of a finite volume, the response of which is obtained from a (meso-)structural computation in which damage growth may localize in part of the structure (e.g. in the mortar joints). From a macroscopic viewpoint, this behaviour can be regarded as a constitutive snap-back, although it is emphasized once more that this is really a mesostructural effect that ensues from a finite volume. Indeed, the existence of constitutive snap-backs at a strictly local level, i.e. for material volumes of infinitesimal sizes and without an underlying mesostructural motivation, cannot be justified from a physical point of view. Path following techniques available in the literature cannot deal with this mesostructural snap-back and an extension is therefore needed in order to deal with this phenomenon which is likely to occur in realistic computations. This can be done by taking into account more information from the mesostructure than the averaged stress and strain tensors at the macroscopic scale, i.e. by including some additional mesoscopic state variables and equations in the macroscopic solution procedure. The path following technique in which these additional variables have to be implemented has to be adapted accordingly.

This paper is organised as follows. The multi-scale scheme proposed in Part I of this contribution is outlined in Section 6.2 in terms of the equations which need to be solved at each scale of representation. The snap-back phenomenon is then introduced in Section 6.3 and its importance for masonry unit cell computations is demonstrated. A methodology to include the mesostructural snap-back behaviour in the enhanced multi-scale framework is proposed in Section 6.4. This methodology requires changes in the conventional extraction of the consistent tangent which are detailed in Section 6.5, where the finite element discretization is introduced. The impact on the path following techniques used for the macroscopic solution procedure are commented on in Section 6.6. Small scale applications of the enhanced framework are given in Section 6.7. Finally, conclusions on the added value of the proposed framework are drawn in Section 6.8.

6.2 Summary of relevant equations

The multi-scale scheme presented in the first part of this contribution involves the numerical solution of equilibrium problems at two scales: the macroscopic or structural scale and the mesostructural scale represented by the size of a unit cell. When localization is triggered, the macroscopic description is enriched by the introduction of an embedded localization band. Two unit cells are then attached to a macroscopic material point, representing the localization band and the surrounding material respectively. Attention will be here focused on this localized state, noting that the algorithm prior to macroscopic localization can be obtained as a straightforward simplification.

At the macroscopic scale, the global equilibrium problem can be written in the usual way as

$$\vec{\nabla}_M.\boldsymbol{\Sigma} + \vec{F} = \vec{0} \tag{6.1a}$$

$$\boldsymbol{\Sigma} = F_{\Sigma}\left(\mathbf{E}\right) \tag{6.1b}$$

where $\boldsymbol{\Sigma}$ denotes the macroscopic stress tensor. Note however, that relation (6.1b) is not a direct functional relation, but requires the numerical solution of two mesoscopic boundary value problems: one for the response of the localization band, and one for the surrounding material. Note also that the solution of the latter is straightforward as the surrounding material is assumed to unload elastically. At the macroscopic scale, the decomposition of the material behaviour in a band and its surrounding material is characterized by the following set of equations

$$\vec{n}.\left(\boldsymbol{\Sigma}^b - \boldsymbol{\Sigma}^s\right) = \vec{0} \tag{6.2a}$$

$$\boldsymbol{\Sigma} = f^b\boldsymbol{\Sigma}^b + f^s\boldsymbol{\Sigma}^s \tag{6.2b}$$

$$\mathbf{E}^b = \mathbf{E} + f^s\left(\vec{m}\vec{n}\right)^{(sym)} \tag{6.2c}$$

$$\mathbf{E}^s = \mathbf{E} - f^b\left(\vec{m}\vec{n}\right)^{(sym)} \tag{6.2d}$$

$$\boldsymbol{\Sigma}^b = F_{\Sigma^b}\left(\mathbf{E}^b\right) \tag{6.2e}$$

$$\boldsymbol{\Sigma}^s = F_{\Sigma^s}\left(\mathbf{E}^s\right) \tag{6.2f}$$

where $(.)^b$ and $(.)^s$ denote quantities related to the band and to the surrounding material respectively, f^b and f^s are the respective volume fractions, $\vec{n}$ is the normal to the localization band and $\vec{m}$ characterizes the strain jump between the band and its surrounding material. The quantity $(\vec{m}\vec{n})$ denotes the second-rank tensor obtained as the dyadic (or outer) product of vectors $\vec{m}$ and $\vec{n}$. The above equations form a non-linear system, which must be solved iteratively.

At the mesoscopic scale, a standard equilibrium problem needs be solved on a unit cell. An implicit gradient damage framework is used in which the following governing equations have to be solved together with the related boundary conditions, which are not reproduced here for brevity:

$$\vec{\nabla}_m.\boldsymbol{\sigma} = \vec{0} \tag{6.3a}$$

$$\overline{\varepsilon}_{eq} - l_c^2\nabla^2\overline{\varepsilon}_{eq} = \varepsilon_{eq} \tag{6.3b}$$

The source term of equation (6.3b) is a scalar equivalent measure of the strain state (i.e. a function of the strain tensor components), the definition of which depends on the considered

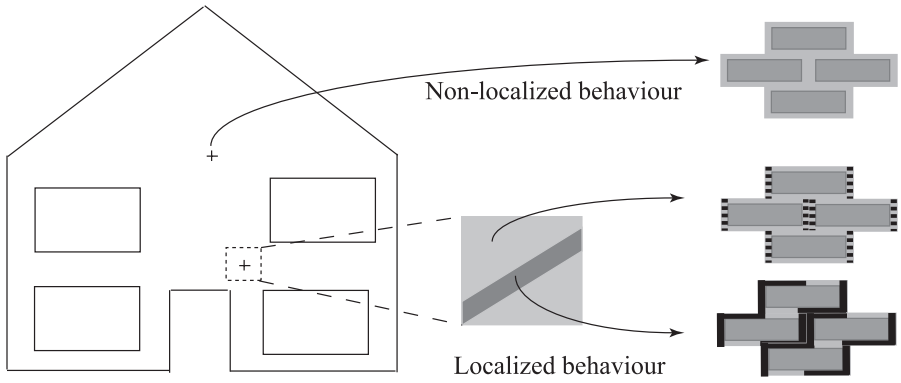

Macroscopic scale		Mesoscopic scale (for each unit cell)
$\vec{\nabla}_M.\boldsymbol{\Sigma} + \vec{F} = \vec{0}$	Field	$\vec{\nabla}_m.\boldsymbol{\sigma} = \vec{0}$
$\vec{n}.\left(\boldsymbol{\Sigma}^b - \boldsymbol{\Sigma}^s\right) = \vec{0}$	Equations	$\overline{\varepsilon}_{eq} - l_c^2\nabla^2\overline{\varepsilon}_{eq} = \varepsilon_{eq}$

Figure 6.1: Schematic representation of the enhanced multi-scale method and of the equations solved for at each scale

material. This equation introduces non-locality in the problem and includes a material dependent intrinsic length parameter l_c. Equations (6.3a) and (6.3b) form a coupled set of equations which must be solved simultaneously. More details on the implementation of this framework are available in Peerlings et al. (1996); Peerlings (1999). Figure 6.1 summarizes the equations to solve at the different scales together with the related unknowns. Equations (6.3a) and (6.3b) are non-linear and must thus be solved iteratively. Note that this iteration process must be repeated for each iteration of the macroscopic solution procedure and for each sampling point of the macroscopic problem.

6.3 Localization and mesostructural snap-back

6.3.1 Snap-back phenomenon and path following techniques

Snap-back is a structural phenomenon which may appear when localization of damage occurs in zones which are thin with respect to the structural size. It is observed when the equilibrium path shows a simultaneous decrease of the displacement imposed on the structure and of the associated load. From an energetic point of view, it is caused by the fact that the rate at which the elastic zone releases elastically stored energy becomes larger than the rate at which energy is consumed by the degradation of the softening material. In practice or in experiments, as well as in displacement controlled simulations, it leads to an instability, and thus calls for special (experimental or computational) control techniques: servo-control in experiments and arc-length methods or path following techniques in computations. A general class of advanced path following techniques has been proposed by Geers (1999a,b), which includes the earlier pro-

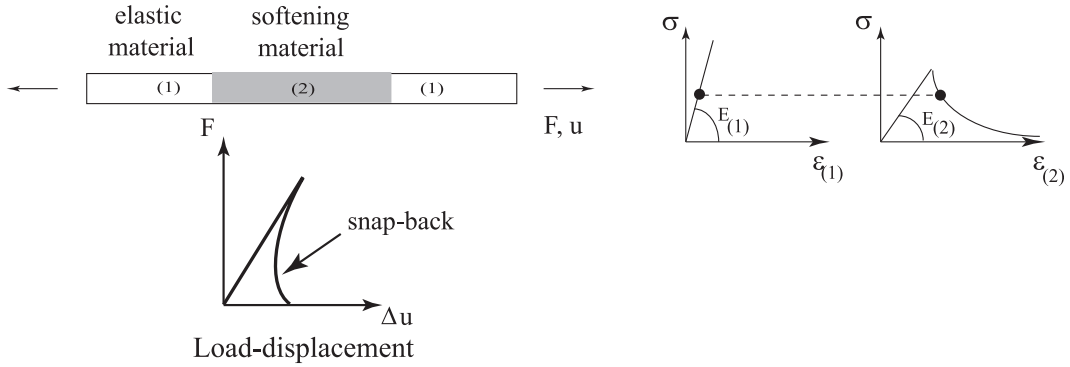

Figure 6.2: One-dimensional snap-back phenomenon with load-displacement curve (left) and corresponding states in the constituents (right).

posals by Crisfield (1981) and de Borst (1987). These methods are designed to trace structural equilibrium paths. They use a generalisation of load control, in which a scalar load factor constitutes an additional unknown. To solve the set of equations, an additional constraint equation is required involving degrees of freedom of the structure and the load factor. A monotonically increasing quantity is generally used to define the constraint and hence to control the computation. For problems involving material non-linearities with damage localization in narrow zones, constraints in terms of only the degrees of freedom related to the damage process zone itself have been shown to perform better than global constraints, see de Borst (1987); Geers (1999a). In the one-dimensional example described in Figure 6.2, the relative displacement between the extremities of the softening material (2) could be selected as a controlling quantity as it continuously grows during the entire degradation process.

The fact that in the multi-scale framework the macroscopic material point response is obtained from a mesostructural computation implies that this behaviour in principle may also show snap-back. Indeed, since relatively brittle mesostructural materials are considered and damage growth tends to localize in the weaker and relatively thin mortar joints, a behaviour similar to that depicted in Figure 6.2 is likely to occur at the level of a masonry unit cell. This presents a problem if classical non-linear displacement-based finite element procedures are used at the macroscopic scale because these assume that for a given strain increment a resulting stress can always be determined. It is thus tacitly assumed in the multi-scale framework that the mesostructural boundary value problem always possesses a solution for the prescribed macroscopic strain increment. This is clearly not true for strains beyond a snap-back point. As a consequence, if the extracted macroscopic material response exhibits a snap-back, a macroscopic displacement-based multi-scale scheme is unable to follow the macroscopic equilibrium path.

6.3.2 Mesostructural snap-back for masonry unit cell computations

To illustrate the occurrence of mesostructural snap-back in masonry, a mesoscale unit cell computation is performed under proportional stress loading, without considering the multi-scale framework, see Massart et al. (2004c). A path following technique is used to control the com-

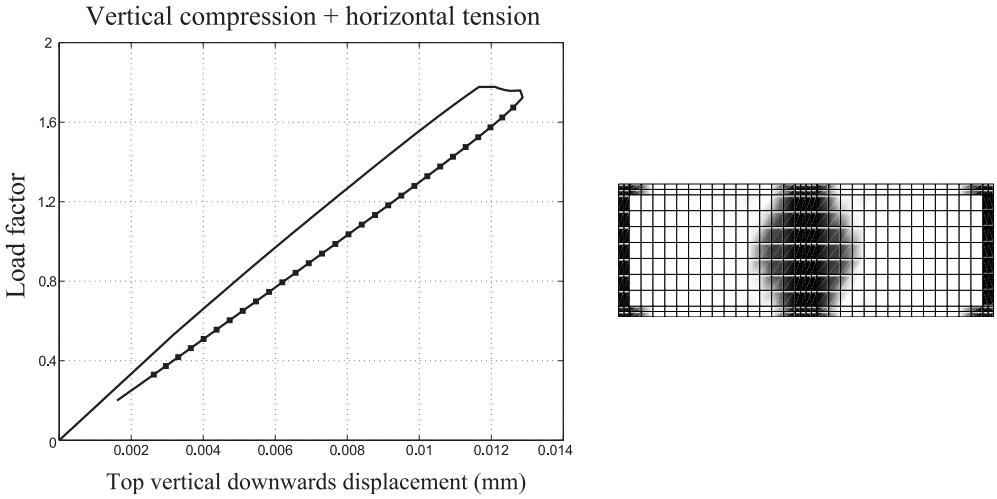

Figure 6.3: Load factor vs vertical displacement of top controlling point of the unit cell; and associated final damage pattern for vertical compression combined with tension. Markers indicate states of the cell corresponding to an homogenized snap-back behaviour detected by conditions (6.4)

putation which is based on a degenerated cylindrical constraint expressed in terms of the most critical non-local degree of freedom detected in each increment, Geers (1999a). A plane stress state is assumed. For the brick material, a maximum principal stress loading function is chosen, while the mortar is modeled with a Drucker-Prager shaped criterion with a compressive cap, see Massart et al. (2004c). Exponential damage evolution laws are used for both materials. The same geometry and material parameters have been used as in Massart et al. (2004c). The cell is loaded with vertical compression combined with horizontal tension along the stress path $(\Sigma_{xx}, \Sigma_{yy}, \Sigma_{xy}) = (0.2, -1, 0)$. The load factor variation is shown as a function of the vertical displacement of the top controlling node of the unit cell in Figure 6.3, together with the obtained damage pattern. Snap-back may be detected numerically by inspecting the first and second order variations of work density. For snap-back to occur, these must satisfy

$$\begin{array}{rcl} \delta W & = & \boldsymbol{\Sigma} : \delta \mathbf{E} \leq 0 \\ \delta^2 W & = & \delta \boldsymbol{\Sigma} : \delta \mathbf{E} \geq 0 \end{array} \tag{6.4}$$

In the numerical analysis, these values are computed based on the incremental variations of macroscopic stresses and strains. The points of the curve marked in Figure 6.3 correspond to states where criteria (6.4) are satisfied and snap-back is thus detected. The resulting damage pattern inside the cell reported in Figure 6.3 is symmetric as a result of the symmetry of the geometry and of the applied loads. Note the extreme brittleness of the material in this loading direction, associated to the occurrence of snap-back.

6.3.3 Snap-back caused by the localization band

A second potential source of snap-back of the deduced macroscopic material response is formed by the averaging relations of the damage localization band equations (6.2b)-(6.2d). These re-

lations take into account localization bands with a characteristic volume which is smaller than the volume attached to the Gauss points where the macroscopic material behaviour is sampled. Since this band is behaving in a quasi-brittle way and the remaining material is assumed to unload elastically, the overall macroscopic material response may show snap-back, even if the average behaviour of the unit cell representing the behaviour within the band does not. This type of snap-back is more likely to occur for relatively coarse meshes, in which the damage band is thin compared with the volume associated to the Gauss points. This source of snap-back is similar to the one-dimensional case illustrated in Paragraph 6.3.1.

6.4 Treatment of mesostructural snap-backs

6.4.1 Principles

To be able to deal with mesostructural snap-back in the multi-scale solution scheme, two difficulties need to be solved, which may be understood from the one-dimensional homogenized response with snap-back depicted in Figure 6.4. First, the macroscopic solution procedure should predict a decreasing macroscopic strain increment as from the start of the snap-back regime (point A in Figure 6.4) for a solution of the mesostructural problem to exist.
Secondly, in the snap-back regime, both the elastic unloading and a dissipative equilibrium paths may be followed for a given negative strain increment. Additional measures need to be taken in order to prevent that the elastic unloading path is followed. In order to avoid an elastic unloading response, the scale transition procedure should apply a decreasing macroscopic strain increment to the mesostructure, along with an additional condition that forces the material to continue to dissipate energy. This additional condition applied on the mesostructural problem should have the effect of 'steering' the solution on the path associated to dissipation by selecting the corresponding tangent within the solution procedure at the mesoscopic level. For instance, in the one-dimensional example given in Section 6.3, introducing such a constraint may be achieved by requiring the strain jump between the softening and the unloading phases to increase.

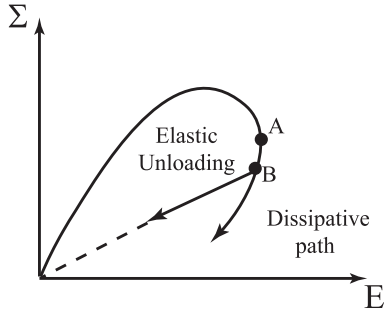

Figure 6.4: Alternative mesostructural responses in snap-back regime

6.4.2 Strain jump control for snap-back induced by localization band

Let us assume again that localization was detected and a localization band has been introduced in the considered material volume (relations (6.2a)- (6.2f)). First, the case where the homogenized unit cell response does not exhibit snap-back will be analyzed. Because of the small width of the band and the brittleness of its behaviour, a snap-back may well appear in the averaged response of the finite volume associated to the considered macroscopic material point.
The kinematic variable which characterises the strain jump between the band and the surrounding material is the vector $\vec{m}$. If the band material follows a softening branch while the surrounding unloads, the strain jump $(\vec{m}\vec{n})^{sym}$ should increase, even if the overall material response exhibits a snap-back. To enforce further dissipation in the material, the macroscopic solution procedure should thus enforce the growth of $\vec{m}$.

The simplest way to enforce this condition is to impose to the localization band model a positive increment for the strain jump vector $\vec{m}$. To do this, the vector $\vec{m}$ is defined as a variable at the macroscopic level in each macroscopic sampling point. In two dimensions, this introduces two additional scalar degrees of freedom for each Gauss point in which localization has been detected. Simultaneously imposing a strain jump $\vec{m}$ and a macroscopic strain $\mathbf{E}$ does not automatically lead to an equilibrium configuration. To enforce equilibrium, an equivalent number of equations conjugate with these unknowns must be formulated at the macroscopic level and solved at this scale. The traction continuity requirement between the band and surrounding material (6.2a) may be used for this purpose.

$$\vec{n}.\left(\boldsymbol{\Sigma}^b - \boldsymbol{\Sigma}^s\right) = \vec{0} \tag{6.5}$$

This equation couples the strain jump to the macroscopic displacement field through the components of the macroscopic strain tensor. This may be realized by introducing the expression of the strain in the band and its surrounding (6.2c) and (6.2d) in their material responses (6.2e) and (6.2f). Due to the non-linear response of the band the overall problem is non-linear, and a given prescribed value of the strain jump $\vec{m}$ and the applied overall strain $\mathbf{E}$ will generally not lead to equilibrium immediatly, meaning that traction continuity will not be satisfied for the prescribed $\vec{m}$. Equation (6.5) therefore has to be solved iteratively, together with the discrete macroscopic equilibrium equations which result from (6.1a). Note that this means that the traction continuity requirement between the band and the surrounding phases (6.5) is only satisfied in macroscopically converged configurations, and not in intermediate macroscopic iterations.

6.4.3 Non-local degree of freedom control for unit cell snap-back

As illustrated in Section 6.3, the averaging of the unit cell behaviour itself may cause mesostructural snap-back in its homogenized response, i.e. in the response of the localization band itself. In order to follow the dissipative equilibrium path of the cell in such a case, an additional condition related to mesoscopic damage growth inside the cell must be added to the data which is prescribed in the mesostructural boundary value problem. Assuming a discontinuous bifurcation, the surrounding material unloads elastically and does not dissipate energy. As a consequence,

the discussion that follows is only relevant for the unit cell computation performed for the material in the localization band. The choice of the quantity which allows to enforce dissipation is similar to that used in advanced path following techniques. Generally, a local information (the degrees of freedom related to the damage process zone) is used in an additional constraint equation in these techniques. In the present approach, an implicit gradient damage model is used at the mesoscopic scale. A mesoscopic non-local equivalent strain field $\overline{\varepsilon}_{eq}$ is thus discretized at the mesoscopic scale and obtained as the solution of the averaging equation (6.3b). The related degrees of freedom are denoted by $\overline{\varepsilon}$. As the non-local strain field drives the mesoscopic damage growth and thus dissipation, the cell may be forced to follow a dissipative equilibrium path if the growth of a properly selected non-local strain degree of freedom is imposed by the macroscopic solution procedure. For this purpose, this non-local degree of freedom has to be transferred to the macroscopic scale, and a conjugate equation has to be solved iteratively at this scale. A proper selection procedure also must be set up to identify which non-local degree of freedom of the cell should be transferred to the macroscopic solution procedure at a given stage of the computation (i.e. for a given state of the cell).

The 'external' prescription of the value of a given degree of freedom of the unit cell gives rise to a conjugate reaction 'force'. In the classical multi-scale framework the kinematical macro-meso scale transition is implemented by prescribing an overall strain increment to the unit cell through 6 controlling displacement increments $\{\Delta u_M\}$. External reaction forces conjugate to these displacements variations arise and are used to compute the macroscopic stress. Similarly, the simultaneous prescription of a non-local degree of freedom increment $\Delta\overline{\varepsilon}$ with the macroscopic strain increment $\Delta\mathbf{E}^b$ will lead to the appearance of a conjugate residual $f_{\overline{\varepsilon}}$, as illustrated in Figure 6.5. Physically, this residual is the generalized 'force' that should be applied externally to the unit cell in order to obtain the prescribed value of the non-local degree of freedom increment $\Delta\overline{\varepsilon}$ simultaneously with the applied macroscopic strain increment $\Delta\mathbf{E}^b$. This residual only vanishes if the imposed non-local degree of freedom increment $\Delta\overline{\varepsilon}$ takes the value that corresponds to the solution of the mesostructural problem in which the prescribed overall strain $\Delta\mathbf{E}^b$ only would be prescribed. Clearly the simultaneous imposition of $\Delta\overline{\varepsilon}$ and $\Delta\mathbf{E}^b$ does not lead to the intended equilibrium configuration in a single iteration. To reach the

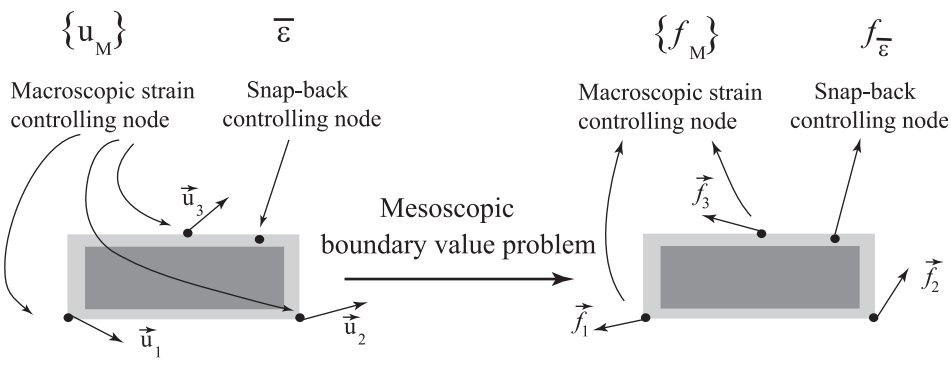

Figure 6.5: Non-local residual conjugate to the imposed non-local degree of freedom for unit cell snap-back control

intended equilibrium, the condition that the residual $f_{\bar{\varepsilon}}$ vanishes furnishes an additional equation conjugate to the non-local degree of freedom that has to be solved at the macroscopic scale:

$$f_{\bar{\varepsilon}} = 0 \tag{6.6}$$

This equation is then satisfied only upon macroscopic convergence. It is emphasized that within this enhanced control approach, an equilibrium configuration of the unit cell is still required at each macroscopic iteration, similarly to the original multi-scale technique. The key difference is however that the imposition of the non-local strain increment modifies the boundary conditions imposed on the cell at each macroscopic iteration, and hence a particular equilibrium configuration of the cell, compatible with these modified boundary conditions, is found. Along the macroscopic iterations, the incorporation of equation (6.6) forces the equilibrium configuration obtained for the cell towards the one with the correct boundary conditions i.e., the one with no external influence on the mesoscopic non-local strain field. Iterative equilibrium states of the cell are thus obtained for different boundary conditions than the ones that apply in the classical multi-scale scheme, but after macroscopic convergence, the cell satisfies equilibrium under the 'standard' imposed macroscopic strain $\Delta\mathbf{E}^b$ only. This feature allows to pass strain control limit points of the homogenized stress-strain behaviour, and, since it selects the corresponding tangent stiffness, to follow the snap-back dissipative solution.

Practically, the residual is obtained directly by the condensation of the meso-structural system of equations, towards the degrees of freedom used for the macroscopic solution procedure, i.e. the displacement degrees of freedom controlling the overall strain as well as the additional non-local degree of freedom. The non-local degree of freedom may be introduced in the macroscopic description at the start of the computation (i.e. when localization is not yet present), as it does not have any effect in the linear elastic regime. It adds one scalar unknown per Gauss point to the macroscopic system of equations.

An essential difference with the treatment of snap-back due to the macroscopic localization band resides in the fact that the selection of the non-local degree of freedom which is used to enforce dissipation at the cell level should evolve as a result of mesoscopic damage evolution. The most critical non-local degree of freedom in each cell, corresponding to the largest incremental damage growth, is selected at the end of each macroscopic increment for controlling dissipation of this unit cell in the subsequent increment. It should be noted that the choice of a mesoscopic non-local degree of freedom is not the only possible solution to set up such a control algorithm. If another type of model is used at the mesoscale, such as a cohesive zone approach, the solution control can also be based on a relative displacement between two nodes, or on other quantities like the fracture energy, as suggested in Gutiérrez (2003).

6.5 Implementation of the full multi-scale scheme

6.5.1 Governing equations and enhanced nested scheme

As a result of the enhancements introduced in order to handle mesostructural snap-backs, mesostructural equations have to be incorporated in the macroscopic solution procedure. The

Table 6.1: Distribution of the field governing equations among the different solution procedures in the enhanced first-order scheme

Solution level	Equations	Physical Meaning	Unknowns
Macroscopic	(6.1a)	Macro-equilibrium	Displacement field $\vec{u}$ (macroscopic variation)
	(6.2a)	Traction continuity	Strain discontinuities $\vec{m}$
	(6.6)	Non-local residual	Mesoscopically prescribed $\overline{\varepsilon}_{eq}$
Mesoscopic	(6.3a)	Mesoscopic equilibrium	Displacement field $\vec{u}$ (mesoscopic variation)
	(6.3b)	Non-local averaging	Non-local field $\overline{\varepsilon}_{eq}$

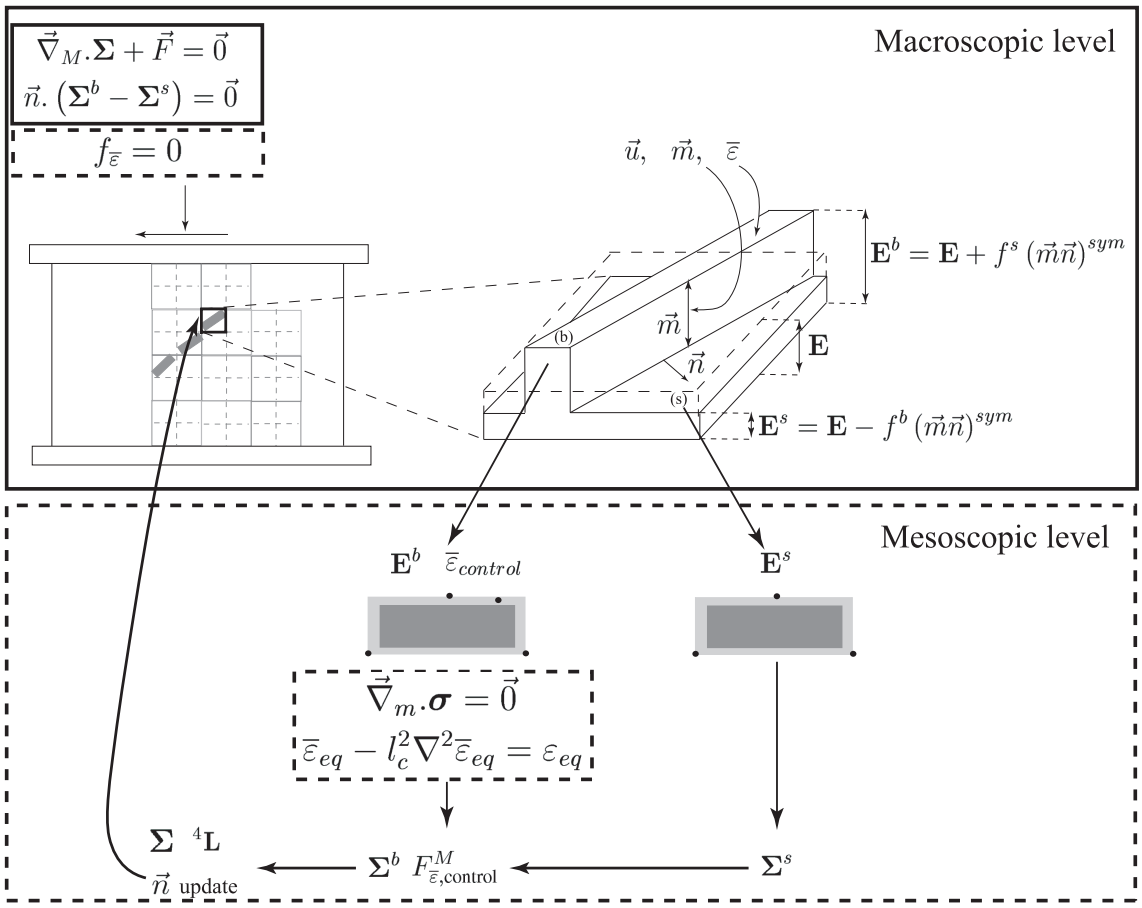

Figure 6.6: Principles of the localization enhanced first order scheme with nested macroscopic and mesoscopic solution procedures and with mesostructural snap-back handling. The upper part of the figure represents the structural scale, including localization band at the level of Gauss point volumes, the lower part represents the mesoscopic unit cell computations.

different governing equations and the level at which they are solved have been summarized in Table 6.1. The inclusion of mesostructural equations in the macroscopic solution procedure requires some modifications of the multi-scale scheme, which are illustrated in Figure 6.6. The essential difference with the initial scheme presented in Figure 6.1 resides in the presence of a set of mesoscopic non-local degrees of freedom in the macroscopic solution procedure. Note that within the macroscopic solution procedure, the band orientation is adapted at the start of each step, based on the evaluation of the tangent operator corresponding to the band material obtained from the previous converged state. In case the band unit cell response undergoes a mesostructural snap-back, its tangent stiffness becomes positive-definite, and no localization direction can be determined anymore. In this case, this orientation is fixed.

6.5.2 Extraction of consistent tangent for the snap-back enhanced scheme

The fact that a non-local mesoscopic degree of freedom which was previously internal to the cell is now included in the set of unknowns at the macroscopic level means that the extraction of the macroscopic tangent operator presented in Kouznetsova (2002) must be adapted as well. This tangent now consists of four tensors which relate variations of the stress $\mathbf{\Sigma}$ and the non-local residual $f_{\overline{\varepsilon}}$ to variations of the strain $\mathbf{E}$ and the non-local variable $\overline{\varepsilon}$ according to:

$$\delta\mathbf{\Sigma} = {}^{4}\mathbf{C}_M^{uu} : \delta\mathbf{E} + {}^{2}\mathbf{C}_M^{ue}\delta\overline{\varepsilon} \tag{6.7}$$

$$\delta f_{\overline{\varepsilon}} = {}^{2}\mathbf{C}_M^{eu} : \delta\mathbf{E} + \mathrm{C}_M^{ee}\delta\overline{\varepsilon} \tag{6.8}$$

Similar to Kouznetsova et al. (2001), these tensors can be retrieved from the discretized system of equations of the unit cell. The tangent matrix of the mesostructural problem can be condensed in terms of the control displacements and the of the non-local degree of freedom which was selected for handling snap-back as follows:

$$\begin{bmatrix} [\mathbf{K}_M^{uu}] & \{\mathbf{K}_M^{ue}\} \\ \langle\mathbf{K}_M^{eu}\rangle & \mathrm{K}_M^{ee} \end{bmatrix} \begin{Bmatrix} \{\delta u_M\} \\ \delta\overline{\varepsilon} \end{Bmatrix} = \begin{Bmatrix} \{\delta f_M\} \\ \delta f_{\overline{\varepsilon}} \end{Bmatrix} \tag{6.9}$$

where $[\mathbf{K}_M^{uu}]$ is a 6×6 matrix coupling external force variations to the displacement variations of the macroscopic strain control nodes, $\{\mathbf{K}_M^{ue}\}$ is a 6×1 column matrix linking the external force variations to the variation of the selected non-local degree of freedom. The row matrix $\langle\mathbf{K}_M^{eu}\rangle$ and the scalar K_M^{ee} link the non-local residual variation to the controlling displacements variations and to the mesoscopic non-local degree of freedom variation respectively. As in the standard multi-scale scheme, this relation may be re-written in a tensor-vector format by separating the contribution of each control node as

$$\begin{aligned} \delta\vec{f}^{(n)} &= \sum_{p=1}^{3} \mathbf{K}_M^{uu(np)}.\delta\vec{u}_M^{(p)} + \vec{\mathbf{K}}_M^{ue(n)}\delta\overline{\varepsilon} \quad n\text{=1,2,3} \\ \delta f_{\overline{\varepsilon}} &= \sum_{p=1}^{3} \vec{\mathbf{K}}_M^{eu(p)}.\delta\vec{u}_M^{(p)} + \mathrm{K}_M^{ee}\delta\overline{\varepsilon} \end{aligned} \tag{6.10}$$

where $\mathbf{K}_M^{uu(np)}$ is a second-order tensor extracted from matrix $[\mathbf{K}_M^{uu}]$ relating the variation of the displacement of controlling point (p) to the external force variation at controlling point (n). The

vector $\vec{\mathbf{K}}_M^{ue(n)}$ which relates the external force variation at controlling point (n) to the variation of the selected non-local degree of freedom is extracted from the column matrix $\{\mathbf{K}_M^{ue}\}$. Similar notations may be used to relate the non-local residual to the controlling degrees of freedom. The variation of stress is related to the variation of the external forces applied to the macroscopic strain controlling points by

$$\delta\boldsymbol{\Sigma} = \frac{1}{V_{cell}} \sum_{n=1}^{3} \vec{x}^{\,(n)} \delta \vec{f}^{\,(n)} \tag{6.11}$$

The variations of the external forces obtained from the condensed tangent stiffness relation of the unit cell (6.10) are next substituted in (6.11), which yields

$$\delta\boldsymbol{\Sigma} = \frac{1}{V_{cell}} \sum_{n=1}^{3} \sum_{p=1}^{3} \vec{x}^{\,(n)} \mathbf{K}_M^{uu(np)} . \delta \vec{u}_M^{(p)} + \frac{1}{V_{cell}} \sum_{n=1}^{3} \vec{x}^{\,(n)} \vec{\mathbf{K}}_M^{ue(n)} \delta\overline{\varepsilon} \tag{6.12}$$

Finally, the displacement variation of the overall strain controlling point (p) may be related to the macroscopic displacement gradient via

$$\delta \vec{u}^{(p)} = \vec{x}^{(p)} . \vec{\nabla}_M \delta \vec{u} \tag{6.13}$$

Introducing (6.13) into (6.12) finally allows to relate the macroscopic stress variation to the macroscopic strain variation and to the variation of the controlling non-local dof. Taking into account that the macroscopic strain is the symmetric part of the displacement gradient, the first part of the consistent tangent operator is retrieved as

$$\delta\boldsymbol{\Sigma} = \underbrace{\frac{1}{V_{cell}} \left(\sum_{n=1}^{3} \sum_{p=1}^{3} \vec{x}^{(n)} \mathbf{K}_M^{uu(np)} \vec{x}^{(p)} \right)^{(rs)}}_{{}^4\mathbf{C}_M^{uu}} : \delta\mathbf{E} + \underbrace{\frac{1}{V_{cell}} \left(\sum_{n=1}^{3} \vec{x}^{(n)} \vec{\mathbf{K}}_M^{ue(n)} \right)}_{{}^2\mathbf{C}_M^{ue}} \delta\overline{\varepsilon} \tag{6.14}$$

where $(.)^{(rs)}$ indicates that the considered tensor is right symmetrized. A similar development may be performed for the variation of the non-local residual force conjugate to the mesoscopic non-local strain degree of freedom. One then obtains the second part of the consistent tangent relation as

$$\delta f_{\overline{\varepsilon}} = \underbrace{\frac{1}{V_{cell}} \left(\sum_{p=1}^{3} \vec{\mathbf{K}}_M^{eu(p)} \vec{x}^{(p)} \right)^{(rs)}}_{{}^2\mathbf{C}_M^{eu}} : \delta\mathbf{E} + \underbrace{\left(\vec{\mathrm{K}}_M^{ee} \right)}_{\mathrm{C}_M^{ee}} \delta\overline{\varepsilon} \tag{6.15}$$

The consistent tangent operator defined by relations (6.14)-(6.15) is not the material tangent in the usual sense, due to the presence of additional information related to the (single) non-local degree of freedom. When macroscopic equilibrium is reached, the unit cell is in equilibrium under the prescribed macroscopic strain increment and the residual $f_{\overline{\varepsilon}}$ vanishes. The material tangent operator may now be recovered by eliminating the non-local controlling degree of freedom from (6.8), yielding

$$\delta\boldsymbol{\Sigma} = {}^4\mathbf{L} : \delta\mathbf{E} \tag{6.16}$$

with

$$ {}^4\mathbf{L} = {}^4\mathbf{C}_M^{uu} - \frac{1}{\mathrm{C}_M^{ee}} {}^2\mathbf{C}_M^{ue} {}^2\mathbf{C}_M^{eu} \tag{6.17} $$

This tangent operator ${}^4\mathbf{L}$ is used in the localization analyses in order to detect or update localization orientations.

6.5.3 Macroscopic solution procedure: discretization and linearization

A finite element scheme is used in order to solve the governing equations according to the scheme given in Table 6.1. To achieve this, unknowns related to the following kinematic variables have to be defined in the macroscopic solution procedure.

- the displacement field $\vec{u}$,
- the strain jump vector $\vec{m}$ in each quadrature point where bifurcation has occurred,
- a single non-local strain degree of freedom $\overline{\varepsilon}$ in each quadrature point.

Three unknowns are thus defined in each integration point: two unknowns related to the strain jump $\vec{m}$ and one related to $\overline{\varepsilon}$. Within the damage localization band model it is assumed that the stresses and strains in each phase are uniform. The displacement field is interpolated according to the usual finite element shape functions. Note that the piecewise uniform strain state assumed in the localization band model is not entirely consistent with the finite element interpolation of the displacements, unless constant strain triangle elements are used. However this restriction is also present in 'classical' embedded discontinuity elements available in literature, the formulation of which is usually well motivated only for constant strain elements, see Wells (2001).

Using the standard finite element displacement interpolation, the discretized form of the governing equations at iteration (k) is given in matrix format as

$$ \int_V [\mathbf{B}]^T \left\{ \boldsymbol{\Sigma}^{(k)} \right\} dV = \left\{ \mathbf{f}_{ext}^{(k)} \right\} \tag{6.18} $$

$$ [n] \left(\left\{ \boldsymbol{\Sigma}^{b,(k)} \right\} - \left\{ \boldsymbol{\Sigma}^{s,(k)} \right\} \right) = \{0\} \tag{6.19} $$

$$ f_{\overline{\varepsilon}}^{(k)} = 0 \tag{6.20} $$

where $[\mathbf{B}]$ is the matrix which links the interpolated strain field to the nodal displacements, and $[n]$ is a matrix containing the components of the normal to the localization band, which is defined taking into account the symmetry of the stress tensor. In equation (6.18), the integral is extended to the entire structure. Equations (6.19) and (6.20) have to be formulated for each quadrature point where the macroscopic material behaviour is sampled. Relations (6.18)-(6.20) are next linearized as (δ denotes an iterative update of a quantity)

$$ \left\{ \boldsymbol{\Sigma}^{(k)} \right\} = \left\{ \boldsymbol{\Sigma}^{(k-1)} \right\} + \{\delta \boldsymbol{\Sigma}\} \tag{6.21} $$

$$ \left\{ m^{(k)} \right\} = \left\{ m^{(k-1)} \right\} + \{\delta m\} \tag{6.22} $$

$$ \overline{\varepsilon}^{(k)} = \overline{\varepsilon}^{(k-1)} + \delta \overline{\varepsilon} \tag{6.23} $$

Macroscopic equilibrium equation

The macroscopic stress variation in a given quadrature point may be obtained using the stress averaging on the localization band and the remaining material according to (6.2b), in which the band and the surrounding responses (6.2e) and (6.2f) are substituted, and in which (6.7) and (6.8) are used for the band. If $[\mathbf{L}^s]$ contains the components of the secant stiffness in the surrounding material, we then have

$$\{\delta\boldsymbol{\Sigma}\} \quad = \quad f^b\left([\mathbf{C}_M^{uu}]\left\{\delta\mathbf{E}^b\right\} + [\mathbf{C}_M^{ue}]\,\delta\overline{\varepsilon}\right) + f^s\,[\mathbf{L}^s]\,\{\delta\mathbf{E}^s\} \tag{6.24}$$

Expressing the strains in the band and in the surrounding in terms of the strain discontinuity through (6.2c) and (6.2d), and introducing the finite element interpolation for the macroscopic strain $\mathbf{E}$, the variation of stress is given as

$$\{\delta\boldsymbol{\Sigma}\} = \left(f^b\,[\mathbf{C}_M^{uu}] + f^s\,[\mathbf{L}^s]\right)[\mathbf{B}]\,\{\delta u\} + f^b f^s\left([\mathbf{C}_M^{uu}] - [\mathbf{L}^s]\right)[n]\,\{\delta m\} + f^b\,[\mathbf{C}_M^{ue}]\,\delta\overline{\varepsilon} \tag{6.25}$$

where the matrix $[n]$ is defined such that its multiplication with $\{\delta m\}$ yields the symmetric part of $\vec{n}\delta\vec{m}$. Note that in this equation, the first term pertains to all displacement degrees of freedom of the macroscopic structure, whereas the remaining terms relate to variations of variables which are local to the present quadrature point. Substituting (6.21) and (6.25) in the discretized macroscopic equilibrium (6.18) yields

$$[\mathbf{K}_{uu}]\,\{\delta u\} + \sum_{(i)}\left(\left[\mathbf{K}_{um,(i)}\right]\left\{\delta m_{(i)}\right\} + \left\{\mathbf{K}_{ue,(i)}\right\}\delta\overline{\varepsilon}_{(i)}\right) = \left\{\mathbf{f}_{ext}^{(k)}\right\} - \left\{\mathbf{f}_{int}^{(k-1)}\right\} \tag{6.26}$$

where $\left\{\mathbf{f}_{ext}^{(k)}\right\}$ are the external nodal forces in iteration (k). The sum over the Gauss points indicated by the index i in this relation reflects that the strain jump and the mesoscopic non-local strain unknowns are associated to these points. The tangent stiffness matrices in (6.26) are given by

$$[\mathbf{K}_{uu}] = \int_V [\mathbf{B}]^T\left(f^b\,[\mathbf{C}_M^{uu}] + f^s\,[\mathbf{L}^s]\right)[\mathbf{B}]\,dV \tag{6.27}$$

$$\left[\mathbf{K}_{um,(i)}\right] = V_{(i)} f^b f^s\,[\mathbf{B}]^T\left([\mathbf{C}_M^{uu}] - [\mathbf{L}^s]\right)[n] \tag{6.28}$$

$$\left\{\mathbf{K}_{ue,(i)}\right\} = V_{(i)} f^b\,[\mathbf{B}]^T\,\{\mathbf{C}_M^{ue}\} \tag{6.29}$$

where all terms in (6.28) and (6.29) are evaluated at the considered Gauss points. and $V_{(i)}$ denotes the volume element associated with the considered Gauss point by the numerical integration scheme.

Traction continuity across the localization band

Traction continuity across the boundary of the localization band (6.19) in a given Gauss point volume can be linearized using similar substitutions as above. This leads to the following linearized equation for iteration (k)

$$[\mathbf{K}_{mu}]\,\{\delta u\} + [\mathbf{K}_{mm}]\,\{\delta m\} + \{\mathbf{K}_{me}\}\,\delta\overline{\varepsilon} = -\,[n]\left(\left\{\boldsymbol{\Sigma}^{b,(k-1)}\right\} - \left\{\boldsymbol{\Sigma}^{s,(k-1)}\right\}\right) \tag{6.30}$$

with the corresponding stiffness matrices defined as

$$[\mathbf{K}_{mu}] = [n]\left([\mathbf{C}_M^{uu}] - [\mathbf{L}^s]\right)[\mathbf{B}] \tag{6.31}$$

$$[\mathbf{K}_{mm}] = [n]\left(f^s\,[\mathbf{C}_M^{uu}] - f^b\,[\mathbf{L}^s]\right)[n] \tag{6.32}$$

$$\{\mathbf{K}_{me}\} = [n]\,\{\mathbf{C}_M^{ue}\} \tag{6.33}$$

Non-local residual equation

Finally, the linearization of equation (6.20) is obtained by substituting the expression of the band strain (6.2c) into the expression of the non-local residual variation (6.8), yielding for iteration (k)

$$\langle\mathbf{K}_{eu}\rangle\,\{\delta u\} + \langle\mathbf{K}_{em}\rangle\,\{\delta m\} + \mathbf{K}_{ee}\delta\overline{\varepsilon} = -f_{\overline{\varepsilon}}^{(k-1)} \tag{6.34}$$

with

$$\langle\mathbf{K}_{eu}\rangle = \langle\mathbf{C}_M^{eu}\rangle\,[\mathbf{B}] \tag{6.35}$$

$$\langle\mathbf{K}_{em}\rangle = f^s\,\langle\mathbf{C}_M^{eu}\rangle\,[n] \tag{6.36}$$

$$\mathbf{K}_{ee} = \mathrm{C}_M^{ee} \tag{6.37}$$

6.5.4 Introduction of localization bands

The full multi-scale scheme presented above is applied when macroscopic localization of strain and damage was initiated. Prior to bifurcation detection, this complete scheme can be simplified as the strain jump degrees of freedom are not activated yet. The non-local degree of freedom is however included in the macroscopic solution scheme as from the start of the computation for reasons of simplicity.

When the localization detection indicates that a localization band should be introduced, a branch switching procedure has to be set up in order to force the integration point onto the localization equilibrium path. In the first increment after localization detection, separate responses of the band and surrounding materials are evaluated in the considered macroscopic material point. Based on the detected localization orientation $\vec{n}$, the branch switching procedure consists in forcing the appearance of a strain jump $(\vec{m}\vec{n})^{sym}$ between the band and the surrounding material. Note, however, that the vector $\vec{m}$ in this expression is yet unknown, and no estimate for it is available from the previous increment. In order to estimate this $\vec{m}$, it is assumed that a discontinuous bifurcation occurs. This means that the rate of the vector $\vec{m}$ must satisfy the linearized form of the traction continuity requirement (6.2a)

$$\left(\vec{n}.\,{}^4\mathbf{L}^b.\vec{n}\right).\,\dot{\vec{m}} = \vec{n}.\left({}^4\mathbf{L}^s - {}^4\mathbf{L}^b\right):\dot{\mathbf{E}} \tag{6.38}$$

where ${}^4\mathbf{L}^b$ denotes the tangent stiffness in the band and ${}^4\mathbf{L}^s$ the tangent stiffness in the remaining material. Initially, the latter is taken equal to the secant stiffness, whereas the tangent stiffness before bifurcation is used as an initial estimate for ${}^4\mathbf{L}^b$. Since the direction $\vec{n}$ is determined by the localization condition, equation (6.38) is used to determine an estimate of the finite

increment $\Delta\vec{m}$ which is consistent with the finite increment of overall strain $\Delta\mathbf{E}$. Note that this estimate of the strain jump is only an approximation since finite increments are estimated from the linearization of a non-linear equation. With this strain jump prediction $\Delta\vec{m}$, the band strain increment may be predicted as

$$\Delta\mathbf{E}^b = \Delta\mathbf{E} + f^s \left(\vec{n}\,\Delta\vec{m}\right)^{sym} \tag{6.39}$$

So far, the prediction of the non-local degree of freedom increment $\Delta\overline{\varepsilon}$ available from the macroscopic solution procedure does not take into account the bifurcation branching, since it still relates to the overall strain increment $\Delta\mathbf{E}$. A new prediction of $\Delta\overline{\varepsilon}$ thus has to be obtained, related to the strain increment $\Delta\mathbf{E}^b$ applied to the band rather than to $\Delta\mathbf{E}$. This new prediction of the non-local degree of freedom may be obtained from relation (6.34) by setting the non-local residual increment $\Delta f_{\overline{\varepsilon}}$ to zero. This delivers a corrected prediction of the non-local degree of freedom which takes into account the appearance of the strain jump

$$\Delta\overline{\varepsilon} = \frac{-1}{\mathbf{K}_{ee}} \left[\langle \mathbf{K}_{eu} \rangle \{\Delta u\} + \langle \mathbf{K}_{em} \rangle \{\Delta m\}\right] \tag{6.40}$$

6.5.5 Selection of the controlling non-local degree of freedom within a unit cell

The selection of the non-local degree of freedom which is used to control a given mesostructural cell analysis (i.e. the unit cell associated to a given Gauss point) is essential to ensure that the cell computation continues to follow a dissipative equilibrium path. It should be located in a part of the cell where damage is growing relatively rapidly. This corresponds to the early stage of damage if exponential evolution laws are used as is the case here. The selection of this controlling degree of freedom in the macroscopic increment $n+1$ is based on the relative increase of the non-local strain in increment n, i.e. on the ratio

$$\frac{\overline{\varepsilon}_n - \overline{\varepsilon}_{n-1}}{\overline{\varepsilon}_{n-1}} \tag{6.41}$$

where $\overline{\varepsilon}_n$ is the value of the non-local strain in the last converged increment and $\overline{\varepsilon}_{n-1}$ in the increment before. From all the nodes in which damage has occurred, i.e. where $\overline{\varepsilon}_n > \kappa_i$, the one with the highest ratio is selected.
Prior to any damage growth in the cell, the controlling non-local degree of freedom is defined as the node with the highest ratio $\overline{\varepsilon}_n/\kappa_i$, i.e. the node where damage will initiate first. These controlling node selection rules will be illustrated by means of an example in Section 6.7.

6.6 Adaptations of the path following strategy

6.6.1 Choice of the control parameter

The structural behaviour of masonry may lead to complex equilibrium paths with limit points and structural snap-backs. A path following technique is therefore required. A detailed presentation of the path following technique which is used here is available in Geers (1999a,b). The

details of the formulation of such methods will not be reviewed here, but their adaptation to the enhanced multi-scale framework will be outlined. In particular, the aspects related to the choice of the control parameters and load step predictions are discussed.

In path following methods, the external force array is defined as a reference load $\{\mathbf{f}_{ext}\}$ multiplied by a scalar load factor λ. The solution strategy consists in applying the external load, controlled by λ, in an incremental manner. In the sequel of this explanation, subscript indices denote macroscopic increment numbers, while the superscript indices indicate the iteration number within an increment. Iterative updates are denoted with a δ while incremental updates are denoted by Δ. At iteration $(k+1)$ of a given increment n, the path following methods use a decomposition of the iterative solution correction of the form, Batoz and Dhatt (1979)

$$\left\{\delta q_n^{(k+1)}\right\} = \left\{\delta^I q_n^{(k+1)}\right\} + \Delta\lambda_n^{(k+1)} \left\{\delta^{II} q_n^{(k+1)}\right\} \tag{6.42}$$

where q denotes here the complete set of unknowns, $\Delta\lambda_n^{k+1}$ is the load factor increment at iteration $k+1$, and the iterative updates $\left\{\delta^I q_n^{(k+1)}\right\}$ and $\left\{\delta^{II} q_n^{(k+1)}\right\}$ are obtained as the solutions of the following linear systems of equations.

$$\left[\mathbf{K}_n^{(k)}\right] \left\{\delta^I q_n^{(k+1)}\right\} = \lambda_{n-1} \{\mathbf{f}_{ext}\} - \left\{\mathbf{f}_{int}^{(k)}\right\} \tag{6.43}$$

$$\left[\mathbf{K}_n^{(k)}\right] \left\{\delta^{II} q_n^{(k+1)}\right\} = \{\mathbf{f}_{ext}\} \tag{6.44}$$

In the split (6.42), the increment of the load factor $\Delta\lambda_n^{(k+1)}$ is an additional unknown. As a consequence, an additional constraint equation is required, which is expressed in terms of this load factor and of degrees of freedom of the problem. The path following method used here employs a cylindrical constraint, modified at each increment and expressed in terms of a single variable used for the control of the increment, see Geers (1999a). A selection rule has to be defined for the selection of the most appropriate variable entering the constraint at each increment. Since in the present framework, not only macroscopic displacement degrees of freedom are used, but also degrees of freedom related to the strain jump in the localization band and a mesoscopic non-local strain degrees of freedom, the path following technique must be adapted accordingly. Indeed, the non-local strain degrees of freedom can be used efficiently in the constraint equation. This constraint requires the choice of a variable which increases monotonically, which is precisely the criterion used for the selection of the controlling non-local degrees of freedom from the unit cells. Among the non-local degrees of freedom available at the macroscopic Gauss points, the one which shows the largest incremental *relative* growth is used for the control of the subsequent increment.

6.6.2 Implementation of non-local strain-based macroscopic path following method

Each of the non-local degrees of freedom used in the macroscopic solution procedure may be associated to different nodes within the associated unit cell in successive macroscopic increments. Indeed the 'physical' or mesoscopic location of these degrees of freedom within the cell varies in each increment, and the resulting numerical values of these macroscopic unknowns

may be strongly different from one macroscopic increment to another. As a result, the rules proposed in Geers (1999a) for the selection of the degree of freedom which enters the additional constraint and the prediction of the load increment size and sign at the beginning of a new step must be adapted.

The selection of the non-local degree of freedom which enters the additional constraint is performed at the start of a macroscopic increment n according to

$$\overline{\varepsilon}_{MC} \text{ such that } \max_{\forall \text{macro } \overline{\varepsilon} \text{ dof}} \left| \frac{\Delta \overline{\varepsilon}_{n-1}}{\overline{\varepsilon}_{n-2}} \right| \tag{6.45}$$

where $\overline{\varepsilon}_{MC}$ is the non-local degree of freedom selected for the control of the macroscopic solution procedure, and where $\Delta\overline{\varepsilon}_{n-1}$ is the converged incremental variation in increment $n-1$ of the set of mesoscopic non-local degrees of freedom selected for the control of the new increment n, and $\overline{\varepsilon}_{n-2}$ is the converged value of this degree of freedom at the end of increment $n-2$. Note that it may be necessary to retrieve data from increment $n-2$ from the cell if the controlling non-local degree of freedom of the cell has changed from increment $n-2$ to $n-1$. The initial value of the load increment used in the first iteration of an increment n is obtained as

$$\left|\Delta\lambda_n^{(0)}\right| = \sqrt{\frac{n_d}{n_c} \frac{\mid \Delta\lambda_{n-1}\Delta\overline{\varepsilon}_{n-1} \mid}{\delta^{II}\,\overline{\varepsilon}}} \tag{6.46}$$

where n_c is the number of iterations needed to reach convergence in increment $n-1$, and n_d is the desired number of iterations in increment n.
Secondly, the sign of a new load increment is determined using the rules proposed by Geers (1999a), based on the following variations of any degree of freedom eligible for macroscopic control: $\delta^{II}\overline{\varepsilon}_{n-1}$, $\Delta\overline{\varepsilon}_{n-1}$ and $\delta^{II}\overline{\varepsilon}_n$. These values should be also made available corresponding to a given location in the unit cell (i.e. related to the selected non-local degree of freedom related to a given increment).

6.7 Applications and discussions

In this section, the numerical multi-scale framework developed above is applied in a number of relevant test problems. Two simple test cases are considered with homogeneous loading at the macroscopic scale in order to illustrate the capability of the algorithm to treat mesostructural snap-back and its sensitivity to the absolute size and the geometrical arrangement of the mesostructure.

6.7.1 Mesostructural snap-back in a tension-compression test

Homogeneous solution path

The multi-scale framework is applied here to reproduce the computation used in Section 6.3 as an illustration of mesostructural unit cell snap-back. The crucial difference between these two analyses is that, whereas the results in Section 6.3 were obtained by directly controlling

the stress state of a single cell, this cell is now considered to be a part of a structure within a multi-scale computation. This means that the unit cell computation is strain-driven and that the special path-following techniques which were developed in the Section 6.6 are now required.

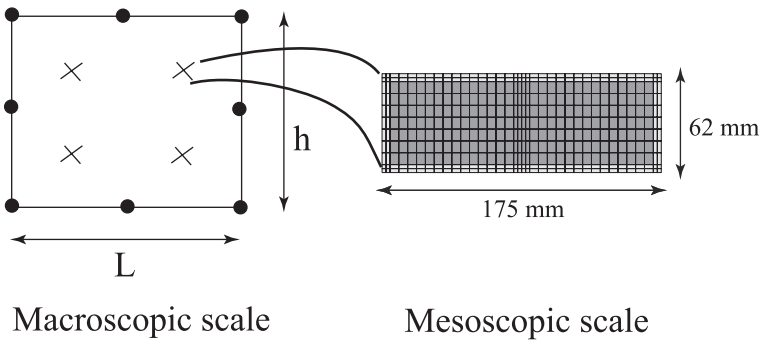

Figure 6.7: Principle of single macroscopic element tests

The macroscopic 'structure' consists of a single finite element under homogeneous macroscopic loading, see Figure 6.7. Horizontal tension is combined with vertical compression along the proportional stress path $(\Sigma_{xx}, \Sigma_{yy}, \Sigma_{xy}) = (0.2, -1, 0)$. The bifurcation detection and branching are not activated in this first computation and the macroscopic 'structural' dimensions are taken such that the volume associated to each Gauss point by the quadrature scheme is identical to that of the unit cell. The macroscopic finite element has a biquadratic serendipity displacement interpolation and a four Gauss point integration scheme. Note that all the Gauss points will exhibit the same response due to the homogeneous character of the macroscopic loading. Since no localization band is introduced, the unit cell response is the only possible cause of snap-back in the homogenized material response. Such a snap-back is dealt with by using the mesoscopic non-local degree of freedom control strategy. The unit cell has dimensions $175 \times 62 \times 100$ mm^3 with 10 mm thick mortar joints. The damage criteria and material properties used for the constituents are taken from Massart et al. (2004c). The load factor evolution is represented in Figure 6.8 as a function of the top vertical displacement of the structure divided by the number of unit cells along the height of the structure, in order to allow the comparison of the curve with the result reported in Figure 6.3. These curves are identical, showing that the unit cell snap-back is correctly dealt with in the multi-scale framework. It is noteworthy that these results were obtained with a comparable number of increments and iterations. The transfer of degrees of freedom from the mesoscale to the macroscopic solution scheme thus does not seem to have a negative influence on the overall efficiency of the computations. For each point of the load-displacement curve marked by a capital letter, the damage state inside the unit cell is also depicted in Figure 6.8. The node used for the non-local strain control in the subsequent increment is identified by a star. At each stage of the damage growth, these selected nodes are clearly in a region in which incremental damage growth is considerable, as prescribed by the selection rules.

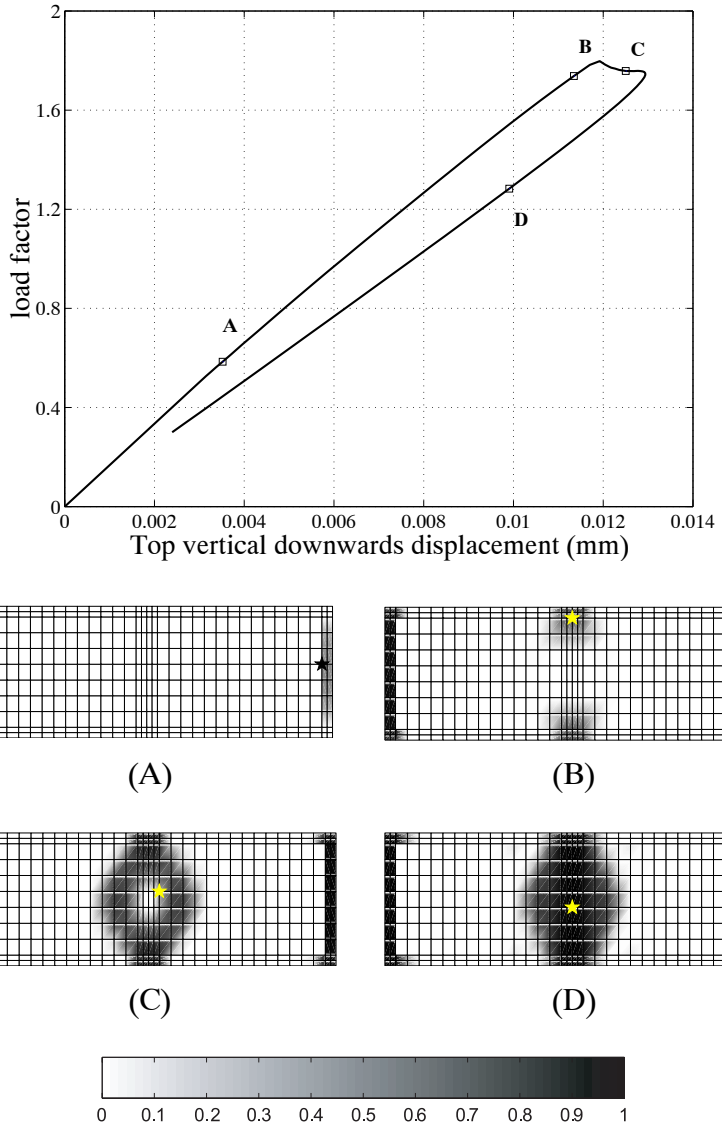

Figure 6.8: Load-displacement curve and damage distribution obtained by the multi-scale modeling for homogeneous macroscopic tension-compression loading. Each damage distribution corresponds to the point denoted in the load-displacement curve. The star in the damage distributions indicate the degree of freedom which is selected for the snap-back control in the next increment.

Localized solution within a 'structural' computation

The analysis is now repeated with a macroscopic 'structure' of modified dimensions 600×300 mm^2. Again, only one macroscopic finite element is used which means that with the chosen dimensions the volume associated to each Gauss point by the quadrature scheme is larger than the unit cell dimensions. The macroscopic loading is kept homogeneous such that all Gauss points will exhibit the same behaviour. For this test, the homogeneous structural solution is

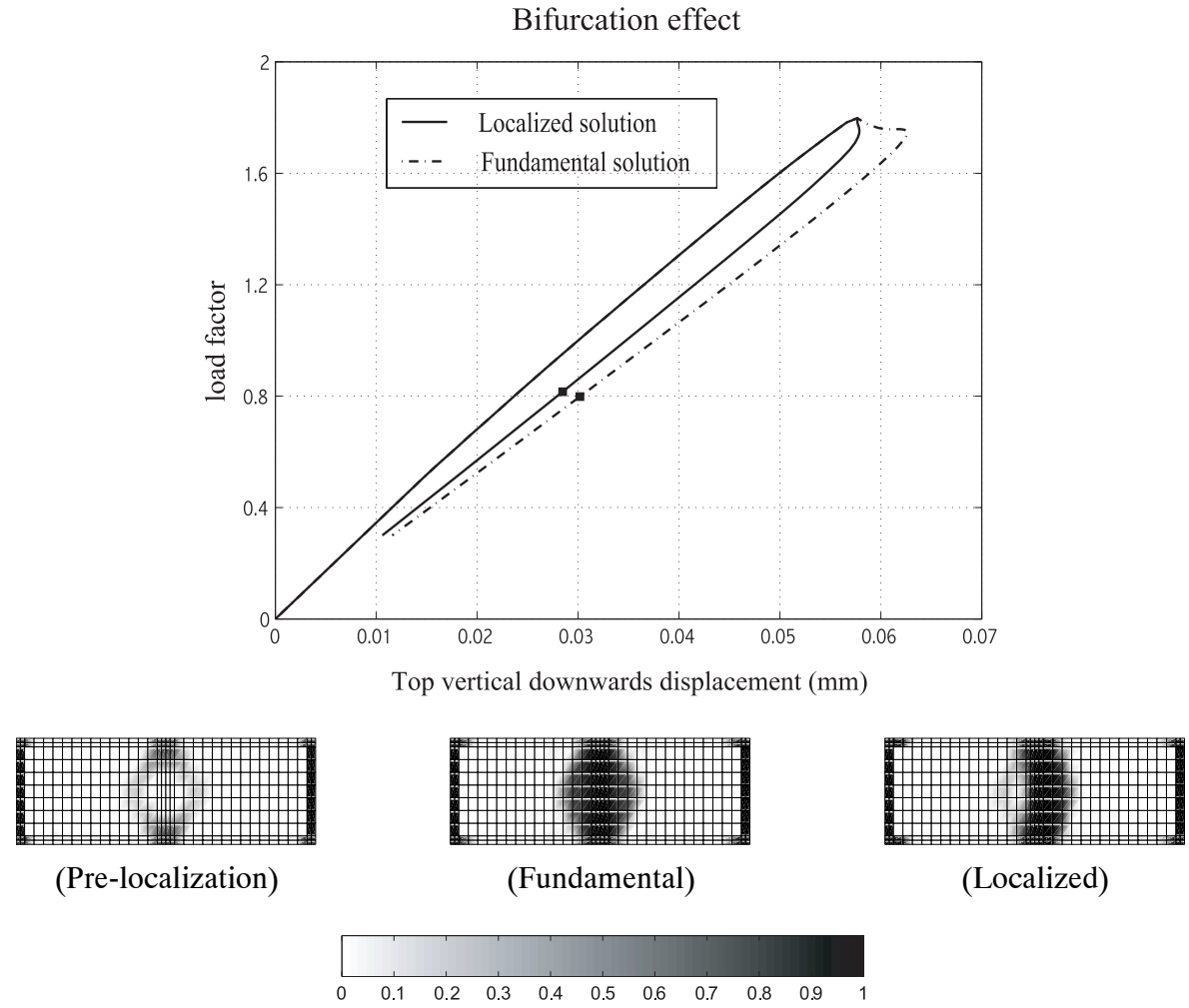

Figure 6.9: Load-displacement curves and damage distribution obtained by multi-scale modeling for macroscopic tension-compression loading for fundamental and localized solutions

compared with the one in which the material response is allowed to localize in all the Gauss points. The damage bands have a vertical orientation, corresponding to the final damage pattern. The effect of the localization band clearly appears in the load-displacement curve in Figure 6.9, where a sharper snap-back is found for the localized solution. Note however that a non-symmetric damage pattern is observed in the cell for the localized solution. This non-symmetry may be explained by the use of the non-local strain control in the multi-scale procedure. As illustrated in Figure 6.9, joint and brick damage is initiated in a symmetric fashion prior to localization, as a result of the symmetry of the geometry and of the loading. This symmetry actually causes a bifurcation to appear at the mesoscopic level. This meso-scale bifurcation is not treated in the stress-controlled, direct unit cell computation presented in Section 6.3. On the contrary, when the enhanced multi-scale technique is used, the non-local strain unit cell control selects one non-local strain degree of freedom for controlling the unit cell even if its counterpart would be equally suitable. As a consequence, the asymmetric solution in which the selected node continues to be damaged is followed. The sharper snap-back observed in Figure

6.9 is caused not only by the presence of the localization band in each Gauss point, but also by the occurrence of a different mesoscopic damage pattern inside the unit cell with respect to the macroscopically uniform solution.

6.7.2 Localization orientation and size effect in shear-compression test

As a second illustration of the multi-scale framework, a single macroscopic element is subjected to vertical compression combined with shear. This case was already extensively studied in terms of localization detection in the first part of this contribution, see Massart et al. (2004b). Here, the influence of the ratio between the structural and the mesostructural dimensions is examined, as well as the influence of the shape of the bricks.

Structural size influence

The fact that the mesostructural size enters the macroscopic computation via the width of the localization band implies that a size effect is observed. If the ratio between the structural dimension and the unit cell dimension increases, a more brittle structural post-peak response should be obtained because the volume in which energy is dissipated becomes smaller compared to the structural size. To show this effect, the vertical compression-shearing test is repeated with the same unit cell dimensions, but with two different structural dimensions, namely 800×800 mm^2 and 1600×1600 mm^2. Figure 6.10 shows the load factor versus the displacement normalized by the structural size, for both structural dimensions together with the structural fundamental paths. For a fixed unit cell size, a larger structure indeed clearly leads to a more brittle structural response as a result of the higher ratio between the structural dimensions and the width of the localization zone.

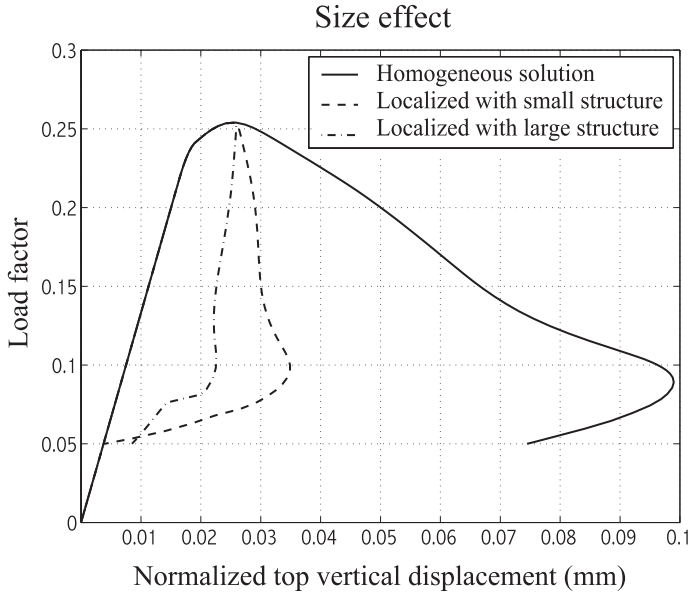

Figure 6.10: Load-displacement curve for vertical compression combined with shear for various structural dimensions and a fixed unit cell.

Influence of geometrical arrangement

Another essential benefit of the multi-scale framework is the fact any modification of mesostructural characteristics is naturally taken into account in the macroscopic response by the scale transition. In order to illustrate the importance of this effect, the vertical compression-shearing test is reproduced on a macroscopic sample of dimensions 800×800 mm^2 for two different unit cells. The geometry of the unit cell is modified while all the material parameters of the constituents are unchanged. The response of the material obtained for the reference cell of dimensions $175 \times 52 \times 100$ mm^3 is compared with that of a cell in which the brick dimensions are changed to $250 \times 40 \times 100$ mm^3. The mortar joint thickness is taken equal to 10 mm in both cells. In both cases a staircase crack pattern is found inside the cell. However, as a result of the different geometries of the cells the average crack orientations associated to the staircase pattern are different. For the reference cell, the final orientation of the macroscopic localization band is approximately $\Theta = 53^\circ$, while it is approximately $\Theta = 68^\circ$ in the modified cell. The corresponding load-displacement curves are compared in Figure 6.11. It can be noticed that the initial stiffness along the vertical direction and the peak load are not strongly affected by the geometry modification. On the contrary, the post-peak response is much less brittle for the modified unit cell than for the original cell. This means that such a change in the geometry of the mesostructure may have a considerable impact on structural computations. When closed-form constitutive description are used, the complete material parameter identification needs to be reproduced for any modification of the geometry. On the contrary, these effects can be included naturally in structural computation when using the proposed multi-scale framework, so that the influence of geometry changes on structural behaviour can be immediately assessed. It is only fair to mention, however, that this flexibility is associated to a higher computational cost.

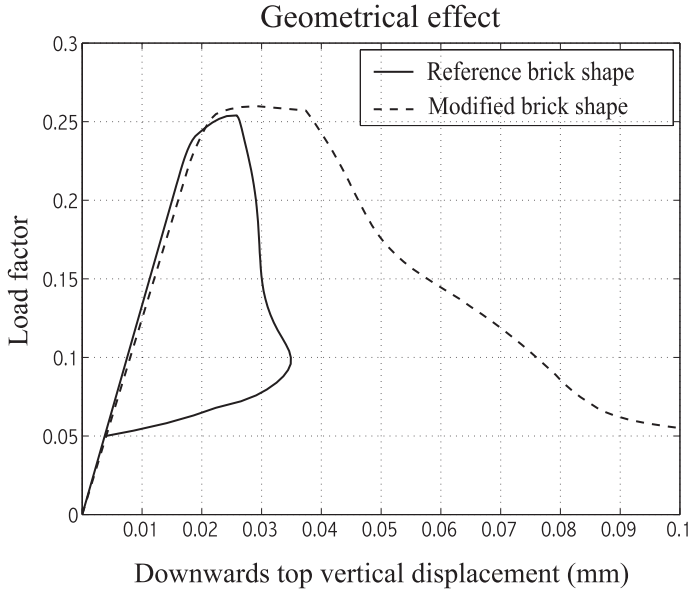

Figure 6.11: Load-displacement curve for vertical compression combined with shear for various mesoscopic unit cell geometries.

6.8 Summary

The computational details related to a multi-scale framework for the computation of planar masonry structures were presented. In relation with the quasi-brittle nature of the constituents, the treatment of damage localization by means of embedded localization bands was detailed. Due to the softening of the constituents, it was shown that a snap-back phenomenon may arise in the homogenized material response extracted from mesoscopic unit cells by the scale transition procedure as well as in the localization band. In order to deal with this mesostructural snap-back, the scale transition and the path following method were adapted by including mesoscopic degrees of freedom and equations in the macroscopic solution procedure. Simple tests on homogeneously loaded macroscopic 'structures' were used in order to illustrate the approach. The mesostructural snap-back was shown to be successfully handled by the proposed approach. It was shown that localized solutions are correctly captured, and that the inclusion of a physically motivated width for the localization band leads to a size effect in the deduced macroscopic response and to a strong dependence on the geometrical arrangement of constituents in the mesosctructure, particularly in the post-peak regime.

Chapter 7

Applications

In this Chapter, the use of the localization-enhanced multi-scale framework presented in Chapters 5 and 6 is illustrated on the basis of some simplified structural applications. The solution procedure detailed in Chapter 6 is implemented based on a parallel computing strategy. A simple uniaxial tensile test in the direction perpendicular to the bed joints is first performed, in order to evaluate the implementation and to show the ability of the embedded band model to describe the propagation of localization bands. Confined shearing tests on a masonry panels with and without an opening are next simulated and compared qualitatively with experimental observations from the literature.

7.1 Implementation of the multi-scale framework

The multi-scale framework detailed in Chapters 5 and 6 nests two solution procedures at different scales. It is based on the extraction of the macroscopic material behaviour of each macroscopic sampling point from the solution of a mesostructural boundary value problem at each iteration of the macroscopic solution procedure. The macroscopic solution estimate available at a given macroscopic iteration allows to define the boundary conditions of all the mesostructural unit cell computations. For a given macroscopic state, these unit cell responses may be determined without any mutual interactions, which facilitates the use of parallel computing. The parallel implementation of the multi-scale framework is based on a master-slave scheme as described in Kouznetsova (2002) and sketched in Figure 7.1. The master program drives the overall computation. For each macroscopic iteration, the macroscopic computation is invoked in order to determine an estimate of the macroscopic solution, which allows to obtain the values of the macroscopic strain and controlling non-local strain to apply to the unit cell corresponding to each macroscopic integration point. The master program then distributes and sends these unit cell computations to the available processors. When all the unit cell computations have been completed, the macroscopic stress tensor, the non-local residual and the corresponding consistent tangents in each of the macroscopic Gauss points are collected by the master program. These quantities are used at the macroscopic scale to determine the internal forces and the convergence norm.

It is noteworthy that the confined shearing wall application presented below requires the load to be applied in several phases, resulting in non-proportional loading effects. The path following technique presented in Chapter 6 was further adapted for this purpose.

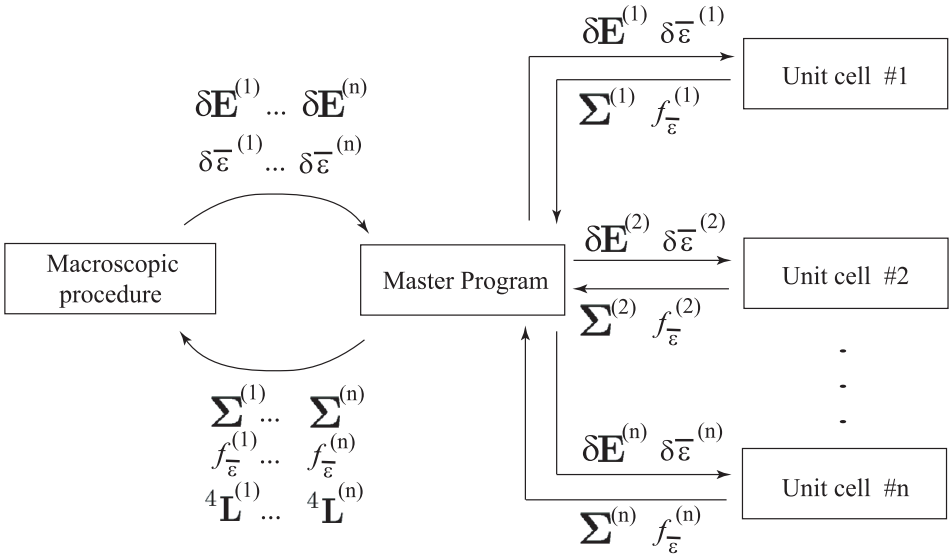

Figure 7.1: Parallel implementation of the multi-scale scheme

7.2 Uniaxial tension test

A uniaxial tension test is used in order to validate the implementation and to show the ability of the embedded band model to describe (in an average sense) the propagation of a crack. The macroscopic structure is a panel of dimensions $2500 \times 2500 \times 100$ mm^3. The top and bottom boundaries of the panel are constrained to remain horizontal; the horizontal displacements on these boundaries are free. A vertical load is applied at the middle of the top boundary of the specimen, while the bottom is fixed. At the macroscopic scale, a coarse mesh of 9 elements with biquadratic displacement interpolation is used with a four-point integration scheme. The mesostructural cell is made of bricks of dimensions $140 \times 40 \times 100$ mm^3 with 10 mm thick mortar joints. The mesoscopic material properties are identical to the ones used in Chapter 4, except for the tensile strength of mortar, which is taken as $f_t = 0.2$ N/mm^2, and its tensile fracture energy, which is taken as $G_f = 1.5$ Nm/m^2. To initiate damage, the bottom left macroscopic Gauss point has a mesostructural unit cell in which the mortar strength is reduced by 5 %. The result of the test is illustrated in Figure 7.2, where it is shown that the full load-displacement curve can be traced. The marked points in the load-displacement curve correspond to the macroscopic states at the bottom of the figure. This shows that the damage growth localizes relatively rapidly across the width of the panel near the peak load. The post-peak path beyond point C is entirely due to the quasi-brittle damage growth within the extending localization band. Figure 7.2 shows that the propagation of embedded bands under mode I loading is able to reproduce typical tensile structural load-displacement curves. In this test, the propagation of these bands however occurs along a straight path, leading to a smooth band propagation. The shear test problems presented next are more demanding in this respect.

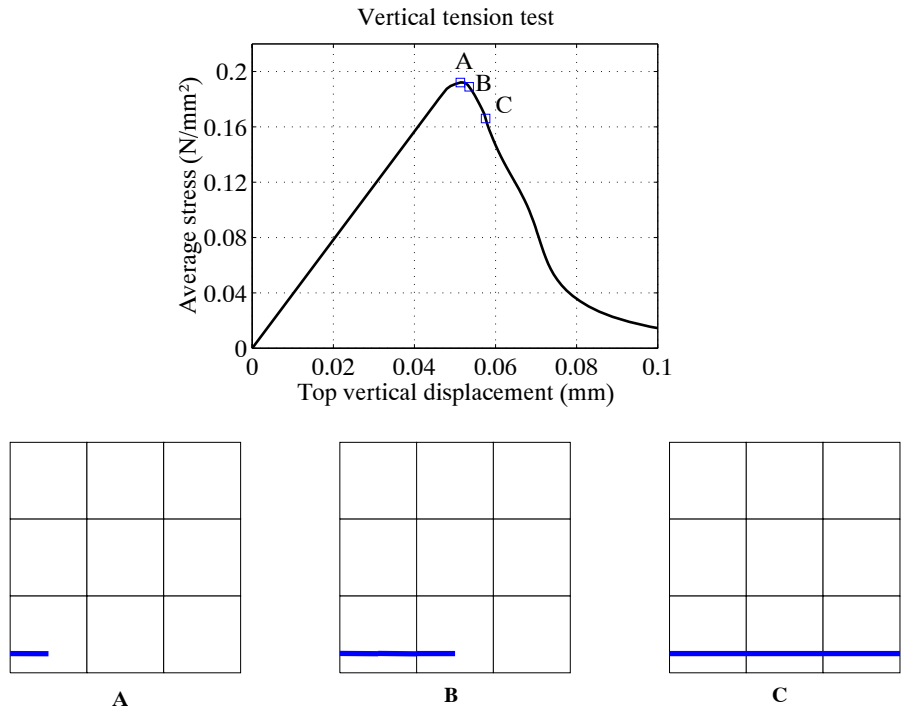

Figure 7.2: Uniaxial vertical tension test: (top) load–deflection curve, (bottom) propagation of embedded localization bands

7.3 Confined shearing of a masonry wall with an opening

Data related to large scale tests on masonry structures is scarce in the literature because of the practical difficulties to realize such experiments. Confined shear wall tests are the most commonly used 'macroscopic' experiments, see for instance Raijmakers and Vermeltfoort (1992). Similar experimental results were already used in Lourenço (1996) for the validation of a discrete mesoscopic masonry model. For practical reasons, the tested structures usually consist of only a few bricks. Since the scale separation between the structural and mesoscopic scales almost vanishes in such panels, the corresponding results cannot be used for the quantitative validation of homogenization models, such as the present. However, given the lack of experimental data on large scale structures, the small scale test data is nevertheless used for a qualitative assessment of the multi-scale modeling. The tests reported in Raijmakers and Vermeltfoort (1992) for shear walls with openings are considered for this purpose. The ratio between the structural dimensions and the size of the bricks is approximately 5-10 in the reported experiments, and different mesoscopic and macroscopic geometrical dimensions will be used here in order for the multi-scale approach to remain applicable. The dimensions of the opening are also modified with respect to the dimensions of the wall.

7.3.1 Problem description and qualitative experimental behaviour

The wall geometry considered in the simulation is shown in Figure 7.3. It consists of a plane masonry wall of dimensions $2500 \times 3000 \times 100$ mm^3. An opening with dimensions 800×1200 mm^2

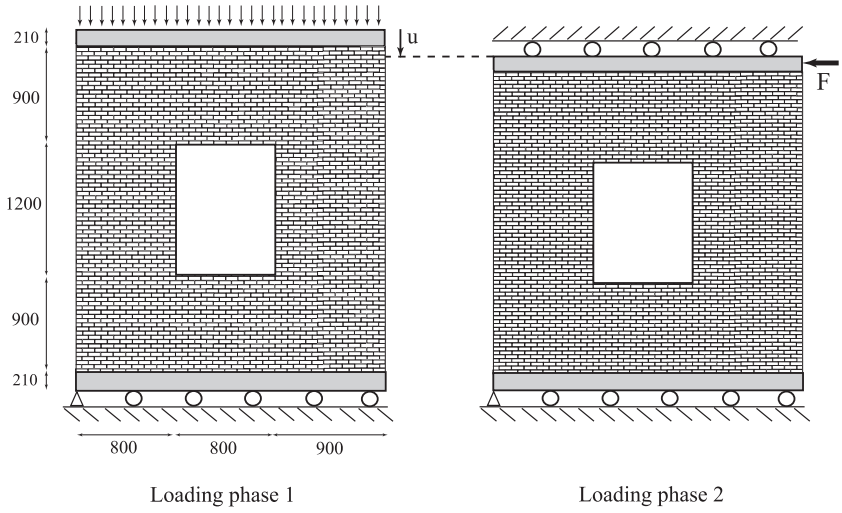

Figure 7.3: Shear test on a wall with opening: two-phase loading and dimensions

is present in the wall. The geometry is made slightly non symmetric in order to avoid extensive symmetry at the macroscopic scale. The totality of bricks consistent with the mesoscopic and structural dimensions is drawn in Figure 7.3 in order to emphasize the costly character of a complete fine scale modeling of this structure. In the experiments reported in Raijmakers and Vermeltfoort (1992), the top and bottom boundaries of the wall were 'clamped' in steel beams. The loading was applied in two phases. In the first phase, the wall was compressed by a vertical distributed load applied to the top beam, resulting in a uniform vertical displacement of the top boundary. In the second loading phase, the vertical displacement of the top boundary was fixed and a horizontal shearing force was applied. In the numerical analysis presented here, the effect of the loading set-up has been represented by two bands of elements with elastic behaviour. The vertical displacement of the top boundary of the top slab has been forced to remain uniform to simulate the presence of a steel beam. In order to represent the (imperfect) clamping of the wall in the steel beam, a lower stiffness (comparable to concrete) was assumed for the two rows of elastic elements. The shearing load has been applied as a distributed load on the right side of this row of elements.

Experimentally, a complex crack evolution pattern was obtained. The average crack pattern stages are illustrated in Figure 7.4, after Raijmakers and Vermeltfoort (1992). Early in the shearing phase, damage was first initiated with diagonal cracks starting at three corners of the opening and in the middle of its top border (Figure 7.4A). These specific damage initiation locations (in particular the middle point of the top border of the opening) were linked to the small number of bricks in the specimen (the opening of the wall had a width of approximately one brick). Shortly after their initiation, these diagonal cracks became inactive upon the appearance of two tensile horizontal cracks at the free boundaries as depicted in Figure 7.4B. At a later stage, these horizontal cracks were arrested and two of the diagonal cracks were then re-actived and propagated towards the top right and bottom left corners of the wall (Figure 7.4C). Finally, a structural failure mechanism was reached with compressive crushing of two corners of the wall and of two corners of the opening in front of the tensile cracks (Figure 7.4D). The created

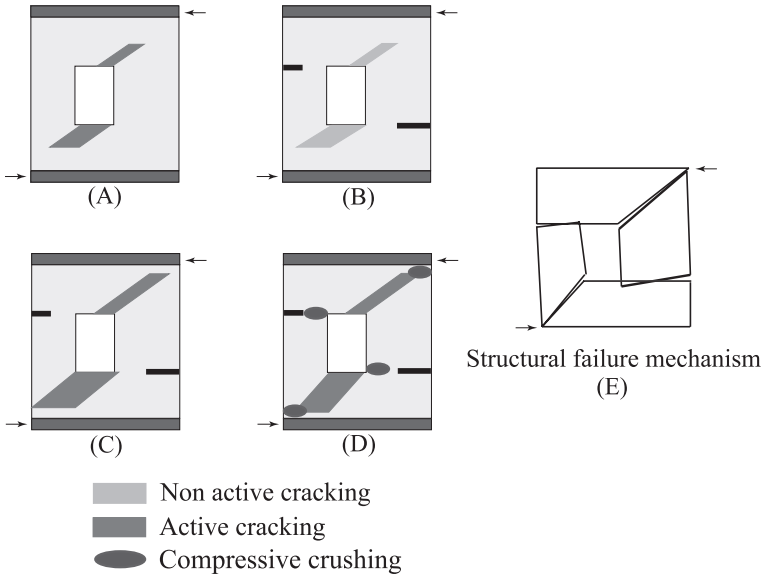

Figure 7.4: Shear test on a wall with opening – successive cracking states observed in experiments by Raijmakers and Vermeltfoort (1992)

cracks define four distinct parts of the wall, rotating with respect to each other in an almost rigid manner, as sketched in Figure 7.4E.

For the numerical simulation, the mesostructure of the material is made of bricks of dimensions $90 \times 30 \times 100$ mm^3 with 10 mm thick mortar joints. The unit cell is discretized with a mesh of 120 elements with a biquadratic interpolation of the displacement field and a bilinear interpolation of the non-local strain field. A plane stress assumption is used at the mesoscopic scale. Note that the compressive crushing experimentally observed in the last cracking stage of the test cannot be captured by a plane stress assumption, see Chapter 4. A generalized plane state description would be useful in this respect, but would require a considerably finer mesoscopic discretization to simulate brick cracking. The maximum principal stress criterion is used for the brick material and a Drucker-Prager criterion with a compressive cap is used for mortar. The same material parameters as in Chapter 4 are used, see table 7.1. At the macroscopic scale a mesh of 48 elements is used with a biquadratic displacement interpolation and a four point integration scheme. As a result, each iteration of the macrosopic solution procedure requires the solution of 192 small mesostructural boundary value problems. A compressive vertical load of 37.5 kN is considered for the first loading phase.

Table 7.1: Mesoscopic material parameters

Material	E (MPa)	ν	l_c (mm)	f_t (MPa)	G_f (Nm/m^2)	f_c (MPa)	f_b (MPa)	f_h (MPa)
Brick	16700	0.15	2.2	0.75	16.2	15	-	-
Mortar	3900	0.20	2.2	0.13	9	5.6	8.72	7.45

7.3.2 Numerical results

The load-displacement curve obtained for the shearing loading phase is shown in Figure 7.5. The computation was continued until convergence failure. The evolution of the macroscopic localization during the computation is illustrated in Figures 7.6 to 7.13 for each of the marked points in the load–displacement curve. In these figures, the embedded localization bands are represented with their respective orientations for the Gauss points in which localization has appeared. For each of these states the mesoscopic damage in typical unit cells is shown. Unless stated otherwise, the unit cell damage patterns are related to the localization band of the Gauss point when such a band is present. The macroscopic stress distribution is shown on the deformed shape of the structure – displacements have been magnified by a factor of 1000. As depicted in

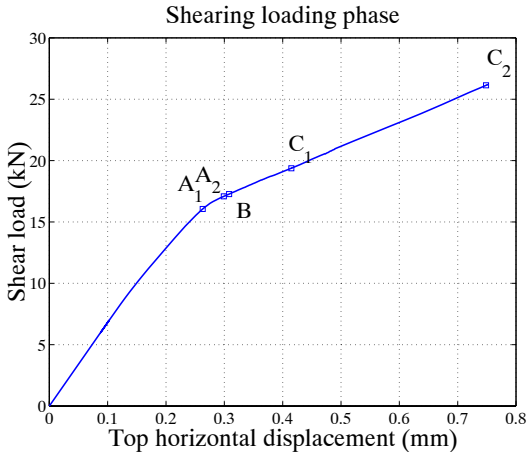

Figure 7.5: Load–displacement curve of shear loading phase

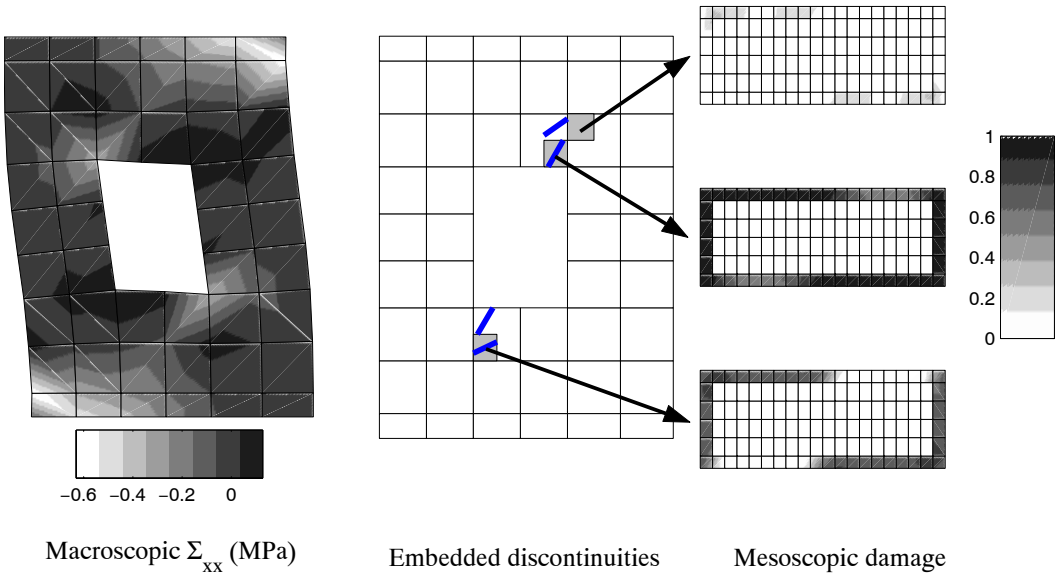

Figure 7.6: Damage state in state A_1 - initiation of diagonal cracking: (left) macroscopic horizontal stress distribution, (center) embedded discontinuities, (right) mesoscopic damage states

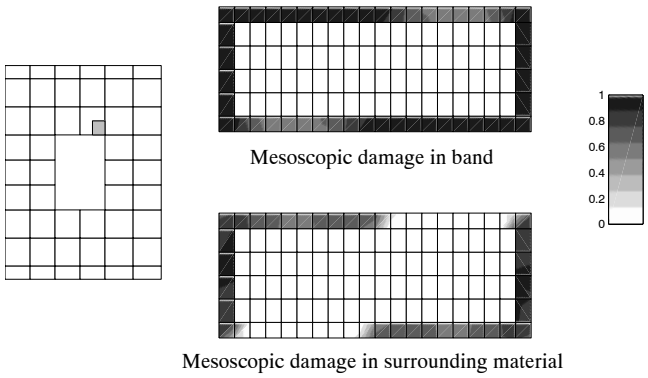

Figure 7.7: Damage state in state A_1 with diagonal cracking: comparison between damage states inside and outside the localization band of the first localized Gauss point above the opening

Figure 7.6, cracking initiates at the top right and bottom left corners of the opening. This crack initiation is due to horizontal tension combined with shear. At this stage, the orientation of the localization bands clearly reflects the staircase damage pattern obtained at the mesoscopic scale. Some further damage evolution is already present in non localized Gauss points, indicating that the diagonal cracking propagates in the direction of the corners of the wall. For the first localization band at the top of the opening, some further damage evolution did already alter somewhat the staircase pattern in the situation represented in Figure 7.6. Fully anisotropic effects are however still present due to the behaviour of the unloading surrounding material. This is illustrated in Figure 7.7 which shows the damage patterns inside and outside the band associated with one particular Gauss point. The (non-evolving) damage state outside the band is

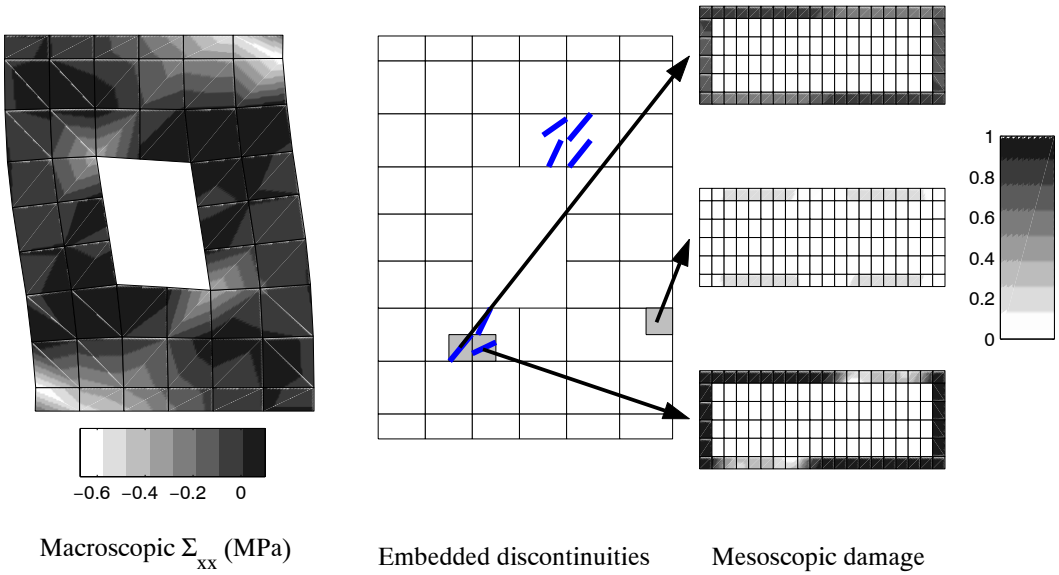

Figure 7.8: Damage state in state A_2 - progression of diagonal cracking: (left) macroscopic horizontal stress distribution, (center) embedded discontinuities, (right) mesoscopic damage states

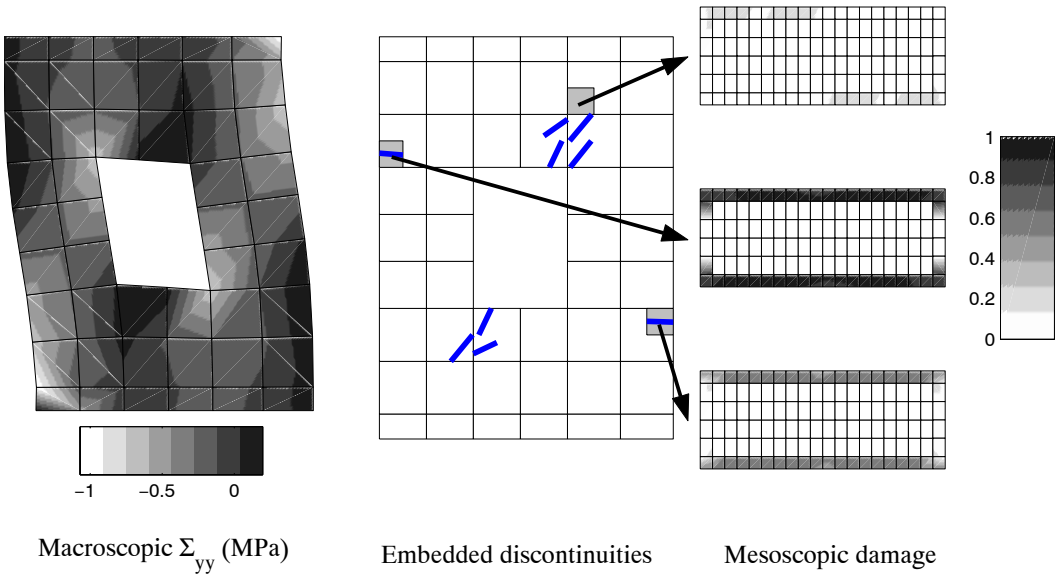

Figure 7.9: Damage state in state B - appearance of lateral horizontal cracks: (left) macroscopic vertical stress distribution, (center) embedded discontinuities, (right) mesoscopic damage states

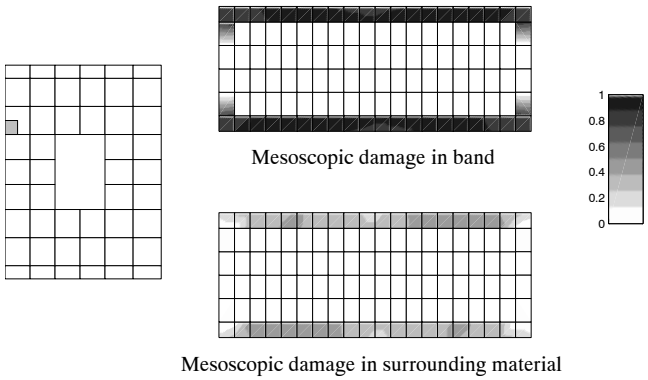

Figure 7.10: Damage state in state B with horizontal tensile cracking: band and surrounding damage states

indeed a staircase pattern. The rather high level of damage reached in the surrounding material before the localization took place has a considerable impact on the aggregate response of the Gauss point, since the band occupies only a limited volume fraction of the associated material volume.

Upon further shearing the diagonal cracking extends slightly with respect to the previous situation (Figure 7.8). In addition, tensile damage is initiated at two locations at the free boundaries (central unit cell in Figure 7.8). Next, these tensile damage zones localize as illustrated in Figure 7.9. During this stage, the existing diagonal cracks at the top and bottom of the opening do not evolve strongly (top unit cell in Figure 7.9). The multi-scale approach is thus able to represent the transition from the diagonal cracking to the tensile lateral cracking as observed in experiments on small structures of a similar shape (Figure 7.4). The comparison of the damaged state of the band and of the surrounding material for the tensile cracks is presented in Figure

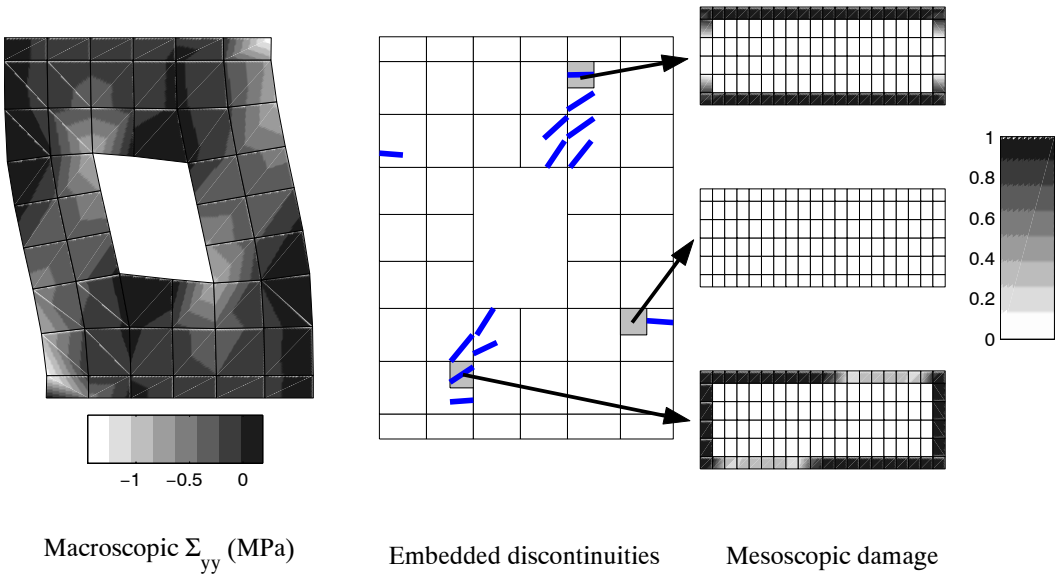

Figure 7.11: Damage state in state C_1 - propagation of diagonal cracking: (left) macroscopic vertical stress distribution, (center) embedded discontinuities, (right) mesoscopic damage states

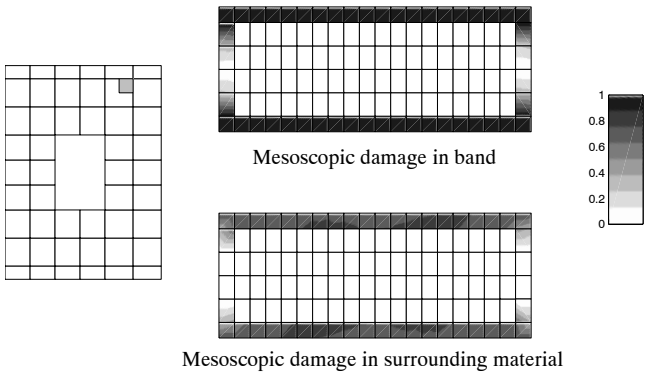

Figure 7.12: Damage state in state C_1 with compressive bed joint damage: band and surrounding damage states

7.10. For this location, a rather low damage level is obtained in the surrounding material as a result of the pure mode I opening of the bed joint for which the behaviour becomes unstable early in the damaging process.

After the opening of the horizontal tensile cracks, the growth of the diagonal cracks near the opening is re-activated as was also observed in the experiments. This further propagation is accompanied by a slower progression of the lateral tensile cracks. It is also observed that the embedded discontinuities near the corners of the wall tend to be inclined towards an horizontal direction, as noticed in Figure 7.11 (top and bottom mesoscopic unit cells). The comparison between the damage state in the band and the surrounding material for a point located just under the top beam is illustrated in Figure 7.12. Even though damage is concentrated in the bed joints like for the horizontal tensile cracks (Figure 7.10), the level of damage in the surrounding is much higher here, which reflects the fact that under the compressive stress path followed by

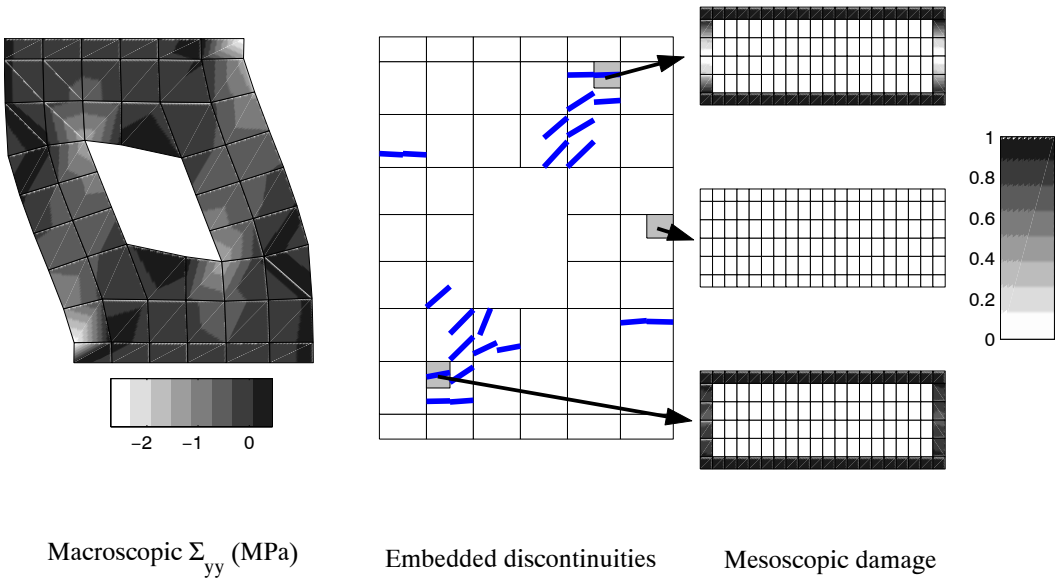

Figure 7.13: Damage state in state C_2 - propagation of diagonal cracking: (left) macroscopic vertical stress distribution, (center) embedded discontinuities, (right) mesoscopic damage states

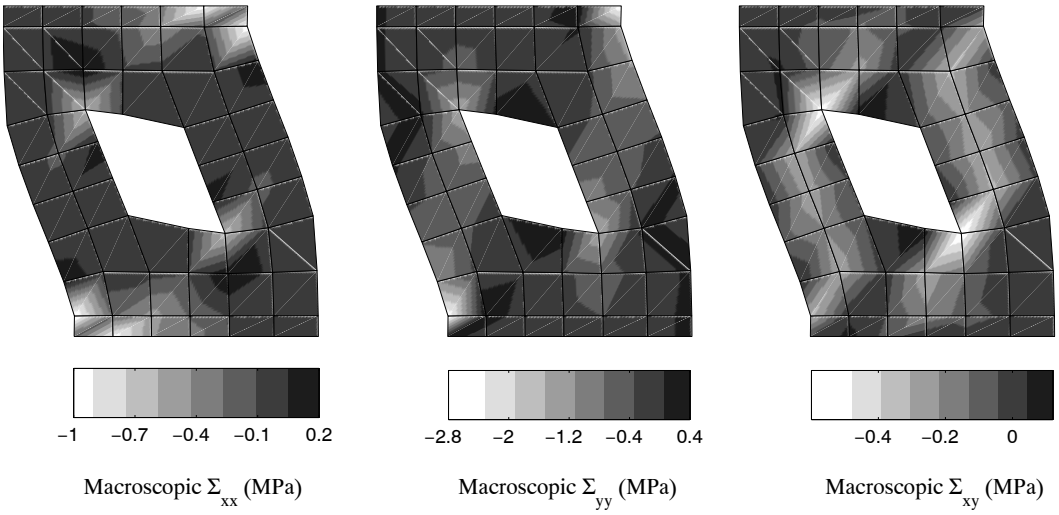

Figure 7.14: Stress distributions at state C_2 of the cracking process

this point, damage may grow substantially before triggering localization.

Finally, damage continues to grow in the direction of the corners of the wall, in parallel with a slow evolution of the lateral horizontal cracks (Figure 7.13). The result of this damage evolution is that strong redistributions of stresses occur, which lead to high compressive vertical stresses at four locations as observed in the experiments (Figure 7.13-left). Note also that the vertical tensile stress field is altered around the horizontal cracks by the presence of the damage, with a corresponding local decrease of this stress component. Figure 7.14 confirms the presence of four highly compressed regions. The compressive failure at these locations represents the last stage of the cracking process as observed in experiments. It is emphasized that the choice of a generalized plane state instead of a plane stress description will have an impact at this

stage of the computation. For a plane stress simulation, compressive failure of the bed mortar joints governs the ultimate load-carrying capacity, whereas the use of a generalized plane state description might lead to tensile brick cracking in the plane of the wall, and thus to a more brittle post-peak response. Noteworthy is the fact that already at this stage, a good indication of the structural failure mechanism is found. The deformed shape of the wall depicted in Figure 7.14 shows that a mechanism is formed with the four parts of the cracked wall, which rotate with respect to each other.

A qualitatively correct prediction of the evolution of damage is thus obtained by the multi-scale approach. In particular, the complex evolution of local cracking mechanisms (coupled to the appearance of mesoscopic damaging zones) is captured with the same sequence as observed experimentally.

7.4 Confined shearing of a full masonry wall

Raijmakers and Vermeltfoort (1992) also performed experiments on shearing walls without an opening. Like for the walls with an opening, these experiments were performed on structures made of a limited number of bricks, and only a qualitative validation in terms of cracking evolution and failure mode may be attempted with the present macroscopic homogenization model. Different mesoscopic and macroscopic dimensions were thus chosen for this test as well. As a consequence, the aim is to verify whether a qualitative agreement can be obtained here as well in terms of the cracking evolution and of the resulting structural failure mode.

7.4.1 Problem description and qualitative experimental behaviour

The tested geometry is shown in Figure 7.15. It consists of a plane masonry wall of dimensions $3000 \times 3000 \times 100$ mm^3. An initial compressive vertical load of 150 kN is applied. As for the open wall test, the imperfect clamping of the top and bottom boundaries of the wall in the loading set-up has been represented by two bands of elements with elastic behaviour, with a stiffness comparable to concrete. The same two-phase loading scheme as for the open wall test was used with compression followed by confined shearing.

The average crack pattern orientations obtained experimentally are illustrated in Figure 7.16, after Raijmakers and Vermeltfoort (1992). The initiation of damage depends on the magnitude of the vertical compression load. For low pre-compression loads, damage is first initiated during the confined shearing phase with the appearance of horizontal tensile cracks at the top left and bottom right corners of the wall (Figure 7.16A). The extension of these tensile damage zones is prohibited by the initial compression, i.e. strong pre-compression states preclude their propagation. The appearance of these tensile cracking zones is followed by the formation of a compressive strut between the bottom left and top right corners. Upon further shearing, diagonal cracking appears in the central zone of the specimen in the compressive strut (Figure 7.16B). Finally, a structural failure mechanism is formed by the propagation of diagonal cracking towards the compressed corners of the wall (Figure 7.16C). Depending on the compressive strength of

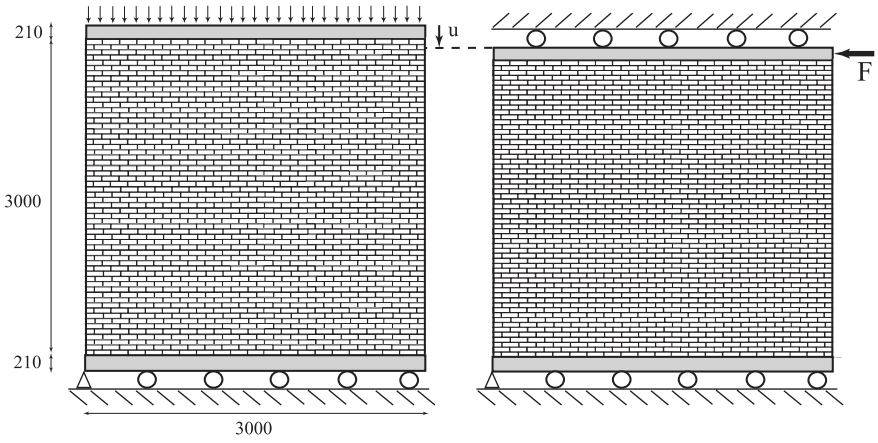

Figure 7.15: Shear test on a full masonry wall: two-phase loading and dimensions

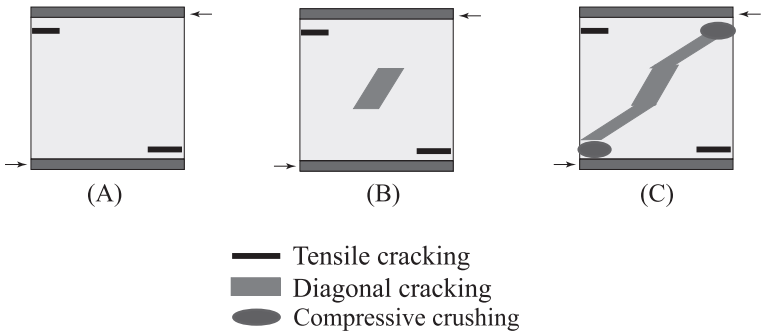

Figure 7.16: Shear test on a full wall – cracking stages observed in experiments by Raijmakers and Vermeltfoort (1992)

the mortar, final failure may occur by compressive crushing at the compressed corners of the wall, associated with brick cracking at the mesoscopic level.

For the numerical simulation, the mesostructure of the material is made of bricks of dimensions $140 \times 65 \times 100$ mm^3 with 10 mm thick mortar joints. The unit cell is discretized with a mesh of 396 elements with a biquadratic interpolation of the displacement field and a bilinear interpolation of the non-local strain field. A generalized plane state assumption is used at the mesoscopic scale, in order to allow an accurate representation of potential brick cracking. The same set of mesoscopic material parameters as used for the open wall test (see also Chapter 4) is applied here. At the macroscopic scale, an unstructured mesh of 114 triangular elements is used with a linear displacement interpolation and a single integration point per element. The use of the multi-scale framework with these discretizations requires the solution of 114 mesoscopic problems containing 2845 independent mesoscopic degrees of freedom each. Based on the ratio between structural and mesoscopic dimensions, a full fine scale modeling of this structure would require the solution of a single equilibrium problem with more than 3 million mesoscopic degrees of freedom.

7.4.2 Numerical results

The load-displacement curve obtained until lack of convergence for the shearing loading phase is shown in Figure 7.17. Again, the evolution of the macroscopic localization during the computation is illustrated in Figures 7.18 to 7.20 for each of the marked points in the load–displacement curve, with the embedded localization bands and the mesoscopic damage in typical unit cells. As depicted in Figure 7.18, cracking indeed initiates at the top left and bottom right corners of the wall. The orientation of the embedded localization bands is almost horizontal, due to vertical tensile stresses. At this stage, nearly no damage is present in the central zone of the specimen as indicated by the two top unit cells depicted in Figure 7.18. Upon further shearing, diagonal cracking is initiated in the compressive strut (Figure 7.19), under the combination of macroscopic vertical compressive and shearing stresses. This stress state causes a fully anisotropic staircase crack pattern to appear at the mesoscopic level, as may be observed

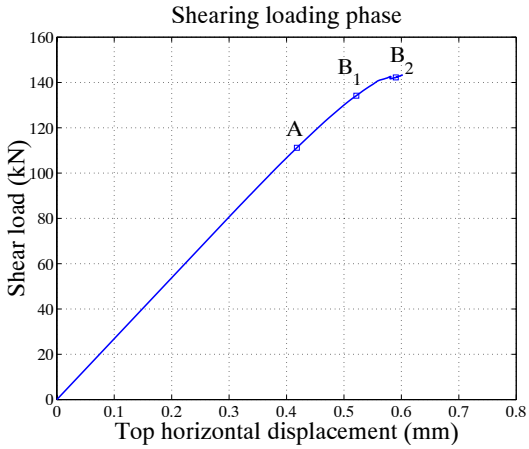

Figure 7.17: Load–displacement curve of shear loading phase for the full shear wall test

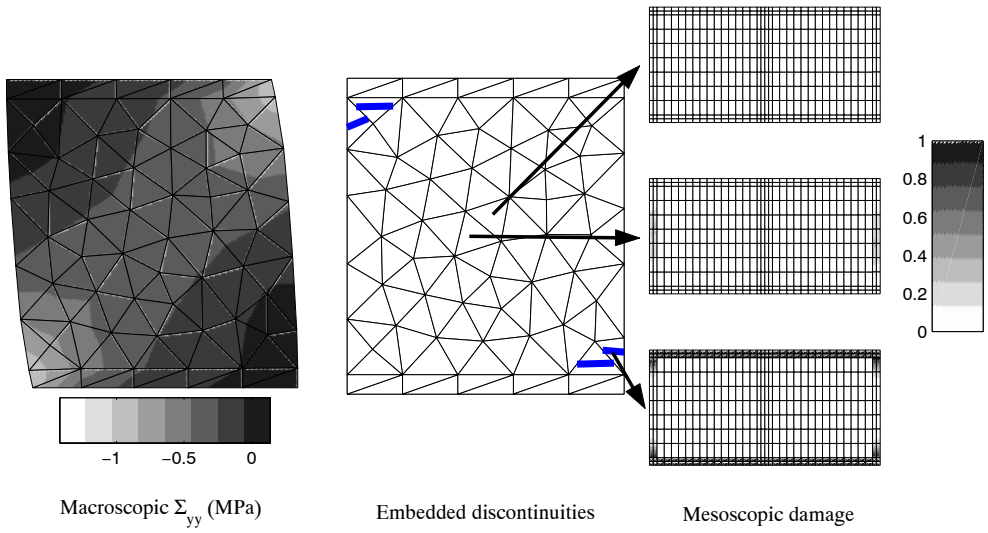

Figure 7.18: Damage state in state A - initiation of tensile cracking: (left) macroscopic vertical stress distribution, (center) embedded discontinuities, (right) mesoscopic damage states

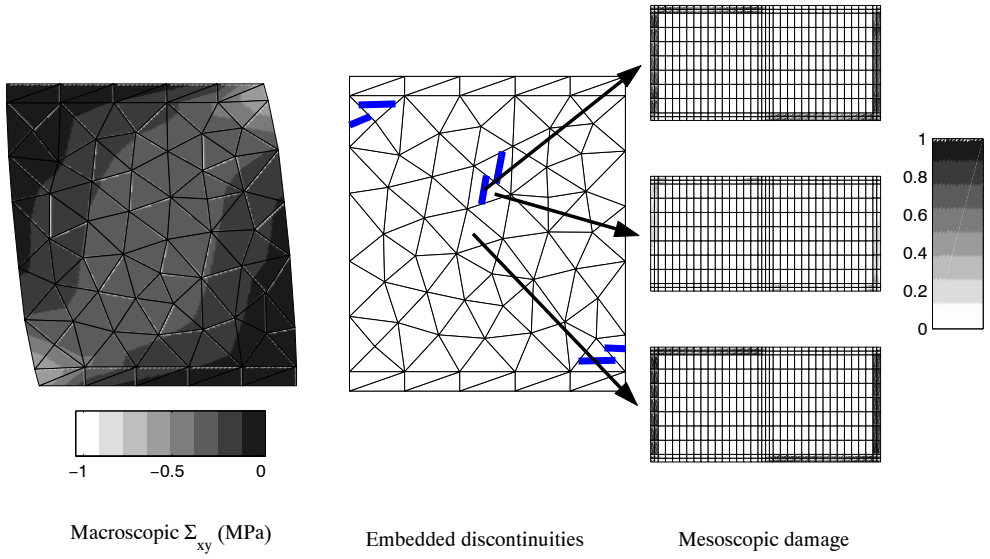

Figure 7.19: Damage state in state B_1 - initiation of diagonal cracking: (left) macroscopic shearing stress distribution, (center) embedded discontinuities, (right) mesoscopic damage states

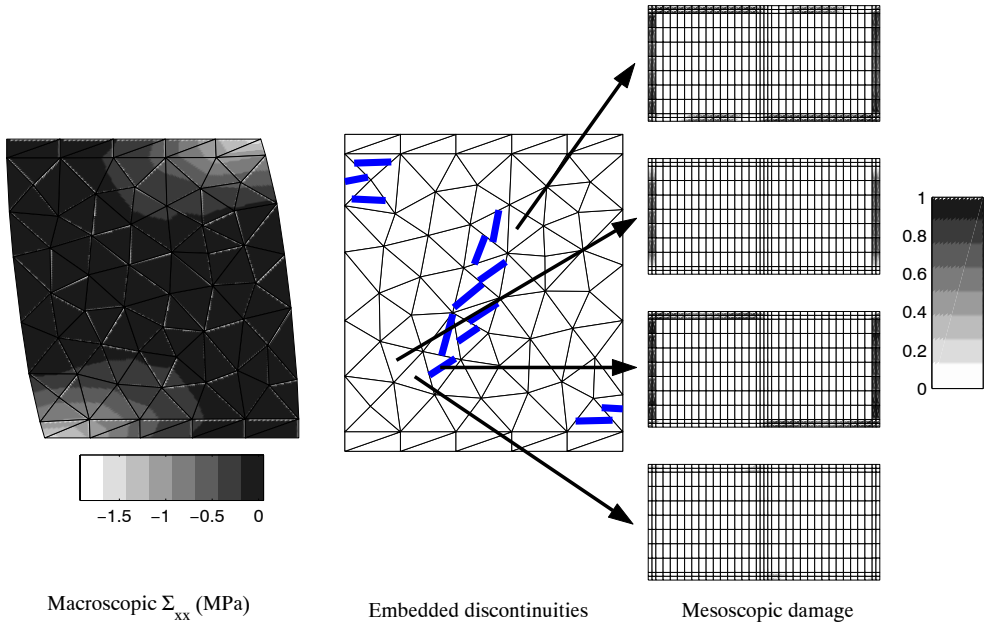

Figure 7.20: Damage state in state B_2 - propagation of diagonal cracking: (left) macroscopic horizontal stress distribution, (center) embedded discontinuities, (right) mesoscopic damage states

for both localized and non localized Gauss points (Figure 7.19 – top and bottom cells). The middle cell in Figure 7.19 represents the damage state of the material surrounding the top cell. This state of damage gives rise to localization exactly at this load level. The rather low values of damage show that the instability is reached relatively early in the damaging process and the nearly vertical orientation of this damage pattern explains the nearly vertical orientation of the localization band in that point. The horizontal cracking bands at the top left and bottom right

corners are the same as in Figure 7.18, showing that these cracking zones become less active at this stage. The diagonal cracking then progresses when the shear load applied to the specimen is increased. This extension of the cracking in the central compressive strut approximately matches the macroscopic shear distribution depicted in Figure 7.19. This is reflected in the set of localization bands present in Figure 7.20, where most bands are oriented in a direction corresponding to the mesoscopic staircase pattern. The mesoscopic damage state of non localized unit cells in Figure 7.20 however shows that damage ultimately tends to progress towards the bottom left and top right corners of the wall.

Chapter 8

Conclusions

The principal objective of the research reported in this dissertation was the development of a mesostructurally based computational tool for the representation of damage effects in masonry structures. Several characteristic aspects of the behaviour of masonry material must be taken into account in order to obtain a sound description of the structural behaviour. Masonry presents a typical ordered mesostructure and is made of quasi-brittle constituents, causing the appearance of anisotropic crack patterns. The natural outcome of these features is that damage localization can be expected at the mesoscopic and macroscopic scales, resulting in complex macroscopic effects such as initial and damage-induced anisotropy, and path dependency. The representation of these effects in structural applications is a considerable challenge, due to the complexity of formulating closed-form constitutive laws formats which take them into account. Such laws in addition have to be identified on the basis of costly and difficult macroscopic experimental procedures, which have to be reproduced for every new mesostructure. Computational homogenization schemes allow to deal with this complexity by retrieving the material response from computations on mesostructural samples (representative volume elements). No macroscopic constitutive format is needed, as the macroscopic material response is obtained from the solution of a deformation-driven mesostructural boundary value problem, in which only the behaviour of the constituents needs to be defined. A macro-meso scale transition is used to define the kinematic boundary conditions of the mesostructural problem in terms of the macroscopic strains. Based on the initial periodicity of the material, periodic boundary conditions are applied on a unit cell to determine the macroscopic material response through a meso-macro scale transition. Any method may be used for the solution of the mesoscopic boundary value problem and any mesoscopic constitutive behaviour may be postulated for the constituents. This flexibility and the numerical derivation of the material response eliminate the need for a macroscopic closed-form constitutive formulation, and render the multi-scale approach particularly attractive for the study of degrading masonry structures.

Any multi-scale approach strongly relies on the accuracy of the constitutive laws postulated for the constituents. A scalar implicit gradient damage model has been used at the mesostructural scale for this purpose in the present study. The accuracy of the applied mesoscopic constitutive models was assessed by computing the response of a unit cell (which is the first order representative volume element for a periodic mesostructure) under various proportional loading

schemes. The use of such a unit cell has been based on a periodic homogenization technique together with some additional assumptions in order to obtain a proper two-dimensional overall description (e.g. a plane stress or a generalized plane state assumption). Specific mesoscopic damage criteria have been chosen to reflect the nature of the constituents. A Drucker-Prager type criterion has been used to reflect the quasi-brittle and frictional nature of mortar, featuring a low tensile strength and a high sensitivity to shear stress states. A compressive cap has been introduced in order to limit the compressive strength of mortar under multi-axial stress states. The brick material has been modeled with a maximum principal stress criterion or a modified von Mises criterion. As illustrated in Chapters 3 and 4, this type of computation allowed to qualitatively capture the influence of the loading direction on the failure load. The characteristic anisotropic shape of the failure envelope was thereby recovered, as well as its dependency on the mesostructural geometry. A reasonable agreement between computational failure envelopes and published results from the literature has been found, as shown in Chapter 4, both with a plane stress and a generalized plane state assumption. This macroscopic strength data has been deduced from mesoscopic geometrical and material data, and it may therefore be expected that the failure modes are also qualitatively captured. For stress states with tension or moderate compression, both the plane stress and generalized plane state assumptions lead to a correct representation of the failure patterns. In particular, failure proved to be accompanied with full damage-induced anisotropy effects when tension and moderate compression are combined with shear, an effect which is mostly neglected in macroscopic models as well as in homogenization procedures in which an orthotropic degradation is assumed. The loss of orthotropy may however have a strong impact on the peak of the stress-strain response as well as on the post-peak regime, as illustrated in Chapter 3. Full anisotropy development may therefore strongly influence the load-carrying capacity predictions due to the resulting stress redistributions. This constitutes an additional motivation for resorting to multi-scale schemes which incorporate this effect in a natural way. For biaxial compressive states however, the plane stress assumption did not allow to represent correctly the out-of-plane failure mode which is observed in experiments. The generalized plane state assumption, takes into account mesoscopic out-of-plane effects linked to the difference between the elastic properties of the constituents and therefore allows to represent this type of failure. Contrarily to other contributions, for the material parameters used in this study, the influence of the mesoscopic assumption on the obtained masonry strength was found to be marginal in proportional loading as shown in Chapter 4, and the use of the generalized plane state did not yield increased strengths. This difference originates from the use of a limited triaxial strength of mortar as explained in Chapter 4. As a result, it was shown that the benefit of unit cell computations independently from their use in multi-scale frameworks is twofold: (i) they allow to validate mesoscopic models before inserting them into the multi-scale framework; (ii) they offer a numerical tool which allows the estimation of strength parameters used in closed-form macroscopic constitutive laws, based on mesoscopic geometrical and material parameters.

Based on the mesoscopic modeling of masonry, a multi-scale approach has been formulated for the response of macroscopic structures. The quasi-brittle nature of the constituents however requires specific enhancements linked to damage localization, the effects of which appear at

both the mesoscopic and macroscopic scales. From a macroscopic point of view, a first consequence of damage localization is the loss of well-posedness of the macroscopic boundary value problem. In order to deal with macroscopic localization, embedded localization bands of a fixed mesostructurally based width have been introduced. A material bifurcation analysis based on the homogenized acoustic tensor has been used to determine the orientation of this localization band. It was shown in Chapter 5 for typical failure patterns encountered in masonry structures that this furnishes a mesostructurally-based criterion for the determination of the localization orientation. The width of the localization bands was obtained from the initial periodicity of the mesostructure. In this study, a localized solution has been considered at a given macroscopic Gauss point when the homogenized behaviour satisfied the bifurcation criterion simultaneously with the appearance of a limit point in the homogenized response. Clearly, this procedure introduces an additional assumption, since a bifurcation may appear in the rising part of the homogenized stress-strain response, especially under shear dominated loading as shown in Chapter 5. However, the localized macroscopic solution at that stage was found to be less critical than the homogeneous solution and it was therefore ignored. This choice was further motivated by the observation that the obtained bifurcation orientation obtained at the limit points matched the underlying damage pattern orientation. Further investigation should however be conducted in order to treat the continuous bifurcation case, based on the properties of the homogenized tangent operator in the vicinity of the detected bifurcation points. As a result of the appearance of a localization band, the energy dissipation was shown to become sensitive to the ratio between the mesostructural and structural (i.e. macroscopic) sizes, thereby introducing a size effect in the description. In order to limit the computational cost, piecewise constant strains and stresses have been considered in the band an in the surrounding material in a localized Gauss point. This assumption leads to a variational inconsistency for cases where a quadratic displacement interpolation is used in the macroscopic description. Although no negative influence of this inconsistency was clearly identified, further developments could be undertaken on this topic as well. The second major consequence of the quasi-brittle nature of the constituents is that the mesoscopic localization of damage in zones of the order of the joint thickness may lead to snap-backs in the homogenized material response. These snap-backs may originate from the response of the unit cell as well as from the averaging used in the localization band model. Since the macro-meso scale transition of the standard multi-scale framework is deformation-driven, an adaptation of the framework was needed to handle such snap-backs. The proposed enhancement consists in solving standard and mesostructural equations in the macrosopic solution procedure in order to force further energy dissipation in the damaging unit cells. These mesoscopic equations were related to the traction continuity requirement in the localization band model and to an additional boundary condition applied to the unit cell computation. Conjugate to these, additional macroscopic unknowns have been defined, related to the strain jump in the localization band model and to a mesoscopic non-local degree of freedom extracted from the mesoscopic unit cell description. The principles of this snap-back enhancement are rather general and can be applied if other mesoscopic descriptions are used. Finally, the additional macroscopic unknowns introduced with this snap-back enhancement may be used in the path following technique used to control the macroscopic solution procedure.

The model presented in this work allows to deal with several specific aspects of masonry structures, such as induced anisotropy or localization. Evidently, further developments might improve the adopted approach and several enhancements can be introduced. The obtained flexibility offered by the use of the multi-scale technique is impeded by its high computational cost compared with purely phenomenological descriptions. A parallel implementation of the framework was therefore used in this study. Other developments may still improve the efficiency of such structural computations. First, the computational cost of the solution of the mesoscopic boundary value problem strongly influences the overall cost for a given structural problem. As a result, any improvement at the mesoscopic scale would significantly improve the overall efficiency. This may be achieved for instance by lumping the behaviour of the mortar joints into cohesive zones, although this choice does not allow to describe mesoscopically out-of-plane failure. More importantly, the multi-scale framework is only needed in those zones where strong mesostructural evolution takes place, e.g. due to damage development. If an efficient way is available to detect elastically behaving zones, homogenized elastic moduli can be used in these zones without repeating the unit cell computations. Mesoscopic scale computations would then only be activated for points in which damage evolution occurs. Further investigations are also required for the choice of the mesoscopic boundary conditions in the macro-meso scale transition. In the approach proposed here, strictly periodic boundary conditions were applied at the boundary of a unit cell. In spite of the fact that this choice was suggested by the initial periodicity of the material and is probably realistic if smoothly varying macroscopic fields are considered, it may be questioned for other loading conditions. This is particularly the case if damage growth localizes, or for points near free boundaries where the periodicity conditions overconstrain the unit cell, leading to an overestimation of its stiffness. Finally, additional features of the behaviour could be included in order to obtain a more accurate representation of the material behaviour. Plasticity effects could be included via cohesive zones to represent dry friction and irreversible straining associated to brick-mortar interface failure under compressive stress states. The use of cohesive zones would also allow an independent representation of the mode II fracture energy of mortar joints. The flexibility of the multi-scale framework makes it an ideal tool for this type of developments, since their effects are naturally accounted for at the macroscopic scale through the proposed scale transition procedure.

Appendix

Homogenised stress state in a 3D masonry cell

The generalised plane state is defined in section 4.3.3 from kinematical assumptions. The symmetry condition with respect to the mid-thickness plane implies that the out-of-plane macroscopic stress components vanish. Using periodic homogenization, the overall stress tensor may be expressed through the relation

$$\mathbf{\Sigma} = \frac{1}{V} \int_{\partial V} \vec{p} \ \vec{x} \ d\partial V \tag{1}$$

The generalised plane state as defined here may be shown to respect the definition of a generalised plane state Anthoine (1997), namely that the macroscopic out-of-plane components vanish

$$\Sigma_{zz} = 0 \qquad \Sigma_{xz} = 0 \qquad \Sigma_{yz} = 0 \tag{2}$$

To this end, a three-dimensional masonry unit cell with in-plane periodicity conditions is considered. The assumptions defined in section 4.3.3 *for the mesoscopic scale* are used (i.e. mesoscopic boundary tractions are considered on the external faces which are constrained to remain planar). The boundary integral in (1) is decomposed in three contributions corresponding to the faces of the cell parallel to the xz, yz and xy planes respectively. Figure 1 represents the position and traction vectors of homologous points on the boundaries of the cell parallel to the xz plane through their projections in the xy and yz planes. The different components of the macroscopic stress tensor may be evaluated from relation (1). For the component Σ_{yz} given by

$$\Sigma_{yz} = \frac{1}{V} \int_{\partial V} p_y x_z \ d\partial V \tag{3}$$

it is always possible (through the imposed symmetry) to find two homologous point such as (1) and (2) for which the contributions in the integral (3) cancel out because

$$x_z^{(1)} = -x_z^{(2)} \qquad \text{and} \qquad p_y^{(1)} = p_y^{(2)} \tag{4}$$

leading to a zero value of the corresponding macroscopic component. Similarly, the contribution of these two boundaries to the component Σ_{zz} also vanishes as it is given by

$$\Sigma_{zz} = \frac{1}{V} \int_{\partial V} p_z x_z \ d\partial V \tag{5}$$

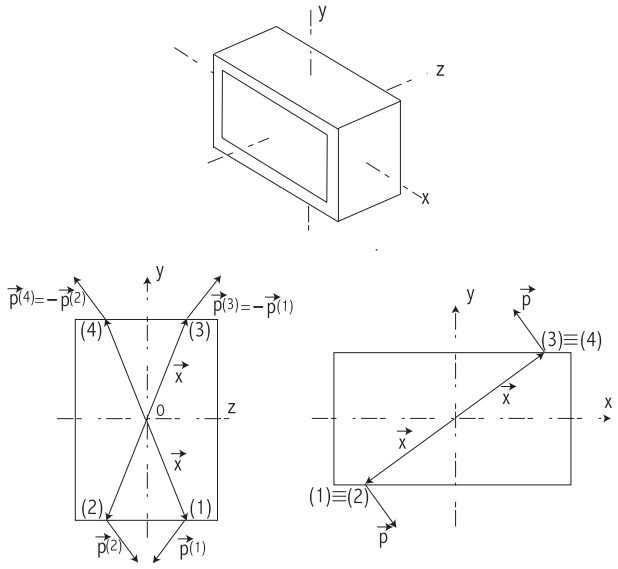

Figure 1: Cell boundary tractions for boundaries parallel to the xz and the xy planes

and it is always possible to find two homologous point such as (1) and (3) for which the contributions in the integral (5) cancel out because

$$x_z^{(1)} = x_z^{(3)} \quad \text{and} \quad p_z^{(1)} = -p_z^{(3)} \tag{6}$$

Finally, the contribution of this pair of boundaries to the Σ_{yy} component may be shown to be different from zero following the same arguments as

$$\Sigma_{yy} = \frac{1}{V} \int_{\partial V} p_y x_y d\partial V \tag{7}$$

and points (1) and (3) are such that

$$x_y^{(1)} = -x_y^{(3)} \quad \text{and} \quad p_y^{(1)} = -p_y^{(3)} \tag{8}$$

A similar reasoning allows to show similar results for the components Σ_{xz} and Σ_{xx} and for the contribution of the other two internal boundaries of the cell to Σ_{zz}. Finally, based on Figure 2 one may deduce the contributions to the macrocopic stress by the external face tractions generated by the generalised plane state assumption. The contributions to the Σ_{xz} and Σ_{yz} components vanish. For instance, the component

$$\Sigma_{yz} = \frac{1}{V} \int_{\partial V_{ext}} p_y x_z \; d\partial V_{ext} \tag{9}$$

vanishes because for homologous points (1) and (2) in Figure 2

$$\begin{array}{rclcrcl} x_z^{(1)} & = & -x_z^{(2)} & \text{and} & p_y^{(1)} & = & p_y^{(2)} \\ x_y^{(1)} & = & x_y^{(2)} & \text{and} & p_z^{(1)} & = & -p_z^{(2)} \end{array} \tag{10}$$

The out-of-plane component Σ_{zz} does not vanish unconditionally because

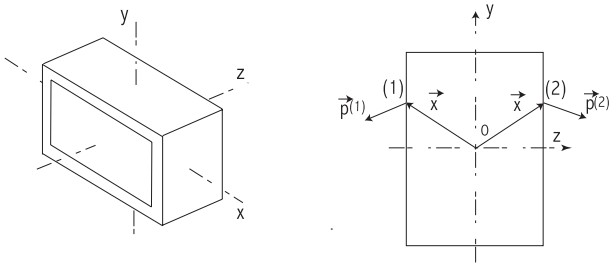

Figure 2: Cell boundary tractions for boundaries parallel to xy plane

$$\Sigma_{zz} = \frac{1}{V} \int_{\partial V_{ext}} p_z x_z \ d\partial V_{ext} \tag{11}$$

and

$$x_z^{(1)} = -x_z^{(2)} = -\frac{e}{2} \quad \text{and} \quad p_z^{(1)} = -p_z^{(2)} \tag{12}$$

The out-of-plane position of the external surface being constant, the overall out-of-plane normal component is given by

$$\Sigma_{zz} = \frac{e}{V} \int_{S_{lat}} p_z \ dS_{lat} \tag{13}$$

where S_{lat} is one of the external faces of the unit cell and e denotes the wall thickness. This overall out-of-plane component should vanish because of equilibrium at the macroscopic scale. Under the generalised plane state assumption, the mesoscopic stress component σ_{zz} is constant in the thickness direction in each phase (because the external faces are constrained to remain planar) and this implies that tractions are acting at the surface S_{lat}. These tractions are such that the integral over a period in (13) vanishes. The external faces are thus stress-free in an average sense under the generalised plane state assumption. Note that in the case of a full three-dimensional representation, the integral (13) vanishes automatically because the external surfaces are stress-free at the mesoscopic scale as well.

Bibliography

Alfano, G., Rosati, L., and Valoroso, N. (2000). A numerical strategy for finite element analysis of no-tension materials. *International Journal for Numerical Methods in Engineering*, 48:317–350.

Anthoine, A. (1995). Derivation of the in-plane elastic characteristics of masonry through homogenization theory. *International Journal of Solids and Structures*, 32(2):137–163.

Anthoine, A. (1997). Homogenization of periodic masonry: plane stress, generalized plane strain or three-dimensional modelling ? *Communications in Numerical Methods in Engineering*, 13:319–326.

Bakhvalov, N. and Panasenko, G. (1989). *Homogenization: Averaging processes in periodic media*. Kluwer Academic Publishers, Dordrecht.

Batoz, J. L. and Dhatt, G. (1979). Incremental displacement algorithms for nonlinear problems. *International Journal for Numerical Methods in Engineering*, 14:1262–1267.

Bažant, Z. P. (1990). Why continuum damage is nonlocal: micromechanics arguments. *Journal of engineering mechanics*, 117(5):1070–1087.

Bažant, Z. P. and Planas, J. (1998). *Fracture and size effect in concrete and other quasi-brittle materials*. CRC Press, Boca Raton.

Bažant, Z. P. and Prat, P. C. (1987). Creep of anisotropic clay: new microplane model. *Journal of Engineering Mechanics*, 113(7):1050–1064.

Bažant, Z. P. and Prat, P. C. (1989). Microplane model for brittle-plastic material: I. theory. *Journal of Engineering Mechanics*, 114(10):1672–1688.

Berto, L., Saetta, A., Scotta, R., and Vitaliani, R. (2002). An orthotropic damage model for masonry structures. *International Journal for Numerical Methods in Engineering*, 55:127–157.

Borre, G. and Maier, G. (1989). On linear versus nonlinear flow rules in strain localization analysis. *Meccanica*, 24:36–41.

Carol, I., Bažant, Z. P., and Prat, P. C. (1992). Geometric damage tensor based on the microplane model. *Journal of Engineering Mechanics*, 117(10):2429–2448.

Carol, I., Rizzi, E., and Willam, K. (2000a). On the formulation of anisotropic elastic degradation: Part I. theory based on a pseudo-logarithmic damage tensor rate. *International Journal of Solids and Structures*, 38(4):491–518.

Carol, I., Rizzi, E., and Willam, K. (2000b). On the formulation of anisotropic elastic degradation: Part II: Generalized pseudo-Rankine model for tensile damage. *International Journal of Solids and Structures*, 38(4):519–546.

Cecchi, A. and Di Marco, R. (2000). Homogenization of masonry walls with a computational oriented procedure. Rigid or elastic blocks ? *European Journal of Mechanics A/Solids*, 19:535–546.

Cecchi, A. and Di Marco, R. (2002). Homogenized strategy towards constitutive identification of masonry. *Journal of Engineering Mechanics*, 128(6):688–697.

Cecchi, A. and Rizzi, N. L. (2001). Heterogeneous elastic solids: a mixed homogenization-rigidification technique. *International Journal of Solids and Structures*, 38:29–36.

Cecchi, A. and Sab, K. (2001). A multi-parameter homogenization study for modeling elastic masonry. *European Journal of Mechanics A/Solids*, 21:249–268.

Cormery, F. (1994). *Contribution à la modélisation de l'endommagement par mésofissuration et du phénomène de localisation associé*. PhD thesis, Université de Poitiers (in French).

Crisfield, M. A. (1981). A fast incremental-iterative solution procedure that handles snap-through. *Computers and Structures*, 13(1-3):55–62.

Cuomo, M. and Ventura, G. (2000). A complementary energy formulation for no tension masonry-like solids. *Computer Methods in Applied Mechanics and Engineering*, 189:313–339.

de Borst, R. (1987). Computation of post-bifurcation and post-failure behavior of strain-softening solids. *Computers and Structures*, 25(2):211–224.

de Borst, R. (2003). Numerical aspects of cohesive-zone models. *Engineering Fracture Mechanics*, 70(14):1743–1757.

de Borst, R., Sluys, L. J., Muhlhaus, H. B., and Pamin, J. (1993). Fundamental issues in finite element analyses of localization of deformation. *Engineering Computations*, 10:99–121.

de Borst, R., Wells, G. N., and Sluys, L. J. (2001). Some observations on embedded discontinuity models. *Engineering Computations*, 18(1-2):241–254.

De Buhan, P. and De Felice, G. (1997). A homogenization approach to the ultimate strength of brick masonry. *Journal of the Mechanics and Physics of Solids*, 45(7):1085–1104.

Dhanasekar, M., Page, A. W., and Kleeman, P. W. (1985). The failure of brick masonry under biaxial stresses. *Proc. Instn Civ. Engrs, Part 2*, pages 295–313.

Dialer, C. P. (2002). Typical masonry failures and repairs: a german engineer's view. *Progress in Structural and Engineering Materials*, 4:332–339.

Dragon, A. (2000). Continuum damage mechanics applied to quasi-brittle materials. In Allix, O. and Hild, F., editors, *Damage mechanics of materials and Structures*, pages 165–203. LMT-ENS Cachan, Elsevier.

Dragon, A., Cormery, F., Desoyer, T., and Halm, D. (1994). Localised failure analysis using damage models. In Chambon, Desrues, and Vardoulakis, editors, *Localisation and bifurcation theory for soils and rocks*. Balkema, Rotterdam.

Evers, L. P., Parks, D. M., Brekelmans, W. A. M., and Geers, M. G. D. (2002). Crystal plasticity model with enhanced hardening by geometrically necessary dislocation accumulation. *Journal of Mechanics and Physics of Solids*, 50:2403–2424.

Feyel, F. and Chaboche, J. L. (2000). FE^2 multiscale approach for modelling the elastovisco-plastic behaviour of long fiber SiC/Ti composite materials. *Computer Methods in Applied Mechanics and Engineering*, 183:309–330.

Geers, M. G. D. (1999a). Enhanced solution control for physically and geometrically non-linear problems. Part I - The subplane control approach. *International Journal for Numerical Methods in Engineering*, 46:177–204.

Geers, M. G. D. (1999b). Enhanced solution control for physically and gometrically non-linear problems. Part II - Comparative performance analysis. *International Journal for Numerical Methods in Engineering*, 46:205–230.

Geers, M. G. D., de Borst, R., Brekelmans, W. A. M., and Peerlings, R. H. J. (1998). Strain-based transient-gradient damage model for failure analyses. *Computer Methods in Applied Mechanics and Engineering*, 160:133–153.

Geers, M. G. D., de Borst, R., and Peerlings, R. H. J. (2000). Damage and crack modeling in single-edge and double-edge notched concrete beams. *Engineering Fracture Mechanics*, 65:247–261.

Giambanco, G. and Di Gati, L. (1997). A cohesive interface model for the structural mechanics of block masonry. *Mechanics Research Communications*, 24(5):503–512.

Giambanco, G., Rizzo, S., and Spallino, R. (2001). Numerical analysis of masonry structures via interface models. *Computer Methods in Applied Mechanics and Engineering*, 190:6493–6511.

Giordano, A., Mele, E., and De Luca, A. (2002). Modelling of historical masonry structures: comparison of different approaches through a case study. *Engineering Structures*, 24:1057–1069.

Godvindjee, S., Kay, G. J., and Simo, J. C. (1995). Anisotropic modelling and numerical simulation of brittle damage in concrete. *International Journal for Numerical Methods in Engineering*, 38:3611–3633.

Grisard, L. (1995). *Modélisation bidimensionnelle de la mise à forme des tôles par la méthode des éléments finis (in French)*. PhD thesis, Université de Liège.

Gutiérrez, M. A. (2003). Path-following constraint based on fracture energy control. In Oñate, E. and Owen, D. R. J., editors, *Proceedings of the VII International Conference on Computational Plasticity - COMPLAS 2003*, Barcelona. CIMNE.

Halm, D. (1997). *Contribution à la modélisation du comportement unilatéral et du frottement dans les matériaux mésofissurés*. PhD thesis, Université de Poitiers (in French).

Halm, D., Dragon, A., and Charles, Y. (2002). A modular damage model for quasi-brittle solids - interaction between initial and induced anisotropy. *Archive of Applied Mechanics*, 72:498–510.

Hanganu, A. D., Oñate, E., and Barbat, A. H. (2002). A finite element methodology for local/global damage evaluation in civil engineering structures. *Computers Structures*, 80:1667–1687.

Jirásek, M. (2000). Comparative study on finite elements with embedded discontinuities. *Computer Methods in Applied Mechanics and Engineering*, 188:307–330.

Kouznetsova, V., Geers, M. G. D., and Brekelmans, W. A. M. (2002). Multi-scale constitutive modelling of heterogeneous materials with a gradient-enhanced computational homogenization scheme. *International Journal for Numerical Methods in Engineering*, 54:1235–1260.

Kouznetsova, V. G. (2002). *Computational homogenization for the multi-scale analysis of multi-phase materials*. PhD thesis, Eindhoven University of Technology.

Kouznetsova, V. G., Brekelmans, W. A. M., and Baaijens, F. T. P. (2001). An approach to micro-macro modeling of heterogeneous materials. *Computational Mechanics*, 27:37–48.

Kuhl, E., de Borst, R., and Ramm, E. (2000). An anisotropic gradient damage model for quasi-brittle materials. *Computer Methods in Applied Mechanics and Engineering*, 183(1-2):87–103.

Kuhl, E. and Ramm, E. (1999). Simulation of strain localization with gradient enhanced damage models. *Computational Materials Science*, 16(1–4):176–185.

Lemaitre, J. (1990). *A course on damage mechanics*. Springer-Verlag, Berlin.

Lourenço, P. B. (1996). *Computational Strategies for Masonry Structures*. PhD thesis, Delft University of Technology.

Lourenço, P. B. (1998). Experimental and numerical issues in the modelling of the mechanical behaviour of masonry. In Roca, P., Gonzalez, J. L., Oñate, E., and Lourenço, P. B., editors, *Structural analysis of historical constructions II*, pages 57 – 91. CIMNE, Barcelona.

Lourenço, P. B. (2002). Computations on historic masonry structures. *Progress in Structural Engineering and Materials*, 4:301–319.

Lourenço, P. B., de Borst, R., and Rots, J. G. (1997). A plane stress softening plasticity model for orthotropic materials. *International Journal for Numerical Methods in Engineering*, 40(21):4033–4057.

Luciano, R. and Sacco, E. (1997). Homogenization technique and damage model for old masonry material. *International Journal of Solids and Structures*, 34(24):3191–3208.

Luciano, R. and Sacco, E. (1998). A damage model for masonry structures. *European Journal of Mechanics A/Solids*, 17(2):285–303.

Massart, T. J., Peerlings, R. H. J., and Geers, M. G. D. (2004a). Mesoscopic modeling of damage-induced anisotropy in brick masonry. *Submitted for publication in European Journal of Mechanics A/Solids*.

Massart, T. J., Peerlings, R. H. J., and Geers, M. G. D. (2004b). A multi-scale approach for structural masonry walls computations - part I: Concepts and treatment of localization. *To be submitted for publication in International Journal for Numerical Methods in Engineering*.

Massart, T. J., Peerlings, R. H. J., Geers, M. G. D., and Gottcheiner, S. (2004c). Mesoscopic modeling of failure in brick masonry accounting for three-dimensional effects. *Submitted for publication in Engineering Fracture Mechanics*.

Mazzolani, F. M. and Mandara, A. (2002). Modern trends in the use of special metals for the improvement of historical and monumental structures. *Engineering Structures*, 24:843–856.

Miehe, C. (2002). Strain-driven homogenization of inelastic microstructures and composites based on an incremental variational formulation. *International Journal for Numerical Methods in Engineering*, 55(11):1285–1322.

Mindlin, R. D. (1964). Micro-structure in linear elasticity. *Archives of Rational Mechanics and Analysis*, 16:51–78.

Page, A. W. (1981). The biaxial compressive strength of brick masonry. *Proc. Instn Civ. Engrs, Part 2*, 71:893–906.

Page, A. W. (1983). The strength of brick masonry under biaxial tension-compression. *International Journal of Masonry Constructions*, 3:26–31.

Pande, G. N., Liang, J. X., and Middleton, J. (1989). Equivalent elastic moduli for brick masonry. *Computers and Geotechnics*, 8:243–265.

Papa, E. (1996). A unilateral damage model for masonry based on a homogenisation procedure. *Mechanics of Cohesive-Frictional Materials*, 1:349–366.

Papa, E. and Nappi, A. (1997). Numerical modelling of masonry: a material model accounting for damage effects and plastic strains. *Applied Mathematics Modelling*, 21:319–335.

Peerlings, R. H. J. (1999). *Enhanced damage modelling for fracture and fatigue*. PhD thesis, Eindhoven University of Technology.

Peerlings, R. H. J., de Borst, R., Brekelmans, W. A. M., and de Vree, J. H. P. (1996). Gradient-enhanced damage for quasi-brittle materials. *International Journal for Numerical Methods in Engineering*, 39:3391–3403.

Peerlings, R. H. J., Geers, M. G. D., de Borst, R., and Brekelmans, W. A. M. (2001). A critical comparison of nonlocal and gradient-enhanced softening continua. *International Journal of Solids and Structures*, 38:7723–7746.

Pegon, P. and Anthoine, A. (1997). Numerical strategies for solving continuum damage problems with softening: application to the homogenization of masonry. *Computers and Structures*, 64(1-4):623–642.

Pietruszczak, S. and Ushaksarei, R. (2003). Description of inelastic behaviour of structural masonry. *International Journal of Solids and Structures*, 40:4003–4019.

Pijaudier-Cabot, G. (1991). *Rupture et calculs à la ruine*. Thèse d'habilitation, Université Paris VI Pierre et Marie Curie - LMT ENS Cachan, (in French).

Prat, P. C. and Gens, A. (1994). Microplane formulation for quasibrittle materials with anisotropy and damage. In Bazant, Z. P., Bittnar, Z., Jirasek, M., and Mazars, J., editors, *Fracture and Damage in quasibrittle structures*, London. E-FN Spon.

Raijmakers, T. M. J. and Vermeltfoort, A. T. (1992). Deformation controlled tests in masonry shear walls (in Dutch). Technical Report B-92-1156, TNO - Bouw, Delft, The Netherlands.

Rice, J. R. (1976). The localization of plastic deformations. In Koiter, W. T., editor, *Theoretical and Applied Mechanics*. North-Holland Publishing Company.

Rice, J. R. and Rudnicki, J. W. (1980). A note on some features of the theory of localization of deformation. *International Journal of Solids and Structures*, 16:597–605.

Rots, J., editor (1997). *Structural Masonry - an experimental-numerical basis for practical design rules*. A.A. Balkema, Rotterdam.

Runesson, K., Ottosen, N. S., and Peric, D. (1991). Discontinuous bifurcations of elastic-plastic solutions at plane stress and plane strain. *International Journal of Plasticity*, 7:99–121.

Sanchez-Hubert, J. and Sanchez-Palencia, E. (1992). *Introduction to asymptotic methods and homogenization (in French)*. Masson, Paris.

Simo, J. C. and Taylor, R. L. (1985). Consistent tangent operators for rate-independent elastoplasticity. *Computer Methods in Applied Mechanics and Engineering*, 48:101–118.

Sluys, L. J. and Berends, A. H. (1998). Discontinuous failure analysis for mode-I and mode-II localization problems. *International Journal of Solids and Structures*, 35(31-32):4257–4274.

Smit, R. (1998). *Toughness of Heterogeneous Polymeric Systems. A Modeling Approach*. PhD thesis, Eindhoven University of Technology.

Smit, R. J. M., Brekelmans, W. A. M., and Meijer, H. E. H. (1998). Prediction of the mechanical behaviour of nonlinear heterogeneous systems by multi-level finite element modeling. *Computer Methods in Applied Mechanics and Engineering*, 155:181–192.

Toupin, R. A. (1962). Elastic materials with couple stress. *Archives of Rational Mechanics and Analysis*, 11:385–414.

Trovalusci, P. and Masiani, R. (1999). Material symmetries of micropolar continua equivalent to lattices. *International Journal of Solids and Structures*, 36:2091–2108.

Trovalusci, P. and Masiani, R. (2003). Non-linear micropolar and classical continua for anisotropic discontinuous materials. *International Journal of Solids and Structures*, 40(5):1281–1297.

van der Pluijm, R. (1992). Deformation controlled shear tests on masonry (in Dutch). Technical Report BI-92-104, TNO Building and Construction, Delft, The Netherlands.

van der Pluijm, R. (1997). Non-linear behaviour of masonry under tension. *Heron*, 42(1):25–54.

van der Pluijm, R. (1999). *Out-of-plane bending of masonry - behaviour and strength*. PhD thesis, Eindhoven University of Technology.

van der Pluijm, R. and Vermeltfoort, A. T. (1991). Overview of deformation controlled combined tensile and shear tests (in Dutch). Technical report, TNO Building and Construction, Delft, The Netherlands.

van der Sluis, O. (2001). *Homogenisation of Structured Elastoviscoplastic Solids*. PhD thesis, Eindhoven University of Technology.

van Zijl, G. P. A. G. (2000). *Computational modelling of masonry creep and shrinkage*. PhD thesis, Delft University of Technology.

van Zijl, G. P. A. G., de Borst, R., and Rots, J. G. (2001). A numerical model for the time-dependent cracking of cementitious materials. *International Journal for Numerical Methods in Engineering*, 52:637–654.

Wells, G. N. (2001). *Discontinuous modelling of strain localization and failure*. PhD thesis, Delft University of Technology.

Willam, K., Kang, H., Shing, B., and Spacone, E. (1998). Analysis of shear failure in concrete materials. In de Borst, R. and van der Giessen, E., editors, *Material instabilities in solids*, chapter 3, pages 27–39. Wiley, Chichester.

Zucchini, A. and Lourenço, P. B. (2002). A micro-mechanical model for the homogenization of masonry. *International Journal of Solids and Structures*, 39:3233–3255.

Summary

The conservation of structures of the historical heritage is an increasing concern nowadays for public authorities. The technical design phase of repair operations for these structures is of prime importance. Such operations usually require an estimation of the residual strength and of the potential structural failure modes of structures to optimize the choice of the repairing techniques. Although rules of thumb and codes are widely used, numerical simulations now start to emerge as valuable tools. Such alternative methods may be useful in this respect only if they are able to account realistically for the possibly complex failure modes of masonry in structural applications. The mechanical behaviour of masonry is characterized by the properties of its constituents (bricks and mortar joints) and their stacking mode. Structural failure mechanisms are strongly connected to the mesostructure of the material, with strong localization and damage-induced anisotropy. The currently available numerical tools for this material are mostly based on approaches incorporating only one scale of representation. Mesoscopic models are used in order to study structural details with an explicit representation of the constituents and of their behaviour. The range of applicability of these descriptions is however restricted by computational costs. At the other end of the spectrum, macroscopic descriptions used in structural computations rely on phenomenological constitutive laws representing the collective behaviour of the constituents. As a result, these macroscopic models are difficult to identify and sometimes lead to wrong failure mode predictions.

The purpose of this study is to bridge the gap between mesoscopic and macroscopic representations and to propose a computational methodology for the analysis of plane masonry walls. To overcome the drawbacks of existing approaches, a multi-scale framework is used which allows to include mesoscopic behaviour features in macroscopic descriptions, without the need for an a priori postulated macroscopic constitutive law. First, a mesoscopic constitutive description is defined for the quasi-brittle constituents of the masonry material, the failure of which mainly occurs through stiffness degradation. The mesoscopic description is therefore based on a scalar damage model. Plane stress and generalized plane state assumptions are used at the mesoscopic scale, leading to two-dimensional macroscopic continuum descriptions. Based on periodic homogenization techniques and unit cell computations, it is shown that the identified mesoscopic constitutive setting allows to reproduce the characteristic shape of (anisotropic) failure envelopes observed experimentally. The failure modes corresponding to various macroscopic loading directions are also shown to be correctly captured. The in-plane failure mechanisms are correctly represented by a plane stress description, while the generalized plane state assumption, introducing simplified three-dimensional effects, is shown to be needed

to represent out-of-plane failure under biaxial compressive loading. Macroscopic damage-induced anisotropy resulting from the constituents' stacking mode in the material, which is complex to represent properly using macroscopic phenomenological constitutive equations, is here obtained in a natural fashion. The identified mesoscopic description is introduced in a scale transition procedure to infer the macroscopic response of the material. The first-order computational homogenization technique is used for this purpose to extract this response from unit cells. Damage localization eventually appears as a natural outcome of the quasi-brittle nature of the constituents. The onset of macroscopic localization is treated as a material bifurcation phenomenon and is detected from an eigenvalue analysis of the homogenized acoustic tensor obtained from the scale transition procedure together with a limit point criterion. The macroscopic localization orientations obtained with this type of detection are shown to be strongly related to the underlying mesostructural failure modes in the unit cells. A well-posed macroscopic description is preserved by embedding localization bands at the macroscopic localization onset, with a width directly deduced from the initial periodicity of the mesostructure of the material. This allows to take into account the finite size of the fracturing zone in the macroscopic description. As a result of mesoscopic damage localization in narrow zones of the order of a mortar joint, the material response computationally deduced from unit cells may exhibit a snap-back behaviour. This precludes the use of such a response in the standard strain-driven multi-scale scheme. Adaptations of the multi-scale framework required to treat the mesostructural response snap-back are proposed. This multi-scale framework is finally applied for a typical confined shear wall problem, which allows to verify its ability to represent complex structural failure modes.

Samenvatting

Het behoud van historische bouwwerken is een toenemende zorg voor lokale en nationale overheden. In het bijzonder het technische ontwerp van reparatiewerkzaamheden is hierbij van belang. Zulke werkzaamheden vereisen meestal een schatting van de residuele sterkte en van mogelijke faalmechanismen om een optimale keuze te kunnen maken tussen de verschillende beschikbare technieken. Hoewel hiervoor veelal vuistregels en normen gebruikt worden, beginnen ook numerieke simulaties een waardevol gereedschap te vormen. Simulaties kunnen echter alleen van nut zijn als ze de verschillende mogelijke faalmechanismen van metselwerk op een realistische wijze kunnen beschrijven. Het mechanische gedrag van metselwerk hangt af van de eigenschappen van de steen en het voegmateriaal en van het gebruikte metselverband. Ook structurele faalmechanismen worden in sterke mate bepaald door de mesostructuur van het materiaal en vertonen daardoor een sterk lokaal karakter en een door schade veroorzaakte anisotropie. De beschikbare numerieke materiaalbeschrijvingen zijn gebaseerd op benaderingen die slechts een enkele schaal van observatie beschouwen. Mesoscopische modellen worden gebruikt voor de bestudering van structurele details en brengen daartoe de volledige mesostructuur in rekening, inclusief het afzonderlijke gedrag van de steen en de voeg. De toepasbaarheid van deze beschrijvingen wordt echter beperkt door de benodigde rekentijd. Aan het andere einde van het spectrum bevinden zich de macroscopische modellen die worden gebruikt in grootschalige berekeningen. Deze modellen gebruiken fenomenologische constitutieve wetten die het collectieve gedrag van het metselwerk beschrijven. Echter, de identificatie van de materiaalparameters in deze wetten verloopt veelal moeizaam en ze leveren soms onjuiste voorspellingen van het faalmechanisme.

Het doel van deze studie is om de kloof tussen mesoscopische en macroscopische beschrijvingen te overbruggen en om daarmee te komen tot meer betrouwbare computer simulaties van vlakke gemetselde muren. Om de tekortkomingen van de bestaande technieken weg te nemen wordt een zogenaamde multi-schaal benadering gebruikt. Deze maakt het mogelijk om mesoscopische effecten te beschrijven in macroscopische berekeningen, zonder vooraf macroscopische constitutieve wetten te poneren. Eerst wordt een mesoscopische constitutieve beschrijving ontwikkeld voor de quasi-brosse componenten van het metselwerk. Het falen van deze componenten wordt met name gekenmerkt door het verlies van stijfheid en wordt daarom beschreven met een isotroop, scalair schademodel. De veronderstelling van een vlakspanningstoestand of een gegeneraliseerde vlakke toestand op de schaal van de mesostructuur leidt tot een tweedimensionale macroscopische continuümbeschrijving. Met behulp van periodieke homogenisatie technieken en eenheidscel-berekeningen wordt aangetoond dat de mesoscopische

modellering de karakteristieke (anisotrope) vorm van experimentele faalcurven kan reproduceren. Tevens wordt voor verscheidene belastingsrichtingen het juiste faalmechanisme voorspeld. Faalmechanismen in het vlak van de muur kunnen correct weergegeven worden met de vlakspanningsbenadering, terwijl de gegeneraliseerde vlakke toestand – die op vereenvoudigde wijze driedimensionale effecten in rekening brengt – nodig is om falen uit vlak te beschrijven, zoals dat optreedt in biaxiale compressie. De macroscopische anisotropie die het gevolg is van de schade-ontwikkeling in combinatie met het gebruikte verband, en die moeilijk beschreven kan worden met fenomenologische macroscopische relaties, manifesteert zich nu op een natuurlijke wijze. Het macroscopische gedrag van het metselwerk wordt rechtstreeks uit de mesoscopische beschrijving bepaald door middel van een schaalovergang. Hiertoe wordt een eerste-orde numerieke homogenisatietechniek toegepast op de resultaten van eenheidscel-analyses. Lokalisatie van schade treedt op als het natuurlijke resultaat van het quasi-brosse schadeproces in de steen en het cement. Het ontstaan van macroscopische lokalisatie wordt beschouwd als een bifurcatieprobleem en wordt gedetecteerd door middel van een eigenwaarde-analyse van de gehomogeniseerde akoestische tensor, gecombineerd met een limietpunt-criterium. Van de macroscopische lokalisatie die op deze wijze wordt verkregen wordt aangetoond dat ze verband houdt met de onderliggende mesostructurele faalmechanismen. Een goed gestelde macroscopische beschrijving wordt gegarandeerd door het aanbrengen van lokalisatiebanden op iedere plek waar aan het lokalisatiecriterium voldaan wordt. De breedte van deze banden wordt rechtstreeks afgeleid uit de periodiciteit van de initiële mesostructuur, wat het mogelijk maakt om de eindige breedte van de proceszone in rekening te brengen in de macroscopische beschrijving. Als gevolg van de sterk gelokaliseerde schade-ontwikkeling op het mesoniveau, in banden met een breedte die vergelijkbaar is met die van de voeg, kan het gehomogeniseerde gedrag zogenaamd snap-back instabiliteiten vertonen. Als gevolg hiervan kan dit gedrag niet rechtstreeks gebruikt worden in het standaard, rekgestuurde multischaal algoritme. Aanpassingen van het algoritme worden daarom voorgesteld, waarmee mesostructurele snap-back wel kan worden gesimuleerd. Tot slot wordt de volledige multischaal rekenwijze toegepast op een typisch probleem uit de praktijk: een opgesloten muur die wordt belast in afschuiving. Deze toepassing toont aan dat de modellering gecompliceerde structurele faalmechanismen kan beschrijven.

Résumé

La conservation du patrimoine historique devient un sujet de préoccupation majeur pour les autorités publiques. La conception des opérations de rénovation de telles structures en acquiert une importance accrue. Celle-ci requiert en général une estimation de la sécurite résiduelle et des modes de ruine potentiels des édifices en vue d'optimiser le choix des techniques de rénovation. Malgré l'utilisation étendue de règles de bonne pratique et de codes dans la majorité des études actuelles, les simulations numériques commencent à être considérées comme des outils essentiels. Ce type de méthode ne peut toutefois être utile que s'il permet la prise en compte réaliste des modes de rupture complexes du materiau maçonnerie dans les calculs structuraux. Le comportement mécanique de la maçonnerie est déterminé par les propriétés de ses constituants (briques et joints) et leur arrangement géométrique. Les modes de rupture observés sont fortement liés à la structure du matériau à l'échelle mésoscopique, avec l'apparition de localisation de l'endommagement et d'effets d'anisotropie induits par l'endommagement. Les modèles numériques existants pour ce type de matériau relèvent essentiellement d'approches n'incluant qu'une échelle de représentation. Des modèles mésoscopiques sont utilisés pour l'étude de détails structuraux, avec une représentation explicite des constituants et de leur comportement. Le domaine d'application de cette approche est toutefois limité par le coût de tels calculs. D'autre part, les descriptions macroscopiques utilisées dans les calculs structuraux sont basées sur des lois constitutives phénoménologiques, représentant le comportement collectif des constituants. Ceci rend l'identification de tels modèles difficile et mène parfois à des prédictions erronées en termes de modes de rupture.

Cette étude présente une approche construisant un lien entre les descriptions mésoscopique et macroscopique, en proposant une approche numérique pour l'étude du comportement de structures planes en maçonnerie. Afin de remédier aux difficultés rencontrées dans les modèles phénoménologiques, les caractéristiques mésoscopiques sont introduites dans la description macroscopique par l'intermédiaire d'un modèle multi-échelles, évitant de devoir formuler a priori des lois constitutives macroscopiques. Une description constitutive est tout d'abord mise au point pour les constituants quasi-fragiles, dont la rupture est principalement caractérisée par une dégradation de la rigidité. Cette description mésoscopique est basée sur un modèle scalaire d'endommagement. L'utilisation des hypothèses de contraintes planes et d'état plan généralisé mène à des descriptions homogénéisées bidimensionnelles. Les techniques d'homogénéisation périodique et des calculs sur des cellules mésoscopiques couplés à ces lois constitutives mésoscopiques permettent de reproduire la forme caractéristique des enveloppes de rupture observée expérimentalement. Les modes de ruptures en plan sont en outre correctement reproduits pour

différents modes de chargement par une description en contraintes planes. L'état plan généralisé est requis afin de traiter la rupture hors plan sous compression biaxiale. Les effets macroscopiques d'anisotropie induite, déterminés par l'arrangement géométrique des constituants et très complexes à représenter phénoménologiquement, sont de plus obtenus naturellement par l'approche proposée. La description mésoscopique est ensuite introduite dans une transition d'échelle pour en déduire la réponse macroscopique du matériau. L'homogénéisation numérique vers un milieu continu du premier ordre est utilisée afin d'extraire cette réponse de calculs sur des cellules mésoscopiques. La nature quasi-fragile des constituants a pour conséquence naturelle la localisation de l'endommagement. L'apparition de la localisation à l'échelle macroscopique est traitée comme un phénomène de bifurcation matérielle et est détectée par une analyse aux valeurs propres du tenseur acoustique homogénéisé obtenu par la transition d'échelle, en conjonction avec un critère de point limite. Les orientations macroscopiques de localisation obtenues par cette approche sont étroitement liées aux mécanismes d'endommagement sous-jacents dans les cellules mésoscopiques. Le caractère bien posé du problème d'équilibre macroscopique est préservé par l'introduction de bandes de localisation, avec une largeur caractéristique directement déduite de la période initiale de la texture du matériau. Ceci permet la prise en compte dans la description macroscopique du caractère fini de la taille de la zone de rupture. D'autre part, la localisation de l'endommagement à l'échelle mésoscopique dans des zones de taille réduite de l'ordre de la taille des joints de mortier cause l'apparition de phénomènes de snap-back dans la réponse matérielle homogénéisée déduite des cellules mésoscopiques. Ce type de comportement ne peut être traité par un schéma multi-échelles classique pour lequel la transition d'échelle est basée sur un contrôle en déformations. Les adaptations complémentaires du schéma multi-échelles nécessaires pour traiter ce type de comportement sont proposées. Le modèle multi-échelles ainsi obtenu est enfin appliqué au calcul d'un panneau de cisaillement permettant de vérifier sa capacité à représenter des modes de ruine complexes au niveau structural.

Acknowledgements - Remerciements

This work was initiated almost five years ago with a come-back to the academic world at Brussels university, l'Université Libre de Bruxelles. The road to the end was everything but a straight road, which made this period very interesting, but also very tough. As often, behind a single author name lies the work and the dedication of several persons who 'enlightened' my way and helped me to get through. A personality is the product of his encounters with others. I had the great opportunity to meet or to re-discover exceptional people along this work period, to whom I would like to express my deep gratitude.

From a professional point of view (and in alphabetical order), I want to acknowledge the guidance and support of Philippe Bouillard, Marc Geers and Ron Peerlings. Philippe Bouillard supported me in this project from the very start, allowing me to take first steps in the computational mechanics world and making my stays in Eindhoven possible in the frame of the Homere contract, stepping out from teaching activities for a while. This strong support has been practical as well as moral during the whole preparation of this dissertation. This project would certainly not have come to an end without a fortunate meeting with my first promotor Marc Geers, in the course of the year 2000, triggered by questions I addressed him via e-mail. This meeting was truly the bifurcation that started this whole 'adventure'. This 'lucky' encounter resulted in a close collaboration with Marc Geers and Ron Peerlings, allowing all the developments presented in this work. During this period the competence, the imagination, the moral support (balancing my natural tendency to skepticism), and the sense of humour of what I called privately my Eindhoven 'dream team' have been invaluable assets for me.
I feel very lucky and very proud of having worked with these three persons and hope that this was only the start of a continued collaboration.
Next, I would like to address a special word for the precious help of Varvara Kouznetsova in adapting the model to parallel computing in the latest stage of the project when the pressure was at its highest.

Special thanks to Guy Warzée, head of my Brussels department, for putting his confidence in me since I came back to academics; and to Guy Paulus, Leo Wouters and Patrick van Brakel for computer-related support. I would also like to acknowledge the interactions with all my colleagues both in Brussels and in Eindhoven and for the good working atmosphere prevailing in both departments. Thanks also to Katy, Rajan, Erik, Valou, Geneviève, Vincent, and to Alpay and Adnan, my room mates in TU/e. Finally, many thanks also to Karel and Elly Lindner for their warm welcome during my stays in The Netherlands.

D'un point de vue plus personnel, je souhaiterais tout d'abord présenter mes excuses à tous les membres de ma famille au sens large et à tous mes amis pour le long silence radio de ces dernières années lié à mes séjours fréquents à Eindhoven. Qu'ils se rassurent, les retrouvailles n'en seront que meilleures. Ces séjours ont constitué une période très difficile pour Christine, Alexandre et Mathieu. Je ne serais très certainement pas arrivé au bout de cette aventure sans l'aide de ma famille proche qui a supporté Christine au quotidien tout au long de cette période. Merci à tous d'avoir mobilisé 'toutes les forces vives' de la famille vers cet objectif. Mes remerciements dans ce sens vont plus spécialement à mes parents, et à Mireille, Danièle et Christian et Micheline, pour les 'séances taxi', les nombreuses gardes d'enfants (je connais un jardin qui en a été transfiguré) et les prêts de voiture.

Je réserve mes remerciements les plus forts à Christine, Alexandre et Mathieu pour leur soutien continu tout au long de cette période. La joie de vivre et la gentillesse de mes deux petits bonshommes Mathieu et Alexandre (qui m'a proposé plusieurs fois d'effectuer une partie de mon travail pour me décharger et qui m'a fréquemment accompagné les week-ends pour lancer 'des petits calculs' ;-) m'ont permis de tenir le coup dans le 'sprint final' de cette dernière année. Le développement harmonieux des enfants a été rendu possible en dépit de cette période difficile grâce à la présence de leur 'mère-veilleuse' Christine ...

Enfin, il me reste à remercier ma Tine, ma petite merveille de femme, sans qui je ne serais rien. Tine, ton amour, ton endurance durant ces dernières années, et ton obstination à me convaincre dans les moments difficiles que le meilleur est à venir et ont été mon principal moteur. Ce travail est au moins autant le tien que le mien ...

Sachez tous les trois que vous avez été présents à mon esprit durant chaque instant de la préparation de ce travail: 'The sweetest harmony is the voice of the beloved ones'. Merci à tous les trois d'avoir été à la fois ma fierté, mon refuge et ma certitude en cette période chahutée.

Après avoir reçu beaucoup, il est temps pour moi de donner, tant sur le plan familial que professionnel ...

Thierry Massart,
Septembre 2003